LOCKHEED MARTIN ENERGY RESEARCH LIBRARIES

3 4456 0515873 5

AL RESEARCH LIBRARY
UMENT COLLECTION

ORNL-4063
UC-20 – Controlled Thermonuclear Processes

THERMONUCLEAR DIVISION
SEMIANNUAL PROGRESS REPORT
FOR PERIOD ENDING OCTOBER 31, 1966

OAK RIDGE NATIONAL LABORATORY
operated by
UNION CARBIDE CORPORATION
for the
U.S. ATOMIC ENERGY COMMISSION

Printed in the United States of America. Available from Clearinghouse for Federal Scientific and Technical Information, National Bureau of Standards, U.S. Department of Commerce, Springfield, Virginia 22151
Price: Printed Copy $3.00; Microfiche $0.65

LEGAL NOTICE

This report was prepared as an account of Government sponsored work. Neither the United States, nor the Commission, nor any person acting on behalf of the Commission:

A. Makes any warranty or representation, expressed or implied, with respect to the accuracy, completeness, or usefulness of the information contained in this report, or that the use of any information, apparatus, method, or process disclosed in this report may not infringe privately owned rights; or

B. Assumes any liabilities with respect to the use of, or for damages resulting from the use of any information, apparatus, method, or process disclosed in this report.

As used in the above, "person acting on behalf of the Commission" includes any employee or contractor of the Commission, or employee of such contractor, to the extent that such employee or contractor of the Commission, or employee of such contractor prepares, disseminates, or provides access to, any information pursuant to his employment or contract with the Commission, or his employment with such contractor.

ORNL-4063

Contract No. W-7405-eng-26

THERMONUCLEAR DIVISION
SEMIANNUAL PROGRESS REPORT
for Period Ending October 31, 1966

JANUARY 1967

OAK RIDGE NATIONAL LABORATORY
Oak Ridge, Tennessee
operated by
UNION CARBIDE CORPORATION
for the
U. S. ATOMIC ENERGY COMMISSION

LOCKHEED MARTIN ENERGY RESEARCH LIBRARIES

3 4456 0515873 5

Contents

INTRODUCTION vii

ABSTRACTS xi

1. INJECTION AND ACCUMULATION: NEUTRAL INJECTION EXPERIMENTS (DCX-1.5) 1
   - 1.1 Introduction 1
   - 1.2 Apparatus 1
     - 1.2.1 General Description of the DCX-1.5 Facility 1
     - 1.2.2 Energy Analyzer 2
   - 1.3 Experimental Results 3
     - 1.3.1 Vacuum 3
     - 1.3.2 Energy Analysis 3
     - 1.3.3 Density Determinations 3
     - 1.3.4 RF Measurements 5
     - 1.3.5 Magnesium Cell and Properties of the Neutral Beam 7
     - 1.3.6 Comparisons with the ALICE Neutral Injection Facility 8
   - 1.4 Summary 9

2. INJECTION AND ACCUMULATION: MULTIPLE-PASS EXPERIMENTS (DCX-2) 10
   - 2.1 Introduction 10
   - 2.2 Analysis of the Molecular-Ion Beam Trajectories 11
   - 2.3 Hydrogen-Arc Dissociation 12
   - 2.4 Energy Analyzer Developments 17
   - 2.5 Measurements of the Cold Plasma with Gridded Probes 18
   - 2.6 Improvements in Vacuum Technology 19

3. ELECTRON-CYCLOTRON HEATING 21
   - 3.1 Injection of Neutrals and Trapping on an Electron Resonant Environmental Medium (INTEREM) 21
     - 3.1.1 Modifications 21
     - 3.1.2 Impurities 21
     - 3.1.3 Spectral Studies in INTEREM 21
   - 3.2 Electron-Cyclotron Heating Experiments in the ELMO Facility 23

4. INJECTION AND ACCUMULATION: NEUTRAL INJECTION INTO MINIMUM $|B|$ (DCX-3 MAGNET DESIGN) 29
   - 4.1 Introduction 29

4.2 Ribbon Coil System 30
4.2.1 General Comments on Application of Ribbon Coils 30
4.2.2 Coil and Electrical Parameters 30
4.2.3 Mechanical Design 31
4.2.4 Cooling System 33
4.3 Superconducting Coil System 33
4.4 Acknowledgments 35
5. PLASMA PHYSICS 36
5.1 Beam-Plasma Interaction Experiments 36
5.1.1 Introduction 36
5.1.2 Modifications 36
5.1.3 Charged-Particle Track Registration on Cellulose Nitrate 36
5.1.4 Scintillation Detection of D-D Protons 38
5.1.5 Nuclear Emulsion Detection of D-D Protons 38
5.2 Ion Heating Using a Modulated Electron Beam 40
5.2.1 Introduction 40
5.2.2 Description of Apparatus 40
5.2.3 Experimental Results 41
5.2.4 Discussion of Possible Heating Mechanism 49
5.2.5 Conclusions 52
5.3 Variation of Ion Acoustic Wave Properties with Electron Temperature 52
5.3.1 Technique for Varying Electron Temperature 52
5.3.2 Variation of Wave Velocity with Electron Temperature 53
5.3.3 Landau Damping 54
5.4 Landau Damping by the Addition of a Light Contaminant to a Plasma of Heavy Ions 55
5.5 Parametric Excitation of Transverse Waves in a Plasma 56
5.6 Hot-Electron Plasma Blanket 57
5.6.1 Two-Arc Performance 57
5.6.2 Effect of Saturation Current Measurements on Plasma Density 57
5.6.3 Magnetic-Field Shielding in the Anode Region 59
5.7 Excitation Heating of Ions to Moderate Temperatures 60
5.7.1 Introduction 60
5.7.2 Ion Densities in the Carbon Arc 61
5.7.3 Mass Spectrometric Data 61
5.7.4 The Near-Resonance Reaction and the Massey-Hasted Adiabatic Maximum Rule 62
5.8 High-Pressure Arc 64
5.9 Beam Stabilization in the Calutron 64
5.10 Levitated Toroidal Quadrupole 65
5.10.1 Introduction 65
5.10.2 Apparatus 66
5.10.3 Levitation 67
5.10.4 Magnetic Field Strength 69
5.10.5 Extended Field Lifetimes 69
5.10.6 Discussion 69
5.10.7 Summary 70

6. ATOMIC AND MOLECULAR CROSS SECTIONS 71
6.1 Rydberg States of Hydrogen Molecules 71
6.2 Secondary Electron Studies 74
6.2.1 Statistics of Secondary Electron Emission 74
6.2.2 Secondary Electron Emission Coefficients 76
6.2.3 Secondary Emission for Single Crystals 77
6.2.4 Development of a Quantitative Secondary Emission Detector 78
6.3 Reflection of Electrons and Neutral Atomic Hydrogen from a Gold-Barrier Silicon Detector 79
6.4 High-Energy Charge Exchange of H^0 and H^+ in Condensable Gases 80
6.5 Measurements of Multiple Charge Transfer of Multiply Charged Argon Ions 84
6.6 Atomic and Molecular Processes Information Center 86
7. HIGH-CURRENT BEAM PRODUCTION AND INJECTION 88
8. PLASMA THEORY AND COMPUTATION 94
8.1 Stability Properties of Open-Ended Magnetic Traps 94
8.2 Effect of Positive Magnetic Field Gradients on the Drift-Cyclotron Instability 97
8.3 Convective vs Absolute Instability Calculations 99
8.4 Flutelike Electrostatic Modes in Two-Component Ion Plasmas 103
8.5 Nonlinear Plasma Phenomena from a Quantum-Mechanical Viewpoint 107
8.5.1 Introduction 107
8.5.2 Plasma with No Magnetic Field 107
8.5.3 Plasma in a Strong Magnetic Field 110
9. MAGNETICS AND SUPERCONDUCTIVITY 111
9.1 Study of Ribbon Coils for Use in B_{min} Magnet Systems 111
9.2 Voltage-Current Characteristics of Compound Conductors 117
9.3 Magnetoresistance of Compound Conductors 120
9.4 Current-Carrying Capacity of a Hard Superconducting Wire in Zero External Field (Theory) 122
9.5 Current-Carrying Capacity of a Hard Superconducting Wire in Zero External Field (Experimental) 124
9.6 AC Measurements on Hard Superconductors 124
9.7 Iron-Core Minimum "B" Magnet 124
10. VACUUM STUDIES 126
10.1 Interpretation of DCX-2 Mass Spectra 126
10.2 Mass Spectrometer Calibration Studies 128
10.3 Water Vapor Chemisorption on Stainless Steel 130
10.4 Decomposition of DC-705 Diffusion Pump Fluid 133
11. DESIGN AND ENGINEERING: SERVICE REPORT 135
PUBLICATIONS, ORNL REPORTS, AND PAPERS 136

Introduction

A. H. Snell

In past Introductions, we have stressed the attractiveness of steady-state injection-accumulation in a magnetic well, with due regard to the reduction of energy sources that can drive instabilities and with acknowledgment also of the dimensions required of the plasma, in terms of Larmor radii, to inhibit the growth of instability waves. This same theme has been pursued during the past half year, and the related activities appear in various forms in the following pages. For example, in the theoretical section (Chap. 8), a discussion is given not only of well depths that are required to suppress the universal, drift-cyclotron, and flute modes (in summary), but also of the convective and nonconvective character of velocity-space modes, with the conclusion that the Harris and low-density loss-cone modes can become dangerously nonconvective unless Landau damping is invoked to inhibit the growth. This would require electrons with $T_e \sim T_i$, and from a practical point of view it revives the old Oak Ridge concept of neutral injection into an electron-cyclotron target plasma, which has the advantage also of a particularly high rate of trapping. Line-tying by means of cold plasma at relatively low density also may have an important stabilizing effect, although it raises the specter of the two-component plasma, and this in turn calls for a study of how widely separated the two components must be in order to make the energy contents sufficiently different to be dangerous (Sect. 8.4). While discussing our theoretical activities, one can point also to the growing interest of the theoretical group in nonlinear phenomena, as exemplified by the quantum-mechanical treatment for several aspects as supplied in Sect. 8.5.

Experimentally, progress toward the optimized, open-ended injection-accumulation systems is to be seen especially in the ion source and neutral beam development and in the planning for DCX-3. The progress in the former is exemplified in Fig. 7.5, which shows the energy spread of 40 to 60% introduced into an H^0 beam centered at 40 keV, under good collimation and, as the integral under the curve shows, with a very respectable H^0 current. We have been pleased to share this beam technology with our sister laboratories. So far as DCX-3 is concerned, the copper ribbon coil concept has been developed to the configuration of Fig. 4.3 (see also Sect. 9.1), but the superconducting concept using niobium-titanium cable (Fig. 4.5) looks better, and the choice has now been made in favor of the superconductors. Our hope is that by flitting about the margins of experimental stability, DCX-3 may give us scaling information as to the size and shape of a device which might be stable at much higher densities.

As for closed systems, we join others in interest in the toroidal multipoles as initiated at General Atomic and Wisconsin, to the extent of a small experiment on a levitated toroidal quadrupole (Sect. 5.10). Here it has been shown that two coaxial coplanar copper rings can be levitated and held stably for times sufficiently long for experiments that can extend plasma duration interestingly beyond the support-limited systems. The field strengths of nearly 2000 G in the initial model are also sufficient to promise a good regime for experimentation, after a moderate scaling into a larger system.

In DCX-1.5, neutral injection has been carried out in a system with parameters closely approximating those of the old ALICE I without multipole field. Somewhat to the astonishment of the experimentalists, densities rose to more than 10 times those of ALICE I (Fig. 1.5); apparently some subtle difference exists that may be associated with the proximity of end walls, for the results

can perhaps be accounted for by a combination of line-tying and finite Larmor orbit stabilization, as suggested a year ago by Guest and Beasley. In DCX-2, the sharp peaks in the dissociation neutrals as seen when the detector was swept through an angle have been accounted for on a geometrical basis (Sect. 2.2), and the molecular ion beam is now seen to follow its path as per single-particle-orbit calculations. Technological improvements have reduced the background pressure in DCX-2 by a factor of 10, and the fast-ion density is now 5×10^9 cm^{-3} when a deuterium arc is used for dissociation. After the 540-keV H_2^+ injected beam is cut off, the plasma decays from a density of about 10^9 cm^{-3} with occasional intermittent instabilities signalized by bursts of radio-frequency activity. The behavior suggests a velocity-space instability; because the classical loss rate of low-energy ions, by charge exchange and scattering, is much greater than the corresponding rate for the faster ions, a gap is produced in the velocity spectrum and is spasmodically filled from the high-energy population. Low-energy ions spit out longitudinally during the rf burst. In spite of all this, the net number of ions lost seems to be a small fraction of the total, as exemplified by the smallness of the steps in integral decay curves such as those of Fig. 2.4. Because of its size, and particularly its length, DCX-2 would seem to offer an opportunity for "afterglow" studies that might yield detailed information on wave-particle instabilities in multicomponent plasmas.

In the work on beam-plasma interactions, we see in Sect. 5.1 that the electron-heated Burnout V experiment has D-D reactions taking place *within its plasma*. In a restricted way, we can therefore claim to have the first steady-state fusion plasma in a laboratory apparatus. Whether the reactions are produced from the main body of plasma (density 5×10^{12}, $T_i \sim \frac{1}{2}$ to 1 keV) or by the known high-energy group of deuterons that circulate trochoidally through the potential well at the axis is not known. Also unknown are the single-particle containment properties of the system, so that a lot of understanding has to be achieved before we can realistically appraise the future for this kind of plasma heating.

Section 5.2 shows that ions can be heated to 200 eV in the self-generated plasma created by a small electron beam, when the electron beam is modulated at a frequency in the neighborhood of the ion plasma frequency. The heating takes place in a pressure range just above 2.6×10^{-4} torr, and with hydrogen the H^+ ions predominantly are heated rather than the H_2^+ ions. Several models are available to offer an explanation of the mechanism, but more work will be required in order to see which model is actually in effect. This small experiment, however, may lead to a significant attack on the heating problem, showing as it does that a penetrating electron beam can produce pronounced heating.

In "pure" plasma physics we note a double-edged observation of ion Landau damping in two simple, complementary experiments. The damping occurs when there is an overlap between the particle thermal velocities and the phase velocity of an ion sound wave. In one experiment (Sect. 5.3) the ion thermal distribution is held fixed, and the overlap is controlled by varying the wave velocity through adjustment of T_e. In the other experiment (Sect. 5.4) the waves are unchanged, and the overlap is induced by the modification in the thermal velocity spread by introducing a light contaminant into a heavy gas.

In the studies of superconductivity (Sect. 9), a network treatment is given to aid in the understanding of the division of current between the superconductor and its surrounding copper matrix, when the superconductor is in the resistanceless or the flux-flow state, and with and without magnetoresistance. Experimentally, the magnetic field is found to have a strong effect upon the transverse conductance across the indium-soldered junction between the superconductor and the copper. This effect is not yet fully understood.

Some elegant new aspects of classical atomic physics are described in Sect. 6. The first concerns the Rydberg states of H_2, that is, the states of H_2 in which one electron is highly excited about the (H_2^+, e) core, so the situation approximates the hydrogen atom. One sidelight of this is that a process akin to internal conversion is possible; if the core has sufficient excitation energy (vibrational-rotational, for example) to exceed the energy required to remove the distant electron, the radiationless transition can take place, and the probability is high compared with the nuclear case because the overlap of the volumes concerned is greater.

In Sect. 6.2 further studies of the numerically resolved secondary electron peaks have demonstrated the Poisson distribution of secondary-electron yield – a result that to many may not seem earth-shaking, but for which contrary evidence has appeared in the literature. The present conclusion is strengthened by the novelty and clarity of the data (Fig. 6.3). With these data, one can evaluate the absolute efficiency of secondary electron detectors of atoms and ions in the difficult energy range below 1 keV (Fig. 6.11). The Cross-Section Group presents also useful new curves for charge-exchange cross sections of H^0 and H^+ in various gases that are likely contaminants in vacuum systems, extending the results to 2.5 MeV. In an extension of the electron exchange concept, multiple-electron transfer has been measured in argon, the results being given in Fig. 6.22 in terms relative to single-electron transfer.

The valuable work of our engineers, mathematicians, and administrative staff has continued to be indispensable, and is not forgotten even if by nature it does not explicitly appear in the technical report.

Abstracts

1. INJECTION AND ACCUMULATION: NEUTRAL INJECTION EXPERIMENTS (DCX-1.5)

In these experiments 15-keV hydrogen atoms are formed and injected into the magnetic mirror field of the DCX-1 facility. The principal motivation is the development of the neutral injector, the beam injection and burial lines, a vacuum system, and special diagnostic equipment which will be required for the DCX-3 facility. The energetic neutrals are formed from 30-keV H_2^+ within a magnesium vapor cell, and up to 40 mA (equivalent) of these neutrals have been injected. The Lorentz trapping fraction is 1.2×10^{-4}, and hot-ion lifetimes of 80 msec for an 18-mA beam and 160 msec for a 7-mA beam have been recorded. Central hot-ion densities of 4×10^8 cm^{-3} have been obtained, apparently not limited by flute instability. A comparison with data from the ALICE facility suggests that the absence of this limitation may be the result of cold-plasma effects. Properties of the magnesium vapor cell and of an energy analyzer for low-energy charge-exchange neutrals are also described.

2. INJECTION AND ACCUMULATION: MULTIPLE-PASS EXPERIMENTS (DCX-2)

Progress is reported in three areas: improved understanding of injected beam properties, studies of regimes of increased plasma density, and improvements in energy analyzer diagnostics and in vacuum.

The distinct peaks seen previously in the pitch-angle scan of the molecular-ion beam are consistent with calculated single-particle orbits for the turns the beam makes from the injector to the detector.

Plasma densities obtained with hydrogen- or deuterium-arc dissociation are an order of magnitude higher than those attained with gas dissociation. At these high densities (up to 5×10^9 hot protons/cm^3), bursts of rf appear even during decay of the plasma. Accompanying these bursts are small but discernibly increased charge-exchange losses. These correlations are related to the velocity distribution of the trapped particles.

At the lower densities obtained with gas dissociation, the radial distribution of the plasma potential has been measured. A much improved energy analyzer is described, and finally the method for obtaining good vacuums in the presence of large hydrogen-gas throughput is given.

3. ELECTRON-CYCLOTRON HEATING

The INTEREM facility is being modified to accommodate a higher intensity 20-keV neutral beam. Spectral studies in the INTEREM ECH plasma suggest the formation of the fast "Franck-Condon" neutrals (N^0) when N_2 is used as a support gas. The ELMO facility has been operated in the double-folded cusp, mirror, and "stuffed" folded cusp magnetic configuration. Macroscopic plasma instabilities are evident, even when the plasma is created and contained in the positive-gradient magnetic field of the folded cusp.

4. INJECTION AND ACCUMULATION: NEUTRAL INJECTION INTO MINIMUM $|B|$ (DCX-3 MAGNET DESIGN)

The DCX-3 program is a study of stability properties of a plasma formed by injection of energetic neutral atoms into a minimum $|B|$ trap. The initial experiments in this program will utilize Lorentz trapping a mirror-quadrupole field. Two designs

of the magnetic bottle are reviewed. Both are steady-state rather than pulsed systems, and in each the maximum central field value is 20 kG. One uses coils formed of copper ribbon, water cooled, and energized by conventional motor-generator sets. The other uses superconducting coils. At present the superconducting system appears the more desirable.

5. PLASMA PHYSICS

In beam-plasma interactions in Burnout V a source of energetic tritons and protons has been localized to the plasma volume. The reaction rate of these D-D products is consistent with the previously measured plasma ion temperature, density, and volume. Measurements were made using detection of tritons on cellulose nitrate and of protons by both scintillation and nuclear emulsion techniques.

Ion heating has been observed in another electron-beam–plasma interaction. In order to have energetic ions, in this case, the electron beam must be modulated at frequencies near the ion plasma frequency (which is also close to the lower hybrid frequency). The beam is injected axially into a 550-G magnetic mirror field and creates a density near $10^9/cm^3$. The energetic charge-exchanged ions are reionized and analyzed; the maximum variations available did not permit ion energies greater than 200 eV.

Using the "electron temperature converter," studies were made of the velocity dependence of ionic sound waves on electron temperature and of the electron temperature dependence of Landau damping of ionic sound waves. The addition of helium ions to a xenon plasma verified the prediction of Landau damping of ionic sound waves by ions in yet another way.

A theoretical treatment shows that in a cold plasma, externally imposed oscillating electric fields excite transverse electromagnetic waves which propagate perpendicular to it.

The density of the intermediate energy group (2-keV electrons) in the hot electron blanket experiment has been increased to 5×10^{11} cm^{-3} by simultaneous use of two radially displaced electron beams. But when the central magnet field was increased by a factor of 3.5 the plasma density decreased by a factor of 5.

Additional data on the vacuum ultraviolet absorption method for analysis of ion densities in energetic carbon arcs are presented. Higher arc currents increase the concentration of C^{3+} and probably reduce the activity of the excitation-heating process involving C^{2+} and C^{2+*}, thus explaining the reduced ion temperatures in higher current arcs. Mass spectrometric analysis of carbon ions in the peripheral region of the arc supports the absorption measurements of ΣC^{2+} and C^{3+} as the most prominent ion species. The near-resonance nature of the intermediate reaction step, $C^{2+*} + C^{2+*} \rightarrow C^{2+\prime} + C^{2+} + 0.29$ eV, is discussed in terms of the Massey-Hasted adiabatic maximum criterion and in terms of the iso-electronic sequence Be, B^+, C^{2+}, N^{3+}, and O^{4+}.

A facility is nearing completion which will permit measurement of the radiation from a magnetically supported high-density arc at high pressures. This measurement will allow quantitative assessment of the feasibility of using gas confinement to contain energetic plasmas.

The use of the inductive end walls suggested by Briggs and Neil for suppressing the negative-mass instability has not proven to be effective in reducing the calutron instability.

Studies of the plasma confinement properties of a toroidal multipole configuration have started. To avoid plasma losses on hangers, magnetic levitation of the internal conducting hoops is required. A small-scale model has successfully demonstrated levitation of two coplanar concentric conducting hoops (a quadrupole). Peak fields were 2 kG, and useful times available for plasma containment were 8 msec.

6. ATOMIC AND MOLECULAR CROSS SECTIONS

The problem of the existence of highly excited Rydberg states in H_2 molecules has been formulated rigorously, and computer solutions are being sought for autoionizing transition rates for such states. Predictions were made that the Rydberg states of HD, because of its dipole moment, would decay faster than those of H_2, which possesses only a quadrupole moment. This hypothesis has been confirmed by observing the population of states $n > 11$ for both HD and H_2.

Analyses have been made of the statistics of secondary electron emission from heavy particles

impinging on metal surfaces. Single particles striking a surface will produce groups of 0, 1, 2, ..., n electrons with a certain probability P_n. These electrons are postaccelerated and counted by a high-resolution silicon barrier detector. The pulse spectrum yields the frequency of electrons in each n group. The probability distribution, P_n, has been found to be a characteristic Poisson distribution, $P_{(n)} = e^{-\gamma}\gamma^n/n!$. Application of this analysis to the measurement of low-energy neutral particles yields information which determines the absolute efficiency of particle detection. For a counting system of an AgMg surface and a silicon barrier detector, the detection efficiency was 77% for H^0 at 500 eV and rose monotonically to a plateau of 100% at an incident energy of 2 keV. Using these same techniques, the average secondary emission coefficient has been determined for H^+, H^0, and N^0 particles on Cu and AgMg in the energy range 500 eV to 50 keV. Measurements have also been made for the secondary emission coefficient for a copper single crystal, and values have been obtained for the reflection coefficient of H^0 and electrons from metal surfaces.

Charge-transfer cross sections of hydrogen particles (H^+, H^0) have been made in H_2, He, Ar, N_2, O_2, CO, CO_2, H_2O, CH_4, and C_2H_6 target gases. The energy range was 100 to 2500 keV. Also, studies have been made of nonresonant charge transfer of one to five electrons for multiply charged rare-gas ions in their own gases. Differential cross sections of these processes are reported in the energy range 0.4 to 2.2 keV times the charge of the primary ion.

7. HIGH-CURRENT BEAM PRODUCTION AND INJECTION

A 20-keV beam of neutral hydrogen atoms has been produced by the dissociation and neutralization of a 40-keV H_2^+ beam by means of a magnesium vapor cell developed and built by the DCX-1 group. The four-electrode H_2^+ ion source and the recently developed 100-kV non-PIG accelerator column described previously were used to produce the beam. The H_2^+ beam was passed through the neutralizer and a system of apertures which simulate the DCX-3 and INTEREM geometries. Equivalent currents of 102 and 222 mA of 20-keV H^0 have been produced in these geometries respectively.

Beam profile measurements have been made of both the 40-keV H_2^+ and the 20-keV H^0 beams. These measurements show that the current density is sharply peaked on axis when the beam is focused to produce maximum current, even through a relatively large aperture. The maximum current density measured was 121 mA/cm^2 for 40-keV H_2^+ and 163 mA/cm^2 for 20-keV H^0 at a distance of 117 cm from the magnetic lens.

8. PLASMA THEORY AND COMPUTATION

In this report we present brief reviews of areas of linear stability theory which are relevant to open-ended magnetic traps and of the present work in nonlinear theories of plasma phenomena. Results from the linear analysis emphasize the importance of magnetic wells and Landau damping: magnetic wells are expected to stabilize all low-frequency modes ($\omega << \omega_{ci}$), and Landau damping may stabilize many of the high-frequency velocity-space instabilities. Attention is then focused on those modes not rigorously subject to these two constraints. Some preliminary discussion is given for two such modes, the drift-cyclotron instability and flutelike gyrofrequency modes in plasmas with distinct groups of fast ions intermixed with colder ion populations. Recent progress in the discrimination between convective and nonconvective instabilities adds more emphasis to the necessity of the Landau damping constraint. The review of the present work on nonlinear phenomena summarizes the classes of elementary plasma excitations for which quasi-linear equations have been obtained. The treatment of plasma phenomena in quantum-mechanical formalism is broadend beyond its earlier status.

9. MAGNETICS AND SUPERCONDUCTIVITY

As was previously reported, development work is being done on "ribbon coils." This design is intended to be used when restricted space calls for magnet coils with very high current densities. In general, an arrangement with water flow parallel to the coil axis is appropriate; however, for elongated coils such as would be employed for Ioffe bar systems, water flow along the ribbon proved to be preferable. A study is being made of how these two types of water-cooled ribbon coils would be

used in a conceptual design of the DCX-3 facility. However, since the power requirement would be very high (23 MW), a superconducting magnet coil system was chosen for DCX-3. Nevertheless, for other B_{min} magnet systems a design utilizing ribbon coils might be a better alternative.

The physical properties of "compound conductors" are important in the design of "stabilized" superconducting magnet coils. A compound conductor consists of superconducting wires or ribbons in close electrical and thermal contact with nonsuperconducting metallic material, the so-called "stabilizer." The performance of a compound conductor depends upon whether the superconductor is in the nonresistive or in the flux flow state. Both cases are considered here in a detailed study. It is shown that in the first case the compound conductor can be replaced by a simple equivalent network. In the second case an application of Kim's flux flow equation leads to a physical understanding of the often used phenomenological concept of the "overflow" of current from the superconductor to the stabilizer. Furthermore, the nonlinear heat transfer from the compound conductor to the surrounding liquid helium is considered. Numerical examples illustrate the new approach to understanding the performance of compound conductors. Finally, a brief report on nonstabilized superconductors is presented.

The previously mentioned performance of compound conductors depends, of course, on the magnetoresistance of the stabilizer. Since the stabilizer and the copper-clad superconductor are interconnected by indium soldering, it was expected that the transverse conductance k between superconductor and stabilizer might be almost independent of the magnetic field. Our experiments clearly showed, however, a strong field dependence of k. This surprising and important fact deserves further investigation.

Several attempts have been made to develop a theory of the current-carrying capacity of a hard superconducting wire founded on the basic properties of superconductors of the third kind. Such a theory would allow one to predict the critical current from data obtained by a magnetization experiment performed with a cylindrical sample in a longitudinal magnetic field. In this report H. W. Koppe presents such a theoretical criterion for the current-carrying capacity of a hard superconducting wire restricted to the case of zero external field. He shows that the critical current is determined by the fact that the radius of a circular field line inside the wire cannot be smaller than a certain critical length. Koppe derives a simple equation for the value of this minimum radius. It depends on basic properties of the hard superconductor which can be determined by magnetization experiments. With Nb–25% Zr samples, magnetization and critical current experiments were made. The data obtained were in excellent agreement with Koppe's theory.

Furthermore, we made oscillographic ac measurements on hard superconductors. The shape of the voltage-time curves can be explained by considering in an appropriate way a certain critical surface current and the magnitude of the pinning forces acting on the vortices in the type III superconductor. The surface currents can be observed with external fields up to $H_{c3} > H_{c2}$, whereas the bulk critical currents become zero at the upper critical field H_{c2}. The values of the critical surface currents and of the critical bulk current density obtained with these ac measurements are in good agreement with the results of static measurements. Finally, it is shown how the pinning force per unit volume and the pinning force acting on a single vortex line can be expressed as a function of the vortex line density.

Improvements in the well depth for an iron-core minimum B are reported.

10. VACUUM STUDIES

Chemical analysis of the DCX-2 vacuum system using residual gas mass spectra was performed in detail for one day's operation. Experimental distinction between four types of impurity species was made. These four groups of impurity gases are classified on the basis of their origin:

1. extraneous species associated with the mass spectrometer,
2. "base" pressure impurities,
3. contaminants in the bleed-gas manifold,
4. gases generated during ion beam injection.

Water was found to be the principal member of the second and third classes listed, while several low-molecular-weight hydrocarbons were found to be generated during beam injection. A study of mass discrimination in the spectrometer is described

which permitted the improvement in the quantitative analysis of these data.

In other research an attempt was made to study the kinetics of water sorption on stainless steel at exposure pressures less than 10^{-4} torr. The results followed chemisorption kinetics. In a fourth study a white solid decomposition product of a silicone diffusion pump fluid was identified. A deposit of this material had impaired the pump's speed.

1. Injection and Accumulation: Neutral Injection Experiments (DCX-1.5)

R. J. Colchin
J. L. Dunlap
R. S. Edwards
L. A. Massengill
H. Postma
R. G. Reinhardt
W. J. Schill
E. R. Wells

1.1 INTRODUCTION

As noted in the last report,[1] the investigations involving injection of 600-keV H_2^+ into the DCX-1 magnetic mirror trap were essentially terminated at the end of the previous report period. We have retained the option of 600-keV H_2^+ injection in anticipation of some experiments to attempt stabilization of the negative-mass instability by inductive end walls, as suggested by Briggs and Neil.[2] However, most of our recent work has been directed toward a new facility, called DCX-3, in which the plasma will be formed by Lorentz ionization of energetic neutrals in a mirror-quadrupole trap.

Development of the neutral injector, the beam injection and burial lines, an adequate vacuum system, and special diagnostic equipment for the DCX-3 is in progress. Much of this development utilizes neutral injection into the magnetic mirror trap of the DCX-1 facility. (We have dubbed this interim facility DCX-1.5.) In the sections that follow, we describe this work and also some properties of the plasma formed in the trap.

Design studies relating to the DCX-3 magnetic bottle are reviewed in Sect. 4.

[1] *Thermonuclear Div. Semiann. Progr. Rept. Apr. 30, 1966*, ORNL-3989, p. 1.

[2] R. J. Briggs and V. K. Neil, *J. Nucl. Energy: Pt. C* 8, 255 (1966). This paper is concerned with relativistic beams, but in private communications the authors have pointed out how the same general ideas can be applied to nonrelativistic beams.

1.2 APPARATUS

1.2.1 General Description of the DCX-1.5 Facility

A schematic layout of the facility is given as Fig. 1.1. The neutral beam is produced in a magnesium neutralizing cell by conversion of 30-keV H_2^+ into 15-keV H^0. The ion source and magnesium cell were developed as a cooperative venture with the Ion Source and Accelerator Group. Details of these components and results of their test stand operation are given in Sect. 7.

The beam is transported in the beam tube through several stages of differential pumping until it enters the liner. The last defining aperture is 1.5 in. in diameter and is located 20 in. from the mirror coil axis and 53 in. from the magnesium cell. After passing through the liner, the beam impinges upon an inclined target provided with a calorimetric monitor. Neutral beams of 40 mA (equivalent) have been injected.

The liner itself is a right circular cylinder 12 in. in diameter, mounted with its axis vertical and perpendicular to the axis of the mirror coil system. The liner walls act as the radial limiter for the plasma. As usual, the liner is cooled with liquid nitrogen, and titanium getter pumping on liquid-nitrogen-cooled surfaces is provided for the interior as well as for the guard vacuum region.

The midplane magnetic field in the plasma region is given by $B = B_0 (1 - \alpha r^2)$, where $\alpha = 6.5 \times 10^{-4}$ cm^{-2}. For the experiments reported here, B_0 was 10 kG.

ORNL-DWG 66-12257

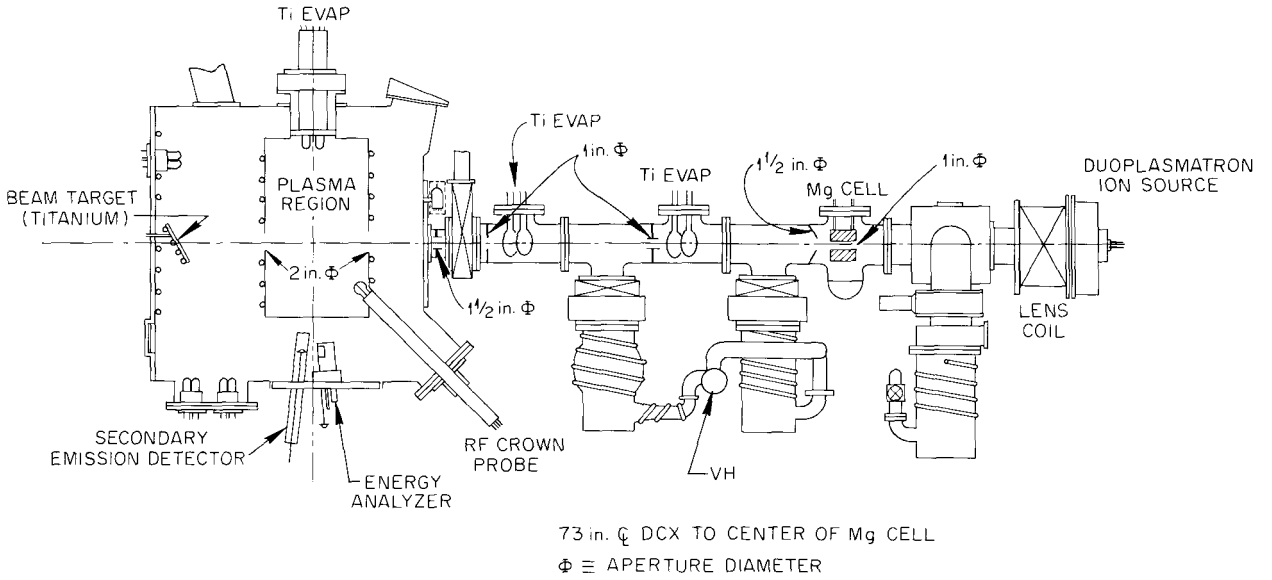

Fig. 1.1. Schematic Outline of the DCX-1.5 Facility. The cut is in the median plane of the mirror coil system. The magnetic field is normal to the paper.

The diagnostics presently employ an rf probe, a secondary electron emission detector for charge-exchange neutrals, and an energy analyzer. The locations are shown in Fig. 1.1. The rf probe is the standard crown probe developed in earlier DCX-1 efforts.[3]

The secondary emission detector (SED), which extends $\frac{3}{4}$ in. in the direction of the magnetic axis, forms secondaries at a copper surface and was operated with sufficient bias to give saturation current of secondary electrons. The detector and associated electronics have a time constant of less than 100 μsec. The detector was calibrated during a high-pressure helium gas run in DCX-1.5. The major assumption involved in the calibration procedure is that a plasma volume of 2.8 liters (from a right circular cylinder of r = 15 cm and L = 4 cm) is an appropriate one over which to average.

A description of the energy analyzer is given in the following section.

[3]*Thermonuclear Div. Semiann. Progr. Rept. Oct. 31, 1963*, ORNL-3564, pp. 1–2.

1.2.2 Energy Analyzer

In cooperation with the Tennelec Instrument Company,[4] an energy analyzer system has been developed for use at the low energies of interest in neutral injection experiments. Here we describe this system and indicate its performance figures.

The system features a silicon surface-barrier detector mounted with a preamplifier stage in a copper probe head that can be cooled to low temperatures by a "cold finger" immersed in liquid nitrogen. Two different detectors, both obtained from the Nuclear Diode Company,[5] have been employed, one with an active area of 20 mm^2 (3 pF capacitance) and one with an active area of 5 mm^2 (0.75 pF). Both detectors were of the ceramic ring mount type with a depletion depth of 700 μ and a gold surface layer thickness of approximately 100 Å. The preamplifier stage uses a single field-effect transistor; it was designed by the Tennelec Instrument Company to replace the four-transistor

[4]140 East Division Road, Oak Ridge, Tenn. 37830.

[5]1640 Old Deerfield Road, Highland Park, Ill., their model RH 6-20.

input section of their TC-130 preamplifier. The signal lead from the probe head connects to an otherwise standard TC-130 preamplifier, which in turn is connected through a Tennelec TC-200 linear amplifier to a multichannel analyzer. The probe head incorporates a variable aperture arrangement that allows adjustment of counting rate under operating vacuum conditions.

System checks with a proton beam at energies to 40 keV were made in cooperation with the Cross Section Group. With the 20-mm^2 detector the system was useful down to 9 keV. In the range 10 to 40 keV the response was linear, and the resolution was about 3 keV full width at half maximum (FWHM). Similar checks with the 5-mm^2 detector resulted in usable spectra down to 6 keV, with resolution of 2.6 keV FWHM at 10 keV.

1.3 EXPERIMENTAL RESULTS

There have been the usual problems which accompany major modifications of an experimental facility, and studies of the plasma formed in the magnetic mirror trap have begun only recently. The results, though preliminary, are quite interesting.

1.3.1 Vacuum

We are considerably encouraged at indications of high vacuum in the plasma region, particularly in view of the present rudimentary beam disposal system. Plasma lifetimes have been as long as 80 msec for an 18-mA neutral beam and as long as 160 msec for a 7-mA beam. The latter figure implies a charge-exchange environment equivalent to a hydrogen background of 1.6×10^{-9} torr. These results compare quite favorably with the performances of ALICE and of PHOENIX.

From a technological point of view, it is important to gage whether streaming from the neutralizing cell was the limiting factor in determining these lifetimes. The τ values varied in the same sense as the pressure indication from the ionization gage monitoring the guard vacuum (there was no liner gage during these runs); so our present data indicate that this limit has not been reached, even with the magnesium cell operated at pressures high enough for equilibrium charge distribution. The data show no need at this time to incorporate paddles or cross jets to limit streaming.

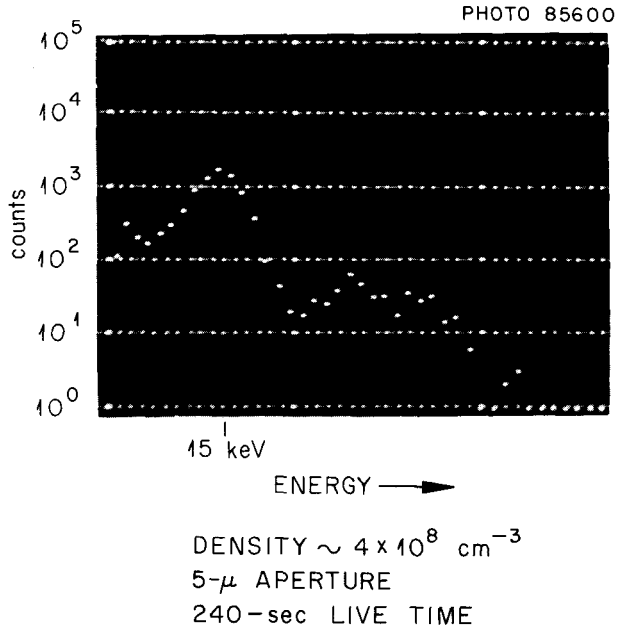

Fig. 1.2. *Energy Spectrum of Charge-Exchange Neutrals from the 15-keV Proton Plasma of DCX-1.5.* Density, $\sim 4 \times 10^8$ cm^{-3}.

1.3.2 Energy Analysis

These data pertain to operation with fast-proton densities in the range $(1\text{–}4) \times 10^8$ cm^{-3}. The energy spread indicated was essentially the resolution of the detector (3 keV FWHM). A typical spectrum is shown as Fig. 1.2. The peak at higher energy is probably due to signals from the H_2^0 formed from charge exchange of H_2^+ in the magnesium cell. If so, the relative counting rates indicate that this component constitutes only about 1% of the trapped plasma.

1.3.3 Density Determinations

These determinations are based on the responses of the SED (the amplitude A and the $1/e$ decay time τ), these responses being interpreted in terms of the high-pressure gas calibration run described in Sect. 1.2.1.

Figure 1.3 shows $A\tau$ (proportional to density) as a function of τ for runs with a fixed neutral beam current (13 mA) obtained with the magnesium conversion cell operated at a variety of temperatures and with a variety of H_2^+ currents. The value of τ was varied by a controlled helium leak.

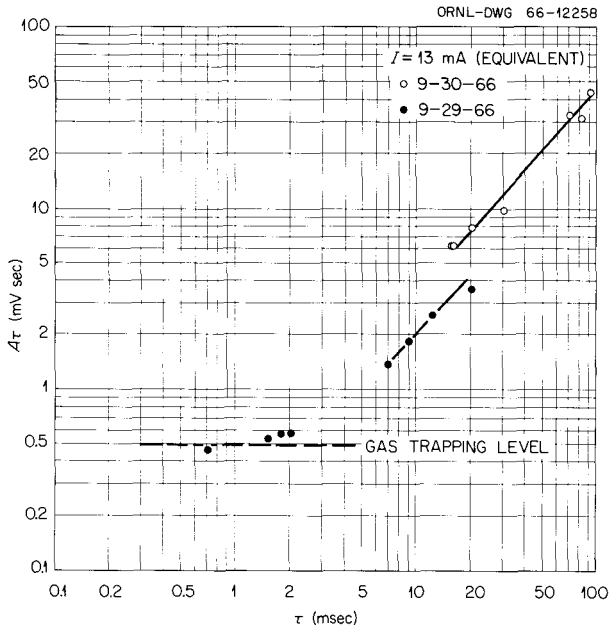

Fig. 1.3. $A\tau$ as a Function of τ with Fixed Neutral Beam Current. The figure shows τ regions dominated by gas and by Lorentz trapping.

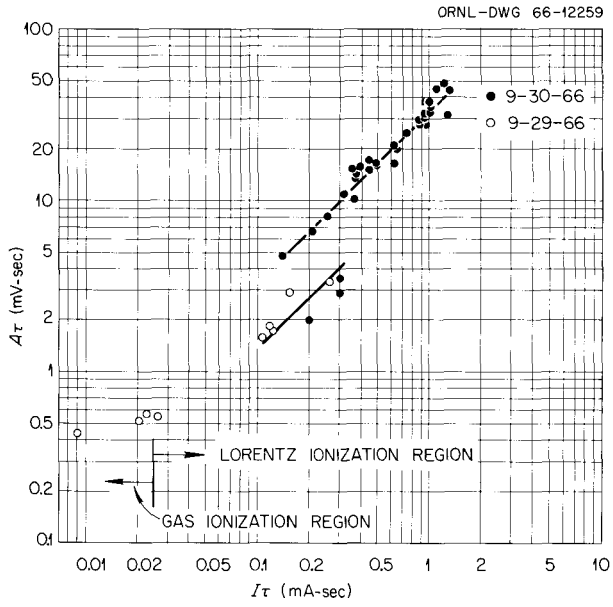

Fig. 1.4. $A\tau$ as a Function of $I\tau$ for a Number of Values of τ and of Neutral Beam Current.

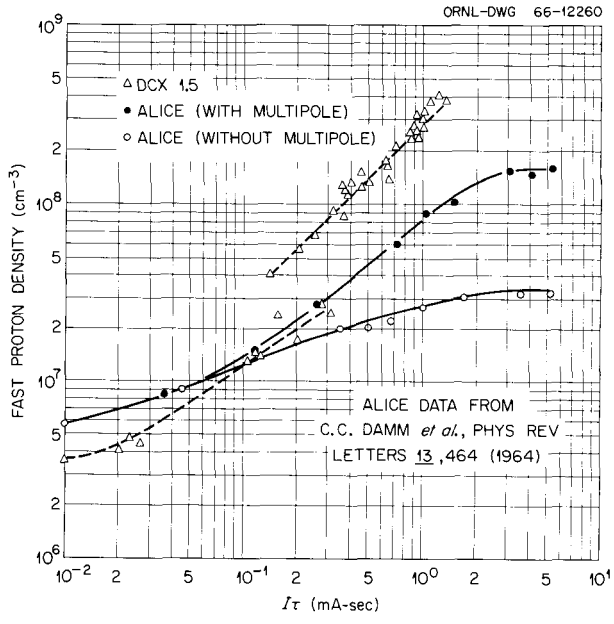

Fig. 1.5. Fast-Proton Density as a Function of $I\tau$, Giving Comparisons of DCX-1.5 and ALICE Data.

The curve shows a region at low τ dominated by gas ionization and a region at high τ dominated by Lorentz ionization. At $\tau = 1$ msec, calculations with the appropriate cross sections yield a gas trapping fraction of 1.2×10^{-4}. The $A\tau$ product for $\tau = 100$ msec is higher by 100 times; so the Lorentz trapping fraction is also 1.2×10^{-4}. In the Lorentz trapping regime, the two days' data fit two lines (with the same slope, near 45°) more closely than a single line. This behavior may simply be scatter of data points, or it may be more significant, possibly involving a density suppression by instabilities. The question will be settled in further work. The behavior does not seem to result from cell operation at different temperatures (see Fig. 1.11 and the discussion of Sect. 1.3.5).

Figure 1.4 shows $A\tau$ as a function of $I\tau$, where I is the equivalent neutral current. The data points are all those obtained in the two runs and so include those given in Fig. 1.3. The fit to two 45° lines is again shown. Figure 1.5 presents the same data, but in the form $n^+(I\tau)$. For purposes of a later comparison, some results[6] from the ALICE neutral injection experiment are also included. The most important feature of these data is the absence of density saturation at high $I\tau$ values in DCX-1.5.

[6]C. C. Damm *et al.*, *Phys. Rev. Letters* **13**, 464 (1964).

1.3.4 RF Measurements

High-frequency electrostatic signals were monitored during the experiments reported in Sect. 1.3.3. Instability signals were observed only in an intermediate density range, approximately 5×10^6 to 2.5×10^8 cm^{-3}. The character of the signals changed within this range, as is shown in Figs. 1.6 and 1.7. At lower densities they were of small amplitude and discontinuous, in the sense that the oscilloscope displays were spiky with frequent returns to the base line. At higher densities there were transitions to signals of much larger amplitude, initially discontinuous and then continuous. As shown in Table 1.1, the density ranges for the characteristic high-frequency, electrostatic rf modes, as determined from measurements during both steady state and plasma buildup, overlapped to a considerable extent.

Table 1.1. RF Modes from High-Frequency Electrostatic Probe Data

Mode	Limits of Density Range
A. Low density, stable	$0 \leqq n^+ \leqq (1 \times 10^7)$ cm^{-3}
B. Low-level instability	$(5 \times 10^6) \leqq n^+ \leqq (1 \times 10^8)$
C. High-level instability	$(1.5 \times 10^7) \leqq n^+ \leqq (2.5 \times 10^8)$
D. High density, stable	$n^+ \geqq (1 \times 10^8)$

The behavior of the rf signals during plasma decay was interesting. Radio frequency of the discontinuous types disappeared almost immediately, long before decay to the initial threshold density. That of the continuous type decayed very gradually in amplitude and persisted about as long as there was detectable plasma. There was

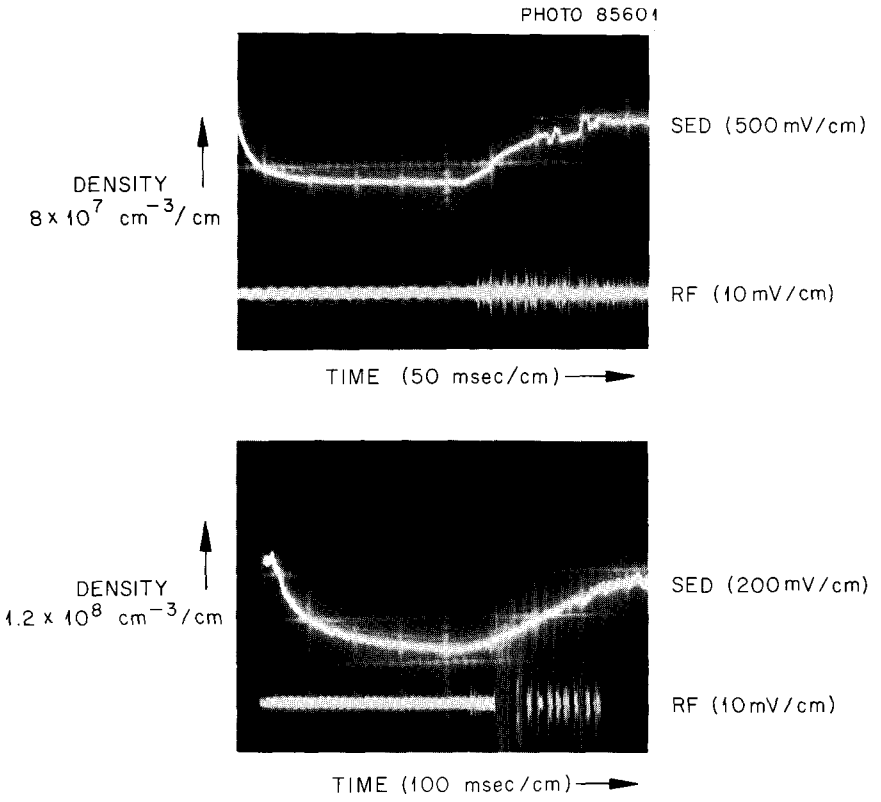

Fig. 1.6. Charge-Exchange (SED) and High-Frequency Electrostatic RF Signals During Periods of Plasma Decay and Accumulation. The plasma was initially in steady state. The neutral beam was then shut off, the plasma allowed to decay, and the beam was cut back on. The low-level mode is illustrated in the upper photograph. In the lower photograph the low-level mode exists between 5.5 and 6.0 cm, and then there is a transition to the high-level mode, initially discontinuous and then continuous.

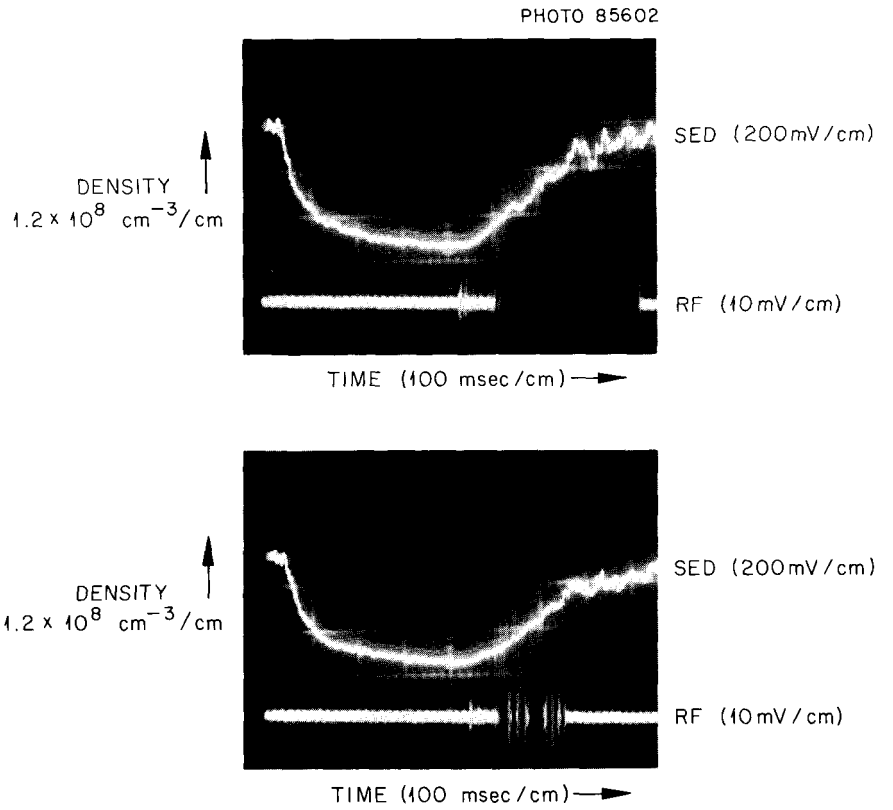

Fig. 1.7. Charge-Exchange and High-Frequency Electrostatic RF Signals During Periods of Plasma Decay and Accumulation. In the upper photograph at 6.0 cm there is a transition to a high-level continuous mode and then at 9.4 cm a transition to a high-frequency stable regime. In the lower photograph the high-level mode is discontinuous.

no transition to discontinuous rf during this type of decay. Decays from the high-density stable regime remained stable throughout the decay.

Very recently, in addition to observations of high-frequency electrostatic signals, there have been brief examinations of magnetically polarized signals and of low-frequency electrostatic signals. These runs were confined to $P \gtrsim 1 \times 10^{-8}$ torr and $n \lesssim 5 \times 10^{7}$ cm^{-3}. The data indicate the presence, at various times, of at least four modes. Much more work is required in this area, and for the present we can give only short descriptions of these modes. In order of increasing plasma density, they are as follows:

1. Weak, burstlike magnetic signals associated with axial currents (I_z); extremely weak corresponding high-frequency signals from the electrostatic probe; no observable low-frequency electrostatic signal.
2. Strong, choppy magnetic signals associated with azimuthal currents (I_θ); strong corresponding high-frequency signals from the electrostatic probe; weak magnetic signals to the I_z probe, these a mixture of corresponding and noncorresponding activities; no observable low-frequency electrostatic signal.
3. Like mode 2, but alternating with strong low-frequency electrostatic oscillations and usually very much reduced high-frequency (both I_θ and electrostatic) signals. The relative amount of time spent in these alternating modes is an extreme variable, but one whose dependence upon other plasma properties is not yet defined.
4. Dominant low-frequency oscillations and no observable high-frequency activity.

Figure 1.8 shows examples of modes 1, 2, and 4 measured during a single period of plasma accumulation. Our present data indicate that mode 3 rarely occurs during buildup, but instead is usually a characteristic of steady-state density for a

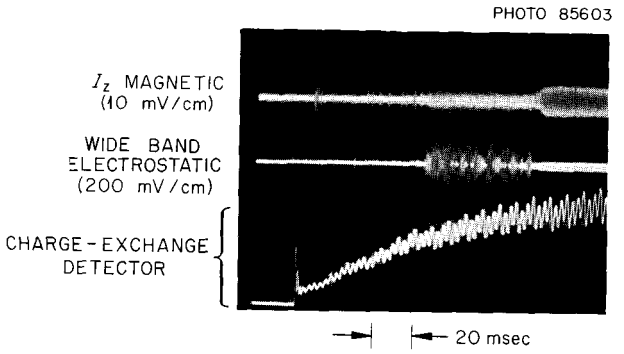

Fig. 1.8. I_z **Magnetic and Wide-Band Electrostatic Signals During a Period of Plasma Accumulation.** Parameters were $P \approx 1.5 \times 10^{-8}$ torr, $I = 40$ mA H^0, and $\tau \approx 4$ msec. The long buildup time occasionally registered by the charge-exchange detector, as shown here, is not yet fully understood.

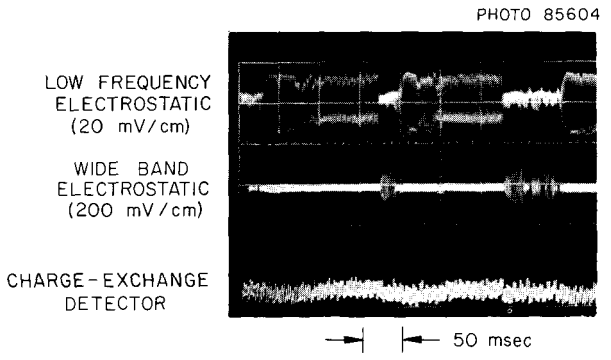

Fig. 1.9. Low-Frequency and Wide-Band Electrostatic Signals During Steady State. Parameters were $P \approx 1 \times 10^{-8}$ torr, $I = 18$ mA H^0, and $\tau \approx 10$ msec. A 1-MHz low-pass filter in the wide-band signal lead provided the low-frequency signal.

limited density range. Figure 1.9 shows mode 3 in steady state. In each case the dominant low-frequency oscillation has been at about 30 kHz, which is near the calculated ∇B precession frequency in this magnetic field.

Only preliminary studies of the frequency distribution of the high-frequency signals have been made. In addition to ion cyclotron harmonics ($\omega_{ci} \approx 15$ MHz), we have occasionally observed strong signals at approximately 25 MHz. This frequency was also that of the axial instability mode for a 300-keV proton plasma in this magnetic field.

Present data are not complete enough to allow definite correlation of modes 1 to 4, just described, with modes B and C, introduced earlier in this section (Table 1.1). It does, however, seem reasonable to associate mode B with mode 1 and the discontinuous mode C with modes 2 and 3. The principal questions regard the properties of the magnetic and the low-frequency electrostatic signals during the continuous mode C and the high-density mode D, in which no high-frequency electrostatic signals were observed.

1.3.5 Magnesium Cell and Properties of the Neutral Beam

As previously noted, these experiments made use of H^0 obtained by conversion of H_2^+ in a magnesium vapor cell. In this section we consider the efficiency of this conversion and the excited-state population of the neutral beam as functions of cell temperature (concentration of magnesium vapor).

The experiments included measurements of the neutral beam current produced as a function of cell temperature with a constant incident current of H_2^+. The total extracted current was held constant at 80 mA, and the equivalent neutral current was monitored calorimetrically at the final beam target as the cell temperature was changed. Figure 1.10 shows the results. The time allowed between cell heater adjustments was not sufficient for an equilibrium temperature to be established. As a consequence the curve obtained while lowering the temperature does not coincide with that obtained while raising the temperature. The general behavior of these curves is consistent with results obtained by the Ion Source and Accelerator Group with essentially the same source and neutralizing cell.

During the course of the temperature variations, the level of charge exchange from the plasma and the plasma lifetime were obtained by use of the secondary emission detector. Knowledge of this $A\tau$ product and the neutral beam current yielded a value for the Lorentz trapping fraction (β_L) at each temperature. The results, shown in Fig. 1.11, indicate a trapping fraction of about 1.2×10^{-4}, independent of cell temperature over the range investigated, which corresponds to a range of 1 to 18 μ for the magnesium vapor pressure.

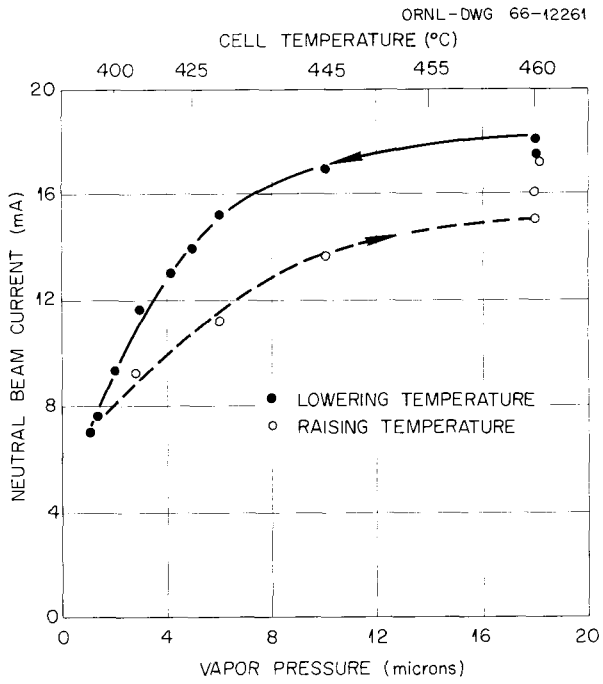

Fig. 1.10. H^0 Beam Current to the Final Beam Stopper as a Function of Magnesium Vapor Pressure in the Oven. Oven temperature was controlled, and pressure was inferred from the recorded temperatures.

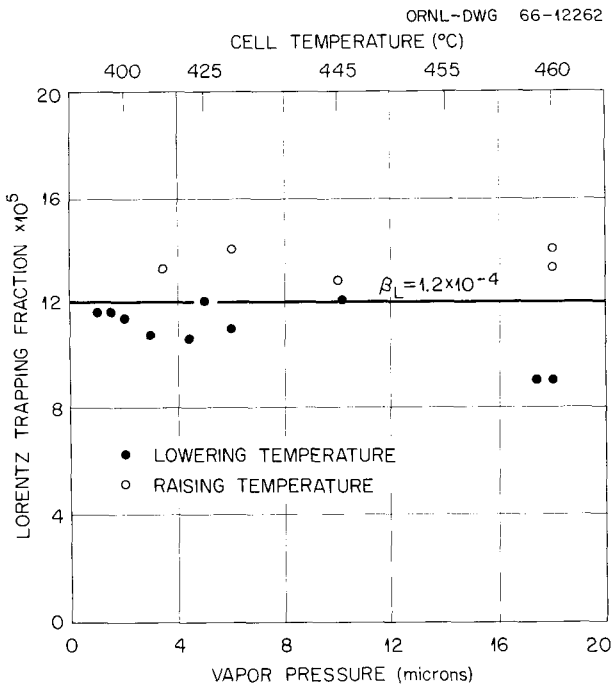

Fig. 1.11. Lorentz Trapping Fraction as a Function of Magnesium Cell Temperature and Inferred Vapor Pressure.

These data are the first we have seen for H_2^+ incident upon a magnesium cell. All other data available to us have involved use of incident protons.

By way of comparison, the trapping fraction (1.2×10^{-4}) obtained here is about seven times that observed in the ALICE mirror field with similar B magnitude, B gradients, and dimensions, but with an $N_2 + H_2$ conversion cell and incident proton beam.[6]

1.3.6 Comparisons with the ALICE Neutral Injection Facility

Superficially, the parameters of the DCX-1.5 experiment are much like those of the ALICE multipole experiment[6] when the latter was operated as a simple mirror. A comparison of the more obvious parameters of these two experiments is given in Table 1.2.

The properties of the two plasmas are, however, quite unlike in that the ALICE plasma was flute limited to $n \approx 3 \times 10^7$ cm^{-3}, whereas that of DCX-1.5 is, from present evidence, not limited at its maximum density of 4×10^8 cm^{-3}. The DCX-1.5 density figure is even above that obtained by ALICE with multipole stabilization (Fig. 1.5).

The enhanced stability of the DCX-1.5 plasma against flute losses is obviously an important feature of this plasma. Stabilization against flutes has generally been attributed to finite-orbit or cold-plasma effects. From the similarities in the more obvious parameters, one would suppose that finite-orbit effects in the two plasmas are of similar magnitude. The suggestion then is that enhanced stability in DCX-1.5 may be due to some feature of cold-plasma stabilization that is quite

Table 1.2. Parameters of the DCX-1.5 and ALICE Experiments

Item	DCX-1.5	ALICE
Injection energy, keV	15	20
α in $B = B_0(1 - \alpha r^2)$, cm^{-2}	$\approx 6.5 \times 10^{-4}$	$\approx 6.5 \times 10^{-4}$
B_0, kG	10	5–8
Plasma radius, cm	15	10–12

different in the two plasmas. One such feature appears to be the proximity of the grounded end walls in the two facilities. Those of DCX-1.5 are no further than 15 cm from the midplane, while those of ALICE were rarely as close as 40 cm.

The theory of Guest and Beasley[7] incorporates both finite-orbit and cold-plasma effects, and this theory is being applied to determine the relative stability of the DCX-1.5 and ALICE configurations. Some experiments involving changes of end-wall locations and of the magnetic-field intensity are planned to investigate these effects.

[7]G. E. Guest and C. O. Beasley, Jr., *Phys. Fluids* **9**, 1798 (1966).

1.4 SUMMARY

The initial studies of the DCX-1.5 plasma have produced encouraging and interesting results. Up to 40 mA of 15-keV H^0 has been injected. The plasma lifetimes, up to 160 msec, are competitive with those of contemporary facilities. The Lorentz ionization fraction is 1.2×10^{-4} for H^0 produced from incident H_2^+. Densities of 4×10^8 cm^{-3} have been obtained. That this density is not limited by flutes suggests stabilizing effects, which are amenable to further investigation. The final high-density state is stable against oscillations which can be detected by high-frequency electrostatic probes.

2. Injection and Accumulation: Multiple-Pass Experiments (DCX-2)

P. R. Bell
J. S. Culver
R. C. Davis
S. M. DeCamp
J. C. Ezell
J. E. Francis
C. F. Harrison[1]
G. G. Kelley
N. H. Lazar
J. F. Lyon
E. C. Moore
O. B. Morgan[2]
T. F. Rayburn
R. F. Stratton
C. W. Wright

2.1 INTRODUCTION

The peaks seen in the pitch-angle scan of the molecular-ion beam have been explained. They are consistent with calculated single-particle orbits for the relatively few turns the beam makes from injector to the axial location of the detector. Their presence indicates that space-charge effects or beam instabilities produce a negligible effect on the beam trajectory, at least over the first quarter of the path length.

Operation with hydrogen- or deuterium-arc dissociation produces plasma densities up to 5×10^9 hot protons/cm^3, an order of magnitude above that attained with gas dissociation. The density, in general, increases as the pressure decreases (to 2×10^{-6} torr). To obtain still lower pressures, the gas fed into the arc must be reduced; this produces changes in the arc and prevents an accurate scaling to lower pressures. Improved pumping speed should permit this determination in future experiments. During the plasma decay after H_2^+ beam turnoff, rf emission is seen at these higher densities, although it was not present at the lower densities with gas dissociation. The rf is not continuous but appears in bursts with quiescent intervals of 100 to 200 msec during which the plasma may be studied without evident instabilities. The bursts are accompanied by a small additional charge-exchange loss rate, apparently related to an energy redistribution of the trapped particles. This rf mode is related to the velocity distribution of the trapped particles, and a detailed theoretical treatment of this mode is reported in Sect. 8.4. From energy spectra taken after beam turnoff, it is estimated that the change in spectra produced by the rate of energy degradation from scattering by arc and cold plasma electrons is compensated by the rate of charge exchange (which would have "hardened" the spectra in the absence of that degradation).

An accurate determination of the energy spectra obtained at the highest densities cannot be made until a collimator penetration difficulty in the neutral-particle spectrometer is repaired. An energy analyzer with resolution of 4.5 keV permits examination of protons down to 15 keV.

Gridded probe measurements of cold plasma yield the radial distribution of plasma potential as a function of pressure (in the range 1.3 to 5×10^{-6} torr) for gas dissociation. Potentials up to 800 V peaked on axis and radial electric fields of 40 V/cm have been measured. Above 3×10^{-6} torr (above the transition which removes the central-peak plasma), the potential falls to less than 50 V with considerably weaker electric fields.

[1]Analytical Chemistry Division.

[2]Present address: University of Wisconsin, Madison.

2.2 ANALYSIS OF THE MOLECULAR-ION BEAM TRAJECTORIES

A persistent problem is that of determining if all the neutral particles seen by the energy analyzers may be attributed to charge exchange. A definitive answer has not yet been given, in part because it had not been established that the molecular-beam location was restricted to single-particle trajectories. In fact, a series of peaks observed[3] when scanning with a perpendicular slit arrangement of the energy analyzer in that location which viewed mostly the H_2^+ beam gave rise to suspicions that the molecular beam might have been unstable (see Fig. 2.1). Of course, it is important to determine if the beam is stable or not and what the consequences of instability might be.

The origin of these peaks has now definitely been established as being a geometric property of single-particle orbits viewed by the highly collimated energy analyzer. To see how this comes about, it is informative to restrict one's attention to a uniform field injection geometry. In that case the distance, z, from the injector for a given pitch angle, α, is given by

$$z = (v \sin \alpha)t \,, \tag{1}$$

where v is the ion velocity, and t is the time. Since the cyclotron frequency, ω_c, is constant in space, the phase angle, ϕ, of the particle in its helix projected on the perpendicular plane is

$$\phi = \phi_0 + \omega_c t \,, \tag{2}$$

with ϕ_0 the phase at the injector. One notes that the detector sees all trajectories from only a specific phase location in the helix, say ϕ_d. Thus all ions, in order to be seen at the detector, independent of the pitch angle, α, travel a phase-angle distance

$$\phi_d = \delta\phi + 2\pi n \,,$$

where $\delta\phi$ is the phase angle between the injection point and the observation angle, and n is an integer. Thus one can write the pitch angle of the helix seen by the detector at a particular z location in the following form:

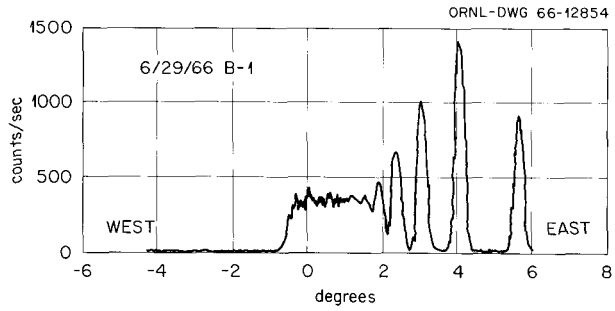

Fig. 2.1. Neutral Particle Flux vs Angle with the Scanner Slit Perpendicular to the Magnetic Axis at a Point 15 in. from the Injector. The peaks are associated with the molecular-ion beam.

$$\sin \alpha_d = \frac{\omega_c}{v} \frac{(z' - l \sin \alpha_d)}{n + (\delta\phi/2\pi)} \,, \tag{3}$$

where $l \sin \alpha_d$ represents the distance from the detector axial position, z', to the point of dissociation; l is the distance from the detector to the observation point. In general, since α_d is a small angle, $l \sin \alpha_d$ is small compared to the axial distance between the detector and the injector. Thus for a detector collimated to view only a small range in pitch angles, for axial distances where n is not too large, only a very small range of angles in the beam will be seen. Other groups of angles will be seen when n changes by integral amounts, and these correspond to the observed peaks. In fact, the ratio of the angles of the peaks is given by

$$\frac{n_1 + (\delta\phi/2\pi)}{n_2 + (\delta\phi/2\pi)} = \frac{\sin \alpha_2}{\sin \alpha_1} \frac{z' - l \sin \alpha_1}{z' - l \sin \alpha_2} \approx \frac{\alpha_2}{\alpha_1} \,.$$

In order to verify that these considerations are valid in the nonuniform field cases which actually exist, the orbits corresponding to particles which produced the peaks and valleys seen in Fig. 2.1 were traced backward in time, and their radial and azimuthal location at the position of the injector (z = 42 in.) was determined. The results (Table 2.1) show that all the trajectories corresponding to the peaks originate plausibly at the location of the injector because they are grouped closely in space, whereas the trajectories corresponding to the valleys fall almost

[3] *Thermonuclear Div. Semiann. Progr. Rept. Apr. 30, 1965*, ORNL-3836, p. 30.

Table 2.1. Pitch Angles (α) and Radial Position of Beam Helix at the Injector Axial Location [$r(z = 42$ in.)] Calculated from the Peaks and Valleys Observed in Fig. 2.1

Also shown are the axial positions of the helix corresponding to the same peaks and valleys for the radial position of the injector [$z(r = 9.30$ in.)]

α_d ($z \simeq 28$ in.) (deg)	α ($z = 42$ in.) (deg)	r ($z = 42$ in.) (in.)	z ($r = 9.30$ in.) (in.)
5.43*	9.20	9.30	42.0
3.82*	8.53	9.33	42.1
2.84*	8.07	9.34	42.0
2.20*	7.73	8.72	42.3
1.70*	7.56	8.37	42.5
4.68**		3.22	39.9 44.7
3.41**		3.53	40.1 44.8
2.52**		3.43	40.0 44.6
1.76**		5.93	38.8 43.1

*Peaks
**Valleys

180° in phase away from the injector at the axial position of the injector. In other words, had one considered the trajectories of orbits with the pitch angles given by the location of the valleys and started from the injector, one would find that at the z location of the detector one would simply not have seen that trajectory.

Since the peaks, corresponding to trajectories that are not disturbed greatly, are still seen beyond the midplane, it appears that the molecular ions do follow single-particle orbits over at least one-fourth of their path. There is no evidence other than some molecular-ion radio-frequency observations that the beam is unstable, and no macroscopic changes in the beam location from that expected have yet been determined. However, the presence of a plasma potential may cause sufficient precession of the beam upon its motion down the machine and back that one cannot be sure that the entire molecular-ion orbit is that theoretically calculated, taking the magnetic field alone.

2.3 HYDROGEN-ARC DISSOCIATION

In previous experiments using a hydrogen arc for dissociation of the molecular-ion beam, we could not get the operating pressure below 4×10^{-6} torr. We had found that cylindrical baffles around the anode and cathode reduced the pressure in the plasma region. These shields caused the gas produced by neutralization of ions ejected from the arc to be reionized by scattering into the arc column. Insufficient pumping in the end regions, however, still prevented lower-pressure operation because of gas streaming through the mirror throats into the plasma region. The use of improved titanium evaporators operated at high evaporation rates (~10 g/h, see Sect. 2.6) has brought the pressure down to 1.2×10^{-6} torr with a hydrogen arc and to 4×10^{-7} torr with a deuterium arc. The arc geometry is shown in Fig. 2.2.

A detailed study of the plasma found has been delayed by our recent discovery that the energy-sensitive detectors have relatively greater sensitivity at high energies (see Sect. 2.4). This fault is particularly troublesome in hydrogen-arc experiments because the observed spectrum shows unusually large fractions of very energetic particles. The difficulty does not affect the foil detectors, and the plasma density obtained by integrating their current gives the density of plasma ions above 50 keV energy. The maximum density so far observed by the foil detectors with H_2 arc dissociation is $\sim 5 \times 10^9$ ions/cm^3, assuming a plasma radius of 15 cm. Because of the difficulties with the collimation system of the energy analyzers, the radial distribution of the plasma is poorly known, and a more accurate value of the density must await future experiments.

We had reported that in gas dissociation experiments, there was no rf activity in the central-peak plasma after beam turnoff.[4] Using a hydrogen arc for dissociation, we now see rf after beam turnoff for densities greater than 10^9 ions/cm^3 in the hot plasma. The rf occurs in bursts with intervals as long as 0.1 to 0.2 sec between bursts, the pattern extending for as long as several seconds after beam turnoff. The rf bursts become more infrequent with time but more numerous at a given time as the plasma density is increased.

[4]P. R. Bell *et al.*, *Phys. Rev. Letters* **16**, 1152 (1966); *Thermonuclear Div. Semiann. Progr. Rept. Apr. 30, 1966*, ORNL-3989, p. 15.

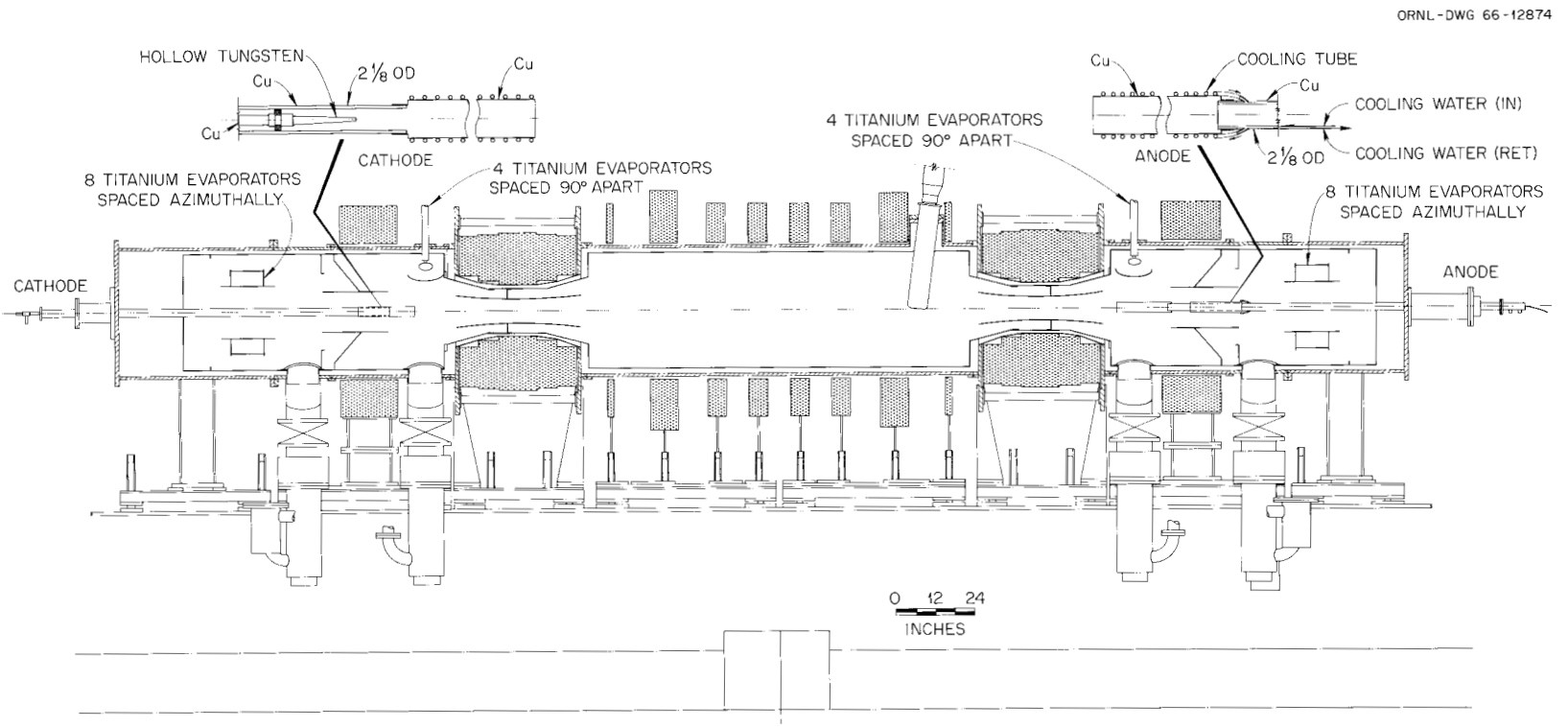

Fig. 2.2. Section of DCX-2 Showing Hydrogen-Arc Electrode Locations and New Baffle and Titanium Evaporator Arrangements.

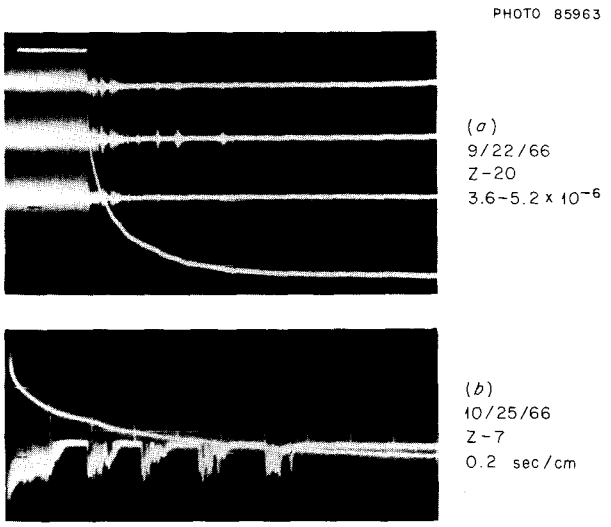

Fig. 2.3. (*a*) Upper Trace Is the Integral of Charge-Exchange Neutral Current After Beam Turnoff; Integral Increases Downward at 3.3×10^{-10} Coulomb/Division. The other traces are broad-band radio frequency in the range 0 to 17 Mc in rings 3, 4, and 5 along the liner. Ring 4 is at the midplane. Pressure, 5.2×10^{-6} torr raised with hydrogen; sweep speed, 0.2 sec/division. (*b*) Upper Trace Is an Integral as in (*a*); the Lower Trace is H^+ Fundamental Detected by an RF Spectrometer from Midplane. Sweep speed, 0.2 sec/division. Note change of slope in the integral curves in coincidence with rf bursts.

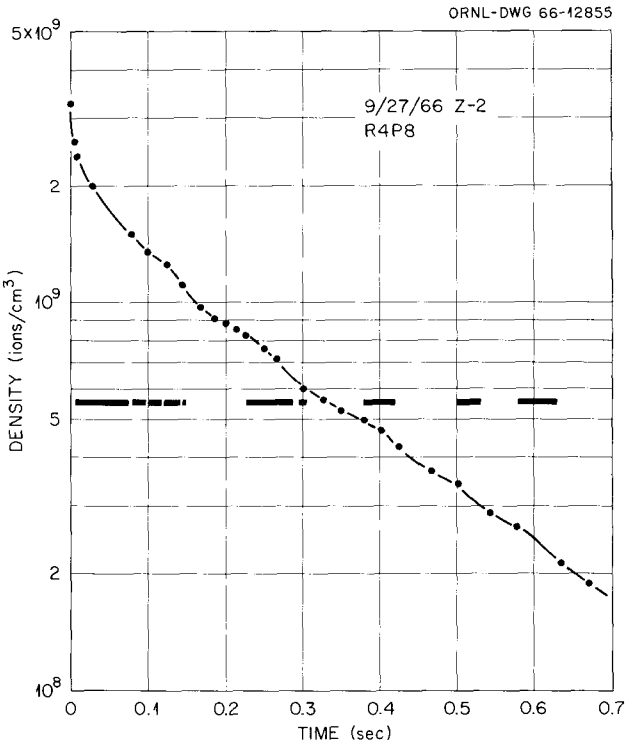

Fig. 2.4. Plot of Foil Detector Integral at DCX-2 Midplane. The heavy broken line represents intervals of rf emission. Pressure, 2.5×10^{-6} torr.

Figure 2.3 shows the typical behavior. Also shown on the same traces are the integrals of the current from one of the neutral detectors. Correlation of the increased charge-exchange loss and the rf bursts is apparent. Another integral curve is plotted semilogarithmically in Fig. 2.4. Several interesting facts can be inferred from these results. First, since the integral of the charge-exchange current increases more rapidly during a burst, energy mixing is throwing some particles to lower energies, where they are lost more rapidly by charge exchange. Second, the fact that the slope of the integral after the burst is not noticeably different from its value just before suggests that only a small fraction of the particles in the machine is lost during any one burst.

A plausible explanation for the observed behavior is that the instability depends on the energy distribution. As more and more low-energy particles are lost through charge exchange, a threshold is exceeded, and the resulting disturbance reestablishes a stable distribution. Hall[5] has presented a theory for such an instability, but we have not been able to establish a quantitative comparison. Further theoretical studies of interaction of two groups of particles of specified energy distribution are in progress (see Sect. 8.4). The instability appears to reestablish equilibrium with only negligible particle loss. Also, it is seen that there is not a strong dependence of threshold on density, since the rf occurs after the plasma has decayed to only a small fraction of the beam-on value. We are encouraged, therefore, to believe that the distribution is altered in steady state by this mechanism without limiting the density that can be achieved.

The harmonic content of the radio frequency emitted during decay was considerably different from that emitted during beam-on intervals. Figure 2.5 shows the spectra for the two cases. The H^+ fundamental is weaker than the second harmonic with beam on, but it is more intense than

[5]L. S. Hall, W. Heckrotte, and T. Kammash, *Phys. Rev. Letters* 13, 603 (1964).

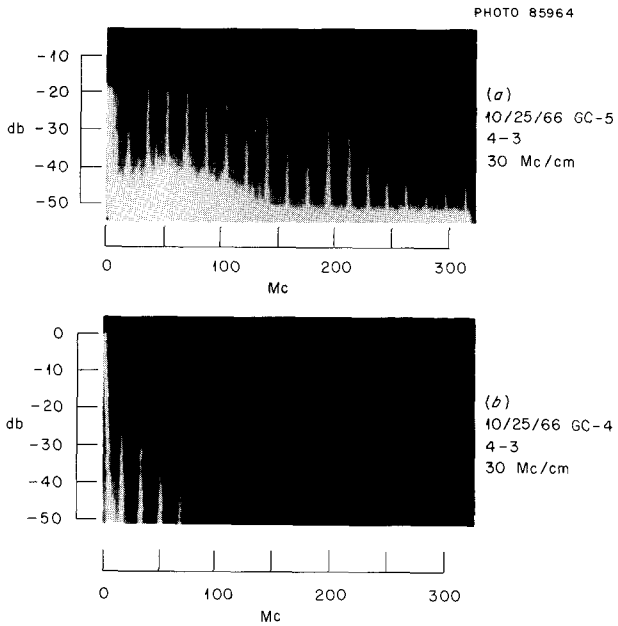

Fig. 2.5. (*a*) **RF Spectrum Emitted During Beam-on Intervals;** (*b*) **That Emitted in Beam-off Intervals During Plasma Decay.**

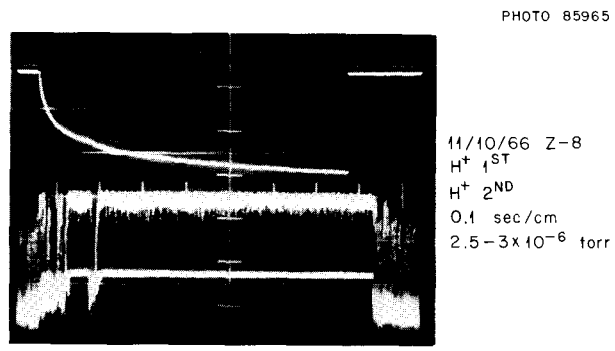

Fig. 2.6. RF Harmonics During Plasma Decay. The upper trace is the gated foil detector integral, the middle trace is the H^+ fundamental, and the lower trace is the second harmonic – both as seen by rf spectrometers. The pressure was 2.5×10^{-6} torr, and the sweep speed was 0.1 sec/division.

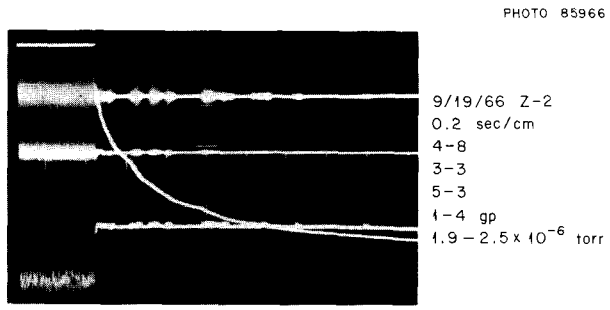

Fig. 2.7. "Warm" Ions Ejected Axially During RF Bursts. Upper three traces similar to the upper three traces of Fig. 2.3*a*. The lower trace is the current to the collector of a gridded probe at +45 V behind a +290-V second grid. The upward direction represents ion collection, and the downward direction represents electron collection. Note the ion collection pulses coincident with rf bursts.

the second harmonic during decay. The time behavior of the fundamental and second harmonic is shown in Fig. 2.6.

The rf bursts during decay have an effect upon the cold plasma streaming out along the field. A gridded probe (see Sect. 2.5) was located inside the main mirror but at a mirror ratio of 1.1 so that no high-energy ions reached it. The probe was adjusted to accept electrons and to reject ions with axial energy less than 290 eV. The response of this probe is shown in Fig. 2.7. When the beam was cut off, the electron current became small. During the decay, there were short bursts of signal coincident with rf bursts. These represented ions of energy above the 290-V repelling potential of the second grid of the probe. These ions are being heated by the rf, producing instability or being ejected by it from an existing warm ion population.

Attempts to observe polarization of the rf from the plasma by measurements at the liner wall have produced poor results except at very low plasma density. A short dipole probe was prepared to measure inside the plasma. By pulsing the injected beam for only a short time (~70 msec), the probe temperature did not go above a red heat. The foil detector integrals were reduced to approximately half with the probe tip ~3 in. from the plasma axis. The rf was considerably more intense with the dipole axis in the azimuthal direction than in the direction of the field lines, as was expected. Figure 2.8 shows the two responses. A spectrum measured with a magnetic loop at the liner wall is shown for comparison.

At the lowest pressures the plasma decayed quite slowly (~0.25 to 0.5 sec time constant after a short period of more rapid decay), and the cold plasma and the plasma of the arc had a long time

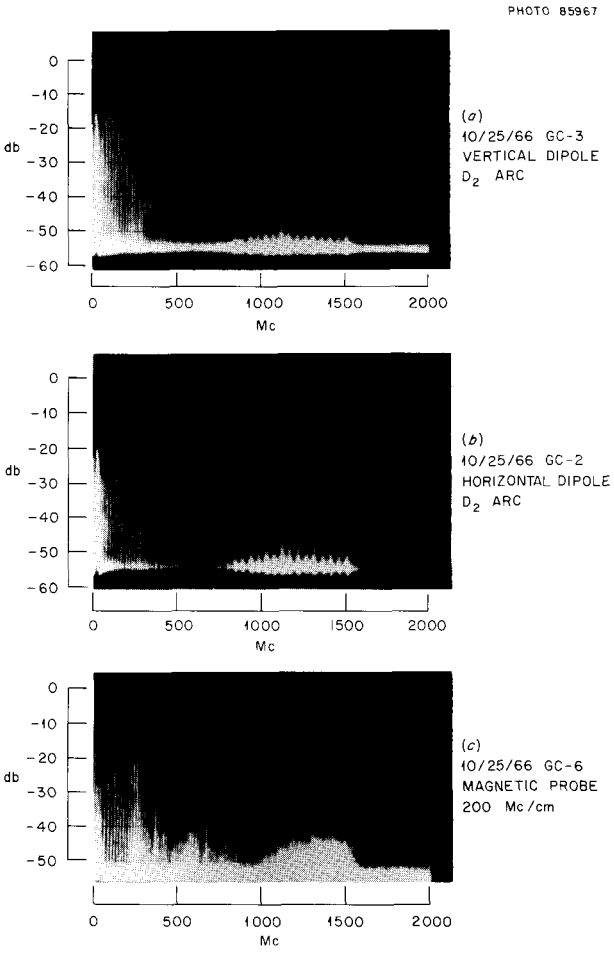

Fig. 2.8. Radio-Frequency Spectra. (*a*) Shows the response of a short dipole probe inside the plasma at 3 in. from the axis. The dipole is pointed along the azimuthal direction. (*b*) Shows the response of the same probe oriented along the field lines. (*c*) Shows the response of a magnetic loop probe at the liner wall. The "white" noise smear ending at about 1500 Mc is produced by the D_2 arc. The sharp cutoff is produced by a 1500-Mc low-pass filter.

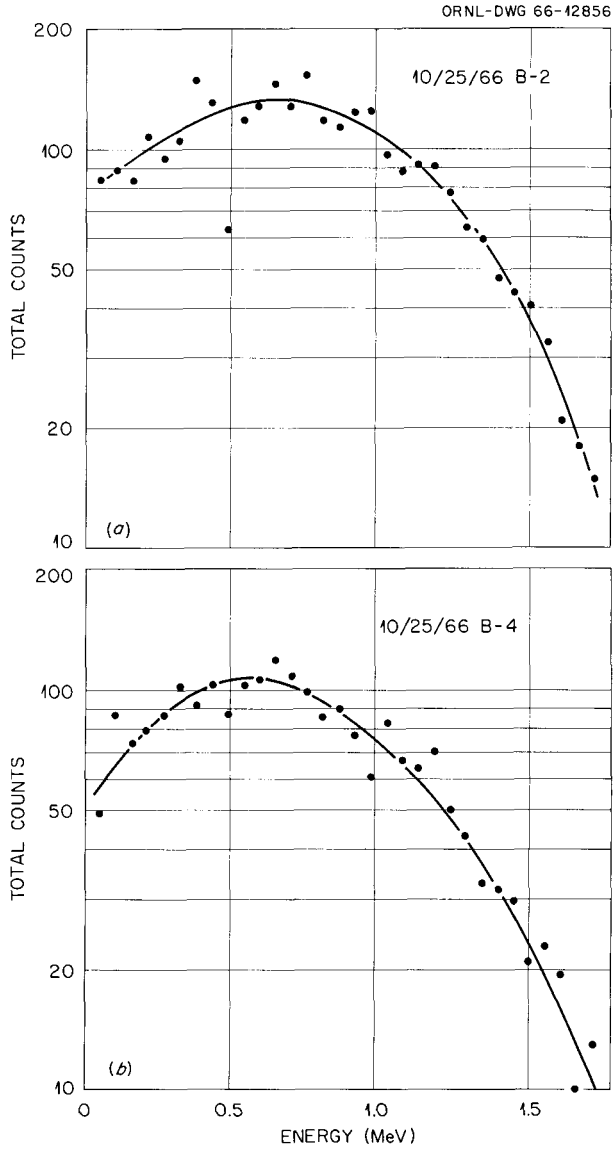

Fig. 2.9. Energy Spectrum of Plasma Protons During Decay of the DCX-2 Plasma. (*a*) From 0 to 15 sec after beam turnoff. (*b*) From 2 to 15 sec after beam turnoff.

to degrade the energy of the trapped ions. To get an estimate of this effect, the beam was operated 2 sec on and 20 sec off. The energy analyzer was switched on during the beam-off interval. The spectrum was that of the ion energies at the time of their escape by charge exchange. This spectrum should be the same as that obtained during beam-on by correcting the neutral flux for the charge-exchange cross section, if the effects of energy degradation and energy spreading were negligible or compensated each other. Figure 2.9*a* is the spectrum obtained. This is quite similar to the beam-on spectrum usually obtained. It is not correct to suppose that the effects of both energy spreading and degradation are negligible, however, because of the great similarity of Fig. 2.9*b*, which is a spectrum obtained in the same manner except that the energy analyzer was switched on after a delay of 2 sec after beam-off. A greater number of decay cycles were of course required. The great similarity of both curves shows that the energy-spreading

process must be unimportant during decay and that the energy degradation process in the arc and cold plasma must be the major factor determining the energy distribution after beam turnoff. The effect of charge exchange in hardening the spectrum must be balanced by the softening effect of energy degradation, since a sort of equilibrium is reached. The plasma decay times observed are close to those expected due to charge exchange alone, showing that the energy degradation is not extremely rapid.

2.4 ENERGY ANALYZER DEVELOPMENTS

The highly collimated scanning silicon barrier detectors used to measure the distributions in energy, pitch angle, and radial position of the charge-exchange neutrals from the trapped energetic protons and the direct dissociation neutrals from the H_2^+ beam have been described previously.[6] Their main limitation in analyzing these energetic neutrals had been the relatively poor energy resolution, ~30 keV full width at half maximum (FWHM) for the complete analyzer system. Except for the sharp dissociation and charge-exchange peaks from the H_2^+ and H_3^+ beams, the energy spectrum of the energetic neutral flux does not change significantly in 30 keV, and the smearing of the spectrum as a result of this lack of resolution was not a serious problem for proton energies above ~100 keV. However, the proton energy region below ~80 keV could not be studied due to detector noise, and the distribution of lower-energy protons in DCX-2 could not be measured. For this reason, a high-resolution analyzer using a cryogenically cooled detector and preamplifier has been constructed in cooperation with ORTEC and used in DCX-2.

Figure 2.10 is a photograph of the assembled probe. The rotating scanning head is visible in the ±45° viewing aperture in the front circular copper plug that seats in the inner vacuum liner. Figure 2.11*a* shows the spherical scanning head with the attached solid-state FET preamplifier. Figure 2.11*b* is an exploded view of this assembly showing the construction details. The

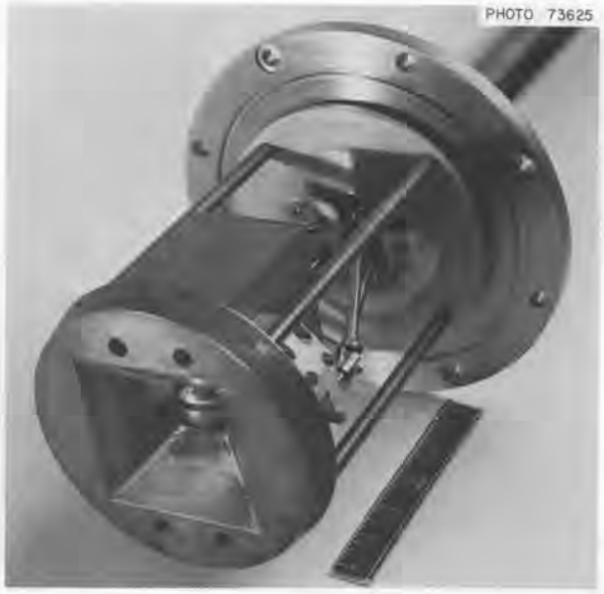

Fig. 2.10. Assembled Cryogenic Energy Analyzer Probe. The scanning head rotates ±45° about its horizontal axis while viewing ±45° in the perpendicular plane. The orientation of the probe in the machine determines whether a perpendicular or parallel slit scan is being made.

scanning assembly shown in Fig. 2.11*a* is enclosed in the liquid-nitrogen-cooled copper box seen behind the front copper plug in Fig. 2.10. Placing the solid-state preamplifier adjacent to the detector reduces the preamplifier input capacitance and its associated noise. Cooling the detector and preamplifier further reduces the noise.

The new analyzer with a detector area of 50 mm^2 has an energy resolution of 13 keV FWHM for 40-keV protons at room temperature and 4.5 keV FWHM at 118°K, its optimum operating temperature. The energy resolution is below 5 keV FWHM over a fairly wide operating range, from ~95 to ~140°K, and protons down to ~15 keV can now be reliably analyzed. The response of the detector to the 270-keV neutrals from dissociation is shown in Fig. 2.12. A fault in the collimation required for reduction of the charge-exchange flux to the detector has recently been recognized. As described previously,[6] the collimation consists of a narrow slit followed by a pinhole. The pinhole typically is a 10-μ-diam hole in a platinum-iridium disk. To reduce analyzer vignetting, the central portion of the disk

[6] *Thermonuclear Div. Semiann. Progr. Rept. Oct. 31, 1963*, ORNL-3564, sect. 2.2; *Thermonuclear Div. Semiann. Progr. Rept. Oct. 31, 1964*, ORNL-3760, sect. 2.4.

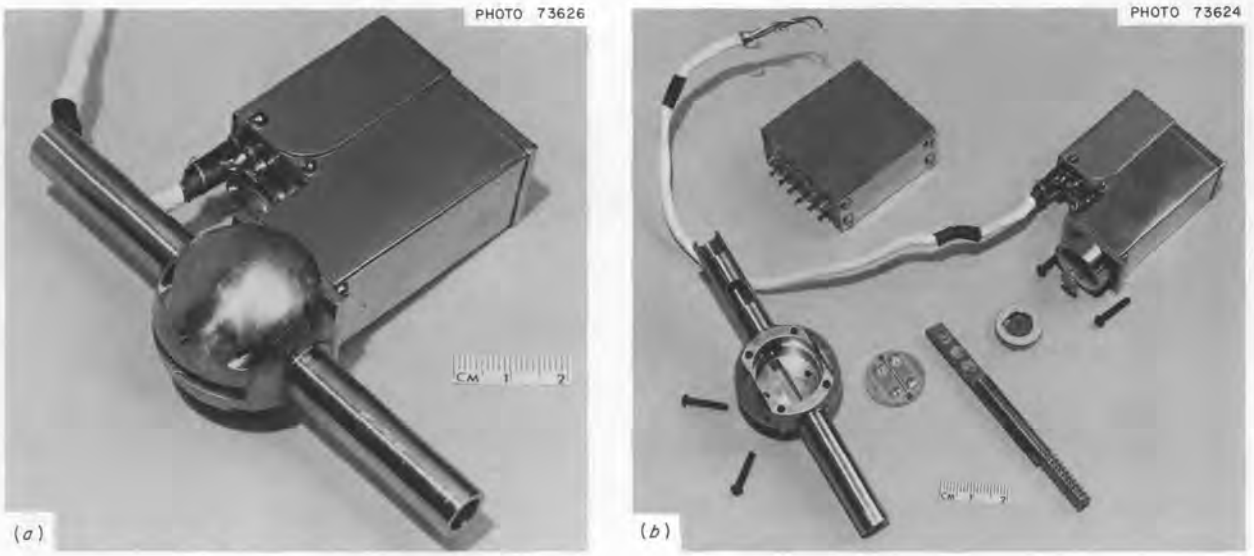

Fig. 2.11. Scanning Head Assembly. The scanning head with attached solid-state preamplifier is shown in (*a*). The shaft holds different size collimating pinholes, and the assembly rotates about the shaft axis. An exploded view of this assembly is shown in (*b*). From bottom left to top right can be seen the back of the scanning head, the collimating 5- or 20-μ optical slit, the stick holding 10-, 20-, and 40-μ pinholes, the circular silicon barrier detector, and the FET preamplifier with attached signal and bias leads. The cable driver is also shown at the top.

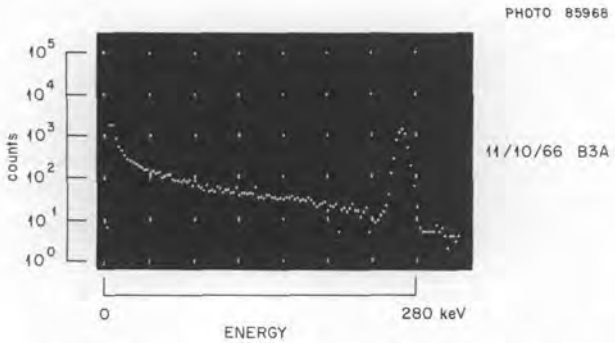

Fig. 2.12. Energy Spectrum of the DCX-2 Plasma Showing Dissociation Neutral Peak at 270 keV. This spectrum was made with the improved energy analyzer and shows improved resolution. Energy calibration is ~40 keV per division.

was made thinner. This thinner portion is penetrated by protons above 1 MeV and was satisfactory when there were relatively few such protons. Recently with hydrogen-arc dissociation the population of high-energy protons has been greatly increased, and the effect of the penetration cannot be neglected. New arrangements are being prepared to eliminate this difficulty. The "thinned" collimators were first used after April 13, 1964. Spectra with arc dissociation with mean ion energies above 1 MeV had been obtained with the old thicker collimators.[7]

2.5 MEASUREMENTS OF THE COLD PLASMA WITH GRIDDED PROBES

Gridded probe measurements of the cold plasma have been made previously and are discussed in earlier semiannual reports.[8] A grounded first grid is used to prevent disturbance of the plasma by the probe potentials. A second grid is strongly biased to repel ions or electrons while the collector plate obtains a repulsion curve of the remaining species as it is swept through a range of voltages.

Improved probe measurements were taken 20 to 30 cm axially beyond the hot-ion plasma at several different radial distances from the axis of the machine during a gas dissociation run. Figure 2.13 shows the variation in average plasma potential as a function of radius for several different pressures. The values of plasma potential

[7] *Thermonuclear Div. Semiann. Progr. Rept. Apr. 30, 1964*, ORNL-3652, sect. 2.2.2.

[8] *Thermonuclear Div. Semiann. Progr. Rept. Apr. 30, 1963*, ORNL-3472, p. 13; *Thermonuclear Div. Semiann. Progr. Rept. Apr. 30, 1966*, ORNL-3989, p. 26.

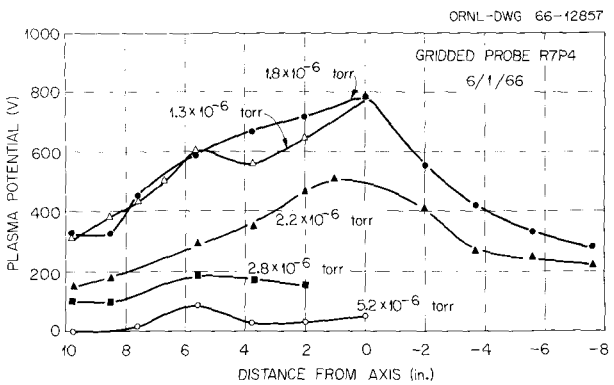

Fig. 2.13. Plasma Potential vs Radial Distance from Plasma Axis at Several Gas Pressures. The plasma was produced by gas dissociation.

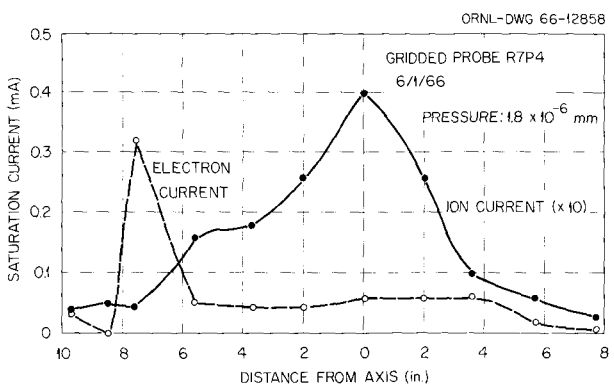

Fig. 2.14. Electron and Ion Saturation Currents as a Function of Radius. The plasma was produced by gas dissociation.

shown have been corrected for a zero shift in the negative direction by using the plasma potential obtained from a hydrogen-arc plasma and assuming that this plasma potential is approximately +5 V. The cause of this negative shift in the gridded probe measurements is not fully understood.

Figure 2.14 shows the variation in the ion and electron saturation currents as a function of distance from the axis of the machine. The large peak in the electron current at $+7\frac{3}{4}$ in. is at the location of the inner face of the injector. This effect is expected, since the Larmor orbits of the "cold" ions are large enough to strike the injector, while the accompanying electrons have small orbits and must leave along flux lines. This peak is present at all pressures for which measurements have been made (from 1.6×10^{-7} to 5.2×10^{-6} torr). The plasma potential in Fig. 2.13 shows a peak at the axis and yields radial electric fields up to 40 V/cm at the lowest pressure. At pressures above that marking the transition from the central-peak plasma to the side-lobe plasma ($\sim 3 \times 10^{-6}$ torr), the plasma potential and the radial electric field are much reduced.

2.6 IMPROVEMENTS IN VACUUM TECHNOLOGY

One purely technical problem which requires continual work is the improvement of the pressure in DCX-2. The problem becomes aggravated in the presence of a hydrogen arc because of the large throughput of hydrogen required to operate the arc. Measurements of pumping speed using the original form of titanium evaporators were disappointingly low ($\sim$10,000 liters/sec) at these large throughputs. Several modifications of the DCX-2 pumping configuration have resulted in improving the net pumping speed in each end to approximately 60,000 liters/sec, even in the presence of the large throughput expected from the hydrogen arc. The modifications include changes in the end liner shown in Fig. 2.2, which incorporates the use of evaporators extended along the field lines in order to increase the condensed titanium area. Taking into account the conductance into the evaporation region, the observed pumping speeds are consistent with a sticking probability for hydrogen which is comparable to those obtained by Clausing[9] at similarly high throughput. Measurements of the evaporation rate from these filaments indicate that with acceptable values of the heater current, the evaporation rate reaches about $\frac{1}{2}$ g/h per filament (the filament length is 12 in.). This corresponds to a gas feed of 0.6×10^{22} atoms/sec or 0.035 cm^3/sec of hydrogen. Under these conditions, in agreement with Clausing's results, we are able to maintain the high pumping speed at the large gas throughputs. This is illustrated in Fig. 2.15. It may be noted that as the throughput is increased, pumping speed remains relatively constant at

[9]R. E. Clausing, *A Large-Scale Getter Pumping Experiment Using Vapor Deposited Potassium Films*, ORNL-3217 (1961).

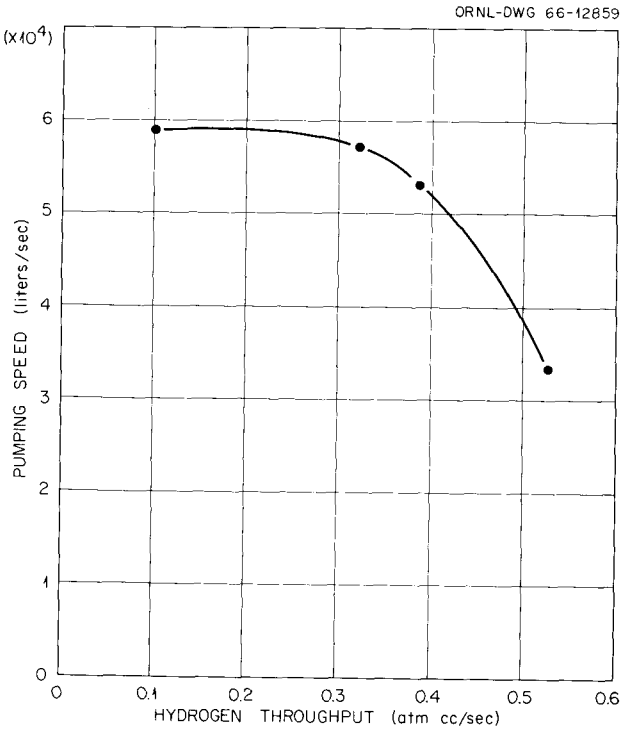

Fig. 2.15. Pumping Speed vs Throughput of Hydrogen for Eight 12-in. Titanium Evaporation Filaments in DCX-2.

6×10^4 liters/sec and then falls rapidly. Raising the evaporation rate by raising the heater current increases the value of throughput at which the break occurs, but only improves the pumping speed slightly. It now appears that the pressures observed with the hydrogen arc are limited primarily by gas flowing from the end regions through the isolation tubes (venturis) into the liner, and that by suitable differential pumping, if the arc continues to run stably, one may reasonably expect lower base pressures. As reported in Sect. 2.3 the base pressures so far obtained are 1.2×10^{-6} torr in the presence of a hydrogen arc fed at 1 to 2 atm cm^3/sec. With a deuterium-fed arc with slightly different geometry, the pressure was 4×10^{-7} torr with reduced gas feed.

3. Electron-Cyclotron Heating

3.1 INJECTION OF NEUTRALS AND TRAPPING ON AN ELECTRON RESONANT ENVIRONMENTAL MEDIUM (INTEREM)

W. B. Ard
M. C. Becker[1]
R. A. Dandl[1]
H. O. Eason
A. C. England
G. M. Haas[2]
R. L. Livesey
O. D. Matlock
M. W. McGuffin

3.1.1 Modifications

During a large portion of this semiannual report period, the INTEREM facility has been undergoing modifications. In particular, a new neutral beam is being added to the facility. The ion source for the beam has been brought considerably closer to the facility, and the beam will enter the facility from directly above the magnetic axis. The new beam should provide about 250 mA equivalent of 20-keV H^0.

The ion source is being supplied by the Ion Source and Accelerator Development Group under the direction of G. G. Kelley (see Sect. 7.1). The beam will be neutralized by a magnesium cell prior to its entrance into the trapping region, as in the DCX-1.5 and the proposed DCX-3 experiments. The facility is expected to be in operation within a few months. Figure 3.1 shows a schematic view of the completed facility.

[1]Instrumentation and Controls Division.

[2]Present Address: Texas A & M University, College Station.

3.1.2 Impurities

Some studies were made of the contamination problem during this report period. The chief sources of contamination that had been observed spectroscopically during the operation of the electron-cyclotron plasma (ECP) were copper and carbon. By the simple expedient of evaporating a thin layer of aluminum over the inside of the microwave cavity, the copper contamination was reduced to a negligible amount. No aluminum contamination was spectroscopically observed in the ECP after the evaporation. However, the carbon contamination remained. It is believed that very extensive modifications on the vacuum system would have to be made to eliminate the carbon, since it probably arises from the presence of diffusion pump oil.

3.1.3 Spectral Studies in INTEREM

J. R. McNally, Jr.
A. C. England
M. W. McGuffin

Earlier,[3] some spectral studies of He and N_2 feed gas to INTEREM revealed the rapid increase in intensity of the spectra of higher states of ionization as the microwave power was increased. Data obtained since that time on the spectral intensity variations of N_2^0, N_2^+, and N^0 with power are illustrated in Fig. 3.2.

The spectra of the molecules N_2^0 and N_2^+ reach a saturation intensity quite rapidly, suggesting

[3]*Thermonuclear Div. Semiann. Progr. Rept. Apr. 30, 1966*, ORNL-3989, p. 35.

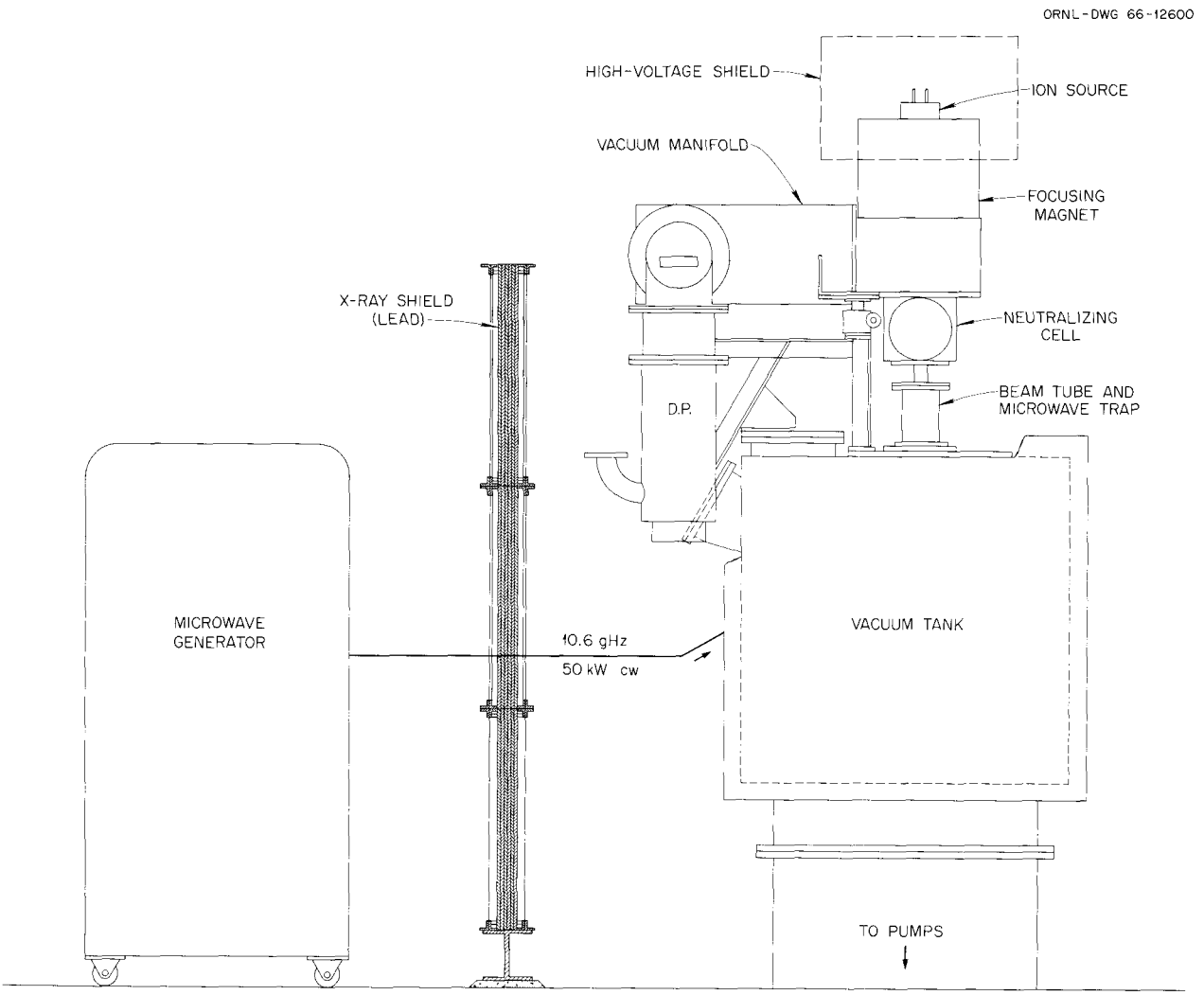

Fig. 3.1. Schematic View of the INTEREM Facility. The vaccum box is about 4 ft square in the section shown, and the magnetic field therein is directed normal to the paper.

that these species are excited and ionized primarily at the surface of the plasma. On the other hand, the spectrum of N^0 (which is probably formed by a Franck-Condon electronic excitation of N_2^0 or N_2^+ to repulsive electronic states which decay and produce fast N^0) continues to increase with very high power. The Franck-Condon neutrals, N^0, can penetrate across the magnetic field, whereas the N^+ cannot (N^+ also revealed a saturation).[3] Since the mean free path of the N^0 due to its higher velocity is probably long even at the highest power levels, the spectrum of N^0 is not expected to be grossly attenuated in the volume of the plasma.

Thus it appears that the N^0's represent Franck-Condon neutrals. Such neutrals would affect adversely the "burnout" criteria for plasmas; however, it should be noted that the Franck-Condon fast-neutral explanation may also represent a mechanism for feeding cold nuclear fuel deep into a fusioning plasma.

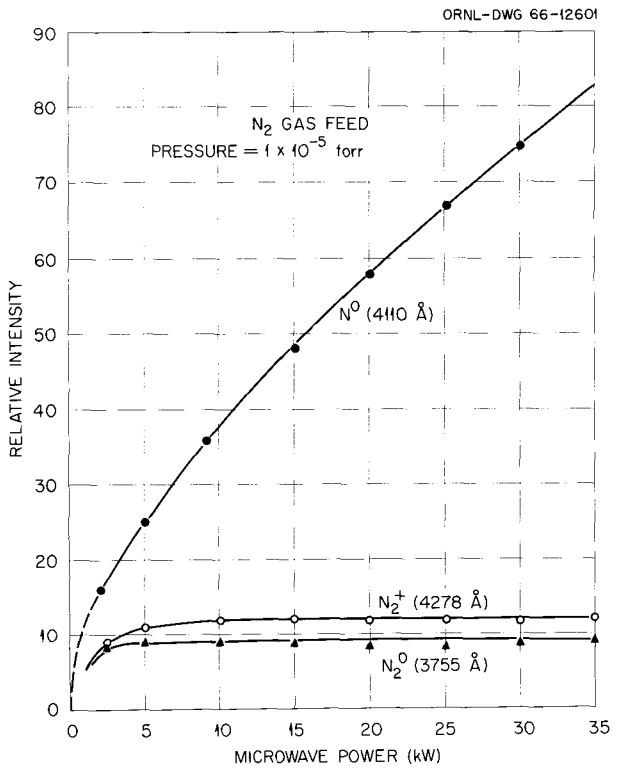

Fig. 3.2. Spectral Emission from a Nitrogen-Fed Plasma in the INTEREM Facility vs Microwave Power. N^+, N^{2+}, and N^{3+} not monitored in this series – see ref. 3, Fig. 3.6.

3.2 ELECTRON-CYCLOTRON HEATING EXPERIMENTS IN THE ELMO FACILITY

W. B. Ard
M. C. Becker[1]
R. A. Dandl[1]
H. O. Eason
A. C. England
G. M. Haas[2]
R. L. Livesey
O. D. Matlock
M. W. McGuffin

During this semiannual report period, ELMO was operated in several open-ended magnetic configurations with electron-cyclotron plasmas heated by 3-cm microwave power. The three magnetic configurations used were double-folded cusp, mirror, and "stuffed" folded cusp. The first two configurations have been described in previous reports.[4,5] The "stuffed" cusp configuration was made by the addition of a current-carrying "stuffing bar" along the axis of the machine.

The microwave cavity used was 57 cm in diameter, 51 cm long, and extended into the axial and annular throat regions to allow good pumping through perforated metal surfaces. In these regions, plasma was expected to leave the containment region along field lines. A maximum of 5.1 kW of microwave power was obtained from a Varian VA-848 klystron amplifier operating at a frequency of 10.6 GHz. The experiment was diagnosed by a variety of slow and fast particle probes (both axial and radial), but experiments designed to analyze several producible instability modes have not yet been performed. The principal observations to date have employed an x-ray pinhole camera and the particle probes.

Figure 3.3 shows a pinhole camera x-ray photograph obtained when the facility was operated with a mirror magnetic field with a mirror ratio of 3.3:1. In this and the following pictures the axis is horizontal and the midplane is vertical. The interesting features of this photograph are as follows: (1) there is evidence of a contained plasma between the mirrors, (2) there are losses to the mirror throats (the bright rings at a radius of 9 cm), and (3) there are losses to the radial wall of the cavity (radius $\simeq$ 28 cm). The bright spots near the midplane were identified as small projections on the interior of the radial wall.

Some neutrons, probably from Coulomb dissociation of deuterium, are observed under these conditions, but the flux is several orders of magnitude lower than that observed with 8-mm radiation.

Figure 3.4 shows a pinhole camera x-ray photograph when the facility is operated as a double-folded cusp. The heating zone is a closed surface with a radius and axial width approximately the same as those of the contained plasma, as seen in the photograph.

The large bright rings (radius $\simeq$ 18 cm) are the side walls of the cavity where the field lines near the separatrix leave the plasma containment zone. These bright rings represent plasma losses out through the line cusps. The photograph shows a fairly uniform plasma filling the region inside the heating zone and with "horns" extending into the line cusp regions. A corresponding "horn" out through the axial point cusp is not seen, probably because of the smaller thickness of plasma along the chord from the pinhole camera.

[4] *Thermonuclear Div. Semiann. Progr. Rept. Oct. 31, 1965*, ORNL-3908, sect. 3.2.

[5] *Thermonuclear Div. Semiann. Progr. Rept. Apr. 30, 1966*, ORNL-3989, sect. 3.2.

An unexpected result from this configuration is that no neutrons are observed when the plasma is fed with deuterium gas. X-ray spectra taken show no x rays with energies exceeding 2 MeV. However, the absence of an energetic tail on the electron distribution may be the result of nonadiabatic losses of the electrons of energy >2.2 MeV necessary for this reaction.

Another surprising feature of this configuration is the existence of an instability that causes axial plasma losses, correlated on several axial probes. This instability could be suppressed by increasing the gas pressure, provided the magnetic-field strength had been so increased as to remove by a least a factor of 2 the closed surface for electron-cyclotron resonance from the region

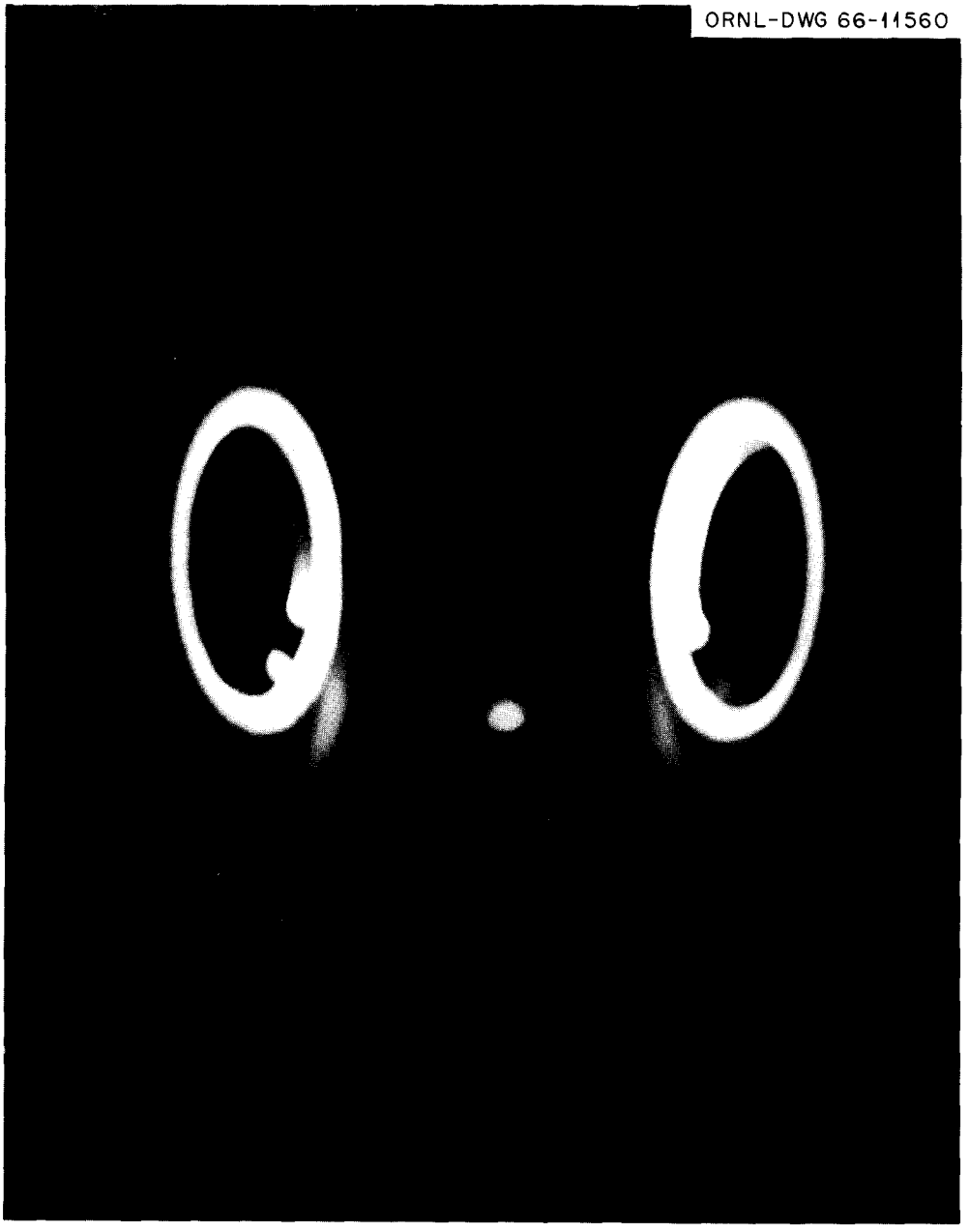

Fig. 3.3. Pinhole X-Ray Photograph of the Plasma when ELMO Is Operated as a Mirror. The plasma is supplied with 3 kW of microwave power. The D_2 gas pressure is 3.0×10^{-5} torr.

of "bad" field curvature in the cusps. This instability might therefore be associated with plasma in regions of bad field curvature in the ring cusp regions communicating with plasma in the main volume.

Figure 3.5 shows a pinhole x-ray photograph with the stuffing bar on the axis of the machine but no current in the bar. The magnetic field is approximately the same as in the previous picture. The losses out the line cusp are observed as are losses to the bar. Losses on the bar are seen both at the magnetic-field zero on the midplane, and axially out into the point cusp regions.

The fact that the bar shows up as two bands of illumination at the top and bottom of the bar rather than being illuminated uniformly is peculiar. We

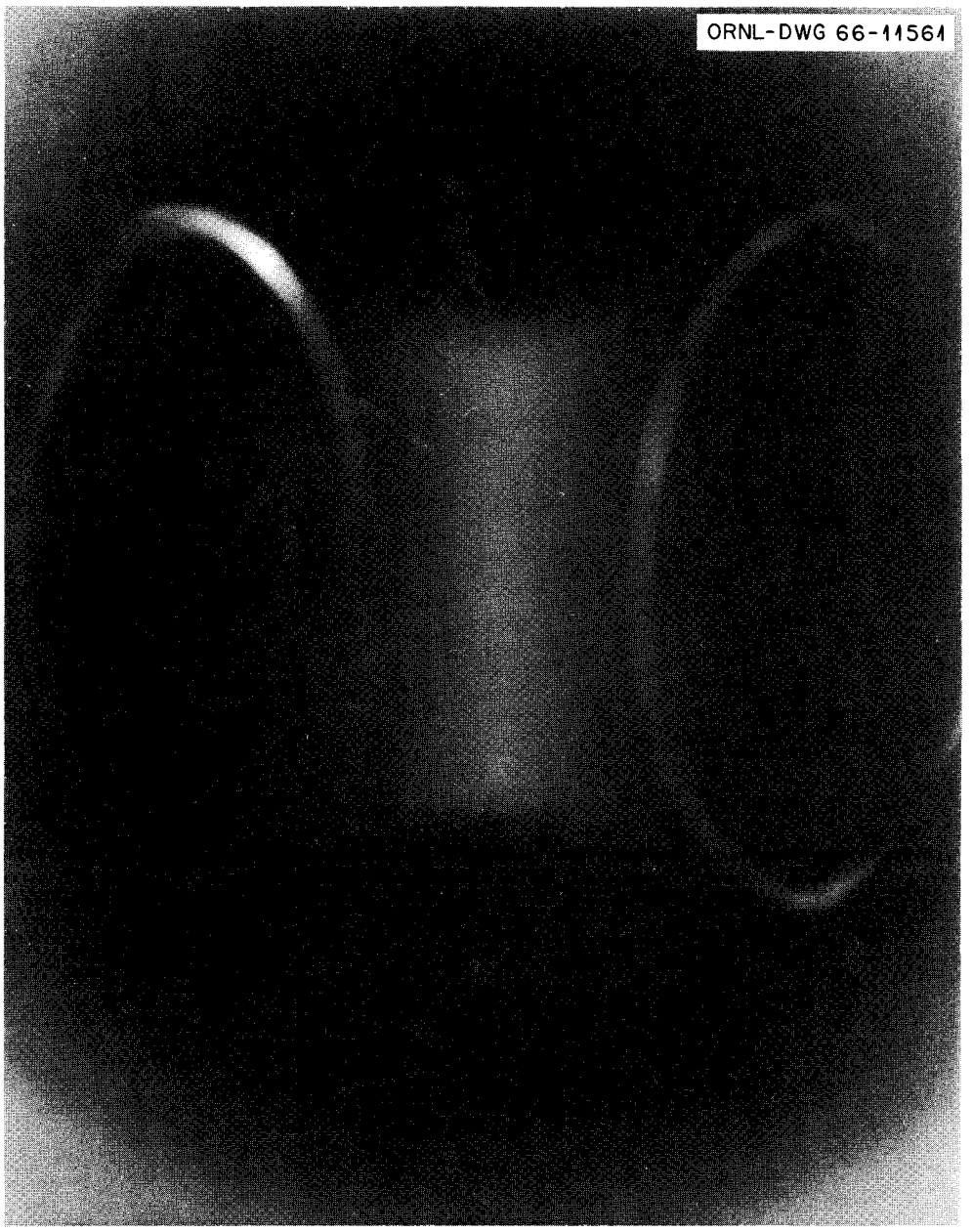

Fig. 3.4. Pinhole X-Ray Photograph of the Plasma when ELMO Is Operated as a Folded Cusp. The plasma is supplied with 3 kW of microwave power at a D_2 gas pressure of 2.0×10^{-5} torr.

interpret this limb brightening as being due to two effects: (1) the energetic electrons striking the bar emit x radiation nonisotropically, and (2) the chord length from the camera through the emitting region is longest near the edges of the bar.

This picture is to be contrasted with the following picture, Fig. 3.6, in which the current in the stuffing bar is on. The total current in the bar is 65,000 A, which produces a minimum-*B* magnetic well near the bar. Another electron-resonance heating zone is also created within a few centimeters of the bar. The picture shows that the losses to the bar are reduced but not entirely eliminated by the presence of the bar field.

Fig. 3.5. Pinhole X-Ray Photograph of the Plasma when ELMO Is Operated as a Folded Cusp. There is a nonenergized stuffing bar on the axis. The gas pressure is 2.0×10^{-5} torr, and the plasma is supplied with 3 kW of microwave power.

On the original photographs of Figs. 3.5 and 3.6, additional rings may be seen concentric with the axis and displaced on either side of the midplane. These rings are in the approximate position of mirror-like regions which are capable of containing a small volume of energetic plasma. It is not understood, however, how this plasma containment region is filled, since it does not intercept a heating surface.

Figure 3.7 is a pinhole x-ray photograph of the plasma with the cusp fields increased, but with the stuffing-bar field the same as in the previous photograph. Again, losses out the line cusp are seen, but, in addition, severe losses to the stuffing bar are evident. The losses to the bar may be of a nonadiabatic nature, since the field gradient is very steep near the bar. Some of the asymmetry seen in the picture may be due to the

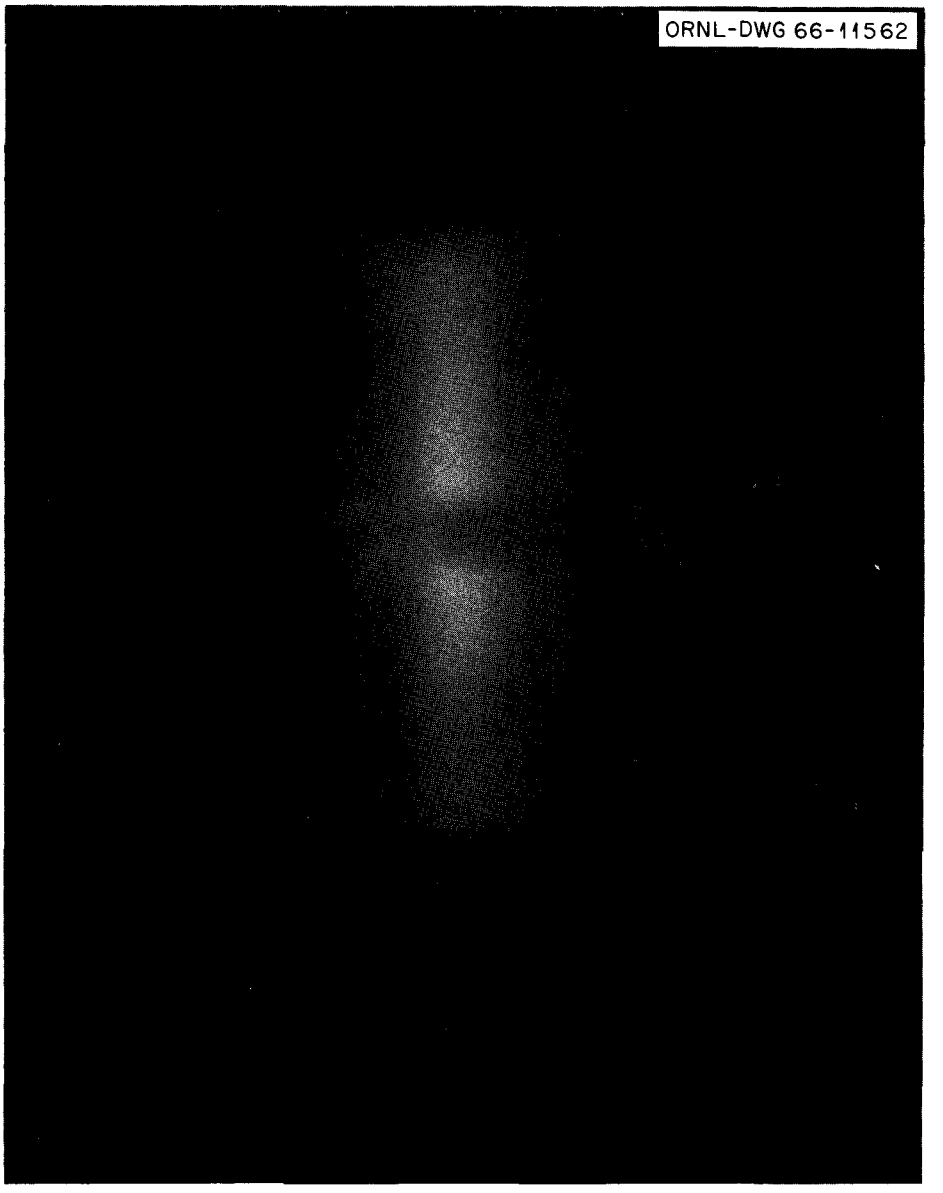

Fig. 3.6. Pinhole X-Ray Photograph of the Plasma when ELMO Is Operated as a Folded Cusp with the Stuffing Bar Energized. In this case the external field coil currents are approximately the same as in Fig. 3.5. The D_2 gas pressure is 2.2×10^{-5} torr, and the plasma is supplied with 2.7 kW of microwave power.

bar axis not being coincident with the magnetic axis of the cusp field. Under the conditions used for this photograph, there are no instabilities present.

Another observation is that the instability observed in the cusp configuration is not affected by the stuffing-bar field. If the instability is associated with particles near the ring cusp loss regions, this is understandable, since the bar field exerts negligible influence in this region. As in the previous case, higher gas pressure still stabilizes the plasma with the stuffing-bar field on.

The facility is presently shut down due to a mirror coil failure.

Fig. 3.7. Pinhole X-Ray Photograph of the Plasma when ELMO Is Operated as a Folded Cusp with the Stuffing Bar Energized. In this case the flat field current is higher than in Fig. 3.6, so that the plasma radius is reduced. The plasma is supplied by 2.6 kW of microwave power at a gas pressure of 2.0×10^{-5} torr.

4. Injection and Accumulation: Neutral Injection into Minimum $|B|$ (DCX-3 Magnet Design)

D. L. Coffey C. E. Parker
J. L. Dunlap J. F. Potts[1]
J. N. Luton Mozelle Rankin
H. L. Watts

4.1 INTRODUCTION

The DCX-3 program is an outgrowth of the long theoretical and experimental experience of ORNL in stability properties of plasma accumulated by energetic particle injection into open-ended magnetic traps. The basic direction of the program was provided by T. K. Fowler's theoretical identification of free energy sources, and the corresponding estimates of the measures necessary to reduce the associated levels of instability to tolerable limits by scaling of plasma dimensions and tailoring of velocity-space distributions.[2] The prime objective of this program is conceived to be the experimental testing of the scaling laws associated with instabilities driven by diamagnetic current.

Since Lorentz-force trapping in a low-pressure environment is to be employed, this objective dictates the use of energetic neutral injection. A confining field of the magnetic-well type was indicated for stability against low-frequency modes. For the first experiments of this program, a flexible field configuration is desired, and a magnetic well of the mirror-multipole configuration was chosen. Consideration of the negative-mass instability dictated quadrupole windings, since reversal of field gradient at small radius is more difficult to achieve with higher-ordered multipole windings.

Developments in beam, vacuum, and diagnostic technology that are specifically oriented toward the DCX-3 experiments are described elsewhere (Sects. 1 and 7). Here, we will review the status of the magnetic-bottle design.

Before giving the details of the two designs that are being considered, we first interject some comments of a more general nature, which in part explain the choice of these designs. The desire for a magnetic bottle of modest physical scale requires operation with extremely high coil-current density. In terms of conventional, hollow, water-cooled copper conductors, the design would then necessarily involve small conductor sizes and short cooling path lengths, and one encounters very difficult design and construction problems in maintaining current connections in series but water connections in parallel. Contemporary facilities, ALICE and PHOENIX, operate with liquid-nitrogen-cooled copper coils. In these, field operation is pulsed, and the pulse length (a few seconds) is restricted by the allowable temperature rise of the copper. Steady-state operation of the DCX-3 field is desired; hence the designs being considered, one using coils of copper ribbon and one using superconducting coils, are even less conventional.

In Sects. 4.2 and 4.3 we describe the design employing ribbon coils and that employing superconducting coils respectively.

[1]Now at Parma Technical Center, Electronics Division, Union Carbide Corporation.

[2]T. K. Fowler, *Phys. Fluids* **8**, 459 (1964).

4.2 RIBBON COIL SYSTEM

4.2.1 General Comments on Application of Ribbon Coils

Our interest in this approach was aroused by J. N. Luton's fabrication techniques[3] and has been sustained by his successful tests of several ribbon coils.[3–5]

Luton's original idea was to start with a copper ribbon the width of the desired coil and long enough to achieve the required winding depth. Closely spaced grooves approximately 10 to 12 mils deep were then rolled transverse to the ribbon length on one surface. The coil is formed by laying a ribbon of insulation over the copper and winding the two around a shaping mandrel. The finished coil is supported against axial forces by insulated "wagon wheels" which bear against the two coil faces perpendicular to the coil axis[4] and is cooled by high-velocity water flowing between plenum chambers at these same two faces. There are a multitude of cooling paths, each only as long as the ribbon is wide.

Such coils with transverse grooves are readily adaptable for use as mirror coils. Their only basic fault seems to be the requirement of plenum chambers between the windings and the median plane. Under some circumstances these chambers might protrude into the plasma confinement volume.

The application of ribbon coils in a quadrupole geometry is more difficult, primarily for two reasons. The first is a matter of the natural geometry of ribbon coils: it is difficult to conceive of winding such coils so that the individual coils of the quadrupole set are deformed from the natural planar geometry to conform to a cylindrical surface. The latter would be preferable, since Ioffe "bars" would then be nearer the mirror coil axis, and for a given number of ampere turns the quadrupole field at points close to this axis would be stronger.

The second problem is that the use of ribbon coils with transverse cooling grooves for the quadrupole set would require a plenum chamber between the copper windings and the mirror coil axis. Thus the conductors would be even further from this axis and the penetration of the quadrupole field further reduced. The solution to this problem is to roll cooling grooves of considerably larger cross section parallel to the length of the ribbon and to communicate to these grooves through the sides perpendicular to the plane of the ribbon or in the planes of the ribbons but from outside (rather than from the plasma side) of the quadrupole set. Either approach involves some difficult steps in coil fabrication, as detailed in Sect. 9.1. The latter approach was chosen for the DCX-3 design.

4.2.2 Coil and Electrical Parameters

The coil designs utilize copper ribbons of 0.028×4 in. cross section for the mirror coils and of 0.036×4 in. and 0.036×3 in. cross sections for the Ioffe coils. The ribbons of the Ioffe coils have 0.125-in.-wide $\times$ 0.016-in.-deep longitudinal grooves and, transverse to these grooves at four points in each turn, 2-in.-wide $\times$ 0.016-in.-deep grooves for connection of these coolant paths to the water supply and return chambers. The insulation between turns is 0.005 in. thick.

The coil system is shown in Fig. 4.1 (median plane section and longitudinal section). The coil dimensions are detailed in Fig. 9.1. The electrical parameters are summarized in Table 4.1, and the proposed generator connections are shown in Fig. 4.2.

At full power the mirror coils establish a 2:1 magnetic mirror with a central field value of 20 kG. In the median plane the mirror field is closely represented by $B = B_0(1 - \alpha r^2)$ for small radius r, with $\alpha = 4.9 \times 10^{-3}$ cm^{-2}.

At full power each Ioffe coil generates 1.1×10^6 ampere turns and a compensation ratio[6] (with full mirror field) of 1.5, which is probably enough to ensure proper behavior of precessional drift surfaces.[7]

Depending upon liner and diagnostic installation, the plasma radius would be 8 to 10 cm. With full power in both coil sets the magnetic well would extend to about half this radius.

---

[3] *Thermonuclear Div. Semiann. Progr. Rept. Oct. 31, 1965*, ORNL-3908, pp. 125–28.

[4] *Thermonuclear Div. Semiann. Progr. Rept. Apr. 30, 1966*, ORNL-3989, pp. 110–13.

[5] Sect. 9.1, this report.

[6] Defined as the ratio of the quadrupole coil current to that required to just compensate for the radial gradient of the mirror field at small radius.

[7] W. Bernstein *et al.*, *Plasma Physics and Controlled Nuclear Fusion Research*, vol. II, pp. 23–44, IAEA, Vienna, 1966.

ORNL-DWG 66-12602

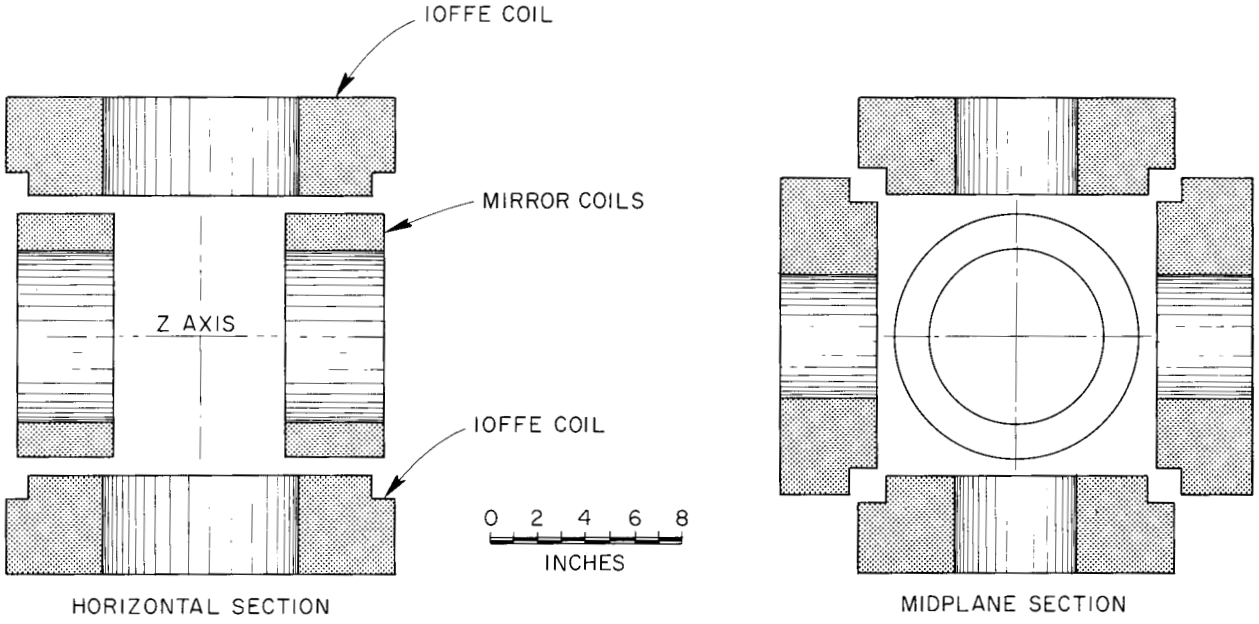

Fig. 4.1. Section Views of the Ribbon Coil System (Conductor Only).

ORNL-DWG 66-12603

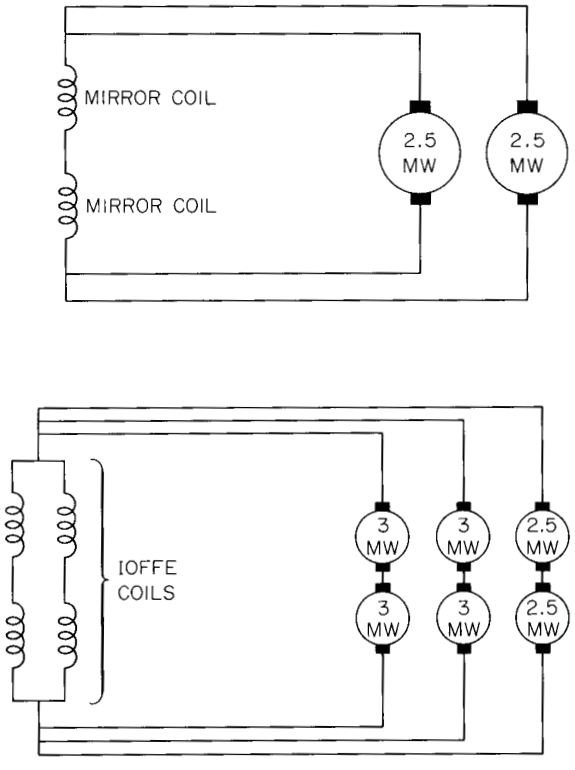

Fig. 4.2. Proposed Generator Connections for the Ribbon Coil System.

Table 4.1. Parameters of Ribbon Coil System

Item	Mirror Coil	Ioffe Coil
Number of turns	43	91
Length per average turn, cm	68	85
Current, maximum, A	17,000	12,350
Ampere turns per coil	7.3×10^5	1.12×10^6
Overall current density, A/in.^{2}	1.3×10^5	7.5×10^4 (in 4-in. section)
		1.0×10^5 (in 3-in. section)
Voltage per coil, V	167	354
Power per coil, MW	2.85	4.37

4.2.3 Mechanical Design

Figure 4.3 shows a pictorial view of the proposed mechanical structure. The construction is of stainless steel, and metal seals are used wherever possible. The design allows reasonably convenient coil replacement and also provides for complete removal of mirror coil cans for liner installation.

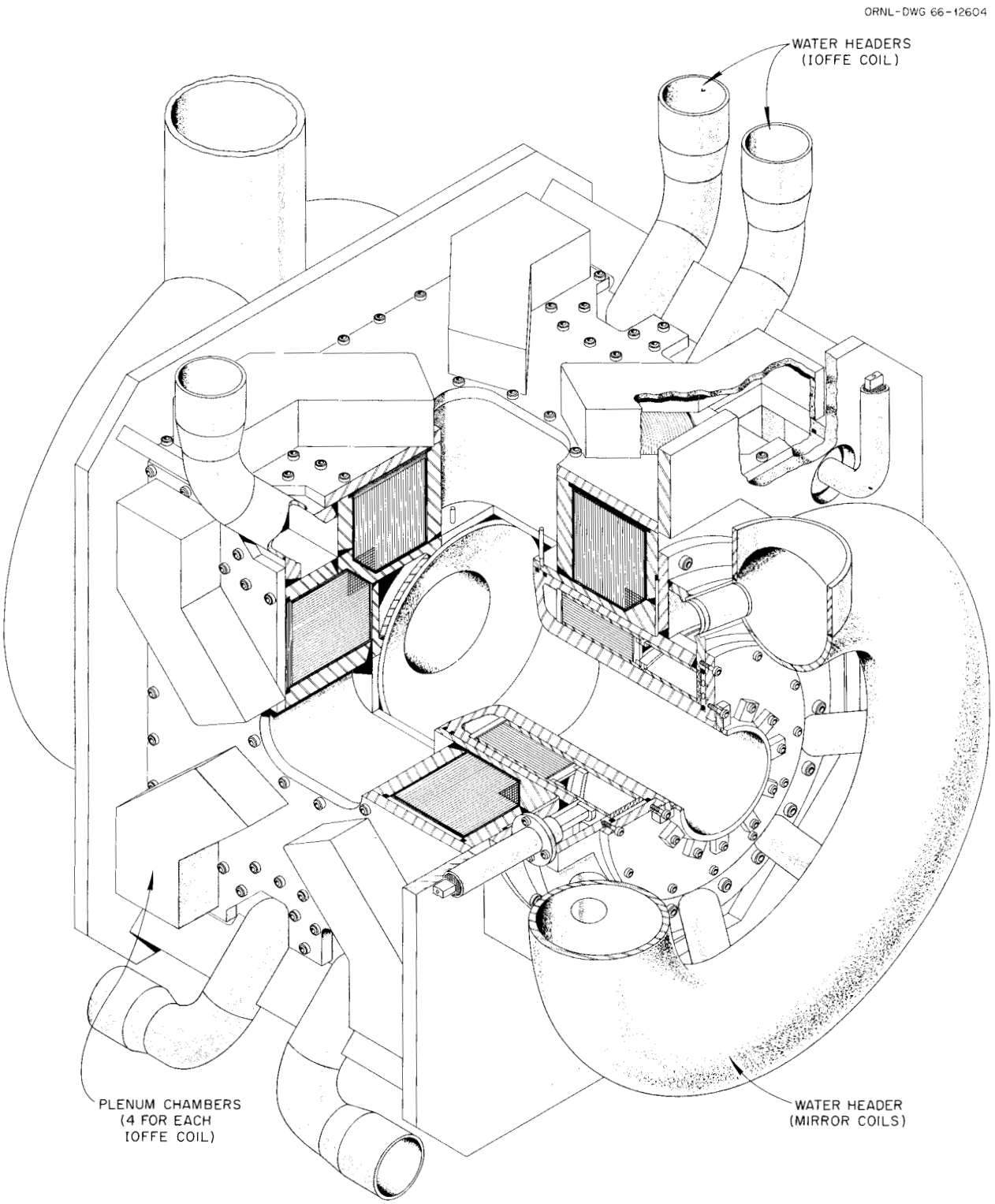

Fig. 4.3. Pictorial View of the Coils and Mechanical Assembly of the Ribbon Coil System.

The entire coil structure would be suspended within a vacuum tank from a large demountable lid. All utility and probe connections would be brought out through this lid. This arrangement permits easy installation of the magnet structure and also allows a degree of flexibility in the alignment of the magnet system with respect to a fixed horizontal beam line.

The magnetic forces generated by the coil system have been calculated, and the action of these forces upon the mechanical structure has been analyzed. The resultant force on individual coils is not extremely large, but the unbalances are such that local forces are higher than the resultants would indicate. For example, the direction of axial force on a mirror coil changes with azimuth, reversing four times, so that the axial force on a single 30° wedge of the coil winding reaches a peak of 16,300 lb outward, even though the net force on the whole winding is only 7500 lb inward. Fortunately, the mechanical calculations indicate that the structure pictured, with only slight modifications, would be able to withstand the magnetic forces even if the coils themselves are considered incapable of restraining any forces.

4.2.4 Cooling System

Under full power the coils will consume 23 MW, and approximately 3000 gpm of demineralized cooling water at 190 psi supply pressure is required. These figures can be easily provided by the generator installations and the cooling system already in use. An additional filter to remove particles down to 20-μ size would be installed.

The coolant flow rate through a single mirror coil is dictated by consideration of heat transfer as a function of flow velocity rather than by consideration of bulk heating; about 1000 gpm is required. This water is first passed through one coil and is then transferred from the inner plenum of that coil to the inner plenum of the second coil. So the same water cools both mirror coils. The transfer utilizes the chambers that are formed beneath adjacent sides of the Ioffe coils.

Bulk temperature rise of the cooling water fixes the flow in the Ioffe coils at about 500 gpm for each coil and further requires that the cooling paths trace out only one-quarter of a turn. As mentioned earlier, communication to the cooling paths is made by means of channels that are perpendicular to the cooling paths. Such channels are provided at four points in each turn, and the arrangement of supply and return headers required to parallel the hydraulic paths is shown in Fig. 4.4. Calculations, flow model tests, and prototype coil tests show that these cooling arrangements are adequate.

ORNL-DWG 66-12605

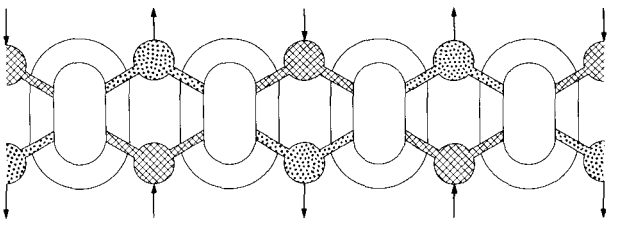

Fig. 4.4. Water Flow Diagram Showing Cooling Arrangement for the Ioffe Coils. Here the four coils are drawn as though they were in a single plane.

4.3 SUPERCONDUCTING COIL SYSTEM

In comparison with a system employing ribbon coils, the use of superconducting coils would in principle afford a number of advantages. Possible conflicts with the operation of other facilities because of generator scheduling would be avoided; the coil system would provide a large cryopumping surface which should result in lower base operating pressures; since power consumption is no longer a limitation, a larger central volume might be available; and the prospects for long-term successful operation of the coils might be enhanced. For these reasons the design of a superconducting coil system has been pursued in parallel with the ribbon coil design.

To date, most of the effort along this line has been devoted to computations and analyses of magnetic-field strengths both within the working volume and within the coils themselves. The object of this work has been to provide a magnetic field within the working volume which is suitable for the proposed experiments, while at the same time ensuring that the field strengths within the coils are low enough to permit use of stabilized conductors at the required current densities. The coil system that has evolved from these studies is shown in Fig. 4.5. The design figures for overall

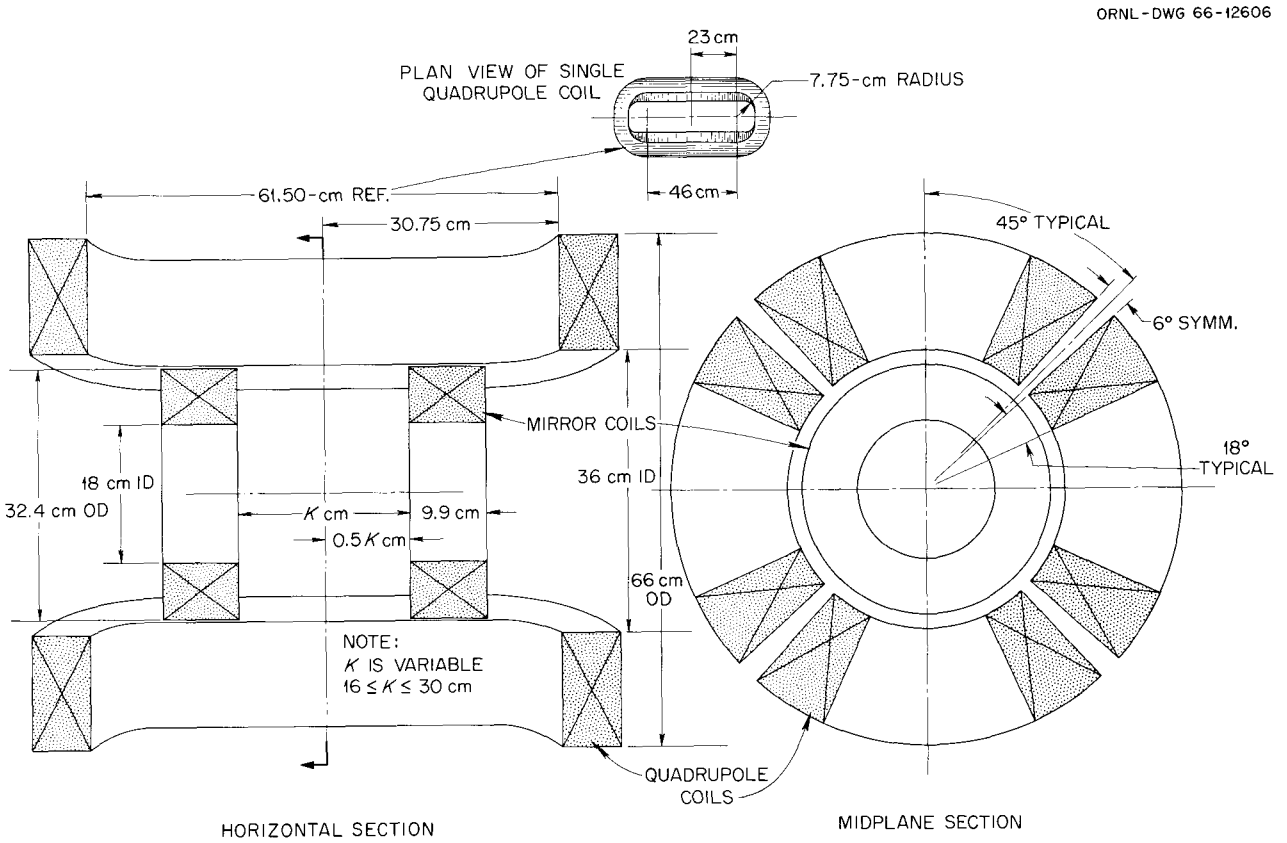

Fig. 4.5. Section Views of the Superconducting System (Conductor Only).

current densities are 7.3×10^4 A/in.^{2} for the mirror coils and 6.8×10^4 A/in.^{2} for the Ioffe coils. These values, with the mirror coils mounted for a 2:1 mirror ratio, provide a central field of 20 kG, a mirror field radial gradient parameter [α in $B = B_0(1 - \alpha r^2)$] of 0.0036 cm^{-2}, and a compensation ratio of 1.75. Maximum field intensities are 68 kG in the mirror coil windings and 73 kG in the Ioffe coil windings.

We anticipate the use of copper-stabilized niobium-titanium cable for the superconducting windings. Cable with suitable magnetic properties appears to be commercially available.

The electromagnetic forces generated by the windings have been calculated. The action of these forces upon the conductor is being analyzed. Some coil tests designed to clarify this area as well as to check conductor performance are planned for the near future.

In operation the superconducting system would be suspended within a vacuum tank whose interior walls are maintained at low temperature by liquid nitrogen. Two conceptual mechanical designs for the superconducting system have been completed. In one, each of the six coils is mounted within a separate vacuum-tight case which restrains the mechanical forces and also serves as the helium containment vessel for that coil. The complete assembly is formed by bolting together these six cans along with other structural members dictated by force considerations. The mirror coil locations can be changed (not during operation) to obtain mirror ratios between 1.5 and 3.0. Since the coil cans themselves act as the helium containment vessels, this design has the advantage of optimum experimental access but the disadvantage of being an unconventional cryogenic system. The assembly is surrounded by a radiation shield, possibly boiloff cooled.

The second design is structurally similar but cryogenically more conventional. The Ioffe coil cans are porous, and the four are surrounded by a single helium containment vessel. The mirror coil cans still act as separate helium vessels. The

latter feature of the design is dictated by the requirement that the cross section of the central volume in the median plane extend unobstructed through one end of the system after some convenient partial disassembly. In this case the disassembly is that of removing a mirror coil and its can. The required access will be necessary for installation of a liner to surround the plasma region and possibly for other operations as well. This feature of the design also allows change of mirror coil locations to obtain different mirror ratios.

The conceptual mechanical designs are now being considered in detail. The various cryogenic problems are also receiving attention.

If the work in progress continues to indicate the feasibility of the superconducting system, this system will be constructed for the DCX-3 experiment.

4.4 ACKNOWLEDGMENTS

Numerous contributions to this work have been made by others at ORNL. In connection with the ribbon coil design, we particularly want to express our appreciation to G. J. Kidd, Jr., and H. W. Hoffman for consideration of the hydraulic problems; to R. C. Gwaltney and J. T. Huffaker for stress analyses; to D. E. Huffman, C. R. Rickard, and their associates for experimental machining; and to F. S. Patton and his associates for estimates of production schedules and costs.

Our work on the superconducting system has benefited considerably from discussions with R. W. Boom and C. N. Whetstone of Atomics International; C. Laverick of Argonne National Laboratory; and H. M. Long of the Linde Company, Union Carbide.

5. Plasma Physics

5.1 BEAM-PLASMA INTERACTION EXPERIMENTS

I. Alexeff W. D. Jones
W. Halchin R. V. Neidigh

5.1.1 Introduction

The experiments resulting in turbulent heating of deuterium ions by an electron beam have continued in the Burnout IV and Burnout V devices.[1] In this report period the Burnout V device was modified by increasing the liner diameter at the midplane and by rotating the magnetic axis within the vacuum chamber so as to use the available space more efficiently. The magnetic axis is now vertical instead of horizontal. We had reported charged-particle track registration on cellulose nitrate which was thought to be tritons, a reaction product from the plasma in the midplane liner region of Burnout V.[1] We have now shown experimentally that 1-MeV tritons are, indeed, above the track registration threshold, and therefore tritons from the D-D reaction are responsible for the tracks we measure. On Burnout IV we have used scintillation detection to observe the 3-MeV protons from the D-D reaction. A similar effort is in progress on Burnout V, but is requiring greater sophistication in x-ray shielding. We are, of course, endeavoring to identify the source of the reaction products with the plasma. Wall reactions are quite common and present an annoying background, usually masking the signal of interest. Nuclear track plate detection of the D-D protons has apparently given the first real evidence that some thermonuclear reactions are taking place in the plasma of this steady-state machine.

[1] *Thermonuclear Div. Semiann. Progr. Rept. Apr. 30, 1966*, ORNL-3989, p. 43.

5.1.2 Modifications

Several improvements of the Burnout V apparatus have been made. The rotation of the magnetic axis to vertical permits more space outside the mirrors. Pumping speed in the region is thereby increased, and the impurity flux from the end electrodes is reduced. The size and shape of the end electrodes can now be optimized to reduce impurities and yet withstand the ion bombardment and reflect the electron beam. Several variations are being tried. New access doors in the face plate permit electrode changes without removal of the apparatus from the vacuum chamber. The diameter of the liner was increased from 8 in. to 14 in. over 4 in. of axial length at the midplane to reduce sputtering of its surface and thus to reduce impurities in the plasma.

5.1.3 Charged-Particle Track Registration on Cellulose Nitrate

The use of polymers for the detection of charged particles, although a fairly recently developed technique, has been explored extensively for heavy nuclei.[2,3] On the other hand, there is very little information available on track registration in polymers by light nuclei, and we have not found references on proton registration. In our application we needed to show that the tracks made on cellulose nitrate and described in the previous report were indeed tritons as assumed. We did this by experimentally investigating the track registration threshold for protons. C. F. Barnett made the apparatus available, and his co-workers did the actual bombardment for us.

[2] R. L. Fleischer *et al.*, *Phys. Rev.* **133**, A1443 (1964).

[3] R. L. Fleischer, P. B. Price, and R. M. Walker, *Science* **149**, 383 (1965).

In our investigation we first calculated the energy loss rate as a function of energy per nucleon by the method of ref. 2. The curve is shown in Fig. 5.1. Note that it peaks at about 100 kV/nucleon. We then measured track registration with protons from 50 to 550 keV and also with deuterons and with alpha particles. The proton results are shown in the photomicrographs of Fig. 5.2*a*. Note that the tracks are most easily seen at 550 keV. It should be remembered that for particle energy just above threshold the damage will be etched away and a track recorded, but the length of the track, and therefore the ease with which it may be observed, increases with energy. It becomes increasingly difficult to detect the direction of the particle as the energy is lowered. The general direction of the impinging proton could barely be determined at 110 keV. The lowest energy at which a proton would produce any marks in the cellulose nitrate appeared to be 55 keV.

A one-to-one incident-particle–to–track registration ratio seemingly was observed down to 110 keV. However, occasionally some variation in the sensitivity of the cellulose nitrate[4] existed; on some plates we found a few small areas void of tracks. This was most common near the registration threshold.

Comparing experiment and theory[2] on the low-energy-per-nucleon side of the energy loss rate curve (see Fig. 5.1), the threshold for track registration in cellulose nitrate appears to us to be about 0.35 MeV mg^{-1} cm^2. Unfortunately, we were not equipped to go higher in energy than 550 keV for protons, and thus could not confirm this value on the high-energy side of the curve. If the energy is so great that dE/dx is below the threshold, the particle will still do etchable damage at the end of its path, but the damage will be below the surface of the cellulose nitrate and may not be reached by the etchant. Due to our upper energy limitation, we did not observe this.

As expected, deuterons and alpha particles having a calculated dE/dx above 0.35 MeV mg^{-1} cm^2 were also found to register tracks in the cellulose nitrate (see Fig. 5.2c). Consistent

[4]The cellulose nitrate was purchased from Almac Plastic, New York, specified Dupont Pyralin, 0.090 in. thick.

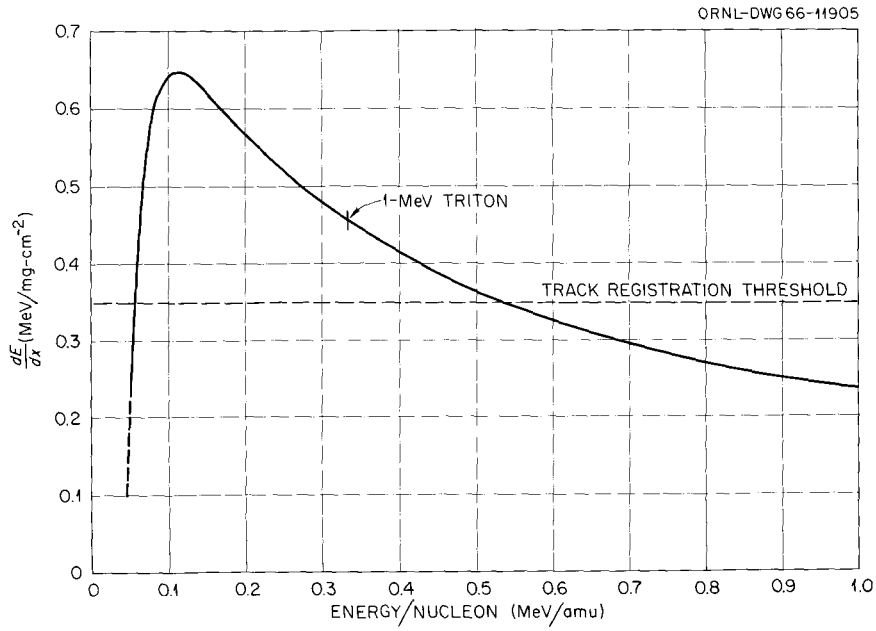

Fig. 5.1. Calculated Energy Loss Rate, dE/dx, for Protons in Cellulose Nitrate. The graph is applicable to deuterons and tritons if the energy scale is multiplied by factors of 2 and 3 respectively. To use for alpha particles, both scales must be modified. The vertical scale must be multiplied by the squared value of the "effective" charge [H. H. Heckman *et al.*, *Phys. Rev.* 117, 544 (1960)], and the energy scale must be multiplied by four.

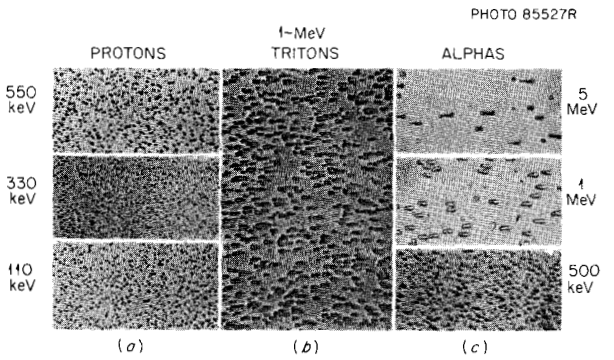

Fig. 5.2. Track Registration in Cellulose Nitrate. The many tracks make the single event recognizable. (*a*) 550-, 330-, 110-keV protons. (*b*) 1-MeV tritons. (*c*) 5-MeV, 1-MeV, 500-keV alphas. The longest alpha tracks are 5 μ in length. The cellulose nitrate was etched with 5 N NaOH for 2 hr at room temperature.

with the calculations, we apparently have seen the tracks of 1-MeV tritons from D-D fusion reactions in Burnout V (see Fig. 5.2*b*). We should not have expected to see tracks of the other two possible candidates from D-D reactions, namely, 3-MeV protons and 0.8-MeV $^3He^{2+}$, for the following reasons: for the energetic protons, as noted above, the etchable damage would have been produced too far beneath the surface of the cellulose nitrate to have been reached by the etchant. In the case of the $^3He^{2+}$, a 30-kG magnetic field should have made it impossible, geometrically, for these reaction products to have reached the cellulose nitrate detector.

In summary, we have found experimentally that the light nuclei, including protons, can produce etchable damage in cellulose nitrate. Comparison of our experimental results with theory indicates that cellulose nitrate has a threshold for track registration of about 0.35 MeV mg^{-1} cm^2. Since this threshold falls in the range of energy loss rate for at least two of the reaction products of D-D fusion reactions, this provides a new diagnostic tool for analysis of the many thermonuclear experiments now in progress.

5.1.4 Scintillation Detection of D-D Protons

Protons from the D-D reaction can be detected by scintillation methods if the x-ray background is not too great. We have observed 3-MeV protons from the midplane region of Burnout IV. Their energy distribution is shown in Fig. 5.3. We could not differentiate between plasma and wall reactions in this experiment, but the yield was about that of a plasma at temperature $T_{ion} = 0.75$ keV and density $n_{ion} = 3 \times 10^{12}$ cm^{-3}. The inset shows schematically how the measurement was made. The Lucite light pipe was necessary to keep the photomultiplier out of the strong magnetic field. The analyzer was calibrated with 5.5-MeV alpha particles from an ^{241}Am source. Apparently, x rays from the plasma and walls contribute to the low-energy distribution seen in the display. In a similar experiment in Burnout V, where the electrons are considerably hotter, the x-ray distribution completely obscured the proton peak.

5.1.5 Nuclear Emulsion Detection of D-D Protons

The use of nuclear track plates to detect protons is also made difficult by the x-ray background which fogs the emulsion. But the record is permanent, and the universal acceptance of the technique made the experiment enticing. Our setup is schematically shown in Fig. 5.4. Notice that the arrangement of the nuclear track plates is such that both plates "see" the same area of the liner, but the upper plate in the drawing "sees" the plasma in addition. Even though the particle path length to the lower plate is considerably shorter and the plate therefore sees a greater solid angle, the upper plate had ten times as many tracks per unit area as the lower plate.

The reaction rate within the plasma may be expressed in terms of density, n; volume, V; and σv, the velocity and cross-section product averaged over a Maxwellian distribution. We write $\frac{1}{4}\, n^2\, \sigma v\, V$ = number/sec of any one reaction product. If in Burnout V, $n = 10^{13}$ cm^{-3}, $V = 100$ cm^3, and $(\sigma v)_{D\text{-}D} = 2 \times 10^{-22}$ cm^3/sec at $kT - 1$ keV, then there should be 5×10^5 protons/sec. We estimate our geometrical factor to be about 10^4. We should, therefore, record about 50 tracks/sec. The yield from the first experiment using nuclear track plates was one track every 36 sec (down by more than 10^3). A later experiment produced a yield five times greater. The proton yield from Burnout IV, using scintillation detection, was about one proton every 10 sec. Only the triton yield in Burnout V, recorded on the cellulose nitrate detector, has been as great as expected

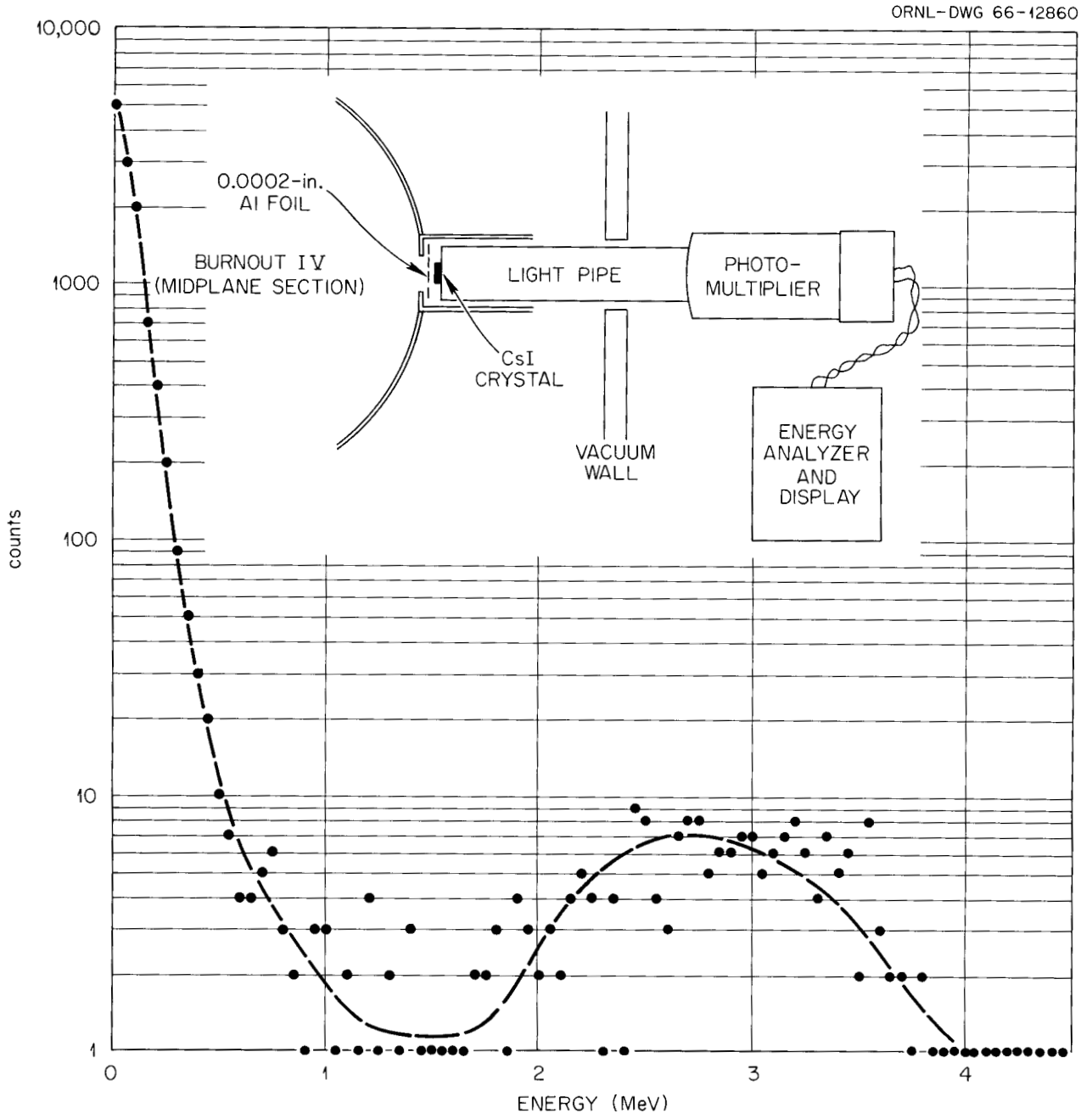

Fig. 5.3. Proton Energy Distribution in Burnout IV. Calibration was made with 5.5-MeV alpha particles from ^{241}Am. The inset schematically describes the scintillator and its location in Burnout IV.

from the temperature and density indicated by spectroscopic and probe measurements.[1] It should be noted that σv is a very steep function of temperature in this range and that the yield also varies as n^2. We think that impurities have caused wide variations in temperature from run to run, and only with the greatest of care do we reach the higher plasma temperature and density.

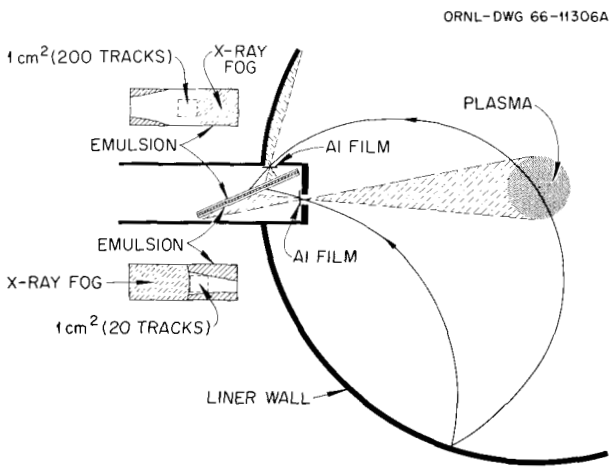

Fig. 5.4. Nuclear Track Plate Location in Burnout V for Proton Detection. Both upper and lower plates "see" the same portion of liner wall. The upper plate "sees" the plasma as well. X-ray fogging is caused by fluorescence of the cylindrical wall, the end walls, and the plasma.

5.2 ION HEATING USING A MODULATED ELECTRON BEAM

G. M. Haas[5] A. C. England
W. B. Ard R. L. Livesey
M. C. Becker[6] O. D. Matlock
R. A. Dandl[6] M. W. McGuffin
H. O. Eason

5.2.1 Introduction

Previous experiments[7] with the modulated electron beam had produced strong oscillations associated with the plasma ions. The results in this semiannual report establish that ion heating does occur with the presence of modulation on the beam. The salient features of this heating are presented.

5.2.2 Description of Apparatus

The apparatus used in the study of the beam-plasma interaction of a modulated electron beam was described in the last semiannual progress report.[7] There have been several changes and additions made since that time. A measurement of the magnetic field showed the maximum $B_z(0, 0)$ to be 550 G. A 100-W transmitter with a frequency range of 350 to 900 kHz was constructed to allow modulation of the beam, both at the proton and molecular ion cyclotron frequencies. In order to ascertain if energy was being transferred to the plasma ions, a gas stripping cell and analyzing system was constructed to look at the charge-exchange neutrals from the plasma. The analyzing system consists of a bending magnet for momentum analysis, a retarding potential energy analyzer, a Bendix electron multiplier to detect the ions, and the necessary differential pumping. Figures 5.5 and 5.6 show the apparatus in its present form. This system of detecting ions has several limitations. First, the ionizing efficiency as a function of the incident neutral particle energy is not known at low energies (i.e., up to several hundred electron volts); therefore it is not possible to obtain the energy distribution of the ions in the plasma. Second, since the acceptance angle is small, only those ions with very little longitudinal velocity can enter the stripping cell. Thus, without scanning the neutral detector in angle, only

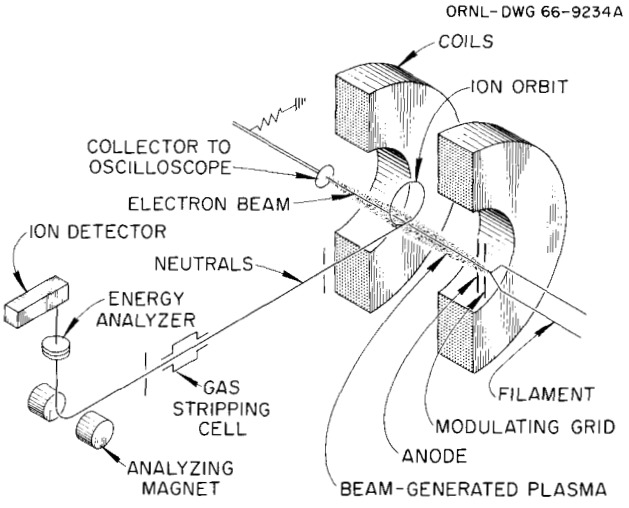

Fig. 5.5. Schematic Diagram of the Modulated Electron Beam Experiment.

[5]Present address: Texas A and M University, College Station.

[6]Instrumentation and Controls Division.

[7]*Themonuclear Div. Semiann. Progr. Rept. Apr. 30, 1966*, ORNL-3989, p. 51.

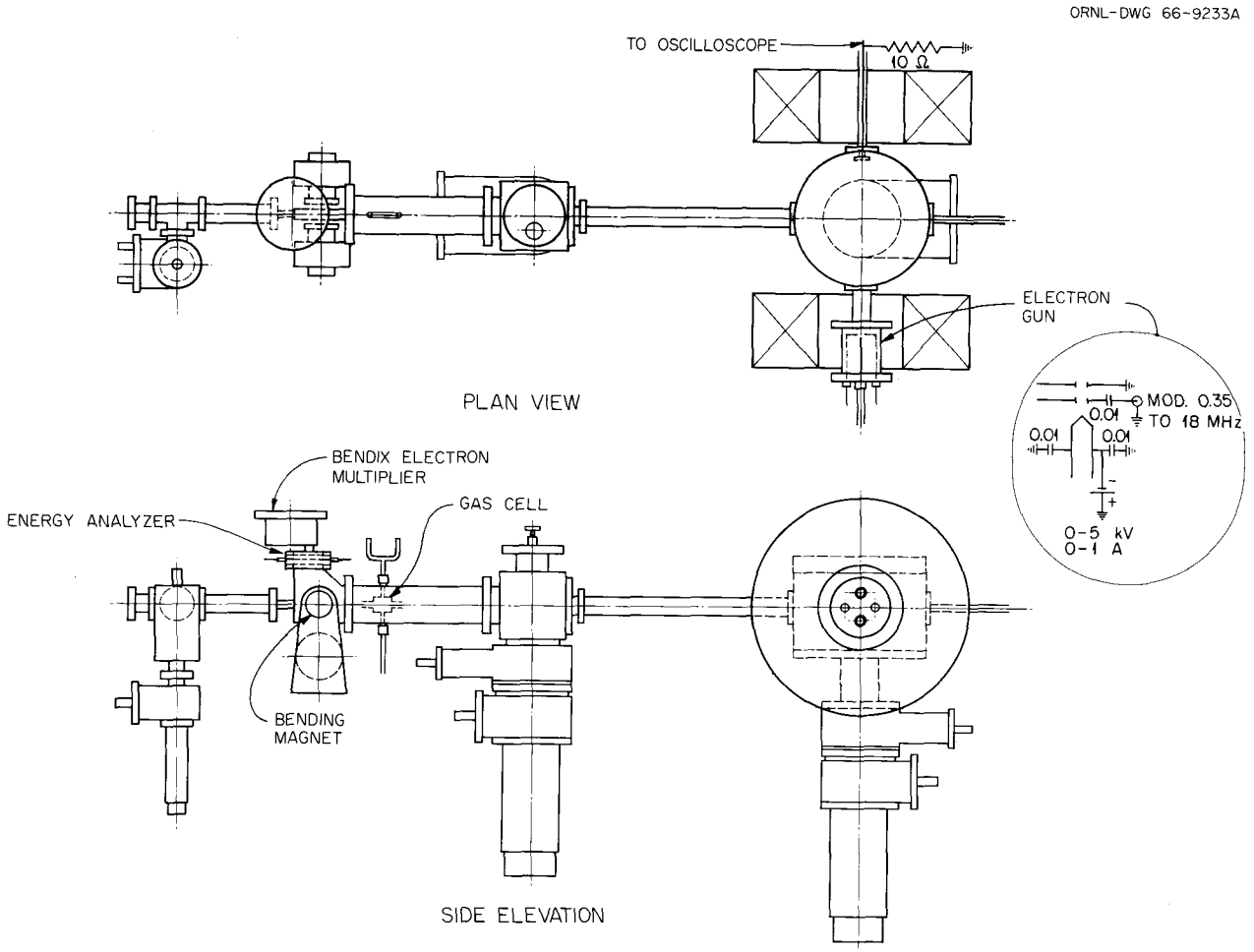

Fig. 5.6. Scale Drawing of the Modulated Electron Beam Experiment.

the presence of energetic ions is measured, with no detailed information as to the spatial distribution.

Figure 5.7 (upper photograph) shows a typical rf envelope modulating the gun and the corresponding beam current; the lower photograph shows the current with the modulation off. The grid is operated at zero bias, and the rf voltage turns the beam off for a fraction of a cycle which depends upon the modulation amplitude and applied accelerating voltage.

5.2.3 Experimental Results

Energetic Neutrals. – With the unmodulated beam, no signal was observed on the neutral-particle detector for any of our conditions of beam current, beam voltage, pressure, or magnetic field. However, when modulation was applied to the beam, energetic neutrals were detected. The output from the electron multiplier as a function of the analyzing magnetic current is shown in Fig. 5.8. Using the retarding potential energy analyzer and knowing the momentum, the ions were found to be protons, and the energy axis is labeled for proton energy. The peak energy occurs at 200 eV. Due to the variation with energy of the efficiency of the stripping cell superimposed on the tail of the ion distribution, changes in the energy distribution in the plasma will only affect the flux out of the stripping cell and will not appreciably affect the ion energy distribution out of the cell. The cutoff at approximately 30 eV is due to the minimum

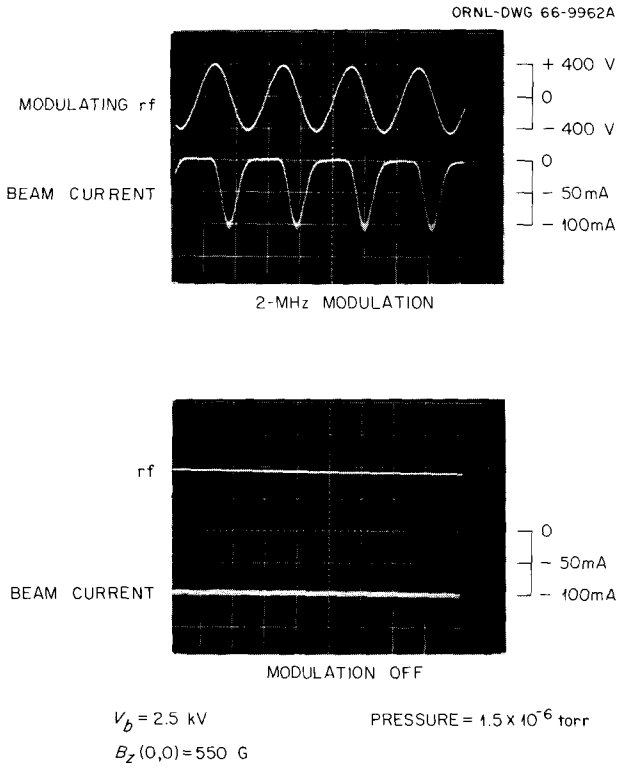

Fig. 5.7. Photographs of the RF Modulation and the Corresponding Electron Beam Current.

neutral energy required to produce ionization by collision in the cell. The peak current for a modulation frequency of 850 kHz is 1×10^{-10} A, with the pressure in the stripping cell adjusted for the maximum ion current. The gain of the electron multiplier was between 10^6 and 10^7, giving a counting rate of between 600 and 60 particles/sec. The resolution for the analyzer system was 70 eV full width at half maximum.

Two modes of heating were observed, as shown in Fig. 5.9. For the low-pressure case (less than 2.6×10^{-4} torr), two peaks are observed: one H^+ and the other predominantly H_2^+. Ion heating in this mode was found to occur only for a modulating frequency near the proton cyclotron frequency, and the flux of ions in this mode was small. For the high-pressure mode (greater than 2.6×10^{-4} torr), only a single peak was observed, and the flux in this mode was larger than that in the low-pressure mode. It was also observed that the energy at the peak ion current out of the stripping cell was relatively independent of the modulation frequency. This is shown in Fig. 5.10, where the modulation frequency was 800 kHz for the lower curve and 7 MHz for the upper curve. The flux increased at the higher frequency. Lowering the peak beam current also reduced the flux of ions without shifting the energy peak.

Figure 5.11 shows the peak flux as a function of the modulation frequency for the high-pressure mode. Two peaks occurred: one at the proton cyclotron frequency of 850 kHz and the other at

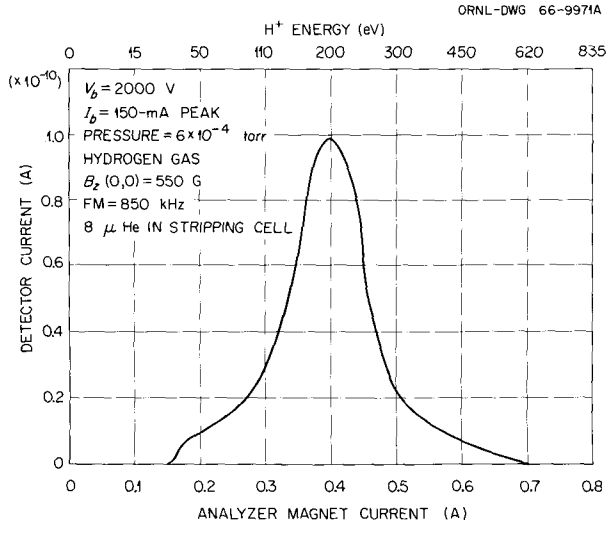

Fig. 5.8. Ion Current Out of the Gas Stripping Cell as a Function of the Analyzer Magnet Current.

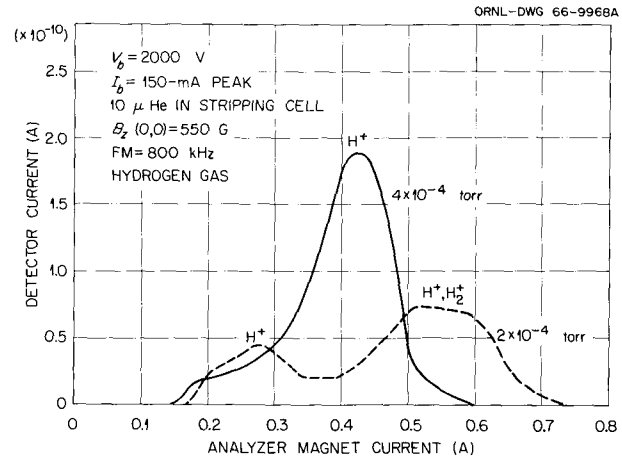

Fig. 5.9. Ion Current Out of the Gas Stripping Cell as a Function of the Analyzer Magnet Current for Two Different Pressures.

6 to 7 MHz. Measurements of the plasma density, as described in the last semiannual, with a microwave cavity operating in the TM010 mode gave an average density of 1.5×10^9 cm^{-3} for a pressure of 4×10^{-4} torr, with a 2-kV, 150-mA-peak beam. This density corresponds to an ion plasma frequency of 5.6 MHz for the H_2^+ ions. Reducing the beam current reduces the plasma density, and the frequency for an 80-mA-peak beam current is seen to shift down.

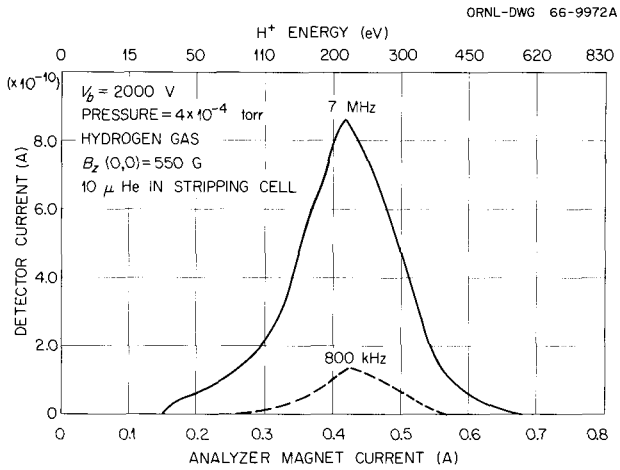

Fig. 5.10. Ion Current Out of the Gas Stripping Cell as a Function of the Analyzer Magnet Current for Two Different Beam Currents.

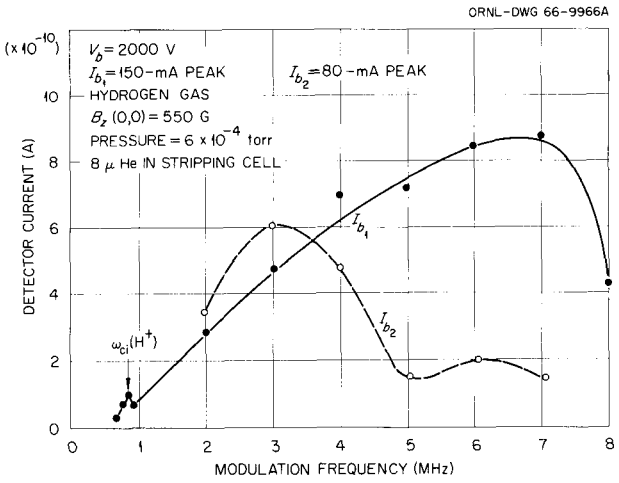

Fig. 5.11. Peak Ion Current Out of the Gas Stripping Cell as a Function of the Modulation Frequency.

Figure 5.12 shows the effect of decreasing the magnetic field for a fixed modulation frequency. Both the flux of energetic ions and the energy distribution are decreased as the magnetic field is lowered.

Figure 5.13 shows the peak ion current for a frequency of 8 MHz as a function of pressure. Below a pressure of 2.6×10^{-4} torr no energetic ions are observed. At this pressure a definite change in the plasma is observed. Above this critical pressure the plasma is observed to in-

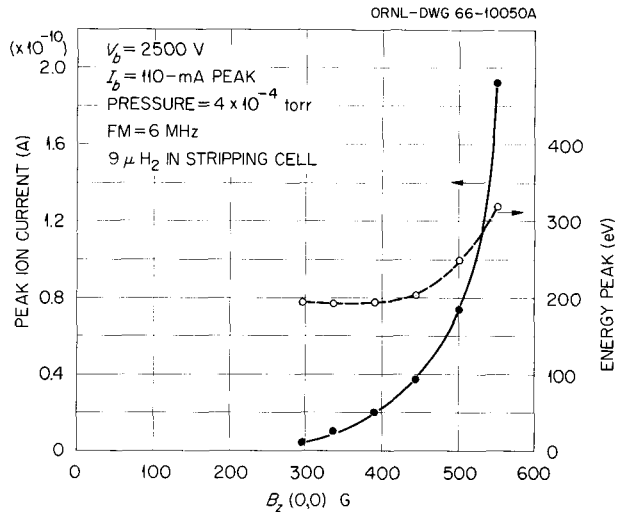

Fig. 5.12. Peak Ion Current Out of the Gas Stripping Cell as a Function of the Magnetic Field for a Fixed Modulation Frequency.

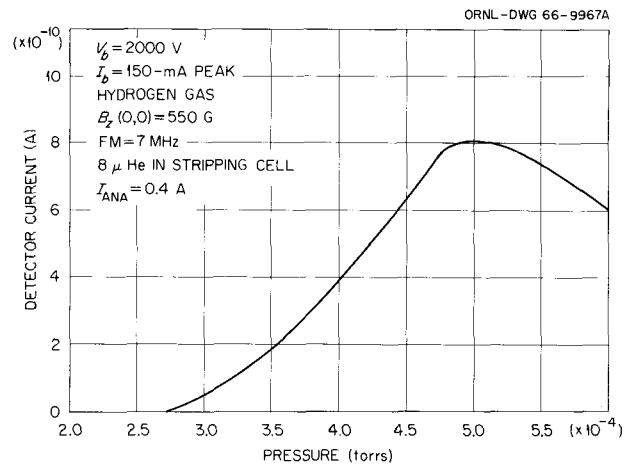

Fig. 5.13. Peak Ion Current Out of the Gas Stripping Cell as a Function of Pressure.

crease in diameter, with a secondary plasma forming around the beam and the visible light output increasing.

Oscillations. – Beyond the critical pressure and accompanying the presence of the energetic ions is a strong oscillation as shown in Fig. 5.14. The oscillations are picked up by an electric probe located 5 cm from the beam and observed on a Panoramic spectrum analyzer. The frequency of this oscillation is found to be relatively insensitive (few percent change) to changes in pressure, beam current, and modulation frequency. Figure 5.15 shows the change in frequency at two different beam currents. Lowering the beam current from 120 mA peak to 70 mA peak increases the frequency of the oscillation from 680 to 730 kHz. Measurements of the polarization of these fields show them to be predominantly azimuthal fields. Figure 5.16 shows the dependence of the frequency on the magnetic field. The signal is linear with B and falls between the H^+ and H_2^+ midplane cyclotron frequencies. Since the plasma is in a 3:1 mirror field, this shift in frequency might have been due to H_2^+ ions having a mirror turning point in the higher magnetic fields. To check this, the current collector was moved toward the midplane

ORNL-DWG 66-9963A

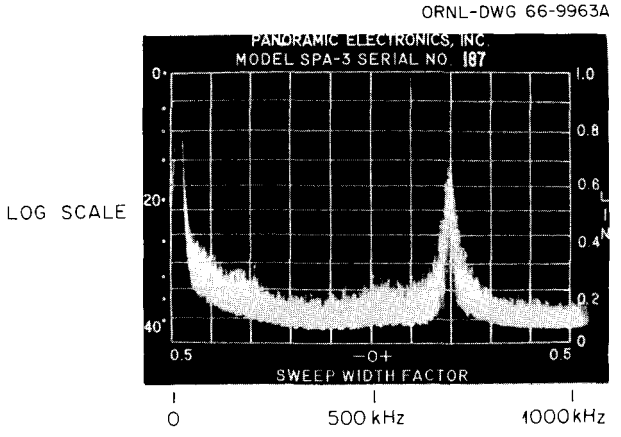

V_b = 2500 V
I_b = 130-mA PEAK
PRESSURE = 4×10^{-4} torr
HYDROGEN GAS
B_z (0,0) = 550 G
FM = 5 MHz
PROBE: 5cm FROM BEAM

Fig. 5.14. Low-Frequency Spectrum, Using an Electric Probe, with the Beam Modulated at 5 MHz.

and the effect on the ion flux observed. No effect was observed until the collector was 3 in. from the midplane. As a second check, a radial limiter was inserted 2 in. off the midplane, and could be moved until it touched the beam without producing any change in the energetic ion current. This indicates that none of the energetic ions have sufficient Z velocity to move into a field higher than 1.15 $B_z(0,0)$, yet the shift in frequency would require a field of 1.67 $B_z(0,0)$. A radial limiter was inserted at the midplane, and the change in ion flux with limiter position observed is shown in Fig. 5.17. It was found that there was no effect on the ion flux with the limiter beyond ~1.5 in. from the beam. The change in the magnetic field to a radius of 1.5 in. is less than 2% and insufficient to shift the H^+ cyclotron frequency down enough to account for the observed shift. Another possibility was that the plasma was rotating and that the observed frequency is shifted due to the plasma rotation.

There is some evidence, however, against an electric-field-driven rotation. Observation of the oscillation shows very little shift in frequency as the beam current is reduced. For a factor of 2 decrease in beam current the frequency shifts up less than 10%. If there were an $E \times B$ driven rotation, one would expect the field, and thus the rotation frequency, to drop with a decrease in beam current, due to the reduction of the electric field from the beam. A stronger argument against rotation is the variation of ion current with the position of the radial limiter. A 200-V proton in a field of 550 G has a Larmor radius of 1.45 in. or a diameter of ~3 in. Only those particles which pass through or near the electron beam with very small Z velocity are seen by the ion detector. If the ions were rotating about the axis in a time less than the charge-exchange time (~70 μsec), then the radial limiter should intercept them at about 3 in. This was not the case, and this rotation period of the ion about the axis must be greater than 70 μsec.

Examination of these 700-kHz oscillations on a short time scale has shown two things. First, the rf came in bursts lasting from 50 to 100 μsec. Second, none of these bursts occurred until 150 μsec after the beam had been turned on. Figure 5.18 shows the amplitude of oscillations as observed on a Panoramic receiver tuned to 700 kHz. The upper and middle pictures show the amplitude of 700-kHz oscillations as a function of time.

ORNL-DWG 66-10717A

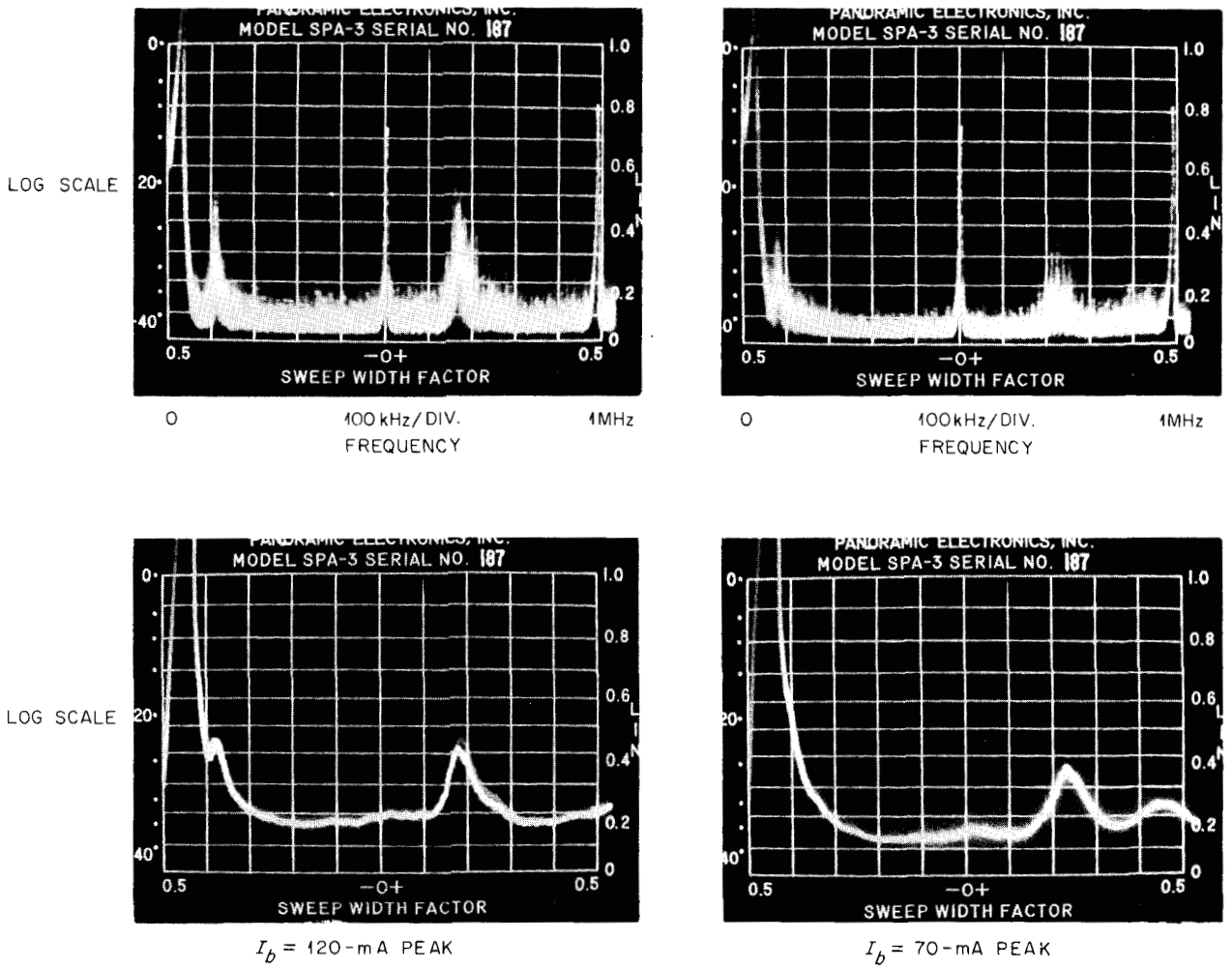

V_b = 2500 V
FM = 7 MHz
PRESSURE = 3.0 X 10^{-4} torr
HYDROGEN GAS
B_z (0,0) = 550 G

Fig. 5.15. Low-Frequency Spectrum, Using an Electric Probe, for Two Different Values of Beam Current. Upper spectra are without video filter, lower spectra with video filter.

The lower picture shows the response of the Panoramic. This was obtained by observing the 7-Mc modulation of the beam at turn-on. Since the beam rf is present within 2 or 3 μsec, the delay observed is that of the Panoramic. The Panoramic response is rather slow (~100 μsec), and thus a further check was performed in order to verify these results. A band-pass filter tuned to 700 kHz was constructed, and with the circuit shown in Fig. 5.19 the amplitude was observed. This system allowed matching the band-pass filter and eliminated the 7-MHz pickup. The time response of the system was approximately 10 μsec. Observations with the circuit confirmed that the rf did indeed come in bursts, and that no bursts were observed until the beam had been on at least 150 μsec. This indicates that this rf is due to an instability associated with the energetic ions.

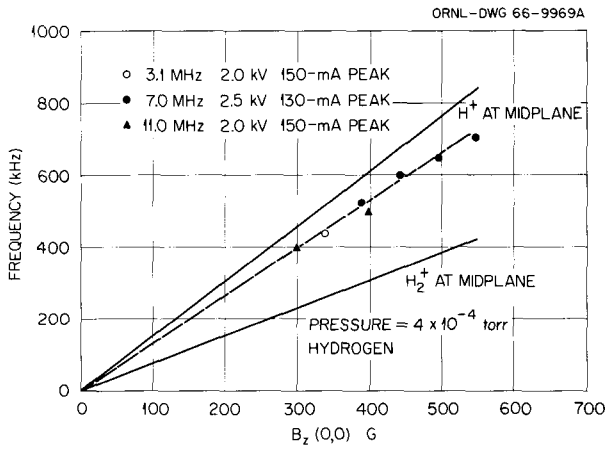

Fig. 5.16. Variation of the Low-Frequency Oscillations as a Function of Midplane Magnetic Field.

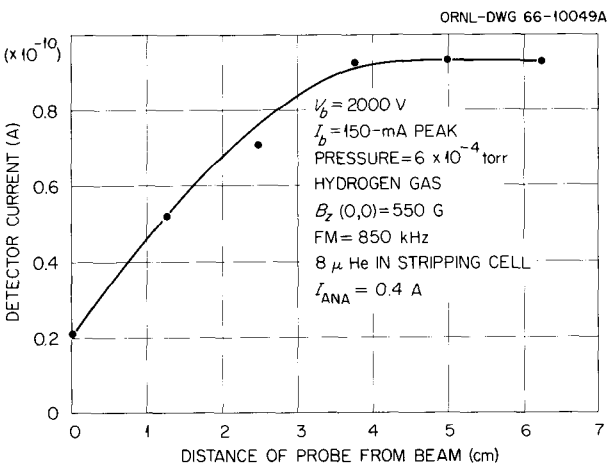

Fig. 5.17. Peak Ion Current Out of the Gas Stripping Cell as a Function of the Midplane Radial Limiter Position.

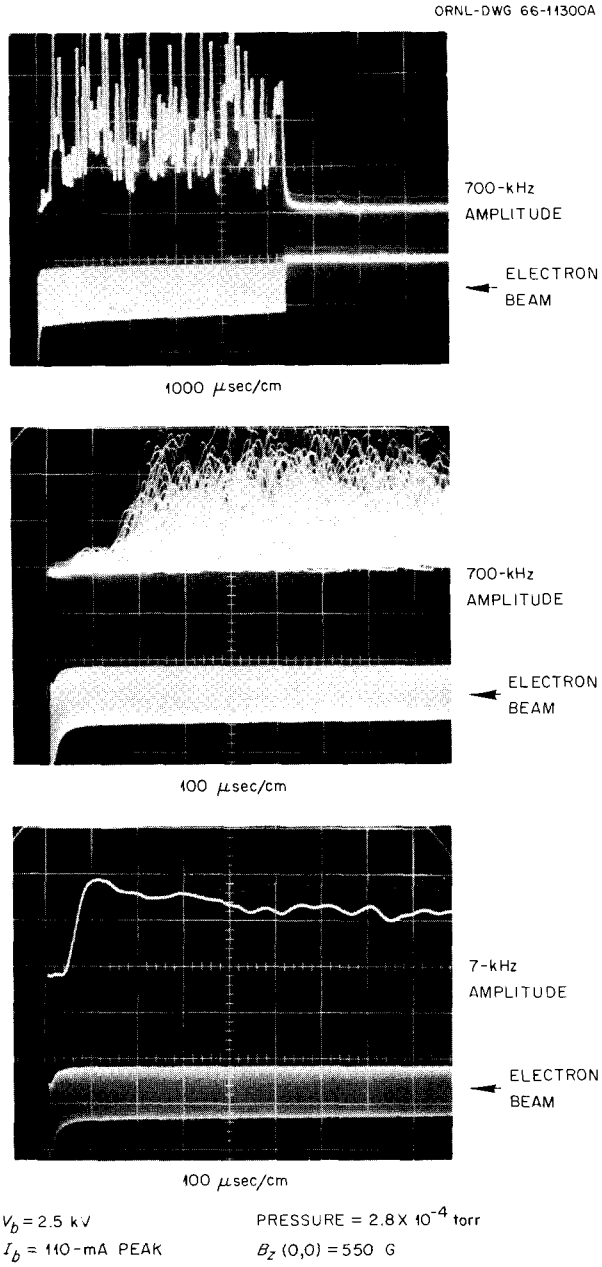

Fig. 5.18. Amplitude of the 700-kHz Oscillations as a Function of Time.

A possible explanation of this 700-kHz oscillation is that given by Nielsen.[8] He finds that there may exist an instability where the electrons may act to transfer energy from proton azimuthal motion to coherent axial proton oscillations. For longitudinal electron oscillations having angular frequency ω_e, the ion oscillation frequency should be $n\omega_\phi - \omega_z$, where ω_ϕ is the ion cyclotron frequency and ω_z is the Z betatron frequency. The frequency ω_e should be below $n\omega_\phi - \omega_z$, and for low densities the frequency should be near $n\omega_\phi - \omega_z$.

For the field used in this experiment, the Z betatron frequency is $\omega_z = 4.6 \times 10^{-2}\ V_i$, where V_i is the ion velocity in centimeters per second.

[8] *Thermonuclear Div. Semiann. Progr. Rept. Apr. 30, 1964*, ORNL-3652, p. 23.

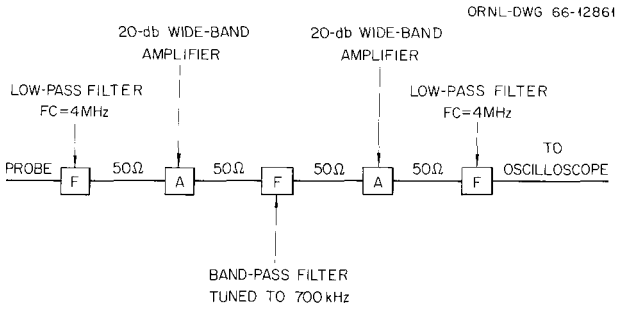

Fig. 5.19. Block Diagram of the Fast-Response Band-Pass Filter Circuit.

For a 200-eV proton this frequency corresponds to 145 kHz. Recalling that ω_ϕ is 850 kHz, $n\omega_\phi - \omega_z$ is very nearly 700 kHz when the ion energy is 200 eV. However, biased probe measurements, to be discussed shortly, indicate that the density of energetic ions below 100 eV is much larger than that at 200 eV. Thus if most of the ions have energies below 100 eV, the betatron frequency should be much lower, unless only the tail of the distribution participates in the instability. An attempt was made to look for oscillating electrons at ω_e. A probe was made consisting of a 1-in.-diam coil of 100 turns shielded electrostatically by a 3-mil stainless steel can. The probe was located approximately 5 cm from the plasma and could be rotated to observe either Z or θ currents. Calibration of the probe sensitivity was achieved by modulating the electron beam at 850 kHz and reducing the beam current to a low level. The resulting signal on the Panoramic receiver was just above the noise for a di/dt of 6.85 mA/μsec. Thus for a 500-kHz oscillation the resulting observable current change would be 3.4 mA. For an area of 1 cm^2 and an electron temperature of a few eV, this would correspond to a density of approximately 10^8/cm^3. Thus oscillation of 10% of the plasma density would be observable. No signals were observed for the magnetic probe in either direction of orientation. Attempts to correlate change in the ion and electron currents to bias probes with the rf bursts were also unsuccessful. If only the tail of the distribution were participating in the instability, the density of ions with energies above 200 eV is several orders of magnitude less than the plasma ion density and might account for the lack of observable effects.

Figure 5.20 shows the electric field due to the beam at a low pressure and at a pressure corresponding to the conditions for ion heating. A definite change in the harmonic content is observed. Figure 5.21 shows the difference in the amplitude of each harmonic at the low and high pressure. The positive db indicates an increase in the amplitude of the harmonic. Two peaks of 20 db are observed: one at 35 MHz and the second at 56 MHz, whereas the fundamental is slightly reduced in amplitude.

Probe Measurement. – In order to study the buildup and decay of the plasma, a pulser was inserted in the high-voltage line supplying the gun. The pulser was capable of turning the beam current full on in 3 μsec and off in 1 μsec. The turn-on possessed some overshoot, which was necessary in order to achieve this rapid turn-on. The buildup

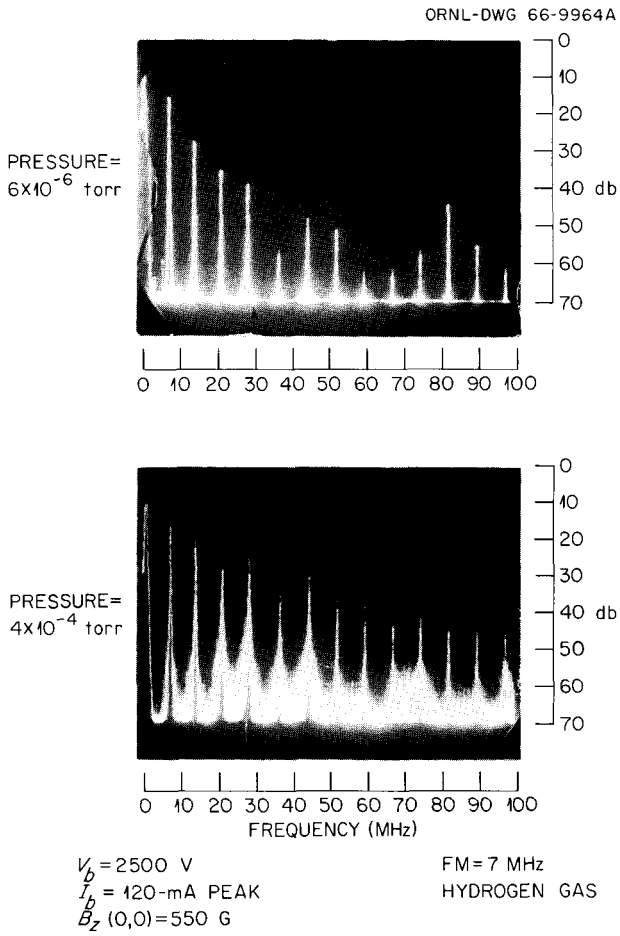

Fig. 5.20. Radio-Frequency Spectrum of the Modulated Electron Beam Up to 100 MHz.

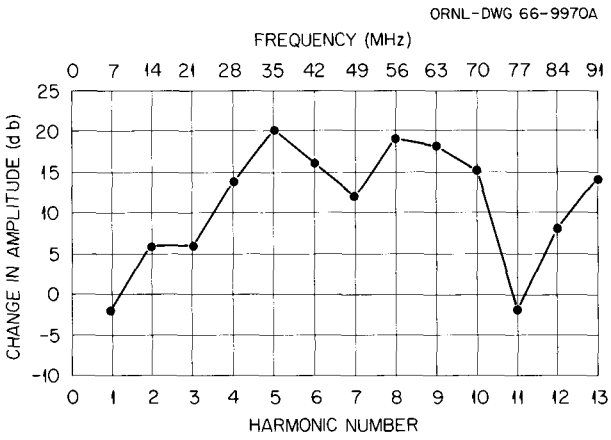

Fig. 5.21. Change in the Amplitude of the RF Harmonic Spectrum Due to the Presence of the Plasma.

time for the energetic ions and plasma was measured by observing the current to a biased probe located 5 cm from the beam in radius and 8 cm in Z from the midplane. Figure 5.22 shows the current to a probe biased at +56 V at beam turn-on. Within a few microseconds after the beam is turned on, there exist ions with energies in excess of 56 V and the ion current to the probe reaches steady state in about 100 μsec after beam turn-on. The upper picture in Fig. 5.23 shows the same current, even though the probe is now biased negatively. This indicates that there is an energetic ion plasma a few centimeters from the beam with most of the ions having energies in excess of 56 V. For a positive bias voltage in excess of 90 V, the current to the probe changed from ion to electron. The lower picture in Fig. 5.23 clearly shows the effect of no modulation. Not only are there no energetic ions, there is no plasma out at a distance of 5 cm from the beam. Thus the modulation of the beam produces energetic ions and increases the volume of plasma.

The current to a biased probe at turnoff is shown in Fig. 5.24. For a positive bias on the probe, the energetic ion current starts to decrease as soon as the beam is turned off, whereas when the current is biased negatively no abrupt change occurs at turnoff. The plasma has decayed away in about 100 μsec. The current to the biased probe after turnoff depends upon the radial position of the probe, as shown in Fig. 5.25. For the probe at the beam edge, both the ion and electron current start to decay as soon as the beam is switched off. With the probe 1 in. from the beam, the current to the probe is positive for either polarity of bias, and the decay time has increased. In addition, the ion current to the negatively biased probe shows no change until about 20 μsec after turnoff. As the probe is moved farther out, a most interesting phenomenon is observed. The current to the probe with the beam on gets much smaller, whereas 20 to 40 μsec after turnoff, there is a burst of plasma at the probe. Figure 5.26 shows the current to the biased probe after an unmodulated beam turnoff. In this case no burst of plasma is observed at the probe after turnoff.

Different Gases. – Experiments were performed in hydrogen, deuterium, and helium. In hydrogen

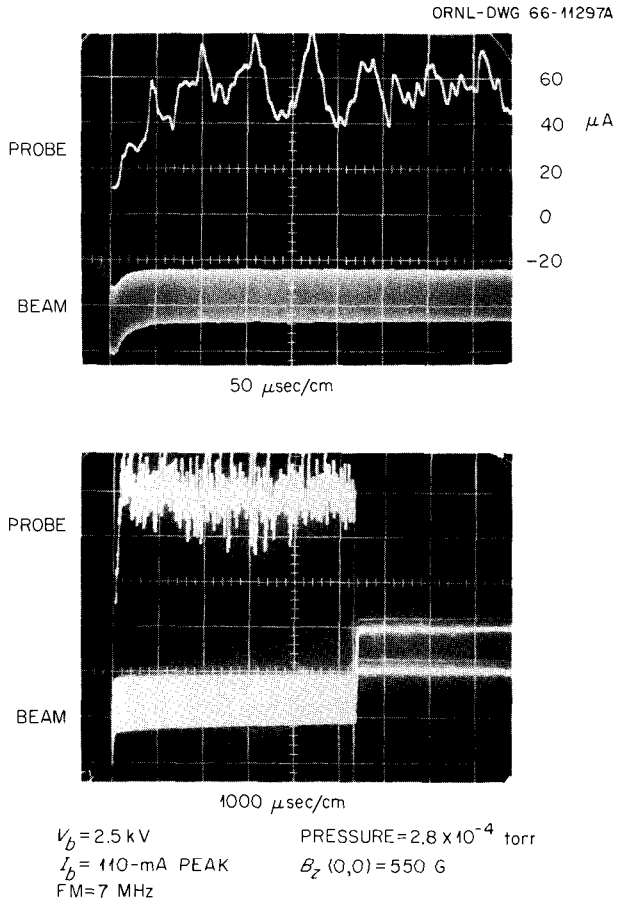

Fig. 5.22. Current to a Probe, 5 cm from the Beam, Biased at +56 V at Beam Turn-on. Beam modulated at 7 MHz.

the condition was observed where only a single charge species was heated. When deuterium replaced hydrogen as the working gas, both D^+ and D_2^+ ions were observed at the lower flux. With helium, there was also some heating observed, but the ion flux was not comparable with that of the protons when heating in the higher-pressure case.

Very High-Pressure Mode. – As in all beam-plasma experiments, if the pressure is raised sufficiently, a dramatic change takes place and the plasma is much larger and brighter. In this mode the density is in excess of $10^{11}/cm^3$, as indicated by the microwave cavity. In this mode no energetic ions were observed for any modulation frequency, including the ion cyclotron frequencies.

ORNL-DWG 66-11299A

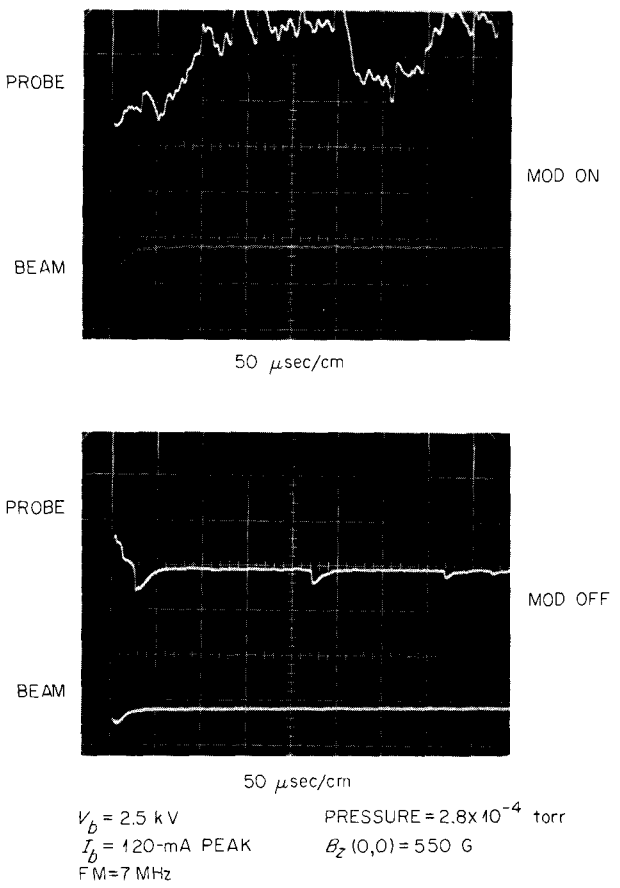

Fig. 5.23. Current to a Probe, 5 cm from the Beam, Biased at –56 V at Beam Turn-on, With and Without Modulation of Beam.

ORNL-DWG 66-11298A

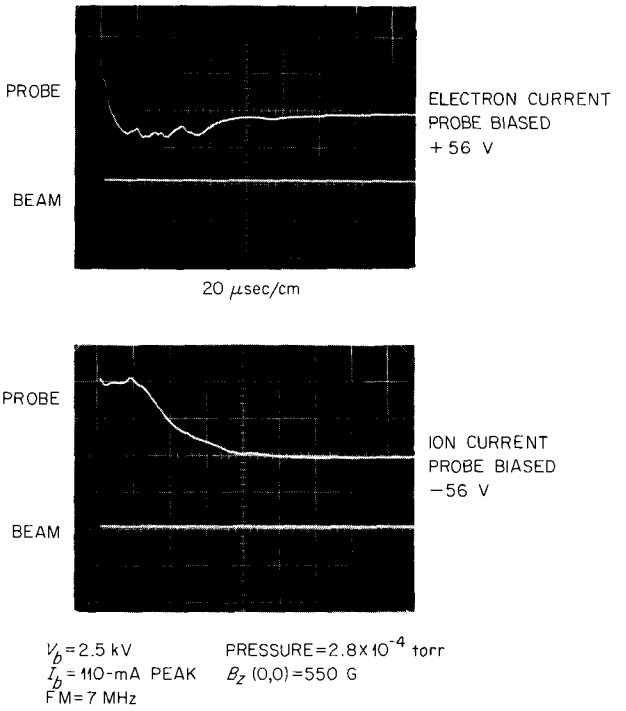

Fig. 5.24. Ion and Electron Current to a Biased Probe 5 cm from the Beam at Beam Turnoff. Beam modulated at 7 MHz.

5.2.4 Discussion of Possible Heating Mechanism

There is as yet no model for the heating mechanism, but some observations are in order. The heating mechanism in the high-pressure case ($>2.6 \times 10^{-4}$ torr) is selective in that it heats only the protons. Although the lifetime of the molecular ions is shorter than that of the protons, the molecular ions were heated in the low-pressure mode, and the small change in pressure required for the transition should not change the molecular-ion lifetime significantly. Thus one would suspect that the heating of the protons only is associated with a plasma resonance rather than just with the presence of a strong oscillating electric field. A resonance of this type was described by Buchsbaum[9] in 1960. It is a hybrid resonance due to the presence of two different ion species in the plasma. This condition is satisfied, as the

[9]S. J. Buchsbaum, *Phys. Fluids* 3, 418 (1960).

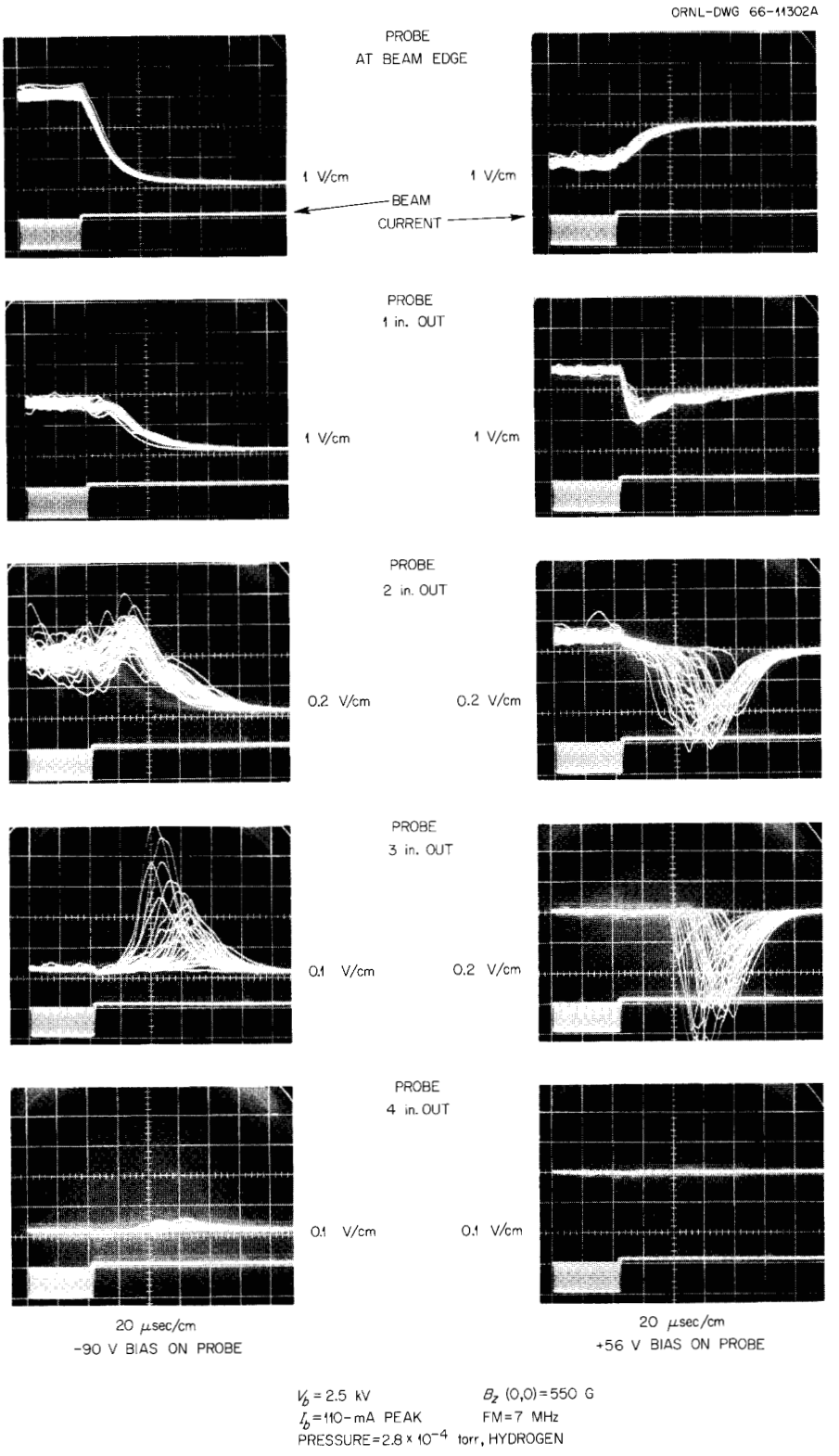

Fig. 5.25. Ion and Electron Current to Biased Probe at Beam Turnoff, for Several Radial Positions of the Probe. Beam modulated at 7 MHz.

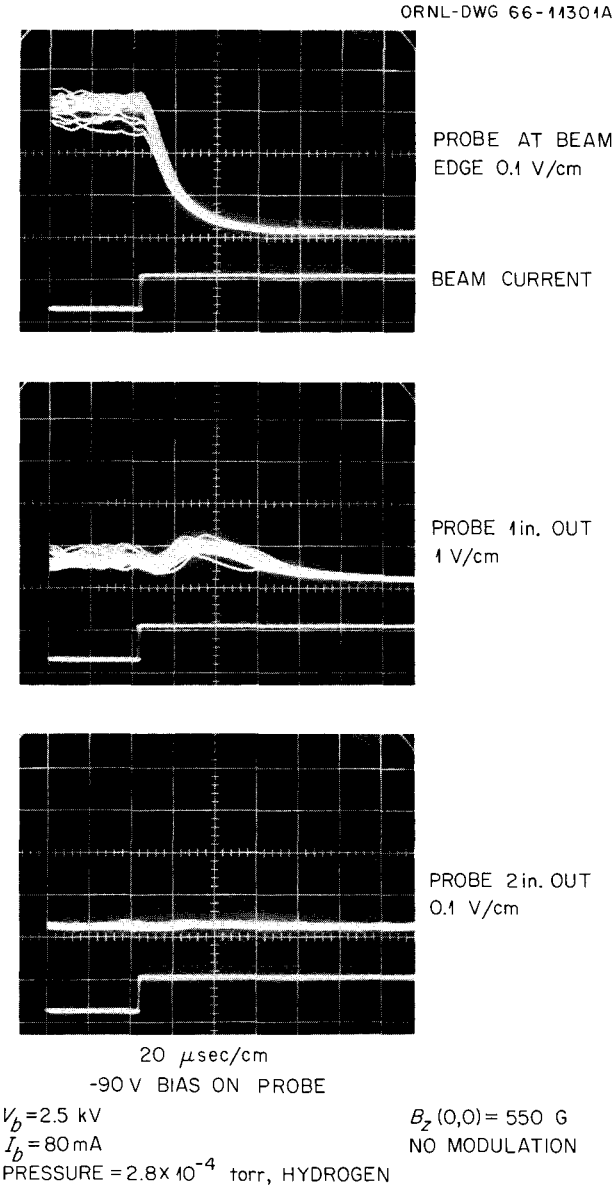

Fig. 5.26. Ion Current to a Biased Probe at Beam Turnoff, with No Modulation of the Beam.

plasma under study consists of both H^+ and H_2^+ ions. The dispersion relation for a plasma with two ion species present predicts two resonant frequencies, ω_1 and ω_2, which depend on the relative concentration of the two species:

$$\omega_1^2 = \left(\frac{x_2 f_1 + x_1 f_2}{x_1 f_1 + x_2 f_2}\right) \omega_{b_1} \omega_{b_2} ,$$

$$\omega_2^2 \cong \omega_b (x_1 \omega_{b_1} + x_2 \omega_{b_2}) ,$$

where

$x_1 + x_2 = 1$,

$x_1 ; x_2$ = relative concentration of the two species 1, 2,

$f_i = \dfrac{m}{M_i}$,

ω_b = electron cyclotron frequency,

ω_{b_i} = ion cyclotron frequency; $i = 1, 2$.

The estimation of the relative concentrations is very difficult. If an electron beam is passed through hydrogen gas, the dominant process for H_2^+ production should be direct ionization:

$$H_2 + e \longrightarrow H_2^+ + 2e ,$$

and the production of H^+ should be predominantly by dissociative ionization:

$$H_2 + e \longrightarrow H^+ + H_0 + 2e ,$$

or

$$H_2 + e \longrightarrow H^+ + H^+ + 3e .$$

The relative concentration in the plasma as a first approximation should be

$$\frac{n_+(H^+)}{n_+(H_2^+)} = \frac{\sigma_i(H^+)}{\sigma_i(H_2^+)} \frac{\tau(H^+)}{\tau(H_2^+)} ,$$

where the σ_i's are the ionization cross sections, and the τ's are the ion lifetimes in the plasma.

From the turnoff in Fig. 5.25, the lifetime of the cold ions is approximately the drift time of a thermal ion. The lifetime of the more energetic ions is a factor of 2 or 3 longer than the drift time. Thus the relative concentration should be of the order of 10%. For the concentration of protons much smaller than the concentration of molecular ions, the resonant frequency ω_1 approaches the proton cyclotron frequency, and the protons should be heating preferentially over the molecular ions. The resonance ω_2 then has a frequency near $\sqrt{\omega_b \omega_{b_2}}$, or for the field in this experiment, about 25 MHz. A 20-db increase in the rf amplitude near this frequency was observed. If, on the other hand, the pressure transition is such that the plasma became primarily protons, then there are at

least two possible explanations for the interactions. Stix[10] has discussed a resonance involving the electrons and ions – the low hybrid resonance. The resonant frequency is

$$\frac{1}{\omega_{LH}^2} = \frac{1}{\omega_{ci}^2} + \frac{1}{\omega_{pi}^2} + \frac{1}{\omega_{ci}\omega_{ce}} ,$$

where

ω_{LH} = low hybrid frequency,

ω_{ci}, ω_{ce} = ion and electron cyclotron frequency,

ω_{pi} = ion plasma frequency.

For the magnetic field and plasma density in this experiment, one has

$$\omega_{LH} \sim \omega_{pi} .$$

Kino and Gerchberg[11] have described a reactive medium instability in a cold plasma, where the growth rate is a maximum at $\omega \sim \omega_{pi}$ if $\omega_{ce}/\omega_{pe} >> 1$. In this experiment $\omega_{ce}/\omega_{pe} \sim 5$.

Response of a plasma to excitation of a line charge source has recently been calculated by Bernard[12] using a linearized hydrodynamic representation of a fully ionized macroscopically neutral electron-ion plasma, with a longitudinal dc magnetic field.

The dispersion relation for the frequencies at which the ion response to the line-charge excitation is maximum is

$$\left(-\omega^2 + \omega_{ci}^2 + \omega_{pi}^2\right)\left(-\omega^2 + \omega_{ce}^2 + \omega_{pe}^2\right) - \omega_{pi}^2\omega_{pe}^2 = 0 ,$$

where ω_{ci}, ω_{ce} are ion and electron cyclotron frequencies; ω_{pi}, ω_{pe} are ion and electron plasma frequencies.

For the magnetic fields and plasma densities in the experiment discussed, the following inequalities are valid:

$$\omega_{pi} >> \omega_{ci} ,$$

$$\omega_{pe} << \omega_{ce} .$$

For these inequalities, the dispersion relation is satisfied for $\omega = \omega_{pi}$, and this fits the frequency experimentally observed to produce the maximum energetic ion flux.

All of these theories are for a cold plasma in a uniform field. Because of the complexity of the plasma in the present experiment (i.e., beam generated), it is not yet possible to determine which of these theoretical descriptions (if any) may be appropriate.

5.2.5 Conclusions

The experiments described have demonstrated that the interaction of a modulated electron beam with the plasma formed by the beam can heat ions to energies of several hundred volts. The following summary lists the salient features:

1. The protons are predominantly heated.
2. The heating is rapid (few cyclotron periods).
3. The energetic ion flux increases with modulation amplitude, beam current, and magnetic field.
4. The frequency of modulation for maximum energetic ion flux is dependent on plasma density (near ion plasma frequency).
5. The modulation of the beam increases the plasma diameter.

In order to provide more quantitative data for development of a model and comparison with theory, the basic phenomena described must be investigated thoroughly in a more flexible facility.

5.3 VARIATION OF ION ACOUSTIC WAVE PROPERTIES WITH ELECTRON TEMPERATURE

I. Alexeff W. D. Jones

5.3.1 Technique for Varying Electron Temperature

As discussed in our previous semiannual report,[13] we have developed a new technique by

[10] T. H. Stix, *The Theory of Plasma Waves*, p. 32, McGraw-Hill, New York, 1962.

[11] G. S. Kino and R. Gerchberg, *Phys. Rev. Letters* 11, 185 (1965).

[12] G. D. Bernard, "Theory of Plasma Excitation by a Line-Charge Source," Quarterly Progress Report No. 82, p. 152, Research Laboratory of Electronics, MIT, July–August 1966.

[13] *Thermonuclear Div. Semiann. Progr. Rept. Apr. 30, 1966*, ORNL-3989, p. 58.

which the electron temperature in our discharge tubes car be varied downward from its normal value of about 1 eV to a lower limit of 0.1 eV.[14] We have used this technique to investigate several properties of our discharge-tube plasma as a function of electron temperature. In particular, we have investigated the dependence of ion-acoustic-wave velocity, and of wave-ion Landau damping on electron temperature.

The apparatus by which the electron temperature is varied is shown in Fig. 5.27. Essentially, we have a large probe that can be electrically heated to emit thermionic electrons (temperature-conversion device). Under this condition of operation, the plate can approach the positive potential of the plasma. The plate then can absorb hot electrons from the plasma and replace them with cooler, thermionically emitted electrons. Thus the plate acts as a heat sink for the plasma electrons. By increasing the emission of the plate, we can cool the plasma electrons to any temperature desired between the limits of about 2 and 0.1 eV.

A basic problem in the use of the above temperature-conversion device is that the heating current in the device produces a magnetic field. This magnetic field greatly impedes the flow of electrons to and from the device. We have overcome this by operating the temperature-conversion device on half-wave-rectified alternating current. On one half cycle of the ac supply, the heating current flows in the temperature converter. On the other half cycle, no current flows, and we then gate on our oscilloscopes to study the plasma during this time of zero magnetic field. The only basic limitation in this method is that apparently one half cycle of the ac (1/120 sec) is not long enough for our plasma to cool much below 0.2 eV. Thus we cannot yet study in detail the electron temperature region between 0.1 and 0.2 eV, using this ac technique.

5.3.2 Variation of Wave Velocity with Electron Temperature

The experimentally found variation of the ion acoustic wave velocity with electron temperature in a xenon plasma is shown in Fig. 5.28. For high electron temperatures, the ion wave velocity does vary as $T_e^{1/2}$, in the expected manner. As T_e is reduced toward T_i, the experimental points deviate from the normal $T_e^{1/2}$ dependence. This new curve is best fitted by a velocity dependence of the form $v = (kT_e + 3kT_i)^{1/2} m_i^{-1/2}$, as shown in Fig. 5.28. This modified equation can be de-

[14] I. Alexeff and W. D. Jones, *Appl. Phys. Letters* **9**, 77 (1966).

ORNL-DWG 66-4976A

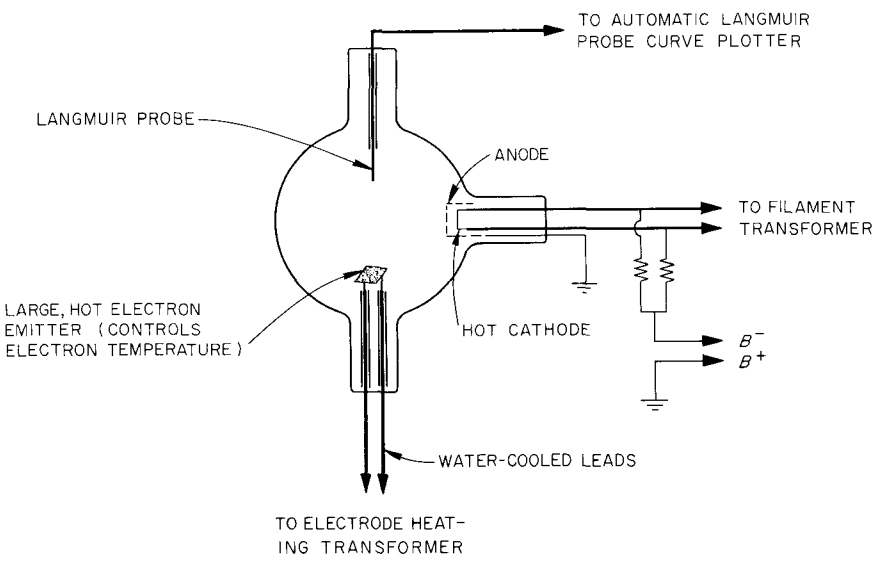

Fig. 5.27. Apparatus Used to Control the Plasma Electron Temperature.

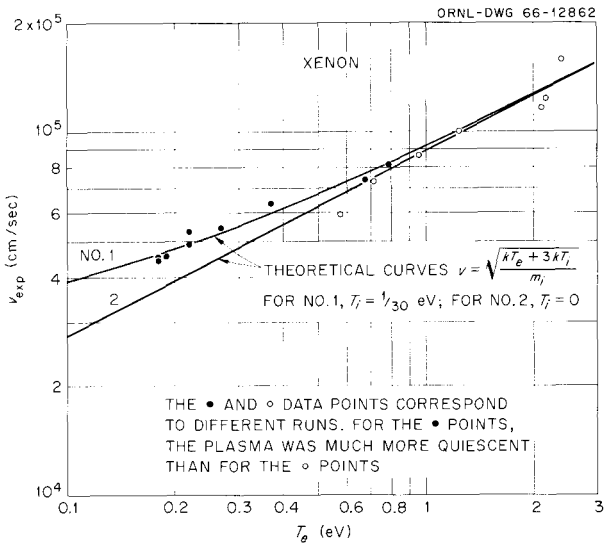

Fig. 5.28. Variation of the Ion Acoustic Wave Velocity with Temperature.

rived[15] as an approximate solution of the Vlasov equation.[16] We were aided by R. A. Dory in solving the required mathematics.

In fitting this curve, the value of T_i is assumed to be 0.03 eV. This ion temperature value is consistent with the values found by several other ion-wave techniques: collisional damping of the ion waves by ion–gas-atom collisions, Doppler shift of the ion wave velocity due to the radial drift of plasma to the discharge-tube wall, Landau damping effects (Sect. 5.3.3), and computations based on the rate of collisional heating of the ions by the electrons in the discharge tube.

One can invert the discussion above to show that for the observed experimental data to occur, the ion temperature *must* be 0.03 eV to within better than a factor of 2. In other words, our ion-wave-velocity measuring technique gives us an ion temperature thermometer.

5.3.3 Landau Damping

As the electron temperature in our xenon plasma is reduced, the ion acoustic velocity,

$$v = (kT_e)^{1/2} m_i^{-1/2} ,$$

is reduced toward the most probable thermal velocity of the ions in the plasma,

$$v_i = (2kT_i)^{1/2} m_i^{-1/2} .$$

Under this condition of operation, the ion wave begins to move with the same velocity as some of the more energetic ions in the high-energy "tail" of the Maxwellian distribution. When this velocity coincidence occurs, a traveling-wave-tube kind of interaction draws energy from the wave and feeds it to the particles. This removal of energy from the wave naturally damps the wave. This collisionless damping process is referred to as *Landau damping*.

We have been able to demonstrate this collisionless, spatial damping in numerous experiments. In Fig. 5.29, we show the propagation of pulses in a xenon plasma for three successively larger spacings between the transmitting and receiving electrodes. In each pair of traces, the upper trace corresponds to $T_e \approx 1$ eV and the lower to $T_e \approx 0.2$ eV. In the top pair of traces, both pulses have

PHOTO 85969

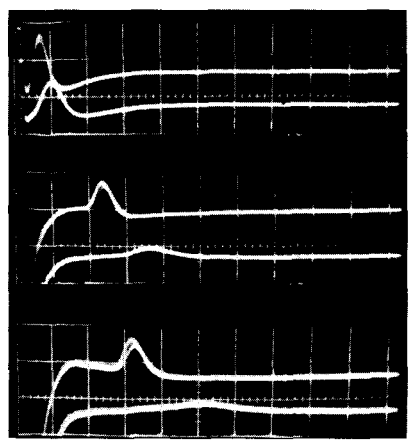

Fig. 5.29. Propagation of Ion Acoustic Wave Pulses in a Discharge-Tube Plasma. In the upper trace of each of the three pairs, the electron temperature is about 1 eV. In the lower trace of each of the three pairs, the electron temperature is about 0.2 eV. The time scale reading from left to right is 20 μsec per large division. The spacing of the transmitting and receiving electrodes is 2 cm, top; 6 cm, middle; 8 cm, bottom. The gas used is xenon.

[15] Private communication, M. G. Payne, summer research participant, 1966.

[16] R. W. Gould, *Phys. Rev.* **136**, A991 (1964).

about the same amplitude, although the lower pulse arrives later in time. In the center pair of traces, the lower pulse of the pair is much smaller than the upper, showing that spatial damping is occurring. The lower pulse is getting broader, showing that high frequencies are being preferentially attenuated. Such a preferential attenuation of high frequencies is expected for Landau damping. In the lower pair of traces, made for a still greater transmitter-receiver spacing, the attenuation of the lower pulse is still more pronounced, and the spreading is even greater. Thus, the pulse work qualitatively and, when mathematics is applied, quantitatively supports our assumption that we are observing Landau damping.

Another group of data supporting this Landau damping interpretation is given in Fig. 5.30. Here, the received amplitude of a sine-wave burst traveling across a fixed gap is plotted as a function of electron temperature. The graph shows three regions of interest. At higher electron temperatures, the received signal decreases gradually with decreasing electron temperature. At the intermediate electron temperature of about 0.25 eV, there is a break in the curve. Below the electron temperature of 0.25 eV, the amplitude of the received signal decreases very rapidly with electron temperature.

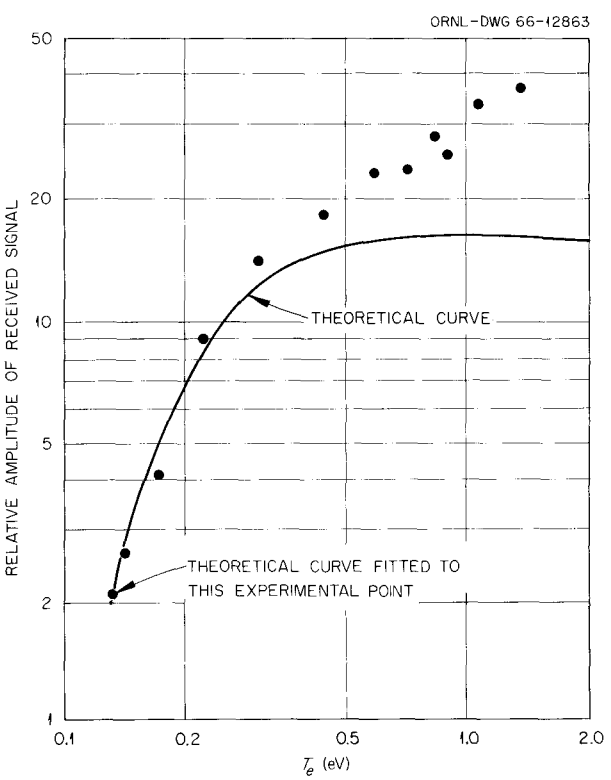

Fig. 5.30. Change in Amplitude of the Received Signal for a Sine-Wave Burst Transmitted Through a Xenon Plasma. The electrode spacing was 7 cm. The frequency of the burst was 20 kc. The ion temperature was assumed to be 0.03 eV.

Aided by R. A. Dory, we computed the predicted Landau damping. Since the computed curve must be normalized to a given point, we have chosen to use the experimental point obtained at the lowest electron temperature. As shown in Fig. 5.30, the theoretical curve fits both the rapidly varying experimental points below 0.25 eV and predicts the "break" in the experimental data at 0.25 eV. In the region above 0.25 eV, the theoretical curve is flat. It does not show the weak dependence of received amplitude with electron temperature that is experimentally observed. We suspect that this observed variation of received amplitude with electron temperature is due to changes in coupling of the wave with the transmitting and receiving electrodes, due to electron-temperature-dependent sheath effects.

In any case, both the pulse experiments and the sine-wave-burst experiments seem to demonstrate the spatial Landau damping of ion waves in a plasma as a function of electron temperature.

5.4 LANDAU DAMPING BY THE ADDITION OF A LIGHT CONTAMINANT TO A PLASMA OF HEAVY IONS

I. Alexeff W. D. Jones

D. Montgomery[17]

The cause of Landau damping is the transfer of energy from a plasma wave to some charged particles in the plasma that happen to be moving with the wave. In our discharge-tube plasmas the velocity of the ion acoustic wave, $v = (kT_e)^{1/2}m_i^{-1/2}$, $T_e = 1$ eV, is much higher than the most probable thermal velocity of the ions, $v_i = (2kT_i)^{1/2}m_i^{-1/2}$, $T_i = 1/30$ eV. But by slowing down the ion wave by reducing the electron temperature (Sect. 5.3), Landau damping can be observed. However, by

[17]Consultant, University of Iowa, Iowa City.

reducing the electron temperature, we are changing the plasma properties. Probably both the ion wave velocity and sheath effects are changing with T_e.

A way of producing Landau damping without changing the bulk properties of the plasma is by adding a trace of a light contaminant to a plasma of heavy ions. Consider a plasma of xenon in our discharge tube, $T_e = 1$ eV, $m_i = 131$ amu; if a trace of helium is added, the helium ions will have a thermal velocity that almost exactly matches the ion acoustic wave velocity. For helium, $T_i = 1/30$ eV, $m_i = 4$ amu, and the decrease in thermal velocity due to the low ion temperature of the helium is almost exactly compensated for by the increase in velocity due to the low atomic mass.

Experimental results showing the damping of an ion acoustic wave due to helium addition in a xenon plasma are given in Fig. 5.31. The upper trace shows a strong ion acoustic wave pulse being received. The second trace shows the signal being damped as helium is added to the plasma. The third trace shows maximum damping, plus spreading of the signal due to the preferential attenuation of high-frequency components. This maximum damping occurs for about 2% helium ion impurity in the xenon plasma.

The lowest trace shows the signal with still more helium impurity added; but there is so great a percentage of helium present that the effective mass in the ion-wave formula is decreasing. As a consequence, the wave is speeding up (moving to shorter times), and the wave begins to move faster than the thermal helium ions. As a result of this speedup, the Landau damping *decreases* – the received signal is larger than for the third trace.

The mathematical theory for this damping by contamination has been worked out by David Montgomery,[17] who has demonstrated that the observed damping is quantitatively correct and that there should be the observed speedup of the waves as the helium concentration is increased.

The theory also predicts a second wave. This wave begins with a velocity comparable to that of the ion acoustic wave in xenon. As the helium concentration is increased, the predicted velocity of this wave decreases toward that of ordinary sound waves in xenon gas. In our particular experiment, this second wave should always be strongly Landau damped. We have not observed this wave. However, when the masses of the two ion species do not greatly differ, this wave should be visible.

PHOTO 85970

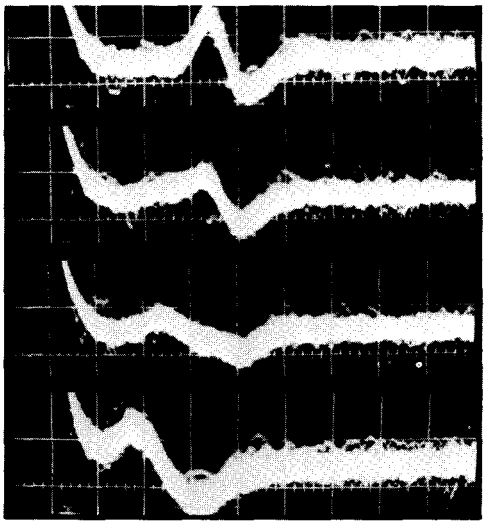

Fig. 5.31. Change in Amplitude of a Received Ion-Acoustic-Wave Signal in Xenon, as Helium Ions Are Added. Top – no helium. Upper middle – a very small fraction of helium ions is present. Note that the amplitude has decreased. Lower middle – maximum damping. About 2% helium ions are present. Bottom – with still more helium ions present, the ion acoustic wave velocity increases, and the damping goes away, as predicted. The electron temperature was 1 eV; the electrode spacing was 7.5 cm; the time scale is 20 μsec per large division.

In conclusion, by adding a few percent He^+ contamination to a xenon plasma, we have been able to produce strong Landau damping. This technique appears to be superior to the earlier technique of slowing down the wave toward the ion thermal velocity, because the bulk plasma parameters – electron temperature and ion wave velocity – are not altered.

5.5 PARAMETRIC EXCITATION OF TRANSVERSE WAVES IN A PLASMA

I. Alexeff D. Montgomery[17]

It is shown that an externally imposed oscillating electric field excites *transverse* electromagnetic waves propagating perpendicularly to

it in a cold plasma. The mechanism is closely related to the parametric excitation of longitudinal plasma oscillations recently predicted by Aliev and Silin. The problem provides an application of nonsecular perturbation methods, when the equations of motion are expanded in powers of the external electric field. Arbitrary small perturbations which arise spontaneously in the plasma are amplified by the action of the electric field, for a certain range of the driving frequency. The growth rate of the oscillations is calculated.

The full text is published in *The Physics of Fluids* **9**, 1362 (1966).

5.6 HOT-ELECTRON PLASMA BLANKET

I. Alexeff V. J. Meece
W. L. Stirling

5.6.1 Two-Arc Performance

We have returned to two-arc operation (Fig. 5.32) in an attempt to increase the trapped plasma density. The arc electrodes are separated 180° in azimuth and 2 in. in radius; one is 4 in. and the other 6 in. off the magnetic axis. Simultaneous operation of the two arcs is stable at 1600 G axial midplane magnetic field. The radial separation of the two arcs does not permit an overlap of the hot-electron shell drifting from each arc. Figure 5.33, which is a measure of the power delivered to a midplane power probe as a function of the probe radial position, shows this clear separation between the two shells. However, as compared with a single arc, there is an increase in total x-ray intensity by a factor of 3 to 5 with both arcs operating.

Operational experience and careful alignment of cathode and anode have permitted an increase to 5×10^{11} cm^{-3} for the intermediate-energy electron density[18] in either plasma blanket. This value is determined both from the electron saturation current streaming through the mirror coil throat and from the power delivered to the midplane power probe (if the energy of the intermediate group is 2 keV). We feel that this energy figure is not off by more than a factor of 2. We may be only a factor of 20 from the density of 10^{13} cm^{-3} required to produce "burnout" of the neutral gas in the center of the hot-electron shell.

5.6.2 Effect of Saturation Current Measurements on Plasma Density

A means has been found for increasing the energy and possibly the density of the intermediate-energy electron group. The method utilizes the same wire probes used for monitoring the electron saturation current streaming out the mirror. With the high plasma density recently achieved in the shell, an application of a positive voltage on the current probe to measure the electron saturation current causes a spreading of the shell and a change in power delivered to the power probe. Figure 5.34 shows the effect on the shell with either a dc bias to the current probe or an rf signal of 300 kc. The bias voltage and the rf signal do not have the same effect on the plasma. However, both cause an increase in the curve area or power delivered to the probe. Figure 5.32 indicates the positions of the current probe and midplane power probe. Both are located about 90° (azimuth) from the streaming electron sheet of the reflex discharge. The bias voltage increased the power by about 20% and the rf signal by about 30%. The power input to the current probe in either case is about 100 W. The total power in the undisturbed shell is about 2 kW out of a total drain of 25 kW on the arc power supply; that is, roughly 8% of the power from the supply appears as hot electrons.

There is a variation in the power delivered to the probe with frequency. The dc bias causes a decrease in the peak power and more radial spreading of the plasma than the rf signal. The applied rf frequency is not critical but seems to have a maximum heating effect below 300 kc and falls off slowly with increasing frequency. Since the period of a 300-kc signal is about equal to the transit time of the cold plasma electrons out of the machine, it is likely that the plasma heating and spreading is being driven by an oscillation of the cold plasma. However, the source of the energy delivered to the trapped plasma must be the primary arc supply, since the power increase shown in Fig. 5.34 is about six times the 100 W delivered to the current probe.

[18] *Thermonuclear Div. Semiann. Progr. Rept. Apr. 30, 1966*, ORNL-3989, p. 61.

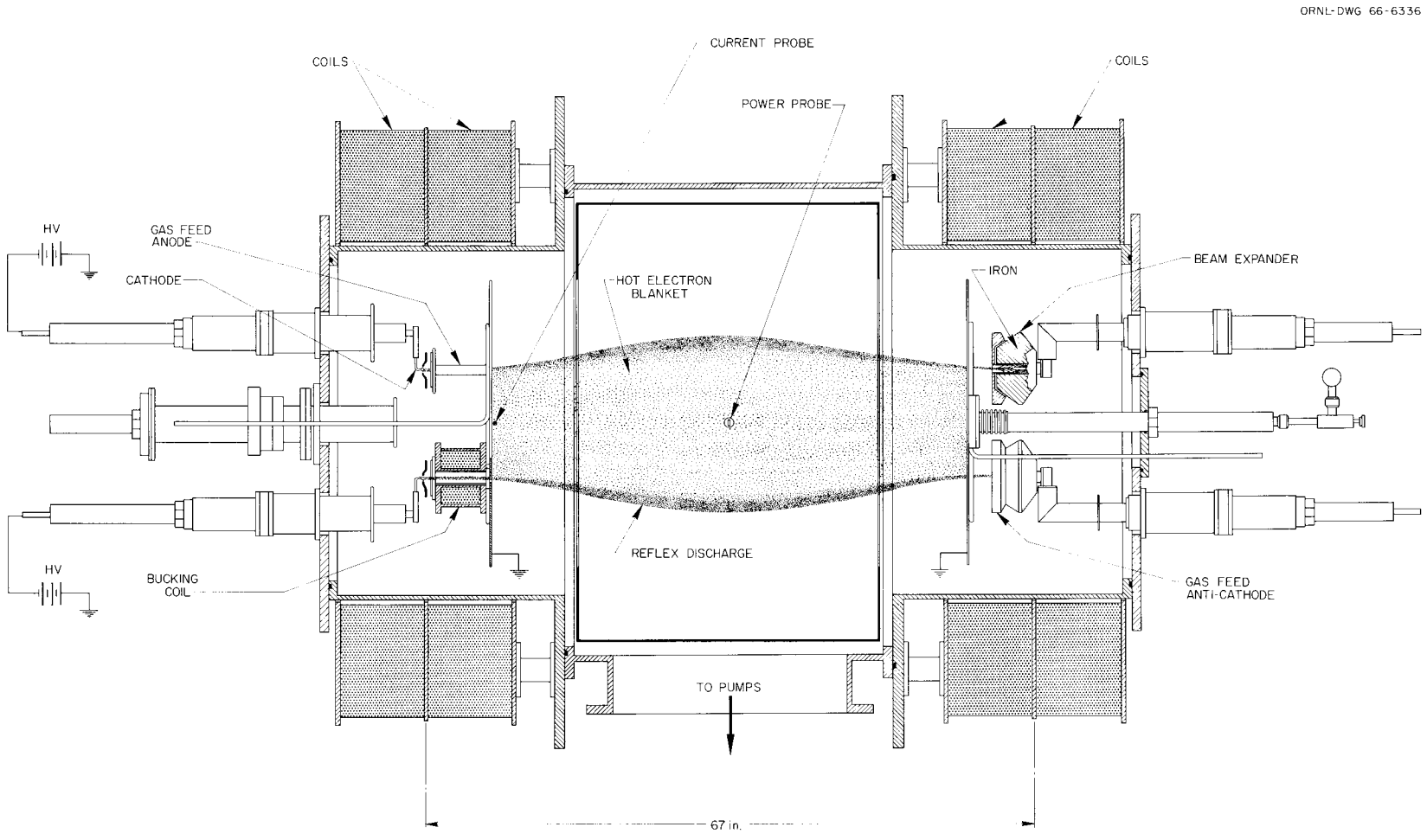

Fig. 5.32. Schematic of Two-Arc Operation.

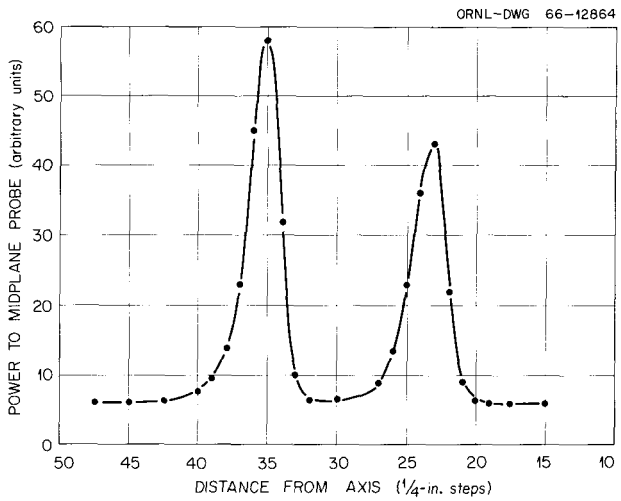

Fig. 5.33. Midplane Density Profile for Two Arcs.

5.6.3 Magnetic-Field Shielding in the Anode Region

We have made several runs with the anode bucking coil, shown on the bottom arc in Fig. 5.32. A schematic of the bucking coil and electrode assembly is shown in a previous report.[18] Figure 5.35 shows a typical field shape obtained with the bucking coil when the axial midplane field is 2000 G. The bucking coil has two advantages over the iron shield previously used to reduce the field in the anode region. First, we can continuously vary the magnetic field strength in the anode channel while operating. Second, the coil produces no regions of enhanced field in a manner similar to the induced field of the iron just outside either end of the iron cylinder. However, the coil effectively reduces the mirror ratio along the flux lines of the discharge column.

The effects thus far observed with the bucking coil may be summarized with the aid of Fig. 5.36. This figure shows the variation of three different physical parameters with the midplane magnetic field. The midplane field has been increased to 5500 G with the bucking coil on. The maximum obtained with the iron was 4000 G. However, the electron saturation current to a probe in a mirror coil throat fell by a factor of about 3 when using the bucking coil. At the same time, the operating pressure or neutral density increased by a factor of less than 2. Since the intermediate-energy electron density varies directly as the electron saturation current and inversely as the neutral density, the electron density decreased by a factor of about 5 for a magnetic field increase of $3\frac{1}{2}$. This density decrease arises from the fact that the grad B drift of the electrons varies inversely with magnetic field, and the relaxation time for scattering out the mirror varies inversely with neutral density.

Figure 5.36 also shows that the discharge operated at magnetic fields in the anode channel above the 4400 G maximum which can be achieved without the bucking coil on. An attempt was made to hold the field in the anode at about 4000 G. By so doing, we could not operate at midplane magnetic fields up to 5500 G. Results with iron shielding indicated that the magnetic field in the anode should stay about constant. However, these preliminary results with the bucking coil suggest that the anode channel magnetic field is an important parameter in the resonance condition responsible for the electron heating observed. Both the coil and the iron shield result in an increase of the maximum magnetic field at which the heating process will operate.

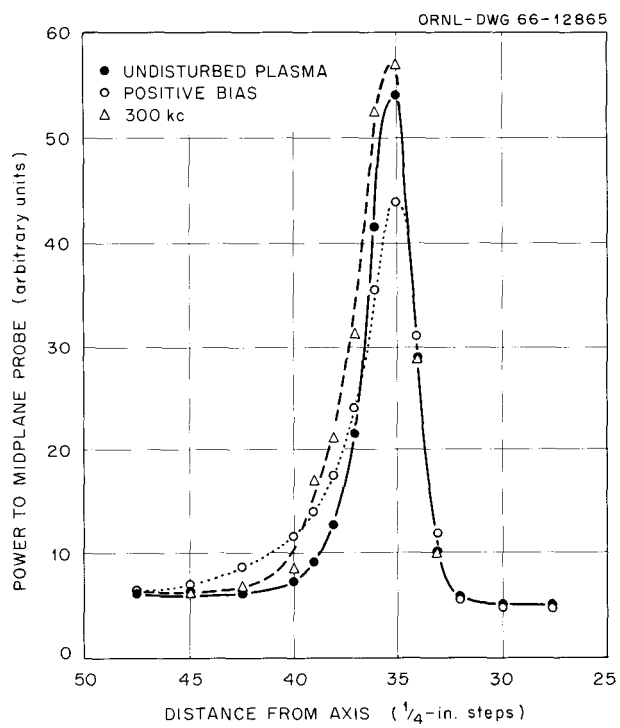

Fig. 5.34. Plasma Spreading Due to a Positive Bias and to a 300-kc rf Drive on a Probe in Mirror.

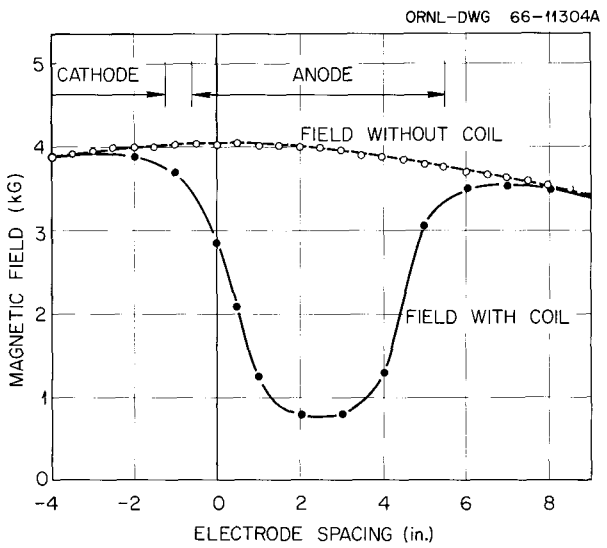

Fig. 5.35. Mirror Field with Bucking Coil Energized.

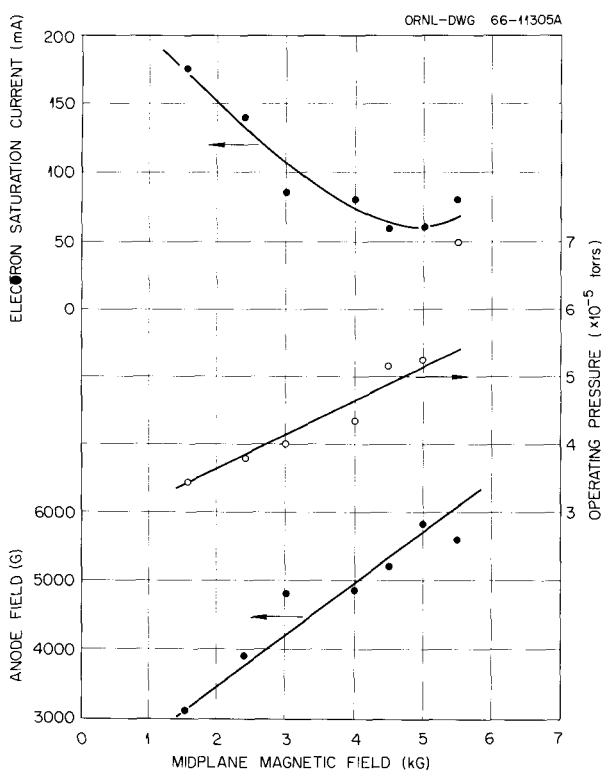

Fig. 5.36. Variation of Electron Saturation Current, Operating Pressure, and Anode Magnetic Field with Midplane Magnetic Field.

5.7 EXCITATION HEATING OF IONS TO MODERATE TEMPERATURES

J. Rand McNally, Jr. P. M. Jenkins

5.7.1 Introduction

The elementary process of electronic excitation followed by heating of atoms and ions is fairly well documented. Perhaps the most well-known case is that of the Franck-Condon excitation of the neutral hydrogen molecule to the repulsive $^3\Sigma_u$ state, which then decays into two free hydrogen atoms having an energy of about 2 eV each.[19] Recently, quite vigorous heating has been observed in the explosive-like dissociation of multiply charged molecular ions; for example, ions up to about 100 eV have been observed in the dissociation into energetic fragment ions of multiply charged methyl iodide (CH_3I), which is produced by x-ray ionization of the iodine *L* electron followed by as many as nine additional electrons "shaken off" the molecule.[20] In the case of our energetic carbon arcs the excitation-heating process is believed to be a more complicated, *multiple* or *chainlike* process which permits the ions to escalate to an equilibrium energy considerably higher than expected from the elementary, isolated excitation-heating step.

These arcs are steady-state, high-current, long, magnetically confined carbon arcs characterized by very high ion "temperatures" and modest electron "temperatures."[21] During this report period brief studies have been continued in the Long Solenoid Facility using two 19-ft-long arcs for vacuum ultraviolet studies.[22]

The carbon ions are believed to escalate to a high energy consistent with their residence time in the arc (estimated ~1 msec) and the following excitation-heating steps (neglecting power feed from the arc, elastic collisional energy transfer from electrons, and radiative losses):

---

[19] See H. S. W. Massey and E. H. S. Burhop, *Electronic and Ionic Impact Phenomena*, p. 232, Clarendon Press, Oxford, 1952.

[20] T. A. Carlson and R. M. White, *J. Chem. Phys.* **44**, 4510 (1966).

[21] J. R. McNally, Jr., and M. R. Skidmore, *Appl. Opt.* **2**, 699 (1963); J. R. McNally, Jr., *et al.*, *Appl. Opt.* **5**, 187 (1966).

[22] *Thermonuclear Div. Semiann. Progr. Rept. Apr. 30, 1966*, ORNL-3989, pp. 74–77.

$$C^{2+}(^1S) + e \rightarrow C^{2+*}(^3P^0) + e - 6.5 \text{ eV, excitation of ions,}$$

$$C^{2+*}(^3P^0) + C^{2+*}(^3P^0) \rightarrow C^{2+}(^1S) + C^{2+}(^1S) + 13.0 \text{ eV, heating of ions.}$$

The mean electron energy of about 4 eV, plus the large statistical weight of 9 for the metastable $^3P^0$ state compared with 1 for the ground ^1S state, suggests an excess population (1.5:1) for the $^3P^0$ state (this has been measured to be about 4:1).[22] In order that the above exothermic reaction[23] proceed, the strongly repulsive Coulomb barrier (estimated $\lesssim$ 50 eV) is apparently overcome by powerful $\mathbf{E} \times \mathbf{H}_z$ drift motion and axial drifts due to $\mathbf{E}_z$, some randomization through collisions, and near head-on collisions which trigger or ignite the excitation-heating cycle. In carbon arcs up to 16 ft in length, the maximum ion "temperature" reached $T_\perp \cong$ 5,000,000°K (~500 eV) as determined by Doppler broadening.[21] To attain such high mean energies, the number of propagation steps for individual carbon ions must be in excess of 100.

5.7.2 Ion Densities in the Carbon Arc

Additional data have been obtained by vacuum ultraviolet absorption spectroscopy techniques and using two parallel 19-ft-long carbon arcs. One arc served as an emitter arc or light source, and the second arc was the absorber arc, in which ion densities of C^{2+}, C^{2+*}, and C^{3+} were measured by standard absorption techniques.[22]

Table 5.1 gives the results on ion and electron ($n_e = \Sigma\, zn_+$) densities (the third column of Table 5.1 is taken from ref. 22). The lower-current arcs produce a larger population of doubly ionized species relative to C^{3+} than the higher-current arcs (4/1 at 175 A vs 1.6/1 at 250 A), confirming the earlier work.[22] Apparently the C^{3+} ion acts as an impurity ion which introduces both (1) a reduction of the excitation-heating process by reducing the number of heating collisions and (2) a cooling effect since the C^{3+} acts essentially as a separate energy reservoir stealing kinetic energy from the active C^{2+} ions and losing it to the electrons.

The abundance of metastable C^{2+} ions relative to ground-state C^{2+} ions is higher than a Boltzmann equilibrium at T_e = 4 eV would predict. Taking an average for the two arc currents in Table 5.1, one gets C^{2+*}/C^{2+} as about 4.6:1. This population ratio suggests that T_e is of order 80,000°K or 10.4 eV (for E^* = 6.5 eV, g^* = 9, and g^G = 1) in contrast with a Saha temperature of 28,000°K, and with the microwave (surface temperature) value of Ard[24] of 4 to 8 eV and other spectroscopic values of 18,000 to 60,000°K (depending on the method of interpretation[21]). The uncertainty is about 15% for this newer technique of obtaining an electron temperature, using the C^{2+*} and C^{2+} relative abundances, suggesting the possibility of a slightly inverted population for the metastable state.

Table 5.1. Ion Densities in the Energetic Carbon Arc (570 cm long)

Ion Species	Density (465 cm from anode)	
	175 A	250 A
C^{2+}	0.4×10^{13} ions/cm^3	0.5×10^{13} ions/cm^3
C^{2+*}	1.6×10^{13}	2.7×10^{13}
C^{3+}	0.5×10^{13}	2.0×10^{13}
e	5.5×10^{13} e/cm^3	12.4×10^{13} e/cm^3

5.7.3 Mass Spectrometric Data

Mass spectrometric analysis of the peripheral region of the carbon arc using the Neidigh mass analyzer[25] gave data much like those shown in Fig. 5.37. Calibration was made by introducing various gases, and the calibration results are shown in Fig. 5.38.

[23]The reaction energy is not naturally present in the carbon ions (as in the case of chemical and nuclear fusion reactions) but rather is pumped there at the expense of energy of the electrons and hence the applied power.

[24]W. B. Ard, Jr., *Thermonuclear Proj. Semiann. Rept. Jan. 31, 1960*, ORNL-2926, p. 43.

[25]*Thermonuclear Proj. Semiann. Rept. Jan. 31, 1960*, ORNL-2926, pp. 30–34.

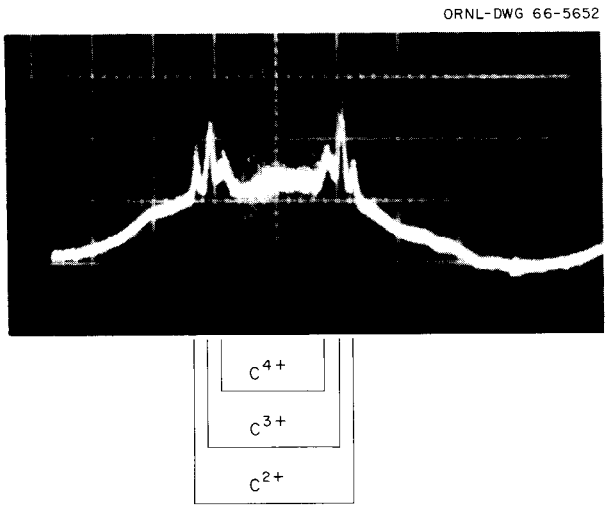

Fig. 5.37. Mass Spectrometric Analysis of the Magnetically Confined (8300 G) Vacuum Carbon Arc (3×10^{-6} Torr, ~130 A, 178 V, 40 in. from Anode in 19-ft-long Arc). (See ref. 25.)

The mass analysis studies consistently gave high abundances for C^{2+} and C^{3+}, lending additional credence to the optical measurements. The concentration of C^{4+} decreased as the analyzer was moved closer to the arc core; also, the C^{2+} peak increased relative to the C^{3+} peak. This dependence on radial motion of the mass analyzer supports the optical data, which give a higher abundance of C^{2+} compared to C^{3+} in the arc core.

5.7.4 The Near-Resonance Reaction and the Massey-Hasted Adiabatic Maximum Rule

Massey[26] suggested that the cross section for charge-transfer reactions to occur has a maximum when the adiabatic criterion $a|\Delta E| \gg h\nu$ becomes an equality, that is,

$$a|\Delta E| = h\nu \ .$$

Hasted[27,28] discussed this in more detail and evaluated an experimentally best value of $a = 7 \times 10^{-8}$ cm for a large number of cases. In cases when m electrons were transferred, the data pointed to using ma instead of a for the atomic parameter.

The excitation-heating cycle is a possible example of such a near-resonance condition; that is, in the reaction:

$$C^{2+*}(^3P^0) + C^{2+*}(^3P^0) \longrightarrow C^{2+}(^1S) + C^{2+}(^1S) + 13.0 \text{ eV} \ ,$$

there is a near resonance for the colliding ions:

$$C^{2+*}(^3P^0) + C^{2+*}(^3P^0) \longrightarrow C^{2+\prime}(^1P^0) + C^{2+}(^1S) + 0.29 \text{ eV} \ .$$

Table 5.2 gives data pertinent to several ions which are isoelectronic with C^{2+}. The predicted v_{rel} for C^{2+*} is 9.8×10^6 cm/sec *at the maximum* of the cross section for a double charge exchange. This corresponds to an energetic C^{2+*} particle of 600 eV striking another at rest or to two 150-eV ions colliding head on. Although we have used $m = 2$ it is possible that $m = 1$ may be more appropriate, since the reaction may go as either double charge exchange or as an excitation-de-excitation process, inasmuch as the identity of the two electrons is lost.

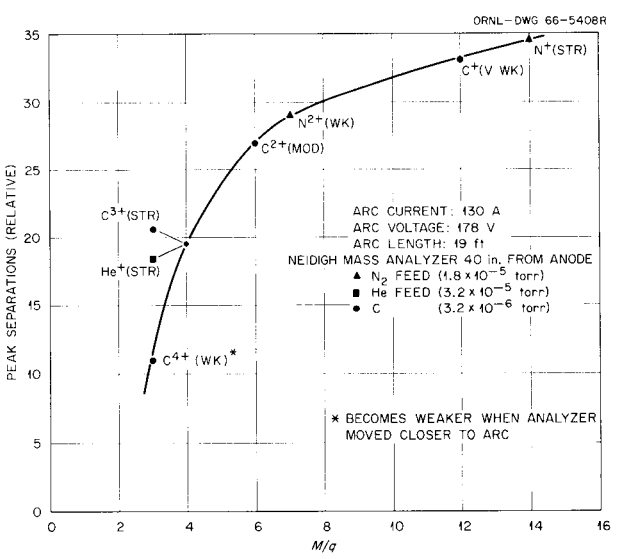

Fig. 5.38. Mass Peaks Observed in Carbon Arc vs m/q, Where q is Charge State. Signal intensities are STR (strong), MOD (moderate), and WK (weak).

[26]See H. S. W. Massey and E. H. S. Burhop, *Electronic and Ionic Impact Phenomena*, p. 515, Clarendon Press, Oxford, 1952.

[27]J. B. Hasted, *Proc. Roy. Soc.* **A212**, 235 (1952).

[28]J. B. Hasted and A. R. Lee, *Proc. Phys. Soc.* **79**, 702 (1962). See also J. B. Hasted, *Physics of Atomic Collisions*, p. 422, Butterworths, 1964.

Table 5.2. Energy Defects and Approximate Locations of Cross-Section Maxima

$$X^* + X^* \rightarrow X' + X + \Delta E$$

Reaction Species	Energy Defect (eV)	v_{rel} (cm/sec)[a]	KE_1 (eV)[b]	KE_2 (eV)[b]
		$\times 10^6$		
Be*	0.17	5.6	140	35
B^{+*}	0.16?[c]	5.4?	150?	38?
C^{2+*}	0.29	9.8	600	150
N^{3+}	0.49	16.4	2000	500
O^{4+*}	0.74	24.8	5100	1300

[a] $v_{rel} = 2a|\Delta E|/hv$.

[b] KE_1 = projectile energy; KE_2 = energy for two projectiles in head-on collision.

[c] Indicates uncertainty in energy defect.

Nitrogen ions require 1.8 times the collisional velocity or almost four times the energy. The exponential shape of the cross section is given by Massey and Burhop[26] as

$$e^{-ca|\Delta E|/v} \sim e^{-c'a|\Delta E|/hv},$$

where c' is about unity for near resonance.[29] Thus, in the adiabatic region (low collisional velocity regime where the time of collision is long compared with the electron rearrangement time), carbon ions are much more likely to react than nitrogen; for example, if the exponential is 0.1 for carbon, it is only 0.015 for nitrogen at the same velocity. This may explain in part (together with the increased Coulomb barrier) the difficulty of obtaining a nitrogen arc containing very hot nitrogen ions.

Two curves (Figs. 5.39 and 5.40) are given in a new form to illustrate the Massey-Hasted relation in terms of experimental data of Flaks and Solov'ev.[30] The cross section is plotted vs ΔE of the charge-exchange reaction *for constant velocity*. The maximum of the curve in Fig. 5.39 is displaced slightly to positive ΔE and does *not* show a double maximum corresponding to $a|\Delta E|/hv = 1$. Reactions in the adiabatic region appear to be very strongly forbidden for large negative values of ΔE but not as strongly forbidden for large positive values of ΔE. In the latter case other final states of excitation may be populated, permitting ΔE to be $\Delta E' = \Delta E - E^*$. Metastable ions in the projectile beam may also introduce bias for some of the negative ΔE values. Figures 5.39 and 5.40 illustrate the very large cross sections which pertain to near-resonance cases when ΔE is positive.

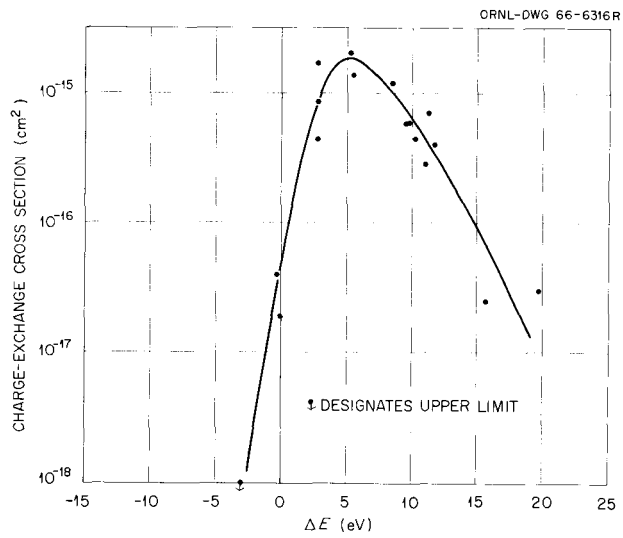

Fig. 5.39. Charge-Exchange Cross Sections σ_{10} and σ_{21} for $v = 3 \times 10^7$ cm/sec vs the Energy Defect, ΔE, for Many Different Ion-Atom Collisions (see ref. 30).

[29] V. I. Rydnik and B. M. Yavorskii, *Bull. Acad. Sci. USSR* 27(8), 981 (1963).

[30] I. P. Flaks and E. S. Solov'ev, *J. Tech. Phys. USSR* 3, 577 (1958).

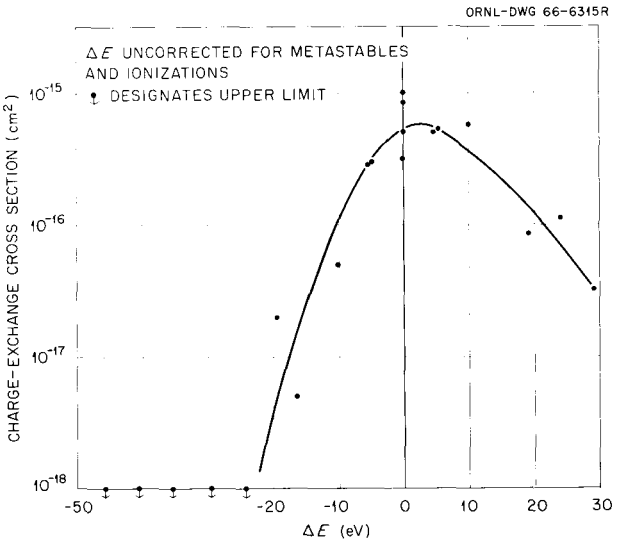

Fig. 5.40. Charge-Exchange Cross Sections for σ_{20} for $v = 3 \times 10^7$ cm/sec vs the Energy Defect, ΔE, for Many Different Ion-Atom Collisions (see ref. 30).

5.8 HIGH-PRESSURE ARC

I. Alexeff
V. J. Meece
C. E. Nielsen[31]
W. Halchin
E. D. Shipley
J. R. McNally, Jr.
W. L. Stirling

We have started an experiment to develop a gas-confined high-density arc. Gas confinement of a plasma was first proposed by Alfven,[32] and Wienecke with co-workers has a strong program in this direction at Garching. More recently, C. E. Nielsen has considered what kind of stationary state might exist in a gas-confined plasma and how this state might be experimentally approached. The proposals envisaged a long cylindrical core of very high-density plasma which is confined by a cold gas. A longitudinal magnetic field is applied only in order to reduce radial conduction losses. Except for radiation, energy will be transmitted primarily longitudinally out the ends.

The first step in developing an exploratory program is to develop sustained kiloampere arcs with electron densities on the order of 10^{16} cm^{-3} for a time sufficiently long to measure electron temperature and radiative energy losses. The complete balance of temperatures and power flow must then be understood in order to evaluate the potentialities of the system.

Figure 5.41 shows an assembly view of the high-pressure arc experimental apparatus. Vacuum pumping is available to operate arcs between 10^{-5} torr and atmospheric pressure. Power supplies are available to run arcs up to 7000 A at 500 V. The solenoidal field can achieve a maximum axial value of 15 kG. The facility is completely assembled, and testing of electrical and gas handling systems has begun.

5.9 BEAM STABILIZATION IN THE CALUTRON

E. D. Shipley
A. M. Veach[33]
J. P. Wood
O. C. Yonts

Briggs and Neil[34] have shown that stabilization of an ion beam against negative-mass instability can be achieved if the net time average magnetic energy of the rf due to the charge perturbation exceeds the electric energy in the region outside the beam. For nonrelativistic ion beams such as those in the calutron, they propose a lumped circuit element system (similar to the slow wave structure used in microwave tubes) which should prevent instability growth.

For the calutron two such boundary walls were constructed, one on each side of the beam. One wall consisted of 50 plates which were series connected by 45-turn, 2-layer coils with a resonant frequency of 1.3 Mc. The other wall contained the same number of plates which were series connected by 27-turn, single-layer coils with a resonant frequency of 6.2 Mc.

In operation, these walls have shown more similarities to the flat conducting plate wall than to the normal parallel-connected Boundary Impedance Network (BIN) wall, which we have used at ORNL in the past. This is shown in Fig. 5.42 in which beam imperfection is plotted against wall-to-wall spacing. Beam imperfection[35] is defined as the

[31]Consultant, Ohio State University.

[32]H. Alfven *et al.*, *Nuclear Fusion:* 1962 Suppl., Pt. 1, pp. 33–38.

[33]Isotopes Division.

[34]R. J. Briggs and V. K. Neil, *Stabilization of Intense Coasting Beams in Particle Accelerators by Means of Inductive Walls*, UCRL-14407 (1965).

[35]E. D. Shipley *et al.*, *Thermonuclear Div. Semiann. Progr. Rept. Oct. 31, 1964*, ORNL-3760, p. 45.

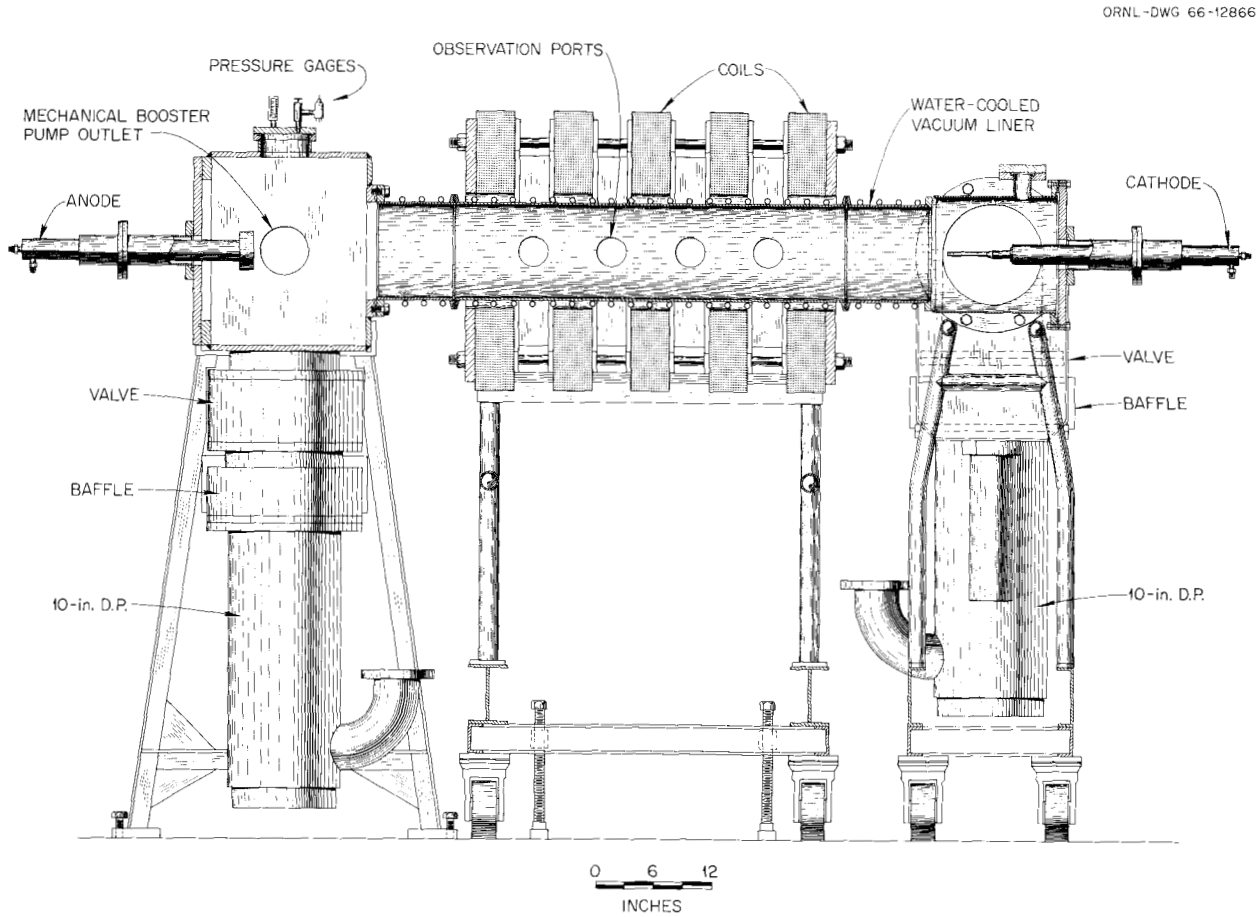

Fig. 5.41. Assembly View of High-Pressure Arc Facility.

ratio of total ion current (of ^{40}Ca in this experiment) at the receiver to that which actually enters an isotope collector pocket. Curve 1 shows results for a parallel coil BIN described previously;[35] curve 2 shows results for a noninductive flat conducting plate. Curves 3 and 4 are for the series coil BIN[36] of which curve 3 shows one of the best curves obtained, and curve 4 shows one of the worst. All the curves shown are in the low-pressure blowup region. Apparently some instability other than the negative mass is responsive to the control that can be imposed by the ORNL BINS in the 180°-focused calutron beams.

[36]The added size of the series coils interfered with the motion of the walls, so that maximum wall-to-wall spacing could not be obtained.

5.10 LEVITATED TOROIDAL QUADRUPOLE

I. Alexeff W. Halchin
M. Roberts

5.10.1 Introduction

A new program investigating some facets of toroidal multipole plasma containment devices has been started in this laboratory. Recent experimental findings at the University of Wisconsin,[37] General Atomic,[38] and the Max-Planck Institute at Munich,[39]

[37]R. A. Dory *et al.*, *Phys. Fluids* 9, 997 (1966).

[38]T. Ohkawa *et al.*, *Plasma Physics and Controlled Nuclear Fusion Research*, vol. II, p. 531, IAEA, Vienna, 1966.

[39]D. Eckhartt, G. von Gierke, and G. Grieger, *Plasma Physics and Controlled Nuclear Fusion Research*, vol. II, p. 719, IAEA, Vienna, 1966.

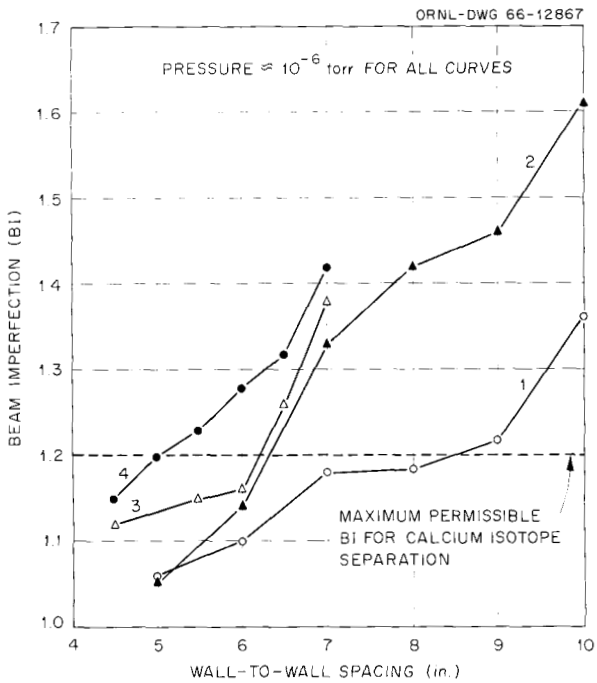

Fig. 5.42. Beam Imperfection vs Wall-to-Wall Spacing Using Different Wall Configurations.

using toroidal octupole plasma machines, have substantiated earlier theoretical predictions[40] of magnetohydrodynamic (MHD) stability in the multipole configuration. In the toroidal multi-($2n$)-pole device, n conducting hoops carry current in the same direction and produce a magnetic field $\overline{B}_{tm} = B_\rho, B_\phi, 0$ (see Fig. 5.43 for definition of coordinates ρ, ϕ, θ) which encompasses the hoops and can be contained completely within a vacuum vessel. The magnitude of the magnetic field between the hoops increases in all directions away from a central zero forming a magnetic well through which pass many flux lines linking one or all hoops. Of those flux lines, Ψ, encircling all the hoops, the ones closer to the hoops than a line designated Ψ_{crit} have sufficiently longer extent within the magnetic well than in the region of decreasing magnetic field adjoining the outer peripheries of the rods and provide MHD stability for plasma guided along the line. Unfortunately, plasma contained in the stability region will necessarily eventually strike any simple mechanical supports holding the conducting hoops in place. In the experiments reported to date,[37–39] all employing simple, mechanical hoop supports, the primary loss mechanism is attributed to interception loss on the hoop supports. The initial emphasis in this toroidal multipole program is eliminating the need for hoop supports (with consequent removal of the prime plasma loss mechanism) by concentrating on magnetic levitation of a two-hoop (quadrupole) system.

The preliminary experimental results described below show three major points: levitation of a quadrupole, production of a moderately high magnetic field strength, and a duration of the magnetic field that is sufficiently long for plasma experiments.

5.10.2 Apparatus

All the experiments were performed with the same basic form of apparatus which was designed both for utilization of available iron cores and for the ease of manufacture. Figure 5.43 shows the plan and cross-sectional views of the copper box and hoops as well as the coordinates and the location of the iron core used to induce currents at 60 Hz in the hoops. Although operation was initially at room temperature, it did become necessary to cool the box to low temperatures, at first by pouring liquid nitrogen through access holes in the top of the box and later by immersing the entire structure in a liquid-nitrogen-filled plastic-foam Dewar. Power was supplied from a large autotransformer for continuous operation, which became limited only by the various effects of heating in the hoops, box, core, and supply.

In addition to straightforward visual and aural observations, diagnostics were performed with multiturn pickup coils with associated sensitive oscilloscope amplifiers to measure dB/dt, and a Hall effect gaussmeter to measure $B(t)$. The coils were attached to the walls to measure both the mechanical oscillation frequency (by amplitude modulation of the induced voltage) and the time decay, or they were used as search coils to measure absolute values of the fields. The gaussmeter probe was similarly used to measure absolute magnitudes and time decay of the magnetic fields.

[40] T. Ohkawa and D. W. Kerst, *Nuovo Cimento* 22, 784 (1961).

ORNL-DWG 66-12868

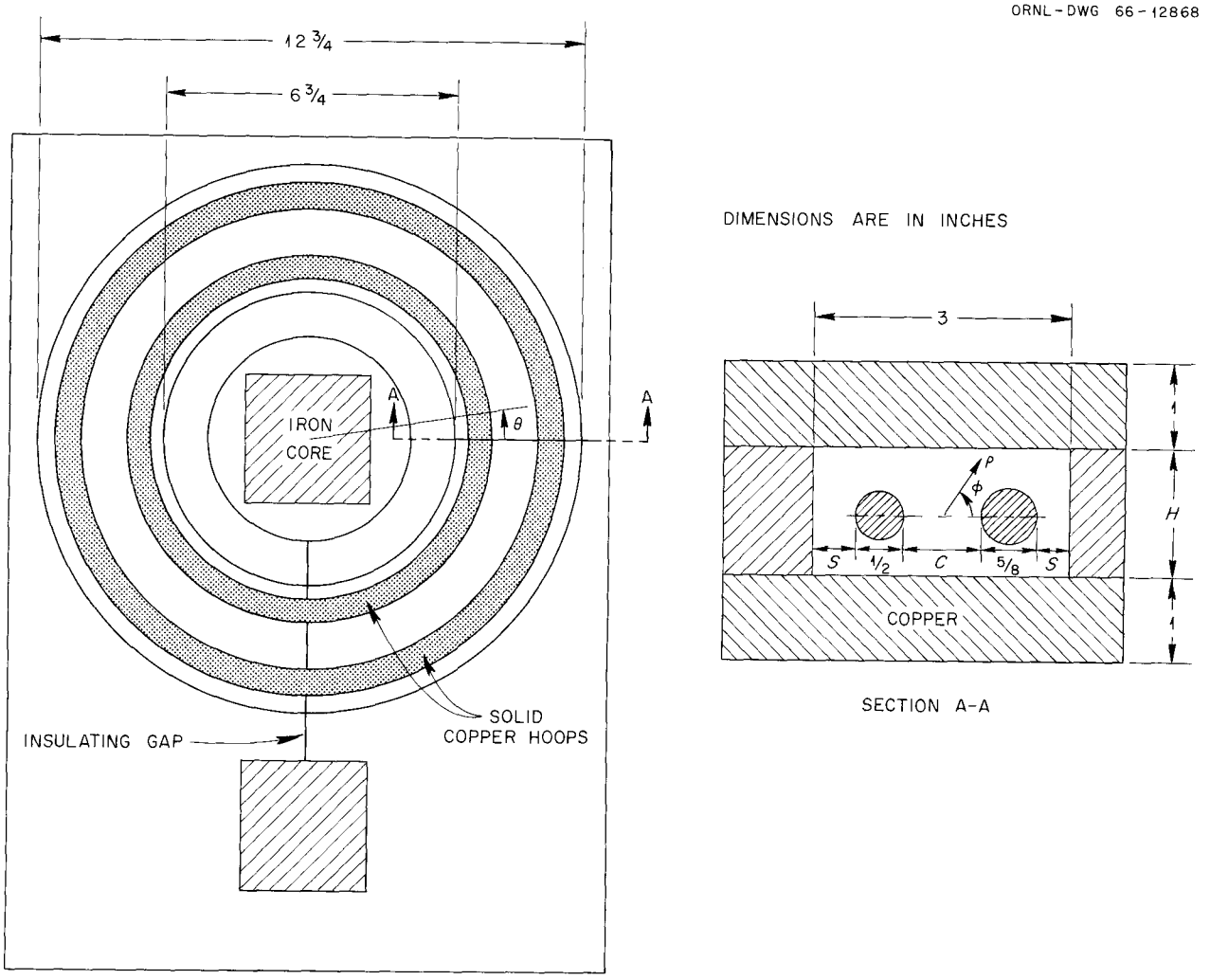

Fig. 5.43. Internal Plan View and Cross Section of Toroidal Quadrupole.

5.10.3 Levitation

Although the electromagnetic levitation of conducting bodies is extensively reported in the literature,[41,42] in all but one case the resultant magnetic field which also performs the levitation is an externally imposed, primary magnetic field. In the case of the Levitron,[43] however, the primary, externally imposed magnetic field is used to induce current in a hoop completely enclosed in a conducting toroidal shell. The resultant self-magnetic field of the internal conductor performs the levitation, and, as such, the experiment differs fundamentally from external field levitation.

Figure 5.44 illustrates the continuous levitation of a single hoop in an open channel of square cross section; this experiment is similar to the early Levitron[43] studies and was performed to gain experience with simple levitation. After being energized from a rest position on the bottom, the single hoop vibrates with a damped oscillation of frequency about 7 Hz and a damping time constant of a few seconds. All later experiments

[41] E. C. Okress *et al.*, *J. Appl. Phys.* **23**, 545, 1413 (1952).

[42] P. Rony, *Trans. Vacuum Met. Conf., 7th, 1964*, American Vacuum Society, Boston, Mass., 55 (1965).

[43] S. A. Colgate and H. P. Furth, *Small-Scale Instabilities of the Pinch and a Suggested Remedy — the Levitron*, UCRL-5392 (1958).

PHOTO 85971

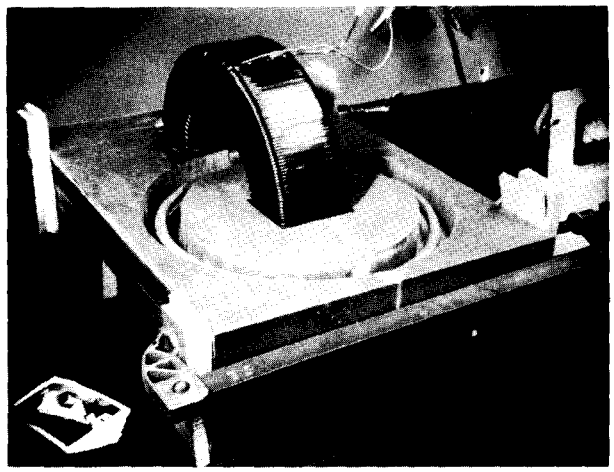

Fig. 5.44. Continuous Levitation of a Single Hoop in the Toroidal Box with Large Inner Piece.

involved two hoops, a channel of rectangular cross section, and a smaller inner radius.

The initial two-ring experiments were performed without the top plate simply to see if the rings would center themselves under two circumstances, namely, when the static friction was overcome and when the quadrupole was barely up off the bottom plate. Table 5.3 gives the various hoop-to-wall spacings S and box heights H used in the two-ring experiments designated 1 through 6.

In experiment 1 the hoops touched as soon as the friction was overcome, and levitation was not achieved. Separating the hoops as far as practical resulted in levitation in experiment 2. Although the spacing from hoop to wall on the side and bottom was too small to be useful, and although the copper box had to be at or below room temperature, the experiment did show that the hoops could be stably centered; that is, the repulsion from the walls was greater than the mutual attraction between the hoops. With the top plate on, the box could become warm and there would still be levitation. In experiment 3, where the hoop-to-wall spacing was doubled, even with the top in place, cooling the box was necessary; the temperature was not measured; liquid nitrogen was simply poured into the box.

Still lower temperatures, probably $\lesssim -100°C$, were required to levitate the hoops in experiment 4, in which the hoop-to-wall spacing S was once again doubled (to $\frac{1}{4}$ in.). The top was in place for experiments 4 and 5, and the hoops could be raised to a level near the center of the box. Without the restoring force and magnetic shielding of the top plate, perturbations in the hoop positions resulted in asymmetric attraction and motion of the hoops out of the box toward the iron core. Strong, low-frequency oscillations built up in tens of seconds, where the time indicates the first striking of a wall by either hoop. The mode of oscillation was primarily a twisting one in which the hoops pivoted about a diameter, eventually striking the top and bottom walls. A second mode observed was a side-to-side motion in which the hoops periodically hit the side walls.

The remainder of the work was done with the dimensions of experiment 5 (the largest hoop-to-wall spacing and smaller box height). At magnetic field strengths $B_{tm} \gtrsim \frac{3}{4}$ kG (measured at the outside of the outer rod), the inner hoop was centered vertically, and the outer, heavier hoop was about 15% below the center; both were centered with respect to the side walls. To obtain horizontal centering, it was necessary to maintain (by immersing the entire device in liquid nitrogen) an equilibrium temperature for the box very nearly equal to that of liquid nitrogen.

A difference between energizing the quadrupole gradually and abruptly is a high-amplitude, low-frequency (<10 Hz) oscillation that damps within a few seconds after an abrupt start. A more important, growing oscillation starts from small displacements and builds up to the maximum excursion pos-

Table 5.3. Hoop-to-Wall Spacing S and Box Height H for Six Different Quadrupole Experiments

Experiment No.	Spacing S (in.)	Height H (in.)
1	$\frac{1}{2}$	$1\frac{1}{2}$
2	$\frac{1}{16}$	$1\frac{1}{2}$
3	$\frac{1}{8}$	$1\frac{1}{2}$
4	$\frac{1}{4}$	$1\frac{1}{2}$
5	$\frac{3}{8}$	$1\frac{1}{2}$
6	$\frac{3}{8}$	1

sible in tens of seconds at the low fields ($B_{tm} \sim 0.5$ kG) and in a second or less at high fields ($B_{tm} \sim 2$ kG). This growing oscillation, which is nearly damped when the hoops are immersed in liquid nitrogen (apparently by the mere presence of the liquid), appears to be associated with the nonlinear properties of the core near saturation which couples the changing inductance of the vibrating hoops to the series resonant circuit described in the next section.

5.10.4 Magnetic Field Strength

The ultimate magnetic field strength in the present system is determined by the saturation value of flux in the core and the impedance of the quadrupole. Applying the autotransformer voltage directly to the coil can result in maximum field strength but at the expense of excessive current drain. This current drain can be reduced a factor of 2 by using a series resonant capacitor to provide the reactive power needed to create the magnetic field. The circuit then presents a lower, resistive impedance to the supply, requiring a lower voltage at the saturation current and consequently lower total power from the supply. Nearly 900 μF capacity in series with the coil reduced the power consumption to produce a $B_{tm} \sim 2$ kG from 14 kVa to 7 kW; field strengths near the inside of the inner rod are about $1\frac{1}{2}$ times larger than at the outer rod for two reasons: the toroidal distortion and the difference in diameters of the two hoops.

5.10.5 Extended Field Lifetimes

Since the quadrupole is energized at 60 Hz and its natural frequency appears to be an order of magnitude lower, the rings remain levitated with a low-frequency fluctuation. The magnetic field, however, is varying at 60 Hz and is relatively constant only for two periods of less than 4 msec in each cycle. Longer periods over which the field is relatively constant can be obtained by forcing the energy stored in the magnetic field to be dissipated through the hoop resistance rather than to be transferred to the capacitance. This clamping of the primary coil or crowbarring of the magnetic field was done by closing a mercury relay across the coil. The shorting of the contacts is somewhat random with respect to the 60-Hz field, and a few tries were needed to obtain a clamping at maximum field. Figure 5.45 shows, on two time scales, the output of a gaussmeter probe inserted in a Pyrex tube placed in the liquid nitrogen next to the outer hoop. The time constant for the decay of the field (about $1\frac{1}{2}$ kG) is measured to be about 18 msec in the upper picture. The hoops are held up in place by the magnetic pressure for about the first e-folding time. A calculation of L/R for a coaxial inductor of the same dimensions and with a skin-depth resistance at the inner rod results in a time constant of about 10 msec.

5.10.6 Discussion

The straightforward levitation of two coplanar hoops in the small-scale apparatus appears to be complicated by two things: the need for liquid-nitrogen cooling and the strong, growing oscillations. Cooling is required to increase the repulsive wall forces sufficiently to overcome the attractive forces between the hoops. This is done by reducing the skin depth a factor of $\sqrt{10}$ below its room temperature value, thus decreasing the

PHOTO 85972

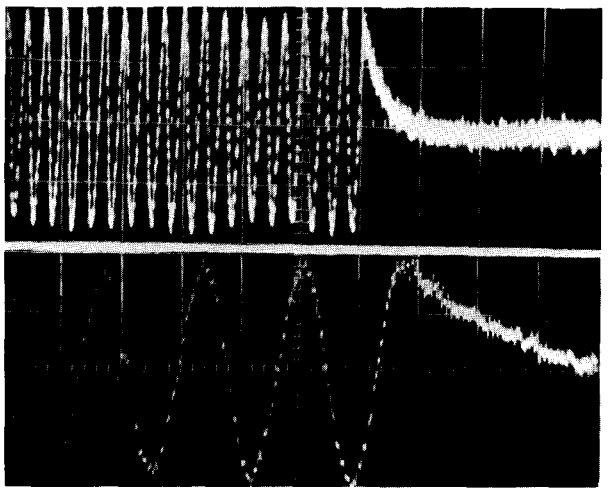

Fig. 5.45. Magnetic Field Strength Near Outer Hoop Showing the Effect of Clamping the Coil at the Peak of a 60-Hz Oscillation. Upper picture – 50 msec/cm, low-frequency variations (<60 Hz) indicate hoop vibrations; lower picture – 10 msec/cm, high-frequency oscillations (>60 Hz) are from gaussmeter measuring circuit.

separation between the hoop and its hypothetical image in the wall. (The resistivity of copper at the temperature of liquid nitrogen is one-tenth the value for copper at room temperature and is the lowest of any common conducting material.) Since the resistance is also reduced by a factor of $\sqrt{10}$, the time-average force is increased, and the quadrupole impedance is reduced and made more inductive. Cooling of the hoops also results in a larger L/R time constant for the field decay. So, although the reduction of the skin depth would no longer be necessary for larger scale sizes, the other two functions performed by cooling are necessary.

The two types of growing oscillations, side to side and up and down, exist because of the nonlinearity in the system (the saturated core) and because of the weak restraining forces. Since all the available area for an iron core in the present model is not used (only one-third of the area is filled with iron), operation at the same field strength, but filling most of the possible area with iron, should result in a more nearly linear circuit and a longer time constant for the growing oscillation. As the inner hoop is lighter and smaller in diameter than the outer hoop, shaping the internal cross section of the box to fit equidistantly around both hoops should also help to reduce the oscillation buildup. In fact, since the field is stronger at the inner hoop than at the outer hoop, the hoop-to-wall spacing can be smaller yet keep the same number of gyroradii and increase the repulsive force. Experiments on the present scale are planned to test plasma confinement with the levitated quadrupole using room-temperature ions having dozens of gyroradii between hoop and wall in the 2-kG field.

5.10.7 Summary

Levitation has been shown to be feasible for supporting a toroidal quadrupole under certain conditions. At the higher field strengths required for plasma confinement, the stability of this quadrupole is drastically reduced but, on the time scale of a plasma experiment, is still usable. Field strengths using a series resonant capacitor and only one-third the available core area are nearly 2 kG at the outer hoop and about 3 kG at the inner rod. Crowbarring of the magnetic field at its peak value results in a relatively constant field lasting 8 msec.

6. Atomic and Molecular Cross Sections

C. F. Barnett
W. E. Hunt[1]
M. O. Krause
R. A. Langley
M. Y. Nakai[2]
J. A. Ray
A. Russek[3]
L. H. Toburen[4]

6.1 RYDBERG STATES OF HYDROGEN MOLECULES

Previous reports have discussed the measurements of excited electronic states of energetic H_2 formed by electron transfer collisions in a gas cell. These excited states have been described as consisting of an ionic core with a single electron removed sufficiently far from the core such that it moves in the field of a unit charge. Thus there should exist a series of Rydberg states with energies $E_n \cong 1/n^2$ Ry, when n is large. This outer electron "sees" a small core whose principal effect is to produce a $-e^2/r$ potential that binds it to the core. Since the core is not simply a point charge, it will, in general, generate higher multipole potentials as well. These will have the effect of perturbing the energy levels from an exact $1/n^2$ sequence, much as an ordinary nucleus that has a magnetic moment and a quadrupole moment will shift the energy levels of the corresponding atom into the various hyperfine levels.

To further push the analogy of the molecular ion core with an atomic nucleus, it may be noted that a process called internal conversion has been well documented in nuclear physics. A nucleus in an excited state can revert to the ground state by the emission of a gamma ray. However, in a small percentage of the cases the excited nucleus interacts directly with one of the atomic electrons (usually a 1s electron), gives up its excitation energy to that electron, and reverts to a lower state. The electron which has received this energy is ejected with a characteristic energy.

Similarly, in a Rydberg state of a diatomic molecule the ion core, which serves as a nucleus, can also be excited. It can be in any one of the vibrational-rotational states characteristic of that molecular ion. When energetically allowed, the ion core can give up some, or all, of its energy to the outer electron, thus reverting to a lower vibrational-rotational state. The outer electron would then be ejected with a characteristic energy of the difference in vibrational-rotational energy of the core minus the original binding energy of the outer electron. This autoionization process has recently been observed by Cook and Metzger[5] in which an H_2 molecule in the $X\ ^1\Sigma_g$ ($\nu = 1$) state absorbs a photon, exciting it to the H_2 $D'\pi_g$ ($\nu = 7$) state which undergoes a spontaneous transition to the $H_2^+\ 1s\sigma_g$ ($\nu = 1$) state.

In considering the analogies between an atomic nucleus and the ion core of a Rydberg state of a diatomic molecule, two differences must be noted. First, the energy levels of a nucleus are considerably greater than those of the orbital electron. Thus in the nucleus, internal conversion is always energetically favorable. The vibrational-rotational states of a molecular ion are low compared with electronic binding energies in general. Thus the

[1]Summer employee, David Lipscomb College.

[2]Health Physics Division.

[3]Summer employee, University of Connecticut.

[4]ORAU Fellow, Health Physics Division.

[5]G. R. Cook and P. H. Metzger, *J. Opt. Soc. Am.* **54**, 968 (1964).

process analogous to internal conversion is not always energetically allowed. Second, the size of the ion core relative to the radius of the outer electron is approximately $2a_0/n^2a_0$, which is generally much larger than the ratio of the radius of the nucleus to that of the 1s electron: 5×10^{-13} cm/ 0.5×10^{-8} cm/Z. Thus the molecular analog to internal conversion is far more likely when the process is energetically allowed than with the true internal conversion process.

This problem has been formulated mathematically by determining the energy shifts in the electronic levels from the predicted Rydberg levels, and also determining the autoionization transition rates. The main force that acts on a highly excited electron in a diatomic molecule is the Coulomb force due to the residual unit charge of the ion core whose motion is virtually undisturbed by the slow-moving outer electron. A graphical representation is shown in Fig. 6.1. The angle γ is the angle between the electron radius vector r and the internuclear separation R. The origin of the electron coordinate r is taken to be the center of mass of the ion core, since the electron mass can be neglected when compared with that of the ion core and, therefore, has a negligible effect on the overall center of mass.

The approximate Hamiltonian for the system is

$$H(r,R) = H_c(R) + H_e(r) + V(R,r) . \qquad (1)$$

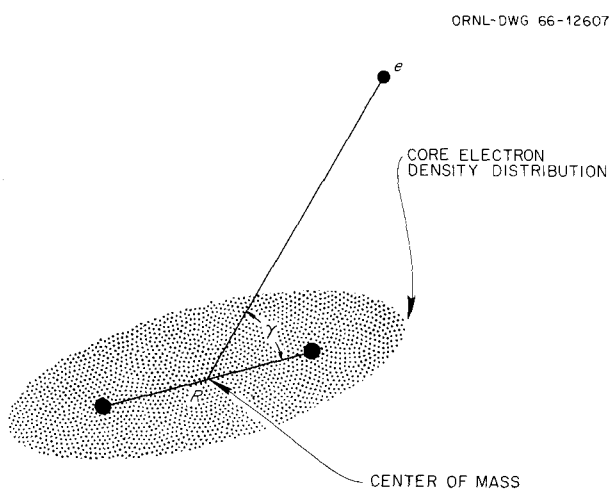

Fig. 6.1. Schematic Illustration of the Hydrogen Molecule with Its Excited Electron Located at Position r. The core consists of two positive charges, the nuclei, and is surrounded by an electron cloud.

Here $H_c(R)$ is the core Hamiltonian in the Born-Oppenheimer approximation,

$$H_c(R) = \frac{P^2}{\mu} + \frac{Z_1 Z_2 e^2}{R} + E_e(R) , \qquad (2)$$

and $E_e(R)$ is the total electronic energy of the core in the Born-Oppenheimer approximation. $H_e(r)$ is

$$H_e(r) = \frac{p^2}{2m} - \frac{e^2}{r}, \qquad (3)$$

and $V(r)$ is given by the expression

$$V(R,r) \cong -\frac{D(R)}{r^2}\cos\gamma - \frac{Q(R)}{r^3}\cos^2\gamma - 1$$

$$\text{for } r \gg R . \qquad (4)$$

The quantities $D(R)$ and $Q(R)$ are, respectively, the core electric dipole moment and electric quadrupole moment calculated in the Born-Oppenheimer approximation when the instantaneous nuclear separation is R. In this formulation the monopole term in the potential produced by the core has been incorporated into the electron Hamiltonian, since it is independent of the nuclear separation R and since the solutions of Eq. (3) are well known. The remaining multipole terms in the potential produced by the core are considered to constitute the perturbation term in the Hamiltonian which shifts the energy levels slightly and is responsible for the autoionization transition in which energy is transferred from the core to the outer electron.

It is to be noted that the core electron is taken into account only through its effect on the core vibrational and rotational motion in the Born-Oppenheimer approximation. The electronic structure of the core is treated as being entirely uncoupled from the outer electron. This treatment is justified on the basis that the outer electron moves very slowly compared with an electron in the core and, therefore, "sees" only the average charge distribution created by the core electronic structure. The lowest-order interaction of the outer electron with the core electronic structure would be via the polarization potential which falls off as r^{-4} and is here being neglected. Also, it must be stressed that the interaction term defined

by Eq. (4) is valid for large r only. When $r \lesssim R$, the outer electron is penetrating the core, and the interaction V does not become singular. If $r < R$, then the results must be corrected for this "penetration" effect.

From Eq. (1) one notes that the total Hamiltonian is composed of the unperturbed Hamiltonian ($H_0 = H_c + H_e$) and V, where V is given by Eq. (4). The unperturbed Hamiltonian consists of the two decoupled terms, so that an eigenfunction of H_0 is simply a product of an eigenfunction of H_c and H_e, each of which can be written as a product of a radial times an angular factor as shown in the following equation:

$$\Psi\nu\lambda\mu nlm(R,r) = F_\nu(R)G_\lambda^\mu(\Theta,\Phi)R_{nl}(r)Y_l^m(\theta,\phi) \ . \quad (5)$$

This wave function describes a state of H_0 where the ion core is in the νth vibrational state and λth rotational state with projection μ on the z axis, while the electron is in the nth Rydberg level with angular momentum l and projection m. The unperturbed energy associated with this state is

$$E^0_{\nu\lambda\mu} = \epsilon_\nu + \frac{\hbar^2}{2I}\lambda(\lambda+1) - \frac{\mathrm{Ry}}{n^2} \ , \quad (6)$$

where ϵ_ν is the vibrational energy of the core and I is its moment of inertia. This level is degenerate with respect to the azimuthal quantum numbers μ and m. Consequently, the actual states for which total angular momentum J with projection M on the z axis are constants of the motion will be linear combinations of these degenerate levels, the coefficients being the well-known Clebsch-Gordan coefficients. The first-order correction to the energy levels given by Eq. (6) is

$$\Delta E = -\langle F_\nu|D(R)|F_\nu\rangle \langle R_{nl}\left|\frac{1}{r^2}\right|R_{nl}\rangle \sum_{m\mu m'\mu'} C^{\mu m}_{\lambda l;JM} C^{\mu' m'}_{\lambda l;JM}$$

$$\times \langle G_\lambda^\mu Y_l^m|P_1(\cos\gamma)|G_\lambda^{\mu'} Y_l^{m'} - \langle F_\nu|Q(R)|F_\nu\rangle$$

$$\times \langle R_{nl}\left|\frac{1}{r^3}\right|R_{nl} \sum_{\mu m\mu' m'} C^{\mu m}_{\lambda l;JM} C^{\mu' m'}_{\lambda l;JM}$$

$$\times \langle G_\lambda^\mu Y_l^m|P_2(\cos\gamma)|G_\lambda^{\mu'} Y_l^{m'}\rangle \ . \quad (7)$$

The autoionization transition rate per unit time w is given by

$$w = \frac{2\pi}{\hbar^2}\,|\langle\Psi_{\nu\lambda nlJM}|V|\Psi_{\nu'\lambda' k' JM}\rangle|^2 \ .$$

This matrix element is identical to the expression for ΔE with added changes of indices k' and l'. The problem then is to solve these equations for ΔE and W using exact wave functions for the vibrational, rotational, and electronic levels for both H_2 and H_2^+. This long tedious task is being solved, and results are expected in the near future.

Two predictions can be made using the model of Rydberg states for molecules. First, any molecule that has a stable ionic core should exist in these states. Following H_2 the next simplest molecule is that of H_3, which is known to be unstable in the ground electronic state. In the previous progress report we discussed the measured relative population of the high n states for H_3. From the preceding theoretical discussion a prediction can be made that an excited molecule possessing a dipole moment would decay by autoionization faster than those with only a quadrupole moment. Previous results indicated a discrepancy in the measured excited-state population of H^0 and H_2, whereas one would expect the population to be identical for the Rydberg states. The lower population found for H_2 could result from autoionizing transitions occurring in the flight path between the point of creation of excited neutrals and the point of measurement, namely, the electric field ionizer. For the homonuclear case, H_2, this transition would be by a quadrupole interaction; however, HD with a dipole moment should have a faster transition rate. Thus the measured population of HD should be less than that of H_2. Results are

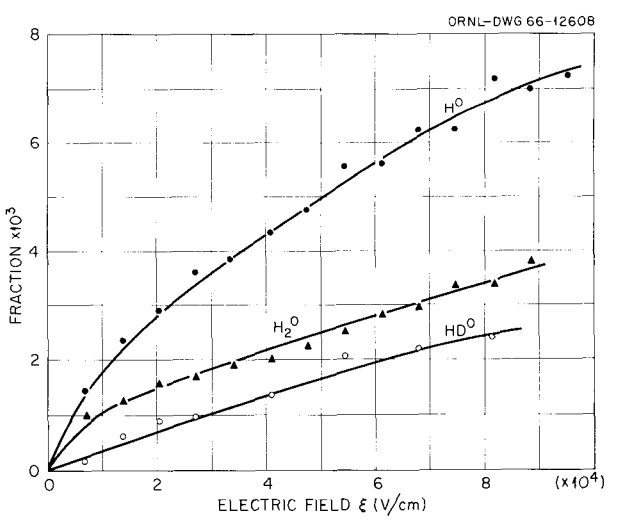

Fig. 6.2. Fraction of Particles in Excited States of H, H_2, and HD as a Function of the Applied Field.

shown in Fig. 6.2, where the fraction ionized is plotted as a function of the applied electric field. Shown also for comparison are the results for both H^0 and H_2, where all the particles are of equal velocity. As predicted, the fraction of HD in excited states was less than that for H_2. These measurements would then indicate that autoionizing transitions with lifetimes smaller than the transit time (10^{-7} sec) are depleting the high n states of the molecule. The present studies must be completed in more detail by investigating competing processes, that is, velocity effects and contamination of HD beams with H_3. Upon completion of the calculations for the autoionization lifetimes, attempts will be made to determine experimentally the lifetimes by measuring the attenuation of the excited-state fraction as a function of the distance between the gas cell and electric field ionizer.

6.2 SECONDARY ELECTRON STUDIES

6.2.1 Statistics of Secondary Electron Emission

In the previous semiannual progress report we discussed the detailed study of using secondary electron emission from metallic surfaces to measure, quantitatively, the flux of energetic neutral particles incident on the surface. Using this technique, the target was negatively biased in order to postaccelerate electrons to 15–20 keV, where they are counted by a high-resolution silicon barrier detector. The pulse-height distribution from the barrier detector was a spectrum composed of many resolvable peaks. The peaks arose when the neutral particle or ion impinged on the target, which emitted n secondary electrons with a certain probability of emission P_n. When more than one electron was emitted for a single incident particle, then the electrons arrived at the detector in coincidence, resulting in a peak equivalent in energy to n times the bias voltage on the target. Integration under each peak then gave the measured frequency of emitting n electrons. Comparisons were then made of the measured statistical frequencies with expected frequencies for various statistical distributions. In the past, several investigators evaluating electron devices, in particular electron multipliers, have assumed that the true distribution is Poisson; that is,

$$P_n = e^{-\gamma}\gamma^n/n! \,, \tag{8}$$

where γ is the average secondary emission coefficient. This distribution has been justified on the premise that the probability of one or more electrons being emitted is not influenced by other electrons being emitted, that is, completely independent and random in nature. Barrington and Anderson[6] were the first to investigate the statistics of secondary emission, and they concluded that a Poisson distribution did not give a good fit to the data and that the probability for groups of even electron emission was greater than that for groups with an odd number of electrons. During the past few years several investigations[7] have also substantiated the previous conclusion that secondary emission does not fit the Poisson distribution law. Analysis of our data presented in the previous semiannual report also verified this viewpoint. Since other similar physical processes have been found to follow some statistical distribution, such as beta decay being described by a binominal distribution, then it is expected that some distribution should fit the secondary emission process. Comparison of our data to several expected discrete distribution functions yielded extremely bad fits. Inquiring further into sources of experimental error revealed that our detector was not intercepting all the electrons. Therefore the 50-mm^2 active-area silicon detector was replaced by a 200-mm^2 detector. Various tests indicated 100% collection with this large detector.

A typical pulse-height spectrum obtained with this larger detector is shown in Fig. 6.3. In this example 40-keV H^0 particles were incident on an AgMg target at an angle of incidence of 45°. The spectrum was produced by accelerating the secondary electrons to 20 keV. Sufficient data are present to obtain knowledge of P_n for $n = 0,1,\ldots, 8$. What is not known is P_0, the probability for an incident particle producing zero secondaries; P_0 was obtained by inserting a second silicon detector in front of the target to measure the incoming particle

[6] R. E. Barrington and J. M. Anderson, *Proc. Phys. Soc.* **72**, 717 (1958).

[7] P. Häussler, *Z. Physik* **179**, 276 (1964); C. F. G. Delaney and P. W. Walton, *IEEE, Trans. Nucl. Sci. NS-13*, 742 (1966); K. H. Simon, M. Herrmann, and P. Schackert, *Z. Physik* **184**, 347 (1965).

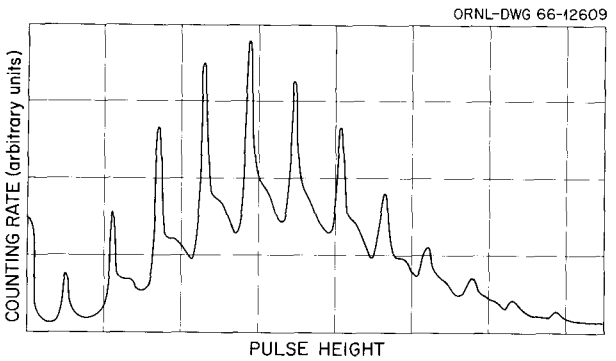

Fig. 6.3. Pulse-Height Spectrum of Secondary Electrons Resulting from 40-keV H^0 Striking an AgMg Target at a 45° Angle of Incidence.

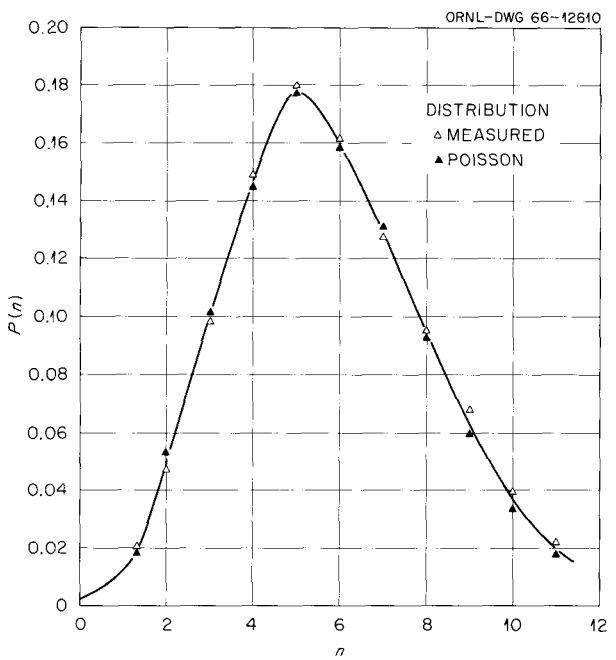

Fig. 6.4. Comparison of the Measured Secondary Electron Distribution with the Expected Poisson Distribution.

flux. Swinging the detector to one side then permitted the secondary electrons from the target to be measured. The ratio of the counting rate of the incoming particles to the counting rate of the secondary electrons gave, directly, the quantity $(1 - P_0)$. Determining P_0 in this manner was valid only for H^0 energies greater than 10 keV, for then the pulse-height spectrum for H^0 was clearly resolvable from crystal and electronic noise. For all energies greater than 10 keV, P_0 was determined to be 0 ± 0.02, with the error being assigned as the repeatability of the measurements.

Table 6.1. Poisson Distribution Compared to Measured Distribution for 40-keV H^0 on an AgMg Target

n	Observed Frequency	Expected Frequency	Deviation (δ)	Divergence (χ^2)
1	34	32	−2	0.12
2	80	89	+9	0.91
3	166	169	+3	0.05
4	249	243	−6	0.15
5	284	280	−4	0.06
6	270	268	−2	0.01
7	214	219	+5	0.11
8	159	157	−2	0.03
9	115	101	−14	2.53
10	67	57	−10	1.75
11	37	30	−7	1.63
				$\Sigma\chi^2 = 7.35$

Knowing P_0 to be zero, then the next step is to determine γ from the relationship

$$\gamma = \sum_n f_n n \Big/ \sum_n f_n \,, \tag{9}$$

where f_n is the observed frequency of group n or the integral number of pulses in group n. Using this measured value of γ the Poisson distribution is readily calculable. Comparison of this Poisson distribution to the observed frequency is shown in Fig. 6.4, in which the probability is plotted as a function of n. As is seen, the agreement of the data and the expected Poisson distribution is very good.

Frequently in statistics it is desired to test mathematically whether measured data are, or are not, consistent with a postulated distribution, whatever its form. One of the most versatile tests is the so-called chi-squared test of significance, which is discussed in most statistical textbooks or handbooks.[8] An example of the application of this test to our data is shown in Table 6.1. In column 1 the number of electrons emitted in group n are tabulated. Column 2 is the observed

[8] R. S. Burington and D. C. May, Jr., *Handbook of Probability and Statistics with Tables*, Handbook Publishers, Sandusky, Ohio, 1958.

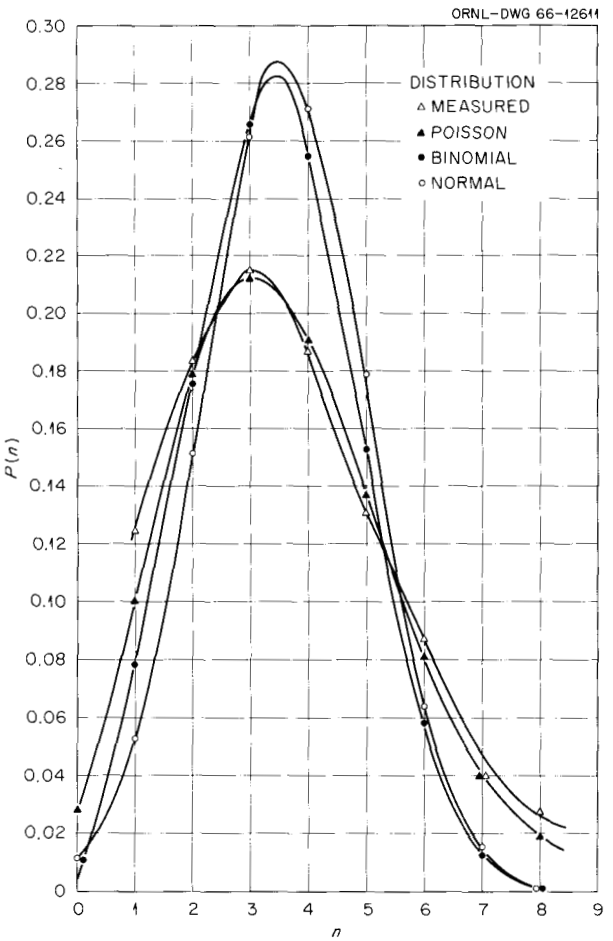

Fig. 6.5. Comparison of the Measured, Poisson, Normal, and Binominal Distributions for Secondary Electrons Emitted from AgMg by 5-keV Protons.

frequency taken from the integrated area of the peaks in Fig. 6.3. Column 3 is the expected frequency found by using the measured γ and assuming a Poisson distribution. Column 4 is the deviation, δ, which is the difference between expected and observed frequency, and finally, column 5 is the divergence, χ^2, which is the deviation squared divided by the expected value. Next we sum all the χ^2's and go to statistical tables to find what probability the assumed distribution has of being the correct one. For the data presented here the probability is 0.6. Usually if this probability is greater than 0.01, then it is concluded that the assumed distribution is plausible and probably the correct one. Applying the chi-squared test of significance to 25 spectra obtained at various energies and surface conditions resulted in 18 of the spectra fitting a Poisson distribution with a high degree of confidence. The remaining seven spectra could be fitted if only one or two values of n were ignored. These n values were usually $n = 1$ or the maximum n. In some of the cases, crystal and electronic noise obscured the true frequency distribution when $n = 1$. For large n the errors associated with integrating the area under the curves are large. In applying the chi-squared test no allowance is made for systematic errors found in the measurements.

In Fig. 6.5 comparison is made for three expected discrete distributions with the measured distribution for 5-keV H^+ incident on an AgMg target. Shown in Fig. 6.5 are expected frequencies if one assumes a Poisson, binominal, or normal distribution.[8] Both the binominal and normal distribution deviate widely from the measured distribution. From these measurements we have concluded that the probability distribution of secondary electron emission from heavy-particle impact on metallic surfaces is a characteristic Poisson distribution.

6.2.2 Secondary Electron Emission Coefficients

Using the method described in the previous section, the average secondary electron emission coefficient as a function of incident particle energy has been determined for a number of different conditions. Shown in Fig. 6.6 are the results obtained with H^0 on AgMg surfaces at angles of incidence of 45 and 30°, and N^0 on AgMg surfaces and H^0 on copper at 30° incidence. As is well known, the smaller the angle of incidence, the greater the secondary emission coefficient. For energies between 1 and 10 keV the coefficient is greater for N^0 impact than for H^0 with identical surfaces and angles of incidence. Below 1 keV the coefficient is less for N^0 than for H^0, which probably emphasizes the importance of surface conditions at low impact energies. No effort has been made to clean the target surfaces under vacuum.

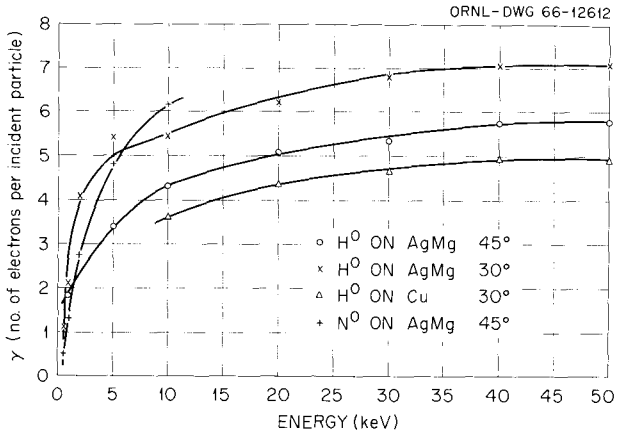

Fig. 6.6. Secondary Electron Emission Coefficients as a Function of Particle Energy for H^0 and N^0 on Cu and AgMg.

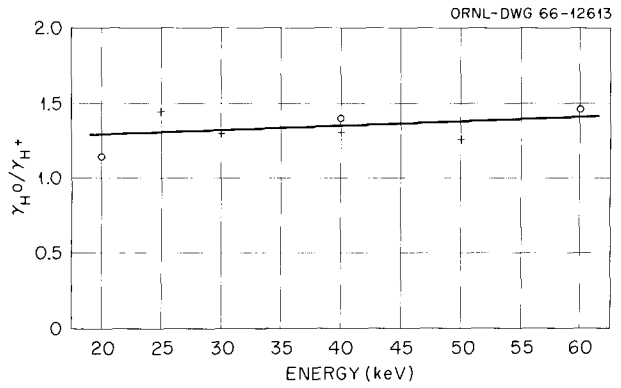

Fig. 6.7. Ratio of Secondary Electron Emission Coefficients for H^0 to that for H^+.

Several years ago, measurements were made at Oak Ridge National Laboratory[9] that indicated that the secondary emission coefficient of H^0 was greater than for H^+. These results have been used extensively through the years to correct secondary electron detectors for enhanced yield from H^0. In Fig. 6.7 the results are shown where this correction has been redetermined using present counting techniques. Previous results were obtained using thermal detectors, brass targets, and a 90° incident beam. The results shown were obtained with an AgMg target at an angle of incidence of 45°. The magnitude of the present results is essentially the same as that of the previous results. Previously it was noted that the ratio increased slightly with energy in the range 10 to 50 keV, while the present results indicate a slight decrease as the energy increased. Apparently this ratio of neutral-atom-to-ion secondary emission is independent of surfaces and the angle of incidence.

6.2.3 Secondary Emission for Single Crystals

Measurements in other laboratories[10] indicate that the average secondary electron emission coefficient for single crystals exhibits structure as the target is rotated about a crystal axis. Minima were detected when the beam was aligned along a crystalline plane, which corresponded to orientations of maximum crystalline transparency. Conversely, the maxima occurred for positions of maximum opacity or where the collision depth is nearest the surface. We have measured the statistical distribution of electrons from copper crystals to determine the feasibility of studying crystalline structure using these techniques. The results of measuring the average secondary emission coefficient for a single copper crystal are shown in Fig. 6.8. Shown are two curves: one for polycrystalline copper and the other for the single copper crystal. The 321 plane of the single copper crystal was oriented perpendicular to the surface, and rotation was about the 110 plane. Consistently, the average secondary emission coefficient of the single crystal was approximately 30% greater than that for the polycrystalline copper. The statistical distribution of the electrons from single crystals was indistinguishable from the polycrystalline target except for greater average coefficient γ. Failure to see maxima and minima probably results from being unable to adjust the crystal orientation in more than one direction or from gas absorbed on the surface obscuring the crystalline structure. To provide complete alignment of the beam with the crystalline planes, the crystal must be capable of being rotated externally in three directions while the data are being taken. Provisions are now being made to mount the crystal and the silicon detector on a goniometer-type mount for improved alignment.

[9] P. M. Stier, C. F. Barnett, and G. E. Evans, *Phys. Rev.* **96**, 973 (1954).

[10] V. A. Kulividze, E. S. Mashkova, and V. A. Molchanov, *Bull. Acad. Sci. USSR* **28**, 1318 (1965); B. Fagot, N. Colombie, C. Fert, *Comp. Rend.* **258**, 4670 (1964); B. Fagot *et al.*, *Comp. Rend.* **262B**, 173 (1966).

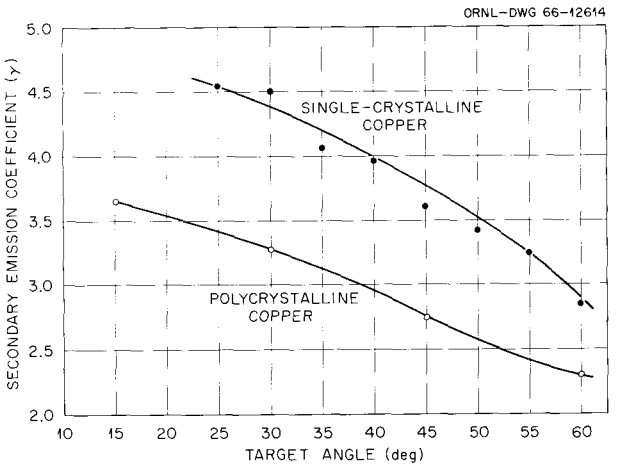

Fig. 6.8. Secondary Electron Emission Coefficients for H^0 on Polycrystalline Copper and Single-Crystal Copper.

6.2.4 Development of a Quantitative Secondary Emission Detector

As noted in the previous semiannual report, techniques of detecting secondary electrons provided a convenient means of measuring the flux of low-energy neutrals escaping a plasma. At the time of that report, nothing was known about the quantitative behavior of the instrument. As described in Sect. 6.2.1, direct measurements indicate that neutral particles in the energy range 10 to 50 keV are essentially 100% efficient in producing secondaries; that is, for every incident neutral particle one or more secondary electrons are emitted. With this information we have shown above that the statistics obey a characteristic Poisson distribution. The assumption is then made that if secondary electrons are described by a Poisson distribution in the energy range 10 to 50 keV, then they will similarly be described for energies less than 10 keV. To obtain the absolute efficiency of low-energy particles, the spectra were obtained as described above, with Fig. 6.9 being a typical spectrum. Shown here is the spectrum obtained from a 500-eV H^0 beam incident on an AgMg surface at a 30° angle of incidence. To determine γ, use is made of the Poisson distribution [Eq. (8)], where ratios are taken of different n frequencies. For example,

$$\frac{P(n-1)}{P(n)} = \frac{\gamma}{n-1} \text{ , or } \frac{P(3)}{P(2)} = \frac{\gamma}{2} \text{ .} \qquad (10)$$

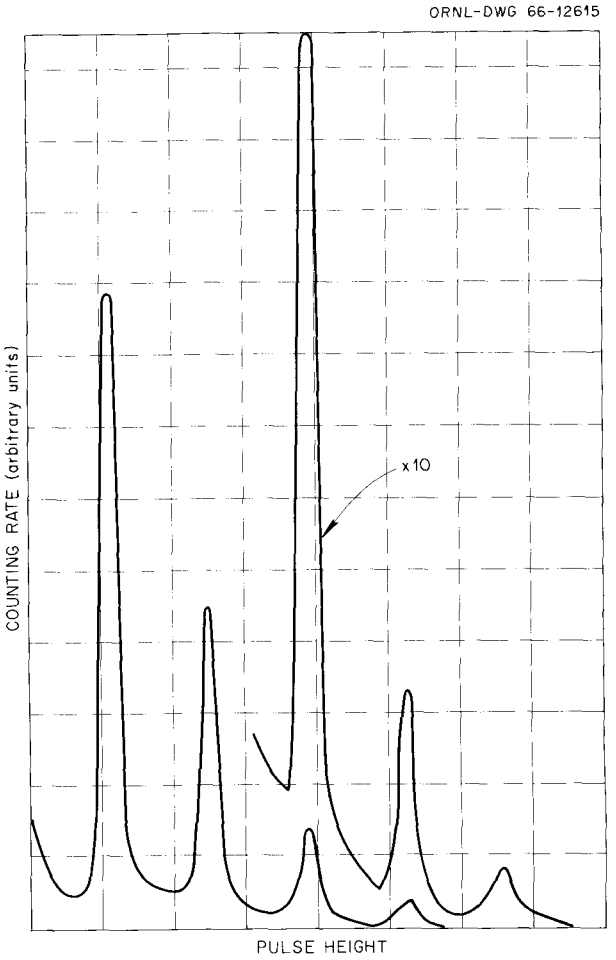

Fig. 6.9. Pulse-Height Spectrum of Secondary Electrons Resulting from 500-eV H^0 on an AgMg Target at an Angle of Incidence of 30°.

In this way a large number of γ's can be obtained with the average value being taken as the correct value to describe the distribution. Then P_0 is simply $e^{-\gamma}$, or the efficiency of the detector is $1 - e^{-\gamma}$. The close comparison of the Poisson distribution and the measured distribution is illustrated in Fig. 6.10 for 500-eV H^0 on AgMg for the spectrum shown in Fig. 6.9. The efficiency of a typical AgMg detector is shown in Fig. 6.11, where the efficiency is plotted as a function of the incident neutral-particle energy. The efficiency increases from 77% at 500 eV to 100% at an energy approximately equal to 2 keV. This minimum energy for 100% efficiency can be decreased by providing for a higher average secondary emission coefficient γ, which can be accomplished by either increasing the surface activation or decreasing the angle of incidence.

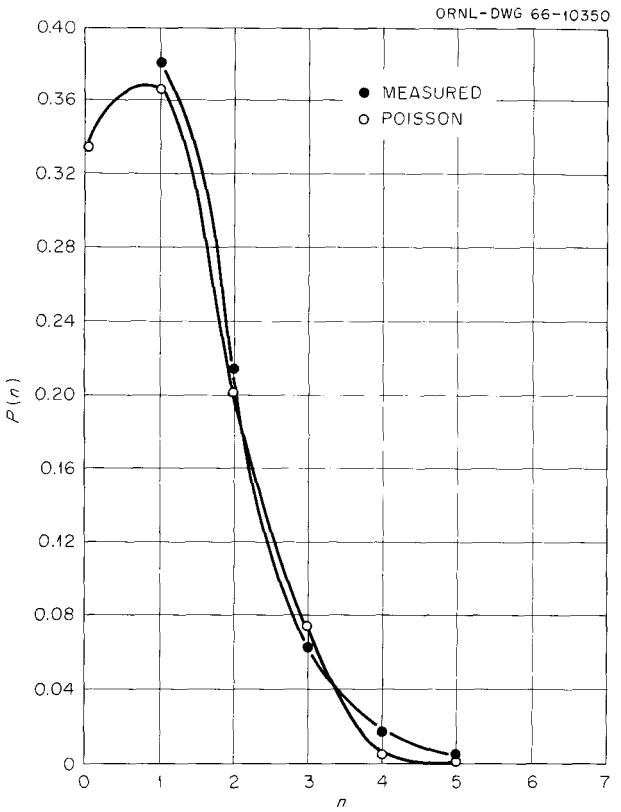

Fig. 6.10. Comparison of the Measured Secondary Electron Distribution with the Expected Poisson Distribution.

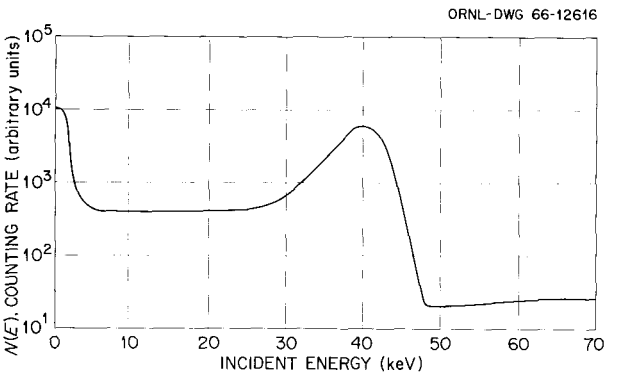

Fig. 6.12. Semilogarithmic Plot of the Pulse-Height Spectrum for 40-keV Electrons Measured with a Silicon Barrier Detector.

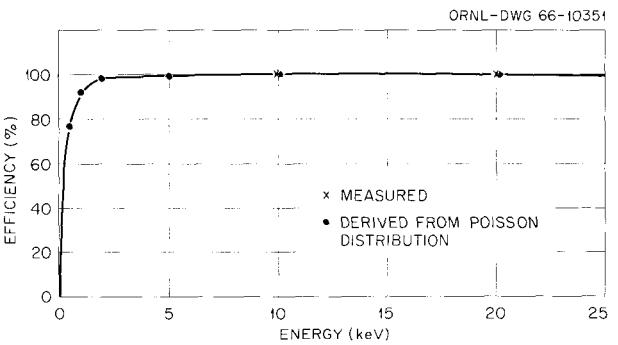

Fig. 6.11. Efficiency of Detecting H^0 with an AgMg Secondary Electron-Emission Detector in the Energy Range 500 eV to 50 keV.

6.3 REFLECTION OF ELECTRONS AND NEUTRAL ATOMIC HYDROGEN FROM A GOLD-BARRIER SILICON DETECTOR

Reflection of electrons and neutral atomic hydrogen from a gold-barrier silicon detector has been studied by observing the pulse-height energy spectrum produced in the silicon crystal by electrons and H^0. A typical semilogarithmic plot of the pulse-height spectrum of 40-keV electrons is shown in Fig. 6.12. The area of the main peak, centered at the energy of the impinging particles, represents the contribution of collected incident particles. Contributions to $N(E)$ for the flat portion of the curve are assumed to arise from electrons which have transferred some of their energy to the detector and are then backscattered through single or multiple collisions out of the front surface. The rise of $N(E)$ at low energy is due to the inherent detector noise and associated electronics.

The energy spectrum of the incident particles is assumed to be symmetrical about the initial energy W, with full width equal to ΔW taken at 1% of maximum $N(E)$. Reflected electrons are considered to be in the energy range 0 to $(W - \frac{1}{2}\Delta W)$ keV. Using the areas under the appropriate portions of the experimental curve, a backscattering or reflection coefficient, η, can be determined.

Figure 6.13 shows the reflection coefficients as a function of electron and H^0 energy. The projectiles were incident perpendicularly to the front surface of the detector. The error limits were derived by using maximum and minimum limits on the variables associated with the

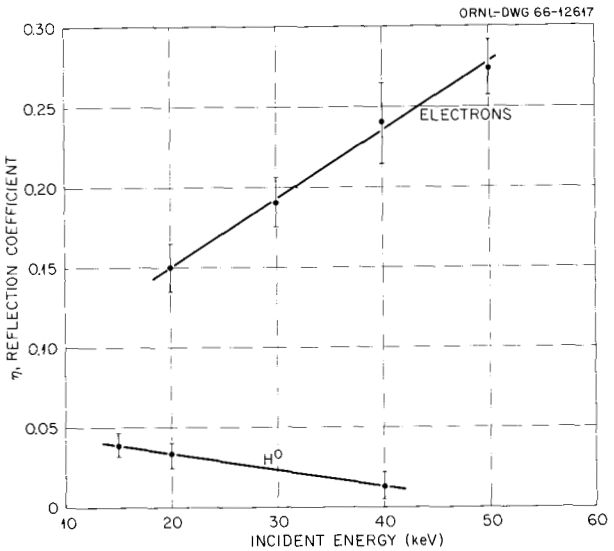

Fig. 6.13. Reflection Coefficient of Electrons and H^0 from a Silicon Crystal in the Energy Range 15 to 50 keV.

problem. As expected, the reflection coefficient for electrons was 20 to 30% in this energy range, with the reflection coefficient for H^0 being less than 5%. Not expected was the increase in electron reflection coefficient as the energy was increased from 20 to 50 keV.

A possible source of error could be soft x rays (11 to 13 keV). The effect of producing x rays in the gold barrier by electrons was determined by placing a 0.001-in. gold foil in front of the detector. This foil was sufficiently thick to stop electrons but attenuate only ~30% of the soft x rays. No x rays were detected with this additional gold foil; thus we have concluded that the observed particles are reflected from the crystal after losing a fraction of their energy.

6.4 HIGH-ENERGY CHARGE EXCHANGE OF H^0 AND H^+ IN CONDENSABLE GASES

Charge-exchange cross sections are of particular interest in the study of thermonuclear devices, such as DCX-2, due to the interaction of the various constituents of the plasma and input beams with residual gas molecules. The use of a capacitance manometer for reliable determinations of target densities for condensable gases has made possible cross-section measurements for the major gas impurities in vacuum systems.

A direct measurement of the electron stripping (σ_{01}) cross section has been made for H^0 incident on H_2, He, Ar, N_2, O_2, CO, CO_2, H_2O, CH_4, and C_2H_6 target gases. The energy range was 100 to 2500 keV. Measurements have also been made for C_2H_4, C_4H_{10}, and Kr gases for incident H^0 in the energy range 800 to 2500 keV. The electron capture cross section (σ_{10}) has been measured directly for incident protons with kinetic energy in the range 800 to 2500 keV and target gases Ar, Kr, N_2, O_2, CO, CO_2, H_2O, CH_4, C_2H_6, C_2H_4, and C_4H_{10}. The values for σ_{10} at low energies (100 to 550 keV) have been calculated from measured equilibrium fractions and σ_{01} values.

The apparatus constructed for the cross-section measurements is shown schematically in Fig. 6.14. This apparatus consisted of two differentially pumped gas cells (a pressure differential of $\sim 10^3$ could be maintained across the apertures), two sets of electrostatic analyzers, and detectors for the determination of the beam intensities. The H^+ beam incident on the first gas cell underwent charge-exchange collisions with either argon or nitrogen gas at a pressure of approximately 0.1 torr. Following the first collision chamber, an electrostatic analyzer deflected all the charged particles emerging from the cell, leaving only H^0 particles incident on the second gas cell. For measurements of σ_{10} the first gas cell was evacuated to $\sim 2 \times 10^{-8}$ torr, and the first set of deflection plates was electrically grounded.

The target gas under study was introduced into the chamber through a variable leak to the desired pressure as measured by a capacitance manometer. The purity of the gas was checked periodically by a residual gas analyzer. After passing through this collision chamber, the beam products were separated into their various charge states by an electric field.

Silicon-gold barrier detectors were used to detect the low-intensity beams ($\sim 10^{-16}$ amp). These detectors had a sensitive area of 50 mm^2 and a depletion depth of approximately 330 μ. At the higher energies the σ_{10} cross section becomes small, requiring the use of proton beams whose intensity was greater than 10^{-14} amp. In these measurements a Faraday cup was used to detect the proton beam.

The calibration of the capacitance manometer was checked against a McLeod gage before and

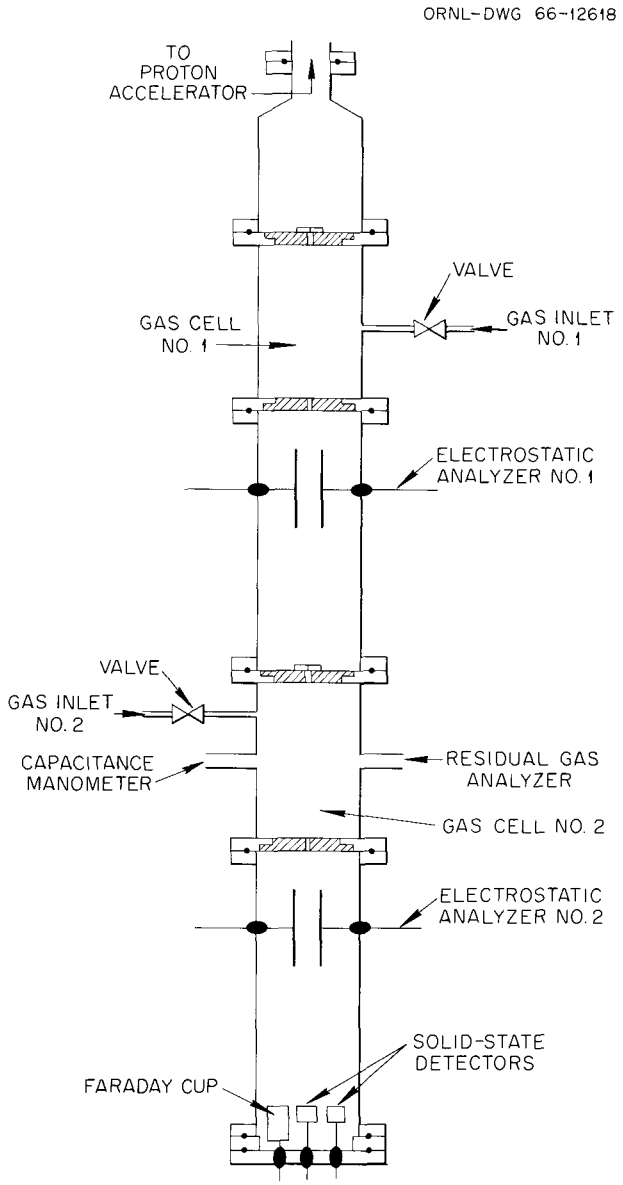

Fig. 6.14. Schematic Diagram of the Apparatus Used for Electron Capture and Stripping Cross Sections.

after the cross-section measurements. After making corrections to account for the standard systematic errors associated with a McLeod gage, including cooling the McLeod gage to −10°C to reduce the mercury pumping effect,[11] the capacitance manometer and McLeod gage were in agreement to within 10% in the pressure range 2×10^{-5} to 10^{-3} torr.

A direct measurement of the cross sections was made by observing the fraction of the beam in each charge state after passing through a "thin" gas target. The cross sections are determined from the relationship

$$\frac{I^f}{(I^i + I^f)} = \Pi P \sigma_{if} ,$$

where

I^i = intensity of the beam in the initial charge state,

I^f = intensity of the beam in the final charged changed state,

Π = number of atoms per square centimeter per torr,

P = target gas pressure in torrs,

σ_{if} = cross section for electron transfer from charge state i to charge state f.

A plot of $I^f/(I^i + I^f)$ vs pressure yields a straight line (for thin target conditions) whose slope is equal to $\Pi\sigma_{if}$, where Π is a constant for each gas. As a check on the internal consistency of the data, as well as a method of calculating the capture cross sections where they were not measured, the equilibrium fractions were determined under "thick" gas target conditions from the measured ratios

$$F_{1\infty} = \frac{H^+}{H^+ + H^0} \text{ incident } H^0 \text{ beam} ,$$

$$F_{0\infty} = \frac{H^0}{H^+ + H^0} \text{ incident } H^+ \text{ beam} .$$

The cross sections and equilibrium fractions are related by

$$F_{1\infty} = \frac{\sigma_{01}}{\sigma_{10} + \sigma_{01}} , \quad F_{0\infty} = \frac{\sigma_{10}}{\sigma_{01} + \sigma_{10}} .$$

Measured equilibrium fractions and those calculated from measured cross sections were in agreement to within experimental error (~10%).

The results of the cross-section measurements for N_2, CO, CO_2, O_2, H_2O, CH_4, and C_2H_6 are shown in Figs. 6.15–6.18.

Figures 6.15 and 6.16 also show the previous work of Barnett and Reynolds[12] for N_2 and O_2, Pyle's[13] values for N_2, and the theoretical values

[11] H. Ishii and K. Nakayana, *Trans. Eighth Vac. Symp.*, vol. 1, p. 519, Pergamon, Oxford, England, 1962.

[12] C. F. Barnett and H. K. Reynolds, *Phys. Rev.* **109**, 355 (1958); P. M. Stier and C. F. Barnett, *Phys. Rev.* **103**, 896 (1956).

[13] R. V. Pyle, private communication.

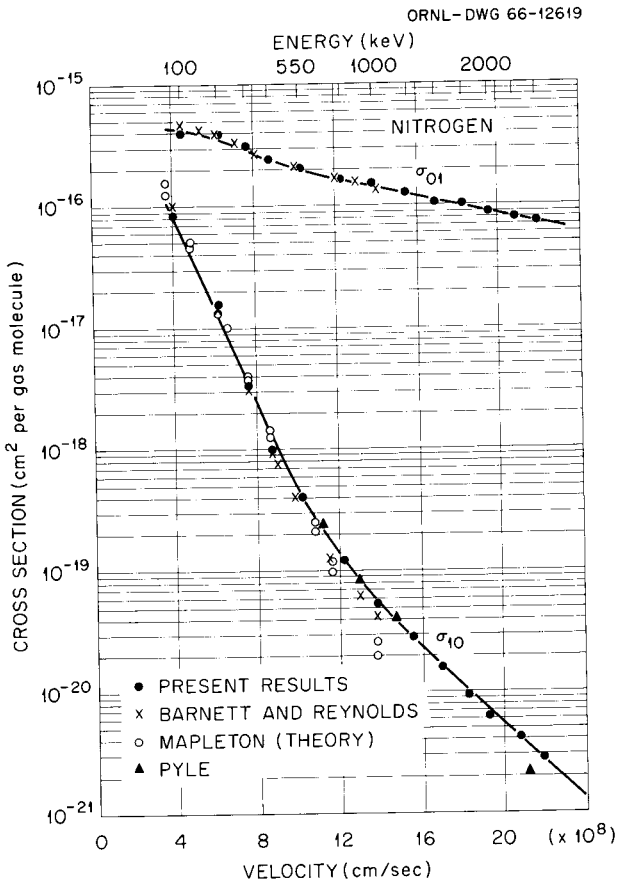

Fig. 6.15. Charge-Transfer Cross Sections per Target Gas Molecule as a Function of Particle Energy and Velocity. Hydrogen ions and atoms in nitrogen gas.

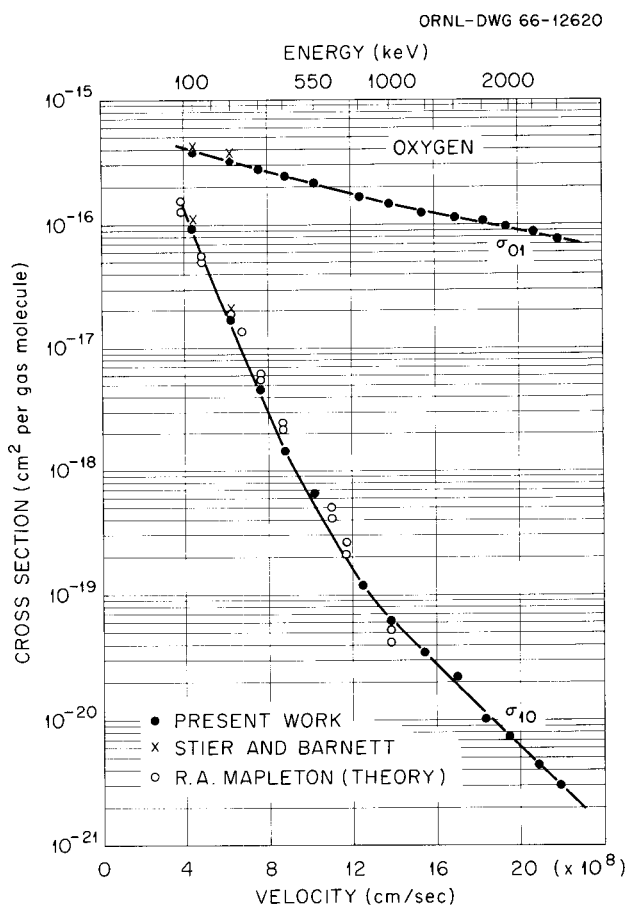

Fig. 6.16. Charge-Transfer Cross Sections per Target Gas Molecule as a Function of Particle Energy and Velocity. Hydrogen ions and atoms in oxygen gas.

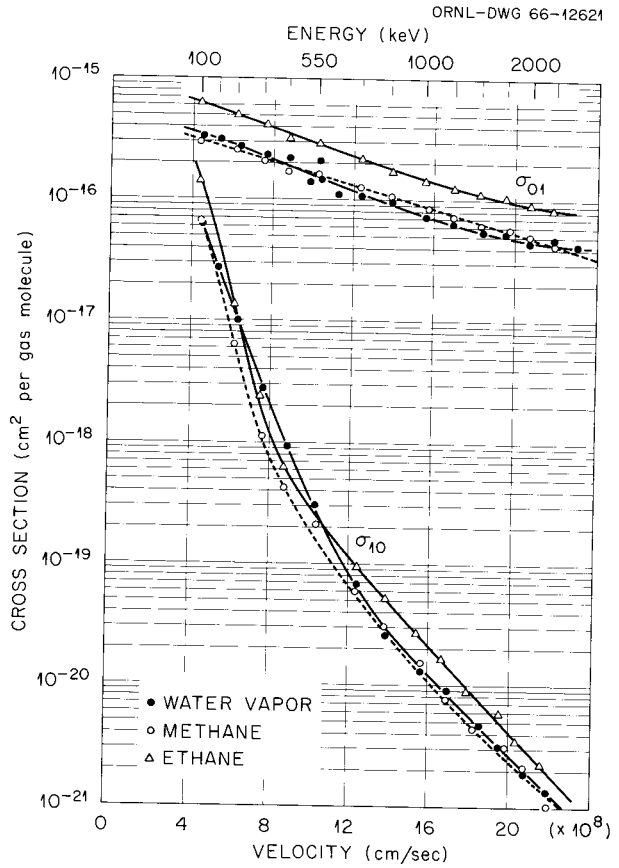

Fig. 6.17. Charge-Transfer Cross Section per Target Gas Molecule as a Function of Particle Velocity and Energy. Hydrogen atoms and ions in H_2O, CH_4, and C_2H_6.

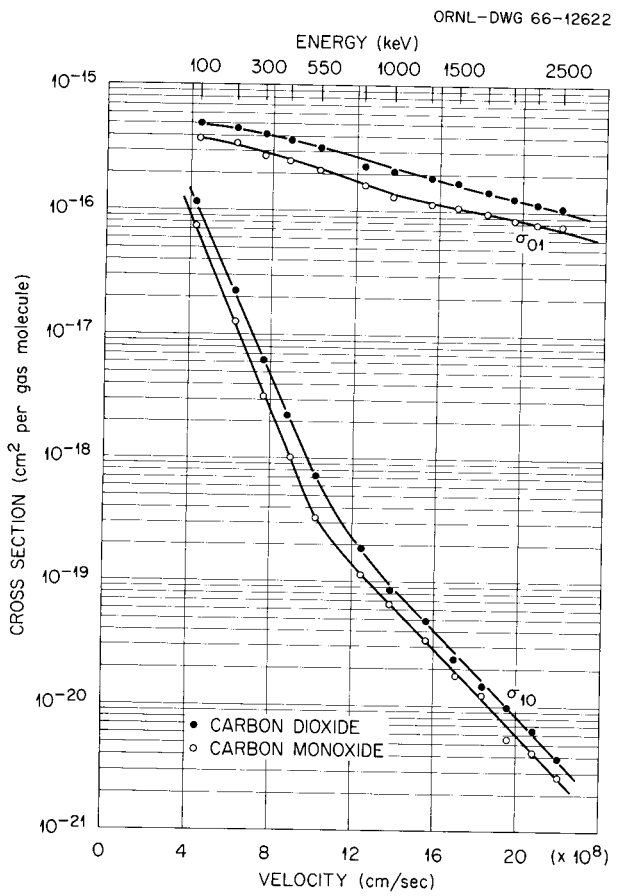

Fig. 6.18. Charge-Transfer Cross Section per Target Gas Molecule as a Function of Particle Velocity and Energy. Hydrogen atoms and ions in CO and CO_2.

of Mapleton[14] for O_2 and N_2. The velocity dependence of the capture cross sections is found to be $v^{-6.8 \pm 0.4}$ for protons with energy greater than 200 keV and all heavy target gases. This is in near agreement with Bohr's[15] prediction of v^{-6}. The velocity dependence of σ_{01} shows more variation with energy; however, for incident H^0 energies greater than ~500 keV the cross section appears to follow a power law with a variation from $v^{-0.8}$ for krypton to $v^{-1.76}$ for methane, which may be compared with Bohr's prediction of a v^{-1} dependence for heavy gases and v^{-2} for the light gases.

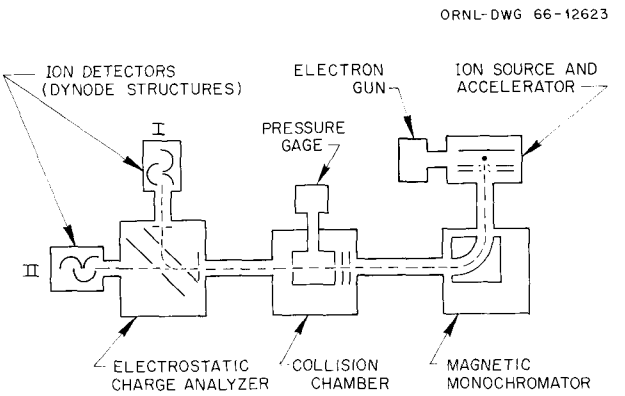

Fig. 6.19. Schematic Diagram of Apparatus Used for Measurement of Multiple-Charge-Transfer Cross Sections.

6.5 MEASUREMENTS OF MULTIPLE CHARGE TRANSFER OF MULTIPLY CHARGED ARGON IONS

Since the measurements of Flaks and Filippenko,[16] it is known that the cross section for capturing two electrons by multiply charged ions is of the same magnitude as the cross section for capturing one electron. Except for the work of Nikolaev *et al.*,[17] which reports the simultaneous capture of four electrons by N ions, no studies have been made on the capture of more than two electrons by ions of charge greater than 3, although cross sections for such processes presumably are not small.

We have begun studies of nonresonant charge transfer of one to five electrons for multiply charged rare-gas ions in their own gases or unlike gases. Measurements have been carried out on transfer of two electrons for Ar^{3+}; of two and three electrons for Ar^{4+}; and of two, three, and four electrons for Ar^{5+} with argon as target gas in all cases. Differential cross sections of these processes relative to the cross section of single-charge transfer are reported in the energy range from 0.4 to 2.2 keV times the charge of the primary ions.

The schematic of the apparatus used is shown in Fig. 6.19. Ions produced by electron bombardment are accelerated to the desired velocity and separated by a magnetic analyzer with a resolution of 0.9% in energy. The ion beam enters the collision chamber through a series of apertures and has a cross section of about 0.15×0.7 cm^2 with a divergence of less than 0.003 rad. Ions that have picked up electrons in the gas cell are separated by an electrostatic parallel-plate analyzer according to their charge. After postacceleration through a potential difference of 3500 V, the ions are detected by an AgMg dynode structure and counted individually. For purposes of alignment and monitoring, a second multiplier is used in line with the "straight-through" beam. This detector may also serve as a counter of atoms that have been completely neutralized in charge-transfer collisions. The charge-degraded beam is accepted by the electrostatic analyzer within a solid angle of $\alpha = 0$ to $\pm 0.6°$. Thus differential cross sections are measured, but since the total angular scattering[18] of the ions following partial neutralization lies within $-1° \lesssim \alpha \lesssim 1°$, our data approximate total cross sections.

Figure 6.20 shows energy profiles of the primary beam and the beam as seen by the ion detector after charge analysis. Peak shapes are independent of the m and n values, where m and n are the charge states of the ions before and after charge-transfer collisions. The flat top distributions (B) obtained by using a narrow entrance and a wide exit aperture for the charge analyzer allowed us

[14] R. A. Mapleton, *Phys. Rev.* **130**, 1829 (1963).

[15] N. Bohr, *Kgl. Danske Videnskab. Selskab, Mat.-Fys. Medd.* **18**, 8 (1948).

[16] I. P. Flaks and L. G. Filippenko, *J. Tech. Phys.* **29**, 1005 (1959).

[17] V. S. Nikolaev *et al.*, *Soviet Phys. JETP (English Transl.)* **14**, 67 (1962).

[18] N. V. Fedorenko, L. G. Filippenko, and I. P. Flaks, *J. Tech. Phys.* **30**, 45 (1960).

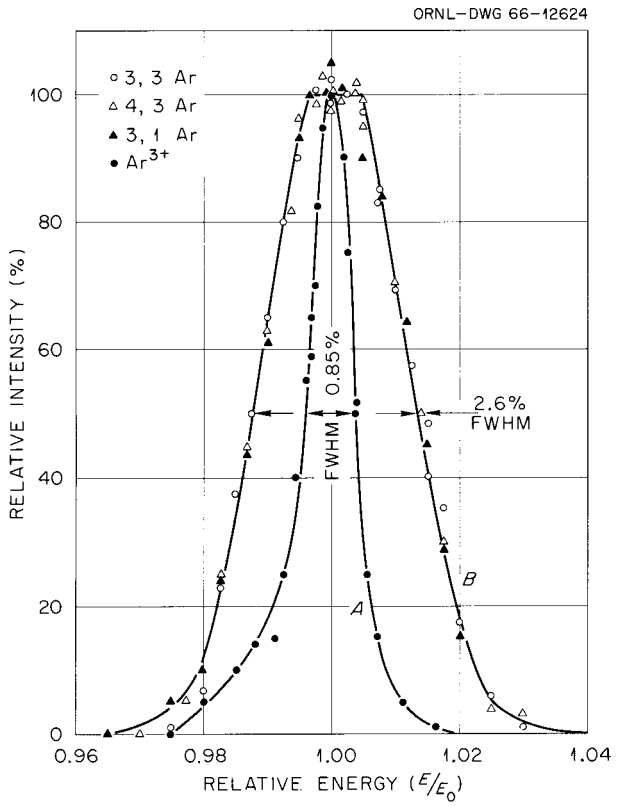

Fig. 6.20. Resolution of Monochromator (*A*) and of Charge Analyzer (*B*).

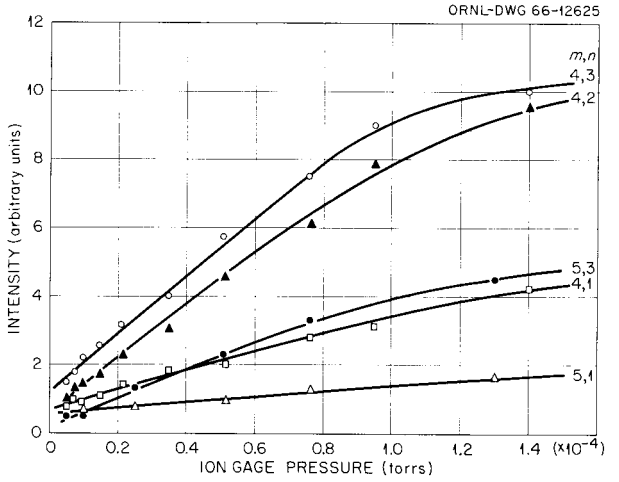

Fig. 6.21. Pressure Dependence of Charge-Transfer Processes m,n Ar^+ in Argon Gas. m is initial charge state and n is final charge state. $E_{ion} = 1460\ Q$ (eV).

to take peak heights as a direct measure of the intensities of the various charge states without correcting for the dispersion of the instrument.[19]

Measurements were carried out at pressures of about 2×10^{-5} torr (ionization gage readings) in the 16-cm-long gas cell. The residual gas pressure ranged from 5 to 10×10^{-7} torr. Operating pressures in the analyzer, and in the tubes connecting the gas cell with monochromator and analyzer, were less than 6×10^{-7} torr and 3×10^{-6} torr respectively. As seen from the linear dependence of the ion count rates on cell pressure, Fig. 6.21, the gas density corresponding to 2×10^{-5} torr constituted thin target conditions so that double collisions could be neglected. We corrected observed intensities for the detection efficiency of the dynode structure which varied slightly (less than 20%) with charge and energy of the ions and for contributions due to charge exchange with residual gas molecules. Errors of the measurements were due to fluctuations of the primary beam and cell pressure (together less than 5%), and to uncertainties in the correction factors and statistical fluctuations.

Fully corrected data of charge-transfer collisions[20] $Ar^{m+} + Ar = Ar^{n+} + Ar^{(m-n)+}$ are plotted in Fig. 6.22 as relative differential cross sections ${}_{m,n}\eta = {}_{m,n}\sigma / {}_{m,m-1}\sigma$ vs acceleration voltage of the primary ion. Also shown are curves of ${}_{3,1}\eta$ for neon and krypton as obtained from total cross-section curves in the paper of Flaks and Filippenko.[16] Our curve of ${}_{3,1}\eta$ for argon lies between those of neon and krypton from ref. 16, and it exhibits a similar character of rising slowly with increasing energy above 5 keV. The cross-section ratio ${}_{3,1}\eta$ of argon should, however, be higher by about 10%, if we were to correct for the loss of ions scattered[21] by more than 0.6°. Curves of ${}_{5,n}\eta$ and ${}_{4,n}\eta$ have wide maxima around energies of 1 keV times the charge; they drop slowly above this energy but more steeply toward lower energies. The probability of reducing the charge of the primary ion by two units is of the same order of magnitude as the probability of single-charge transfer, namely, 30 to 60% in the keV range. We also see that double-charge transfer becomes more likely with increasing charge of the primary ion.

[19] R. Kollath, *Ann. Physik* **27**, 721 (1936).

[20] In the reaction equation we neglect emission of electrons by various possible mechanisms.

[21] According to ref. 17, charge-transfer reactions involving two electrons have a wider angular distribution than those involving one electron.

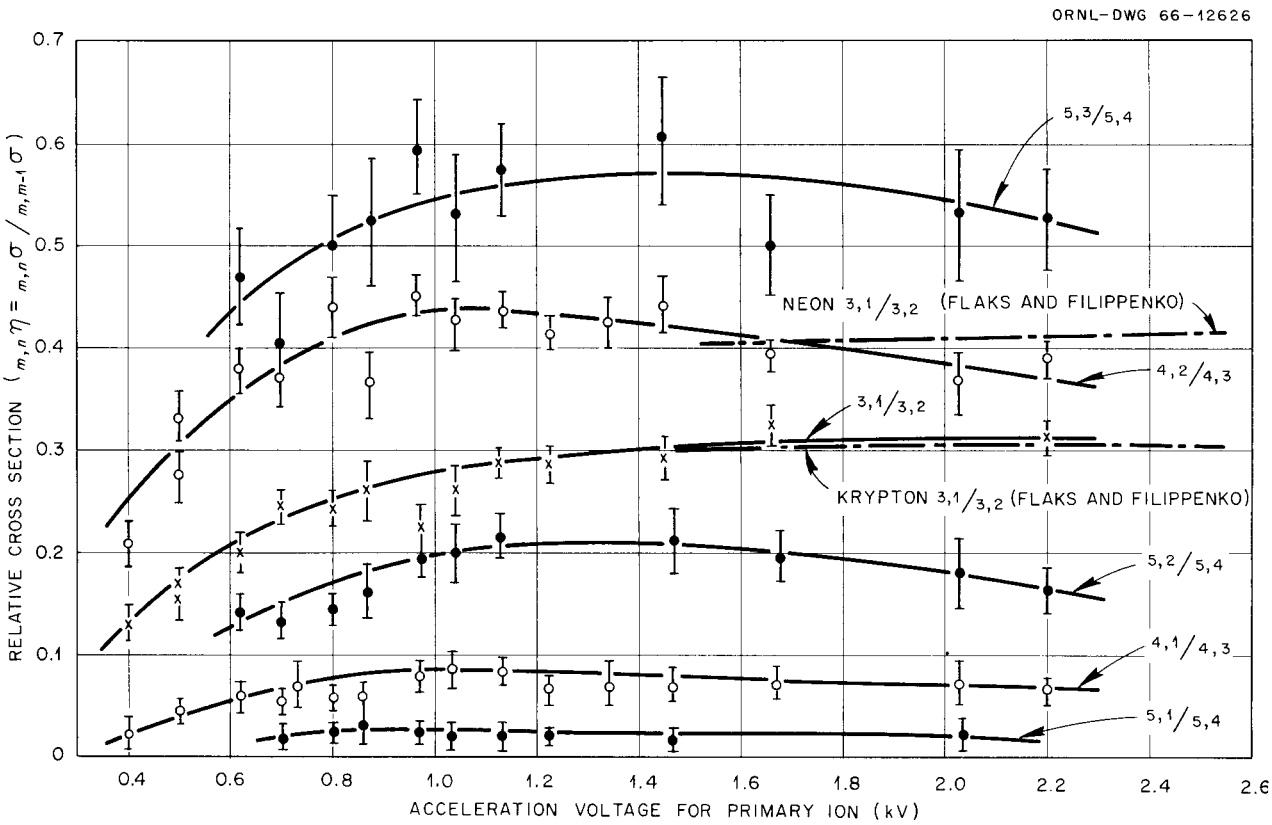

Fig. 6.22. Cross Sections of Multiple-Charge-Transfer Processes *m,n* Ar in Argon Gas Relative to Single-Charge Transfer *m,m*-1 Ar. Scattering angle $\alpha = 0$ to $\pm 0.6°$.

This behavior is accentuated in processes of triple-charge exchange. Values of ${}_{5,2}\eta$, ${}_{4,1}\eta$, and ${}_{5,1}\eta$ are close to 20, 7, and 2.5%, respectively, in the observed range of energies.

With the present measurements we have shown that multiple-charge transfer of multiply charged ions in their own gas is of considerable magnitude in the keV region and becomes more probable with increasing charge of the primary ion. Further efforts will be directed toward (1) absolute charge-transfer reactions of Ar^{n+}, Ne^{n+}, Kr^{n+}, and Xe^{n+}, $n = 3$ and greater, in their own gases and in unlike monatomic and molecular gases and (2) investigation of electrons emitted in charge-transfer collisions. Particularly the latter study should offer a better insight in the mechanism of charge-transfer collisions by testing the following contentions: (1) the positive energy defect in the transfer of one or more electrons – most of the reactions considered are exothermic – appears as kinetic energy of an electron emitted from the target atom; (2) two or more electrons are transferred into *excited* levels of the incident projectile and are, therefore, bound to decay by autoionization; and (3) in certain special cases an inner electron of the target atom is transferred to the collision partner.

6.6 ATOMIC AND MOLECULAR PROCESSES INFORMATION CENTER

C. F. Barnett
D. A. Griffin
M. O. Krause
R. A. Langley
J. R. McNally, Jr.
J. A. Ray

Delays have been encountered in issuing our current annotated bibliographies. In order to make the bibliographies a more useful document to specialists in the respective fields, the reactants, energy range, preliminary evaluation, and category of each reference in the bibliography will be made

available in tabulated form. Attempts will be made to reduce publication costs of these bibliographies by using a computer printout suitable for direct photographic reproduction. It has been necessary to write an extensive program to obtain a useful printout format suitable for reproduction. This program has been written and is in the process of debugging. As soon as the accurate program becomes available, two past bibliographies (1965, first half of 1966) will be published. It is anticipated that with such a system the annotated bibliographies can be in the user's hands one month after a literature search is complete.

Our *International Directory of Workers in the Field of Atomic Collisions* is being revised and brought up to date. This effort is 90% complete and will be published in the near future. All entries are now being machine stored such that revisions and publications can be made with minimum effort.

A contract has been signed with John Wiley and Sons to publish the results of our evaluations and reviews in the form of monographs. The manuscript (authored by A. Dalgarno, V. Cermak, E. Ferguson, L. Friedman, and E. McDaniel) of the first review, "Ion-Atom Interchange Reactions," is in the final process of editing and will be ready to send to the publisher in January 1967. The second review, "Ionization, Excitation and Dissociation by Heavy Particles," has been planned in detail. The authors (J. Hooper, E. Thomas, A. Russek, G. McClure, and F. Bingham) have been chosen, the chapter outline completed, and the writing begun. The planned completion date is December 1967.

Most of the activities of the data center have consisted in review and preliminary evaluation of pertinent papers in the current and past literature, performing literature searches, writing retrieval programs, and filling requests for copies of hard-to-obtain reports. At the request of the editors of *Physical Review* we have supplied a list of qualified specialists to referee papers appearing in *Physical Review*. Three to six persons were recommended for 22 subjects taken from the *Physical Review Subject Index*. It is believed that information centers with their intimate knowledge of workers in a narrow field can increase the usefulness of the referee system by providing more qualified referees.

7. High-Current Beam Production and Injection

R. C. Davis G. G. Kelley
R. R. Hall O. B. Morgan[1]
R. F. Stratton

The four-electrode source for the production of H_2^+, which was described previously,[2] has been used on the 100-kV test stand[3] together with a magnesium vapor cell to produce neutral particle beams. Molecular ions at 40 keV are dissociated and neutralized in the cell to produce 20-keV atoms. The source configuration which has produced the most intense beams is shown in Fig. 7.1. Various parameters of the assembly were changed to determine the best arrangement. Also, several changes were made in magnetic configuration, in the axial position of the source with respect to the magnetic lens, and in the sizes of the apertures in the electrodes. The best aperture sizes were $^{11}/_{32}$ in. for the intermediate electrode and anode and $^{7}/_{16}$ in. for the target cathode. Previously it had been determined, using a conventional duoplasmatron, that the field of the auxiliary coil and source coil should oppose the field of the main lens to produce a null at the plasma surface.[4] The same polarities give best results with the four-electrode source, but field scans have not been made. The aperture arrangement in Fig. 7.4 is used, because at 117 cm it represents the injection geometry of INTEREM and at 240 cm it is similar to DCX-3 injection geometry.

We have used a magnesium cell, Fig. 7.2, which was developed and made by Postma and Reinhardt to neutralize the 40-keV ion beam. The cell consists of a 4-in. stack of radially corrugated stainless steel rings surrounded by an oven containing heated magnesium. The top plate is a water-cooled $^{1}/_{4}$-in.-thick copper sheet with a poorly cooled tantalum ring insert having a $1\,^{1}/_{2}$-in. ID. The purpose of the tantalum ring is to prevent magnesium vapors from condensing on the cooled top plate and reducing the aperture size. The cell is heated by two 500-W tubular heating units. The outer shell of the cell is water cooled to prevent heating of the vacuum manifold.

The vapor cell was positioned 58 cm below the center of the lens coil. Closer positions were tried, but the H_2^+ component of the beam, which is crossed over above the cell and is strongly divergent, seems to heat the inside of the cell quite badly and makes control of the temperature difficult. Figure 7.3 shows current vs cell temperature at the various apertures and the 240-cm target while extracting 180 mA total current at 40 kV. This shows the best operating temperature of the cell to be 480°C.

Using the source and accelerator column shown in Fig. 7.1, we have obtained the results shown in Fig. 7.4. The accelerating electrode is operated at −12 kV. Thus the beam is extracted at 52 kV and deaccelerated to 40 kV. The −12-kV potential of the accelerating electrode with respect to ground is the minimum value which provides sufficient electron trapping to neutralize the space charge of the beam. The currents shown in the figure at 117 cm and 240 cm are available for INTEREM and DCX-3 respectively. The maximum H_2^+ current obtained at 117 and 240 cm with the aperture arrangement shown in Fig. 7.4 is 146 and 70 mA respectively.

[1]Present address: University of Wisconsin, Madison.

[2]*Thermonuclear Div. Semiann. Progr. Rept. Apr. 30, 1966*, ORNL-3989, pp. 89–94.

[3]*Thermonuclear Div. Semiann. Progr. Rept. Oct. 31, 1965*, ORNL-3908, pp. 100–107.

[4]*Thermonuclear Div. Semiann. Progr. Rept. Apr. 30, 1965*, ORNL-3836, pp. 74–80.

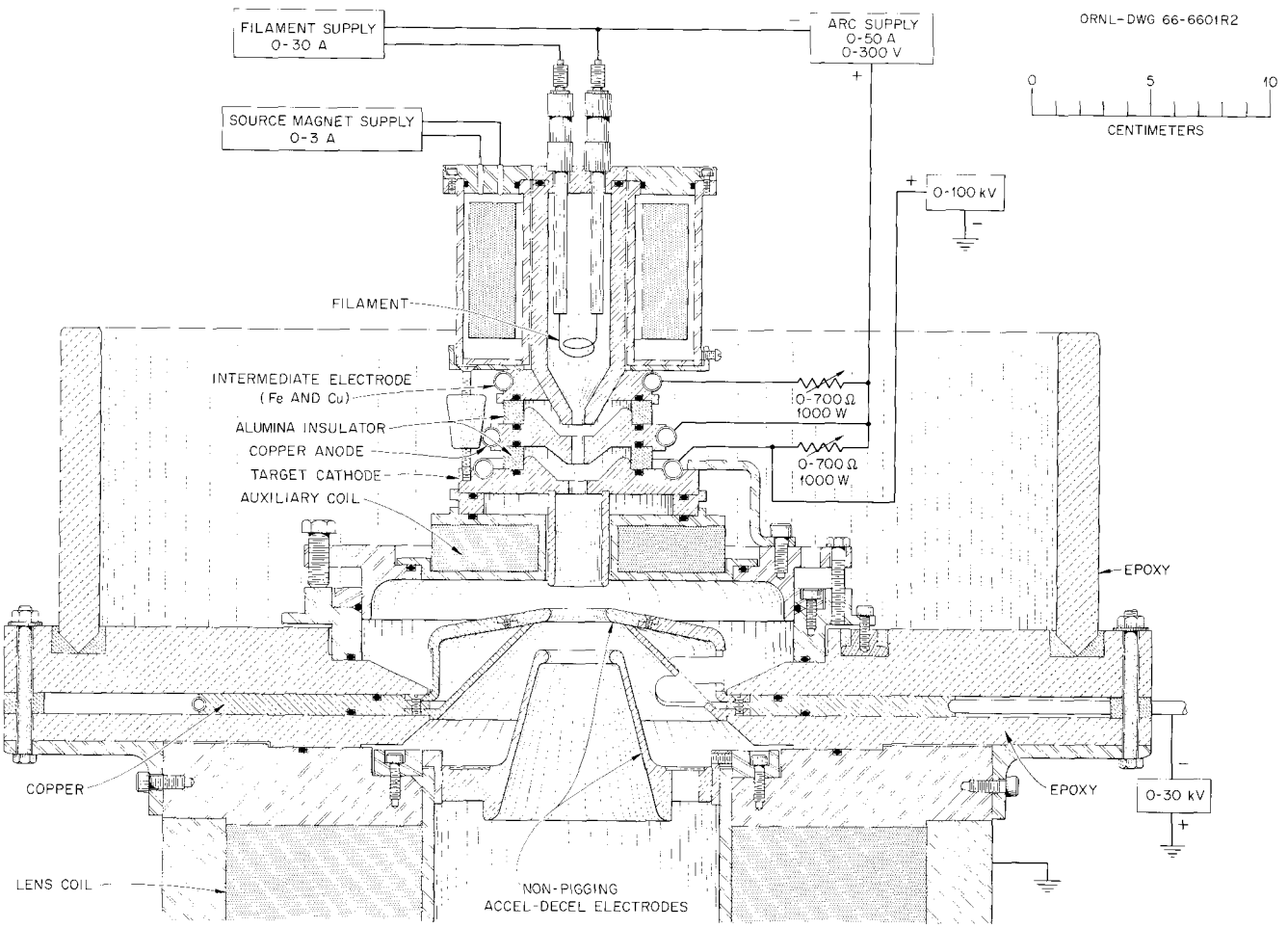

Fig. 7.1. Four-Electrode H_2^+ Ion Source Using 100-kV Accelerator Column with Non-PIG Design.

Since energy modulation of the beam will be desirable in DCX-3 experiments, we have determined the effect of a variation of the accelerating voltage on target current both with and without reoptimization of the magnetic lens. Figure 7.5 shows these results. The bottom curve shows a 40% FWHM (full width at half maximum) energy spread without reoptimization of the lens, and the upper curve shows a 60% FWHM energy spread in the other case. Variation of only the high voltage was tried in DCX-1.5. Due to the more stringent beam collimation in DCX-1.5, an FWHM of only 25% was obtained.

Beam probe measurements have been started using the water-cooled copper probe shown in Fig. 7.6. The power density is measured at 0.1-in. intervals along a diameter. Measurements were made both of the H_2^+ beams without the neutralizer on and of the resultant neutral beam with the neutralizer on. Figure 7.7 shows the current density as a function of radius of a 142-mA 40-keV ion beam and the resultant 20-keV neutral beam at 117 cm below the lens coil. Parameters were adjusted for maximum current through a $1\frac{3}{4}$-in.-diam aperture at 117 cm. Figure 7.8 is a plot from the same data showing current vs beam radius, indicating the effect of aperture size at 117 cm below the lens coil on the current transmitted. A complete description of the performance of the system requires the determination of a family of these curves for several aperture sizes, since the optimum focal conditions depend on the aperture. Figures 7.9 and 7.10 show the result of scanning a 92-mA 40-keV beam at 240 cm from the lens coil. In this case there was no aperture directly above the 240-cm target, and the parameters were adjusted for

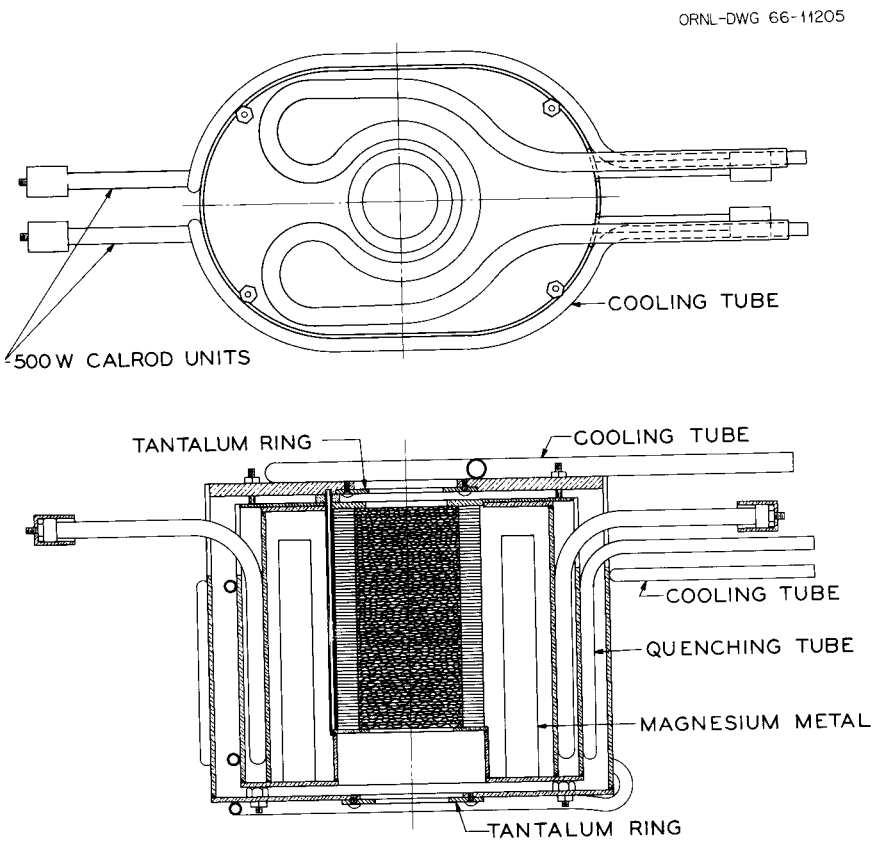

Fig. 7.2. Magnesium Vapor Cell Used in Production of Intense Neutral Beams.

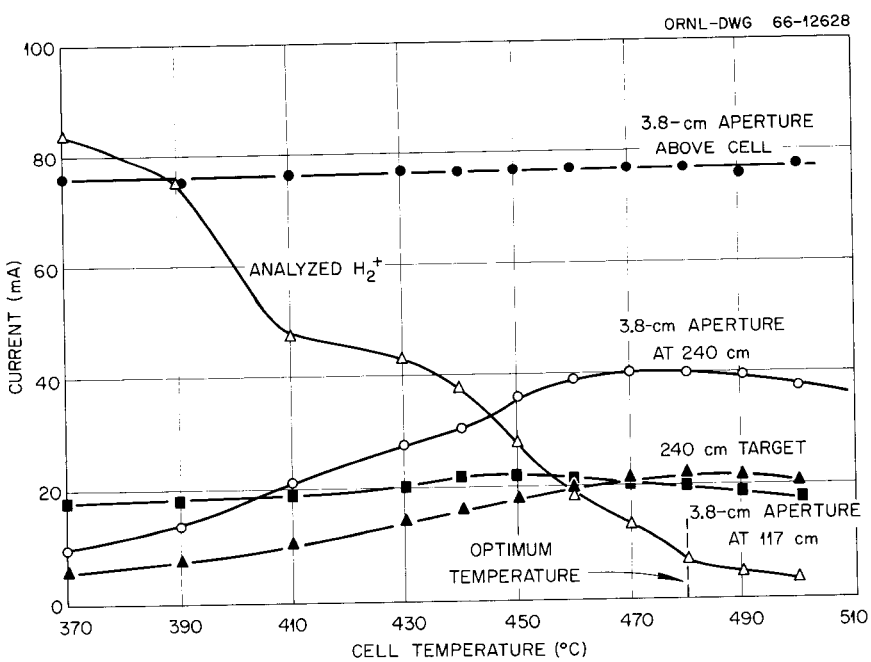

Fig. 7. 3. Dependence of Accelerated Beam Current upon Temperature of the Magnesium Vapor Neutralizing Cell Measured at Various Apertures. 40 kV and 180 mA total extracted current.

maximum total current on the target. For this reason the results are not directly comparable with those at 117 cm.

The measurements made with the probe arrangement shown in Fig. 7.6 are slightly in error because there is some power radiated to the probe from the target below and because the length of the probe tip exposed to the beam is not precisely defined. A new system is being made which eliminates these difficulties and provides for automatic scanning and plotting.

Magnetic asymmetries in the auxiliary coil and source expansion cup were discovered and found to be due to the use of ferromagnetic welding rod on nonmagnetic materials. This trouble has been rectified, and there is no longer any beam shift as parameters are changed, and the optic and magnetic alignments are the same.

ORNL-DWG 66-9128R

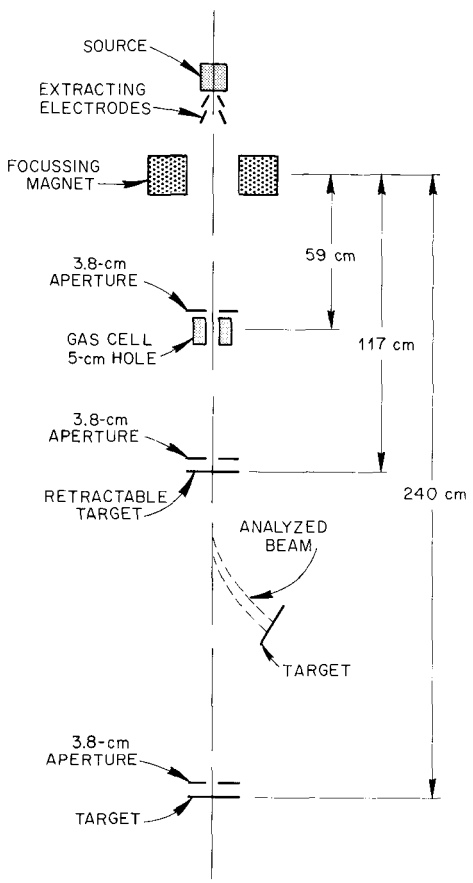

ACCELERATED mA	TARGET LOCATION	NEUTRALIZATION	mA ON TARGET
200	240 cm	OFF	66
200	240 cm	ON	92 mA EQUIVALENT OF 20 keV H^0
200	117 cm	OFF	126
220	117 cm	ON	222 mA EQUIVALENT OF 20 keV H^0
200	H_2^+ ANAL	OFF	90
200	H_2^+ ANAL	ON	7
200	240 cm*	OFF	83
214	240 cm*	ON	102 mA EQUIVALENT OF 20 keV H^0

* 5 cm APERTURE AT 234 cm

Fig. 7.4. Table Showing the H_2^+ and H^0 Currents Available at 117 and 240 cm Through Defining Apertures Representing INTEREM and DCX-3 Geometries Respectively.

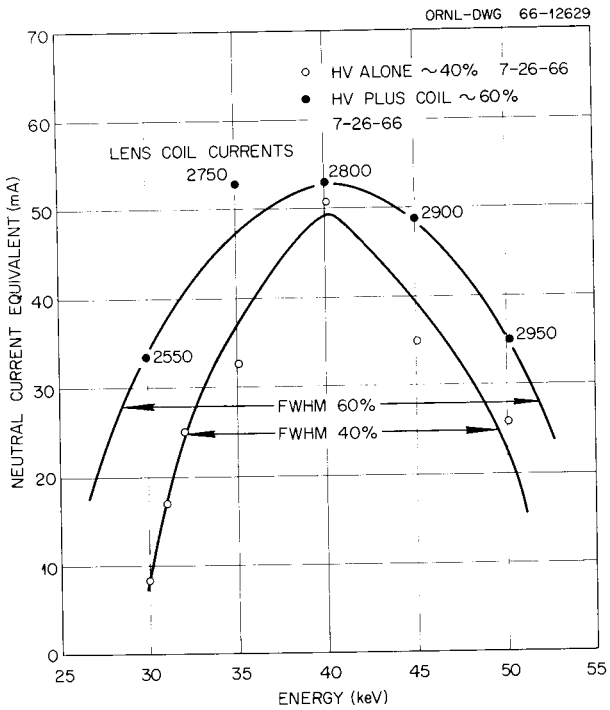

Fig. 7.5. Variation of Neutral Beam Current with Injection Energy in DCX-3 Geometry. The curves show the performance which can be expected using modulation of injection voltage to spread the injected particle energy with and without readjustment of the strength of the magnetic lens.

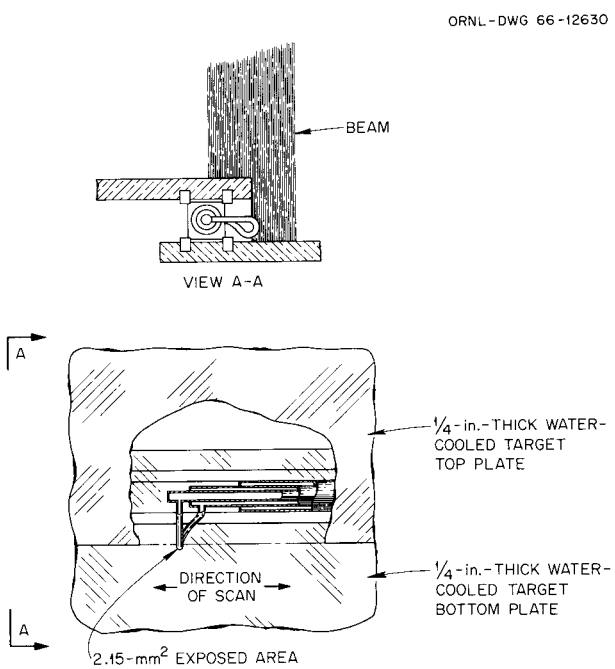

Fig. 7.6. Probe for the Calorimetric Determination of Current Density Profile in a Beam of Energetic Particles.

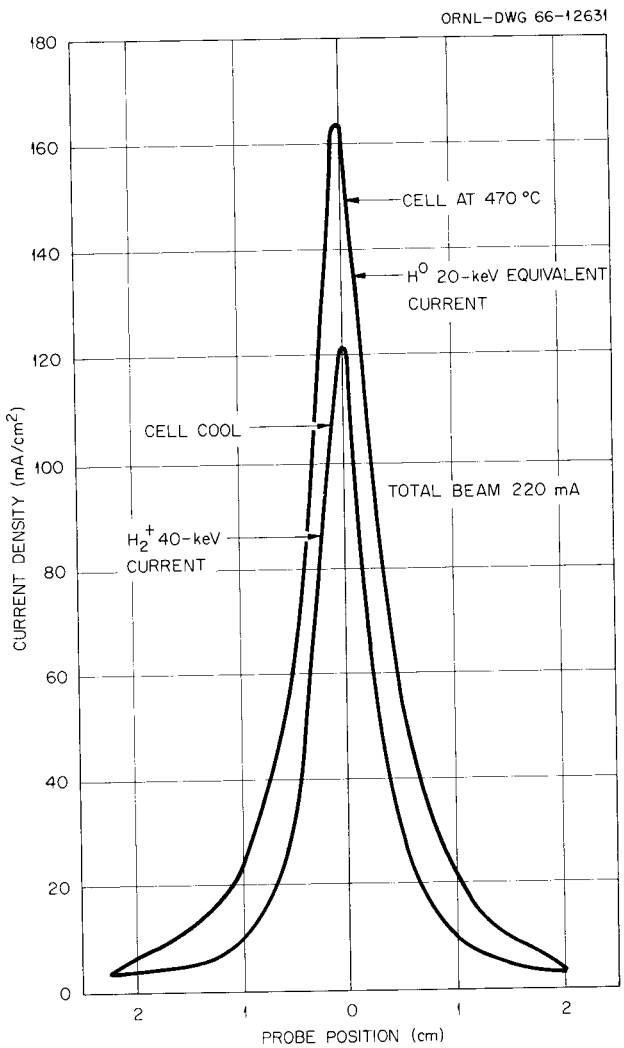

Fig. 7.7. Scan of Current Density of a 142-mA H_2^+ Beam and Resultant H^0 Beam at 117 cm Below Lens Coil. Probe area, 2.15 mm^2. Magnesium cell with 3.8-cm aperture located 58 cm below lens coil.

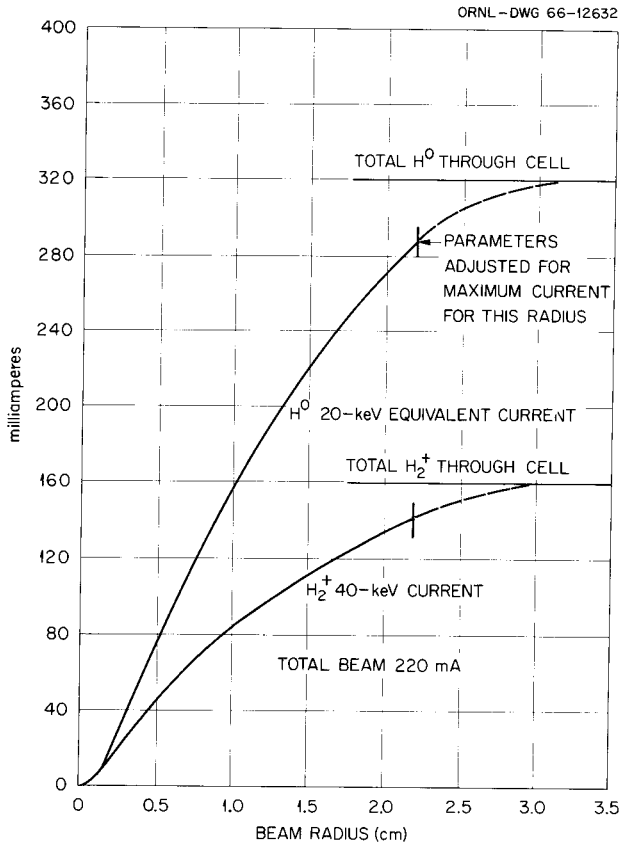

Fig. 7.8. Plot of H_2^+ and H^0 Current in the System Shown in Fig. 7.3 as a Function of Beam Radius at 117 cm. Parameters were adjusted to maximize the current through a 3.8-cm aperture.

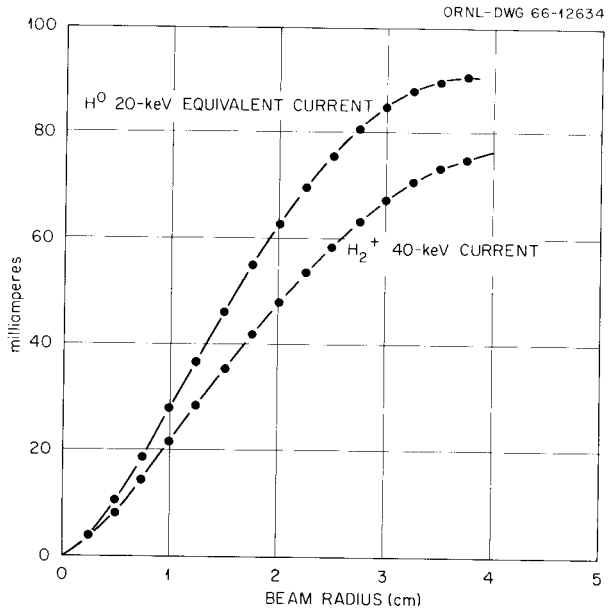

Fig. 7.10. Plot of H_2^+ and H^0 Current in the System Shown in Fig. 7.3 as a Function of Beam Radius at 240 cm. Parameters were adjusted to maximize the total current at 240 cm.

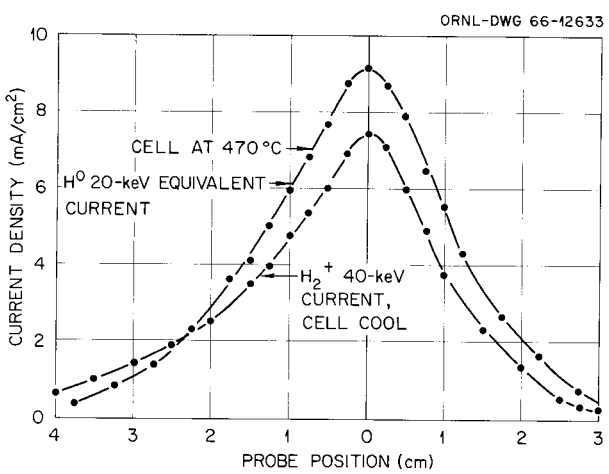

Fig. 7.9. Scan of Current Density of a 92-mA H_2^+ Beam and Resultant H^0 Beam at 240 cm Below the Lens Coil.

8. Plasma Theory and Computation

C. O. Beasley, Jr.[1]
R. E. Budwine[2]
R. A. Dory
W. M. Farr
G. E. Guest
K. C. Hines[3]
C. E. Parker
F. M. Rankin
D. J. Sigmar

8.1 STABILITY PROPERTIES OF OPEN-ENDED MAGNETIC TRAPS

In this section we shall review very briefly those results from plasma stability theory which bear on various aspects of the ORNL fusion program. In the interest of clarity we shall adopt the viewpoint and language of the "thermodynamics of unstable plasmas,"[4] in which one seeks to identify the sources of free energy which can drive instabilities. For although some sources are inevitable in a confined plasma, one can, to a limited extent at least, choose which energy reservoirs are to be retained by his experimental approach. In addition to the identification of sources of free energy, it is also necessary to recognize the various constraints which can prevent the transfer of this energy into growing collective oscillations. We shall begin by enumerating the free-energy reservoirs characteristic of the Oak Ridge program, the related instabilities, and some of the important constraints available in open-ended traps.

All confinement schemes currently being studied require a diamagnetic current to balance the pressure gradient associated with confinement. This diamagnetic current can trigger a number of modes of instability, of which we shall mention only the low-frequency "universal" or "drift" modes and the high-frequency "drift-cyclotron" instability.

Since the characteristic frequencies of the universal modes are very much less than the ion gyrofrequency, they are expected to be stabilized in a magnetic well.[5] The necessary well depth has been estimated[6,7] to be

$$\frac{\Delta B}{B} \gtrsim \frac{1}{6} \frac{T_e}{T_i + T_e}$$

for stability, where $\Delta B/B$ is the relative well depth, and T_e and T_i are the electron and ion temperatures. As yet there is no clear experimental confirmation of this estimate.

A second way of preventing these instabilities relies on ion Landau damping and the constraints inherent in the limited length of an open-ended trap. If the waves are to grow, their axial phase velocity must exceed the ion thermal speed by a factor of about 3. But, subject to some uncertainty regarding boundary conditions, axial wavelengths must be less than the plasma length. These two conditions imply stabilization in plasmas shorter than a critical length,[8]

$$L_{\text{critical}} \approx (2\pi)^{3/2} R_p ,$$

[1]On leave September 1966–September 1967 to Culham Laboratory, Culham, Abingdon, Berks., England.

[2]On leave from North Texas State University, Denton.

[3]On leave from Melbourne University, Melbourne, Australia.

[4]T. K. Fowler, *Phys. Fluids* **8**, 459 (1965).

[5]J. B. Taylor and R. J. Hastie, *Phys. Fluids* **8**, 323 (1965).

[6]T. K. Fowler and G. E. Guest, *Plasma Physics and Controlled Nuclear Fusion Research*, vol. I, p. 383 (CN 21/99), IAEA, Vienna, 1966.

[7]J. D. Jukes, *Plasma Physics and Controlled Nuclear Fusion Research*, vol. I, p. 643 (CN 21/39), IAEA, Vienna, 1966.

[8]M. N. Rosenbluth in *Plasma Physics*, IAEA, Vienna, 1965.

where R_p is approximately the plasma radius. Experiments in cesium and potassium plasmas[9] have demonstrated this constraint at least qualitatively.

A second instability made possible by the diamagnetic current is the drift-cyclotron instability, first discussed by Mikhailovskii and Timofeev[10] but subsequently generalized by a number of authors.[11–13] Since the frequencies of these oscillations are near harmonics of the ion gyrofrequency, one might not expect them to be stabilized in a magnetic well. Recent investigations[14,15] have shown, however, that it may be possible to prevent these modes in a sufficiently deep well. The necessary well depth is given roughly by

$$\frac{\Delta B}{B} \gtrsim \frac{1}{2} \frac{T_i}{T_i + T_e}$$

for stability. In shallower wells the density thresholds, summarized in Sect. 8.2, are slightly lower than in the uniform magnetic fields considered earlier. These density criteria, of the form

$$(\omega_{pi}^2/\omega_{ci}^2) \gtrsim (R_p/\rho_i)^P$$

for instability, have received considerable attention, since they imply that a dense plasma may be stable provided the radius exceeds a critical value.[13] The exponent P depends on the plasma distribution function; for a well-thermalized plasma with a smooth density profile, $P = 2$.

At this point it might be well to mention the flute modes, since, if the pressure gradient associated with confinement is parallel to the gradient of an inhomogeneous confining magnetic field, the usual flute instabilities may occur. Again, since the characteristic frequencies are much less than the ion gyrofrequencies in systems of interest, they may be stabilized in a magnetic well of depth[5]

$$\Delta B/B \gtrsim \beta$$

for stability, where $\beta \cong nkT/(\frac{1}{2}\mathbf{B}\cdot\mathbf{H})$ is the usual ratio of particle pressure to magnetic field pressure.

It is also possible to bring about some degree of stabilization of these modes through "line-tying" mechanisms.[16] For example, if the confined plasma is in good electrical contact with conducting end walls, it is not possible for the flute disturbances to exist without some axial electric field fluctuations near the end walls. A small amount of cold plasma in this region can have a strong stabilizing effect on the longer-wavelength flutes. A very striking feature of this finite length effect is the appearance of a high-density stable regime.

A second free-energy reservoir of considerable importance to open-ended confinement schemes is the departure of the trapped particles from thermal equilibrium. Complete thermalization is prevented by the loss-cone effect, in which particles with small perpendicular velocities (with respect to the magnetic field) escape rapidly from the trap. In addition, injection plasmas are usually created with highly anisotropic (initial) ion velocity distributions, although schemes have been advanced which might circumvent this energy reservoir.

The non-Maxwellian distributions associated with the loss-cone effect are now known to support a wide variety of unstable oscillations. At low densities, $\omega_{pe} \sim (10\text{–}50) \times \omega_{ci}$, unstable cyclotron waves may be excited[17] while at high densities the plasma can support very high-frequency growing waves.[13] If the spread in ion energies is less than 70% of the mean energy, flutelike modes at $\omega \doteq 0, \omega_{ci}, 2\omega_{ci}, \ldots$ may occur.[18] In the presence of a group of relatively cold ions, a monoenergetic group of ions can drive growing waves at the gyrofrequency.[19] The more important of these "velocity-space" instabilities have been listed in Table 8.1. From the standpoint of sta-

[9] F. F. Chen, *Phys. Fluids* **8**, 752 (1965).

[10] A. B. Mikhailovskii and A. V. Timofeev, *Soviet Phys. JETP* **17**, 626 (1963).

[11] A. B. Mikhailovskii, *Nucl. Fusion* **5**, 125 (1965).

[12] Y. Shima and T. K. Fowler, *Phys. Fluids* **8**, 2245 (1965).

[13] R. F. Post and M. N. Rosenbluth, *Phys. Fluids* **9**, 730 (1966).

[14] N. A. Krall and T. K. Fowler, *Effect of Magnetic Curvature on the Drift-Cyclotron Instability*, GA-7393 (1966).

[15] W. M. Farr, Ph.D. thesis, University of Michigan, 1966.

[16] G. E. Guest and C. O. Beasley, Jr., *Phys. Fluids* **9**, 1798 (1966).

[17] G. E. Guest and R. A. Dory, *Phys. Fluids* **8**, 1853 (1965).

[18] R. A. Dory, G. E. Guest, and E. G. Harris, *Phys. Rev. Letters* **14**, 131 (1965).

[19] L. S. Hall, W. Heckrotte, and T. Kammash, *Phys. Rev.* **139**, A1117 (1965).

Table 8.1. Some Important High-Frequency Velocity-Space Instabilities

Reference	Energy Source	Threshold Conditions	$k_{\parallel}$	Means for Stabilization
Harris[20]	Anisotropy	$T_{\perp}/T_{\parallel} > 2n$ $\omega_{pe}/\omega_{ci} \gtrsim n$	$\neq 0$	Landau damping Thermalization
Guest and Dory[17]	Loss cone	$\frac{\omega_{pe}}{\omega_{ci}} \gtrsim n \sqrt{1 + 8a^2 \frac{M}{m} \frac{T_{\parallel e}}{T_{\perp i}}}$ $a^2 = \ln \left[\frac{T_{\perp i}}{T_{\parallel e}} \sqrt{\frac{m}{M} \frac{T_{\parallel i}}{T_{\parallel e}}} \left\lvert D_n^j \right\rvert^{-1} \right]$	$\neq 0$	Landau damping
Post and Rosenbluth[13]	Loss cone	$\omega_{pi} \gg \omega_{ci}$	$\neq 0$	Short length; $L_p \gtrsim 100\ \rho_i$ for stability ???
Dory, Guest, and Harris[18]	Loss cone	$\omega_{pi}/\omega_{ci} \gtrsim 4$ $\Delta E/\bar{E} \lesssim 70\%$	$=0$	Broaden the ion distribution
Hall, Heckrotte, and Kammash[19]	Loss cone (plus cold ions to trigger)	See ref. 19	Arbitrary	Under study

bilization it is important to distinguish, first of all, the flutelike modes ($k_{\parallel} = 0$) from those propagating along the magnetic field ($k_{\parallel} \neq 0$), since only the second class of waves is subject to Landau damping. A second distinction, between convective and nonconvective, is also important in the second case ($k_{\parallel} \neq 0$) if a detailed comparison between theory and experiment is required. It has been found, however, that in the case of Harris modes and the low-density loss-cone modes, as the density is increased above its threshold value, the unstable growth changes character from convective to nonconvective. This transition is discussed in more detail in Sect. 8.3. It now seems likely, in view of these results, that one will have to rely on Landau damping to stabilize these modes, since they can no longer be expected to convect out of the system in plasmas of reasonable density.

One can again make crude estimates of the electron temperature required for this Landau damping:

$$\bar{v}_e \approx \frac{\omega}{k_{\parallel}}$$

for stability; or

$$T_e \approx \frac{m}{M} \left(\frac{n}{2\pi} \frac{L_p}{\rho_i} \right)^2 T_i$$

for $\omega \approx n\omega_{ci}$.

Since the high-density loss-cone mode[13] is expected to have $\omega \gg \omega_{ci}$, impractical electron temperatures are required for Landau damping. This mode is predicted to be convective,[13] and a critical unanswered question concerns the reflection coefficient for these waves at the extremities of the plasma. If reflection is weak, growing waves may not reach observable amplitudes in plasmas shorter than $\sim 100\ \rho_i$.[13]

A very important question, under active study, is the effect of cold ions on the flutelike instabilities driven by nearly monoenergetic distributions of fast ions. To date, only the very special case of a delta-function distribution has been examined,[19] but experience with the single-species case[18] showed a strong stabilizing effect

[20] E. G. Harris, *J. Nucl. Energy* **C2**, 138 (1961).

as the relative width of the distribution of fast particles was increased (see Sect. 8.4).

In assessing the seriousness of the high-frequency instabilities, it is important to bear in mind that Lorentz trapping of injected neutral atoms is at present very inefficient, trapping fractions usually falling below 10^{-3}. Even relatively weak instabilities can lead to sufficiently rapid losses to prevent the accumulation of dense plasmas by such a slow trapping process.

To a large extent the energy reservoirs mentioned above, due to confinement and departures from thermal equilibrium, are inescapable in open-ended traps. The most pressing questions concern the means for stabilizing the associated instabilities. In several Oak Ridge experiments, however, additional sources of free energy have been introduced in the form of directed streams of energetic particles. For these plasmas a very different question is most urgent, namely, the effect of the resulting instabilities on the properties of the trapped plasma. In the DCX-2 device a moderately dense, very energetic, and highly anisotropic plasma is produced as the result of gyrofrequency instabilities thought to be attributable to the directed motion of the initially trapped protons. In the beam-plasma experiments, dense energetic plasmas are produced by the intense fluctuating fields driven by the electron beam. The effort to understand the evolution of instabilities beyond the small amplitude limits inherent in the linearized stability theory discussed above has led to a set of modified quasi-linear equations, discussed in Sect. 8.5.

In summary, we stress the importance of the two very strong constraints possible in open-ended containment devices:

1. Because it is possible to make a true magnetic well in such devices, it appears possible to stabilize not only all low-frequency modes but perhaps the drift-cyclotron instability as well.
2. Because axial wavelengths must be limited to the length of the plasma (again, subject to the uncertain boundary conditions), Landau damping of the high-frequency ($\omega \sim n\omega_{ci}$, $k_{\parallel} \neq 0$) modes is possible provided the electrons can be raised to temperatures comparable to T_i.

Important unresolved questions are (1) reflection of Rosenbluth-Post loss-cone modes at the plasma extremities, and (2) stabilization of the flutelike instabilities due to sharply peaked fast-particle distributions superimposed on a low-temperature background ion population. Considerable progress has been reported recently in the first area;[21] a vigorous investigation of the second question has been initiated by the ORNL theory group (Sect. 8.4).

8.2 EFFECT OF POSITIVE MAGNETIC FIELD GRADIENTS ON THE DRIFT-CYCLOTRON INSTABILITY

The density and temperature gradients associated with confinement lead to a diamagnetic current which may be characterized by the (artificial) diamagnetic drift speed, U_0, where

$$U_{0j} \approx \frac{T_j}{eBR_p} . \tag{1}$$

Here T_j is the temperature of the jth species, B is the magnetic field strength, R_p is roughly the plasma radius, and e is the electronic charge. This diamagnetic drift can change the character of the cyclotron waves at $\omega \approx n\omega_{ci}$ if

$$\mathbf{k} \cdot \mathbf{U}_{0i} > n\omega_{ci} \tag{2}$$

for instability. Provided a prescribed density threshold is exceeded, the distorted cyclotron wave can then couple unstably to the drift wave associated with the precessional drift of electrons in the slightly inhomogeneous magnetic field.[22,23] From condition (2) it is clear that only waves of rather small wavelength can grow:

$$\frac{k_\perp U_{0i}}{n\omega_{ci}} \approx \frac{k_\perp \rho_i^2}{2nR_p} > 1 \text{ implies } \lambda_\perp < \left(\frac{\pi}{n}\frac{\rho_i}{R_p}\right)\rho_i .$$

A small positive gradient in the magnetic field strength leads to a precessional drift of the electrons and ions at a speed

$$V_{gj} \approx \frac{T_j}{eBR_c} , \tag{3}$$

[21] H. L. Berk *et al.*, Eighth Annual Meeting, Div. of Plasma Physics, American Physical Society, Boston, Mass., Nov. 2–5, 1966, paper 5P-6.

[22] N. A. Krall and T. K. Fowler, *Effect of Magnetic Curvature on the Drift-Cyclotron Instability*, GA-7393 (1966).

[23] W. M. Farr, Ph.D. thesis, University of Michigan (1966).

where $R_c^{-1} = (1/B)\,(dB/dr)$. These particle drifts introduce Doppler shifts, $\mathbf{k}\cdot\mathbf{V}_{ge}$ and $\mathbf{k}\cdot\mathbf{V}_{gi}$, which enhance the (unstable) electron drift wave–ion cyclotron wave coupling and which, by condition (2), can be relatively large. However, if the net shift, $|kV_{ge}| + |kV_{gi}|$, exceeds $n\omega_{ci}$, the original coupling is no longer possible and the drift-cyclotron mode cannot occur. The resulting criterion for stability is then roughly determined by

$$kV_{ge} + kV_{gi} > n\omega_{ci}\,,$$

while

$$kU_{0i} > n\omega_{ci}\,;$$

or

$$\frac{n\omega_{ci}}{U_{0i}}(V_{ge} + V_{gi}) > n\omega_{ci}\,;$$

hence

$$\left(\frac{T_e + T_i}{T_i}\right)\frac{R_p}{R_c} > 1\,.$$

These qualitative conclusions follow from the approximate dispersion relation

$$\epsilon(k,\tilde{\omega}) \simeq 1 + \frac{\omega_{pi}^2}{\omega_{ci}^2}\left[\frac{m}{M} + \frac{1 - Q_{0i}}{\lambda} + \frac{Q_{0i}}{kR_p}\frac{\omega_{ci}}{\tilde{\omega}} - \frac{Q_{0e}}{kR_p}\frac{\omega_{ci}}{\tilde{\omega} - \mathbf{k}\cdot(\mathbf{V}_{ge} - \mathbf{V}_{gi})} + \frac{Q_{ni}}{\lambda}\frac{\mathbf{k}\cdot\mathbf{U}_{0i} - \tilde{\omega}}{\tilde{\omega} - n\omega_{ci}}\right] = 0\,.$$

Here ω_{pi} and ω_{ci} are the ion plasma and gyrofrequencies, m/M is the ratio of electron to ion mass, $\lambda \equiv k^2\rho_i^2/2$, where ρ_i is the average ion gyroradius, $Q_{0i} \equiv e^{-\lambda}I_0(\lambda)$, $\tilde{\omega} \equiv \omega - \mathbf{k}\cdot\mathbf{V}_{gi}$, $Q_{0e} = e^{-\lambda_e}I_0(\lambda_e) \approx 1$, and $Q_{ni} \equiv e^{-\lambda}I_n(\lambda)$.

This dispersion relation is derived under the assumptions of (1) Maxwellian particle distributions, (2) equal densities of ions and electrons, and (3) sufficiently gentle magnetic gradients that the precessional speeds of the particles are much less than the orbital speed.

We have obtained the following approximate threshold condition:

$$\left(\frac{\omega_{ci}^2}{\omega_{pi}^2} + \frac{m}{M}\right)_{\text{threshold}} \approx \left(\frac{\rho_i}{2R_p}\right)^2\left(\frac{\omega_{ci}}{\mathbf{k}\cdot\mathbf{U}_{0i}}\right)^2\left[n - \frac{\mathbf{k}\cdot\mathbf{U}_{0i}}{\omega_{ci}}\left(\frac{T_i + T_e}{T_i}\right)\frac{\Delta B}{B}\right]^{-1}$$
$$\times\left\{\frac{\mathbf{k}\cdot\mathbf{U}_{0i}}{\omega_{ci}} - 2\left[n - \frac{\mathbf{k}\cdot\mathbf{U}_{0i}}{\omega_{ci}}\left(\frac{T_i + T_e}{T_i}\right)\frac{\Delta B}{B}\right] \pm 2\sqrt{\frac{2}{\sqrt{\pi}}\left(\frac{\rho_i}{2R_p}\right)\left(\frac{\mathbf{k}\cdot\mathbf{U}_{0i}}{\omega_{ci}} - n\right)}\right.$$
$$\left. + \frac{2}{\sqrt{\pi}}\left(\frac{\rho_i}{2R_p}\right)\left(1 - \frac{T_i + T_e}{T_i}\frac{\Delta B}{B}\right)\right\}\,.$$

Although it might appear from the factor

$$\left[n - \frac{\mathbf{k}\cdot\mathbf{U}_{0i}}{\omega_{ci}}\left(\frac{T_i + T_e}{T_i}\right)\frac{\Delta B}{B}\right]^{-1}$$

that arbitrarily small threshold densities might be possible, the maximum growth rate is given roughly by

$$\left(\frac{Im\,\omega}{\omega_{ci}}\right)_{\max} \approx \left[n - \frac{\mathbf{k}\cdot\mathbf{U}_{0i}}{\omega_{ci}}\left(\frac{T_i + T_e}{T_i}\right)\frac{\Delta B}{B}\right]\sqrt{\frac{2e^{-\lambda}I_n(\lambda)\left(\frac{\mathbf{k}\cdot\mathbf{U}_{0i}}{\omega_{ci}} - n\right)}{(\mathbf{k}\cdot\mathbf{U}_{0i}/\omega_{ci})}}\,,$$

so that the maximum growth rate goes to zero as the threshold density decreases. In fact, one sees that the maximum growth rate is limited in roughly the following way:

$$\left(\frac{\operatorname{Im}\omega}{\omega_{ci}}\right)_{\max} \lesssim \left[n - \frac{\mathbf{k}\cdot\mathbf{U}_{0i}}{\omega_{ci}}\left(\frac{T_i + T_e}{T_i}\right)\frac{\Delta B}{B}\right] \sqrt{\frac{\rho_i}{2n\sqrt{\pi}R_p}} \; .$$

8.3 CONVECTIVE VS ABSOLUTE INSTABILITY CALCULATIONS

With the motivation presented in Sect. 8.1, we have constructed codes for investigating solutions $\tilde{\omega}(k)$ and $\tilde{k}(\omega)$ of dispersion relations $D(\omega,k) = 0$, where ω and k are complex. Earlier versions of these codes were described in the preceding semiannual report.[24] In the present form, solutions $\tilde{\omega}(k)$ are tabulated[25] on a grid in the complex k plane, or solutions $\tilde{k}(\omega)$ are tabulated on a grid in the complex ω plane. The dispersion relation is that of Guest and Dory,[26] except that provision is made for having three species, "hot" and "warm" ions as well as "warm" electrons. The new codes have been used to verify and extend the work of Beasley and Guest,[27] which included a demonstration that the Harris two-temperature instabilities[28,29] of infinite, homogeneous, uniformly magnetized plasmas could be either convective or absolute, depending upon the plasma density.

The dispersion relation considered is

$$1 = \sum_{\text{species}} \left(\frac{\omega_p}{k\alpha_{\parallel}}\right)^2 \sum_{m=-\infty}^{\infty} \left[C_m(\lambda)\, Z'\left(\frac{\omega - m\Omega}{k_{\parallel}\alpha_{\parallel}}\right) - 2m\frac{\alpha_{\parallel}^2}{\alpha_{\perp}^2} D_m(\lambda)\frac{\Omega}{k_{\parallel}\alpha_{\parallel}}\, Z\left(\frac{\omega - m\Omega}{k_{\parallel}\alpha_{\parallel}}\right)\right] , \quad (1)$$

where $Z(\zeta) = i\pi^{1/2}\exp(-\zeta^2)\,[1 + \operatorname{erf}(i\zeta)]$, ω_p = plasma frequency, Ω = cyclotron frequency, $C_m(\lambda) = 2\pi\int_0^\infty dv_\perp v_\perp J_m^2(k_\perp v_\perp/\Omega)\; g(v_\perp/\alpha_\perp)$, $D_m(\lambda) = -\pi\alpha_\perp \times \int_0^\infty dv_\perp J_m^2(k_\perp v_\perp/\Omega)\; g'(v_\perp/\alpha_\perp)$, assuming that the particle distribution functions are $\propto \exp(-v_{\parallel}^2/\alpha_{\parallel}^2)\; g(v_\perp/\alpha_\perp)$. For the present results, $g_{\text{ion}}(x) = x^2 e^{-x^2}$, and $g_{\text{electron}}(x) = e^{-x^2}$.

The dispersion relation may be written

$$1 = \sum_{\text{species}} \left(\frac{\omega_p}{\Omega h}\right)^2 \sum_{-\infty}^{\infty} \left[C_m(\lambda)\, Z'\left(\frac{z-m}{h}\right) - 2mT\, D_m(\lambda)\frac{1}{h} Z\left(\frac{z-m}{h}\right)\right] , \quad (2)$$

where species subscripts are implied on ω_p, Ω, h, C, D, λ, z, and T. Notice that $h = k_{\parallel}\alpha_{\parallel}/\Omega$, $\lambda = k_\perp^2\alpha_\perp^2/2\Omega^2$, $z = \omega/\Omega$, and $T = \alpha_{\parallel}^2/\alpha_\perp^2$.

In the present work we investigate the "loss-cone" modes of ref. 26. The "hot" ion distribution function behaves as $(v_\perp/\alpha_\perp)^2 \cdot \exp(-v_\perp^2/\alpha_\perp^2 - v_{\parallel}^2/\alpha_{\parallel}^2)$ and the electron distribution function like $\exp(-v^2/\alpha_e^2)$. No "warm" ion terms have been included so far. We consider cylindrical waves propagating parallel to the external magnetic field ($\chi_{\parallel}$ direction), so that perturbed potentials behave as $\exp(-i\omega t + ik_{\parallel}\chi_{\parallel} + il\theta) \times J_l(k_\perp r)$. For high densities, where large $k_\perp$ solutions could be unstable, one would have to investigate the propagation properties of the radial potential dependence by allowing $k_\perp$ to be complex. The present work considers only the properties of propagation parallel to the field. We rely on

[24] *Thermonuclear Div. Semiann. Progr. Rept. Apr. 30, 1966*, ORNL-3989.

[25] Solutions to $F(z) = 0$ are found by Muller's technique: $F(z)$ is approximated by a function of the form $G(z) = (z - a)/(bz + c)$, where a, b, and c are determined by setting $G(z_j) = F(z_j)$ at three points z_1, z_2, z_3 near an initial estimate for a solution. The value a is then an improved estimate, and the method can be iterated. This procedure gives very rapid convergence and seems to be more suitable than that described in ref. 24.

[26] G. E. Guest and R. A. Dory, *Phys. Fluids* **8**, 1853 (1965).

[27] C. O. Beasley, Jr., and G. E. Guest, Eighth Annual Meeting, Div. of Plasma Physics, American Physical Society, Boston, Mass., Nov. 2–5, 1966, paper 8L-2.

[28] E. G. Harris, *J. Nucl. Energy* **C2**, 138 (1961).

[29] G. K. Soper and E. G. Harris, *Phys. Fluids* **8**, 984 (1965).

boundary conditions such as zero perturbed potential at nearby conducting vacuum tank walls to determine the allowed spectrum of real $k_\perp$.

The parameterization is as follows: $T \equiv \alpha_{\parallel}^2/\alpha_\perp^2$, $\theta \equiv \alpha_e^2/\alpha_{\parallel}^2$, $\lambda \equiv k_\perp^2\ \alpha_\perp^2/2\Omega_i^2$, $z \equiv x + iy \equiv \omega/\Omega_i$, and $h \equiv k_{\parallel}\ \alpha_{\parallel}/\Omega_i$, where Ω_i = ion cyclotron frequency, and ω_e = electron plasma frequency.

Table 8.2 presents the results of several cases investigated. For convective cases we tabulate the maximum positive $y = \mathrm{Im}(\omega/\Omega_i)$ for real h and the value of complex h at which y [maximized over $\mathrm{Re}(h)$] vanishes as $|\mathrm{Im}(h)|$ increases. For absolute cases we list $h = h_r + ih_i$ at the saddle point of $\widetilde{\mathrm{Re}}\ \tilde{z}(h)$, which is also a saddle point of $\mathrm{Im}\ \tilde{z}(h)$.

Parameters for this survey were chosen in the following way. The results of ref. 26 indicate that λ in the vicinity 1 to 10 is interesting for low-density $[\omega_e/\Omega_i \lesssim (M_i/M_e)^{1/2}]$ cases; we chose $\lambda = 5$ as a starting point because the ion $D_m(\lambda)$ is then most negative. This makes the radial "wavelength" $\sim k^{-1} = \rho_i(2\lambda)^{-1/2} \cong 0.3\rho_i$, where $\rho_i \equiv \alpha_\perp/\Omega_i$ is a representative ion gyroradius. We took $T = 1/2$ to make the distribution sufficiently "isotropic" to eliminate the Soper-Harris anisotropy modes[28,29] and restricted our attention to the cyclotron-loss-cone modes of ref. 26. The electron temperature θ was given a value regarded as representative both of present experiments and projected "fusion reactors." The variation of thresholds with θ has been shown in ref. 26 to be slow. The product θT enters characteristically, and cases 3 and 10 were run to verify that the results do not depend critically on α_e, electron thermal speed. In doubling θT we find that the threshold between absolute and convective zones moves only slightly, from $\omega_e/\Omega \cong 43$ to about 52. Parameter n tells which cyclotron resonance term is important for the unstable mode in question. Thus $\mathrm{Re}\ \omega/\Omega_i \cong n$.

At $\omega_e/\Omega_i = 46.9$, where the $n = 1$ mode is absolute, we have scanned λ to find the "worst" mode, which is $\lambda = 2.5 \pm 0.25$. This value maximizes $\mathrm{Im}\ \omega$ and $|\mathrm{Im}(k_{\parallel})|$ at the saddle point.

In accordance with the approximate analytical results suggested in ref. 26 and obtained by keeping only the electron contribution and the "resonant" nth ion term in the sum on m in Eq. (1), the instabilities occur only for those λ's that make the ion $D_m(\lambda)$ negative. Figure 8.1 shows the first few $D_m(\lambda)$ as functions of λ for the distribution $g(x) = x^2\, e^{-x^2}$.

Table 8.2. Summary of Results of Convective/Absolute Test on Discrete Loss-Cone Modes

Case	ω_e/Ω_i	λ	T	Θ	n	Result	$x = \mathrm{Re}\frac{\omega}{\Omega_i}$	$y = \mathrm{Im}\frac{\omega}{\Omega_i}$	$h_r = \mathrm{Re}\frac{k_{\parallel}\alpha_{\parallel}}{\Omega_i}$	$h_i = \mathrm{Im}\frac{k_{\parallel}\alpha_{\parallel}}{\Omega_i}$
1	41.25	5.0	½	1/20	1	Convective		0.036	0.042	−0.0063
2	46.90	5.0	½	1/20	1	Absolute	0.962	0.0021	0.029	−0.011
3	46.90	5.0	1	1/20	1	Convective		0.016	0.048	−0.005
4	46.90	2.5	½	1/20	1	Absolute	0.966	0.013	0.022	−0.013
5	46.90	1.0	½	1/20	1	Stable				
6	46.90	2.0	½	1/20	1	Absolute	0.970	0.0092	0.022	−0.011
7	46.90	3.0	½	1/20	1	Absolute	0.964	0.0125	0.023	−0.013
8	46.90	4.0	½	1/20	1	Absolute	0.962	0.0081	0.027	−0.012
9	46.90	10.0	½	1/20	1	Stable				
10	52.00	5.0	1	1/20	1	Absolute	0.955	0.0006	0.036	−0.011
11	66.55	5.0	½	1/20	1	Absolute	0.963	0.019	0.021	−0.015
12	66.55	5.0	½	1/20	2	Convective		0.051	0.065	−0.0044
13	66.55	5.0	½	1/20	3	Stable				

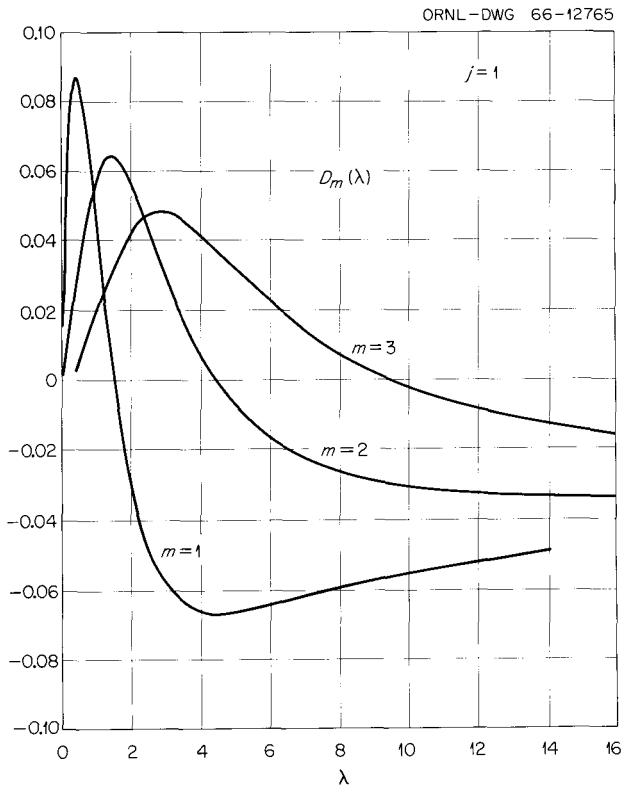

Fig. 8.1. The Function $D_m(\lambda)$ vs λ for $m = 1, 2, 3$.

Cases 11 to 13 further verify the last point and show that the saddle-point values for $\mathrm{Im}(\omega)$ and $|\mathrm{Im}(k_{\parallel})|$ increase markedly with increasing density, and that higher harmonics become unstable as the density increases.

Cases 14 to 25 (Table 8.3) are at sufficiently high density and small radial "wavelength" ($\cong 0.06\ \rho_i$) that we expect to approach the "continuum" case analyzed by Post and Rosenbluth.[30] Since the first 12 D_m are negative at $\lambda = 150$, we expect the $n = 1$ through 12 modes to be unstable. Figure 8.2 shows $\mathrm{Im}(\omega)$ as a function of $\mathrm{Re}(k_{\parallel})$ very near but not on the real $k_{\parallel}$ axis. Exactly on the axis, there appear to be some numerical difficulties concerned with the proximity of another Riemann sheet and with the choice of initial estimates for the solution. This problem is being investigated very carefully.

We see that a continuum exists because the widths of the various peaks in $\mathrm{Im}(\omega)$ exceed the separations. The values become a large fraction of gyrofrequency, but we have not observed growth rates in excess of ion gyrofrequency, so that it

[30] R. F. Post and M. N. Rosenbluth, *Phys. Fluids* **9**, 730 (1966).

Table 8.3. Characteristics of the Individual Resonances in a Continuum Case

Case	ω_e/Ω_i	λ	T	Θ	l	$y = \mathrm{Im}\dfrac{\omega}{\Omega_i}$	$h_r = \mathrm{Re}\dfrac{k_{\parallel}\alpha_{\parallel}}{\Omega_i}$
14	400	150	$\frac{1}{2}$	$\frac{1}{20}$	1	0.056	0.029
15	400	150	$\frac{1}{2}$	$\frac{1}{20}$	2	0.114	0.059
16	400	150	$\frac{1}{2}$	$\frac{1}{20}$	3	0.167	0.089
17	400	150	$\frac{1}{2}$	$\frac{1}{20}$	4	0.218	0.120
18	400	150	$\frac{1}{2}$	$\frac{1}{20}$	5	0.260	0.151
19	400	150	$\frac{1}{2}$	$\frac{1}{20}$	6	0.294	0.184
20	400	150	$\frac{1}{2}$	$\frac{1}{20}$	7	0.308	0.216
21	400	150	$\frac{1}{2}$	$\frac{1}{20}$	8	0.307	0.250
22	400	150	$\frac{1}{2}$	$\frac{1}{20}$	9	0.282	0.282
23	400	150	$\frac{1}{2}$	$\frac{1}{20}$	10	0.243	0.315
24	400	150	$\frac{1}{2}$	$\frac{1}{20}$	11	0.158	0.348
25	400	150	$\frac{1}{2}$	$\frac{1}{20}$	12	0.058	0.378

remains an open question how the cyclotron-loss-cone modes of ref. 26 become the continuum modes of ref. 30.

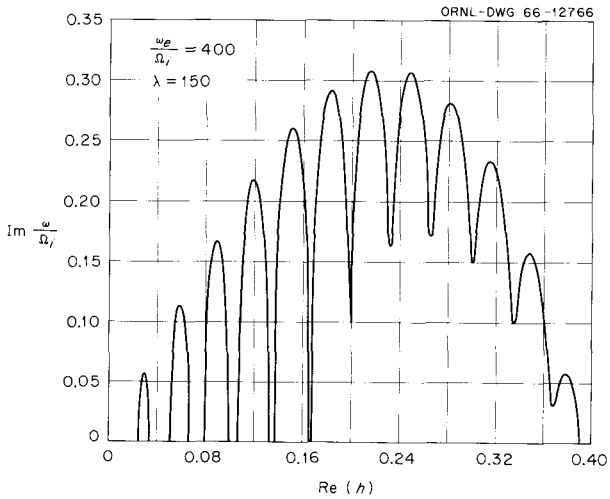

Fig. 8.2. Im ω/Ω_i vs Re h = Re $k_{\parallel}\alpha_{\parallel}/\Omega_i$ for the Continuum Case: $\omega_e/\Omega_i = 400$, $\lambda = 150$.

We would like to comment on our interpretation of the numerical data in terms of the Briggs-Bers[31] criteria for the determination whether waves are convective or absolute. It is of course impossible to investigate the entire complex $k_{\parallel}$ plane on vanishingly small grid, and as mentioned earlier, numerical uncertainties arise in regions where different Riemann sheets approach each other. At this time it seems best to hedge on the results quoted so far. It is felt that they are correct, but there are some questions not yet fully resolved. The investigation of these points is in progress.

To make the unresolved points more clear, we give in Fig. 8.3 a sketch of Re(ω) and Im(ω) contours in the complex h plane for case 4. Dashed lines represent loci where Re(ω) is constant and solid lines those where Im(ω) is constant. We see that on the real-h axis, Im(ω) is

[31] R. J. Briggs, *Electron-Stream Interaction with Plasmas*, Research Monograph No. 29, MIT Press, Cambridge, Mass., 1964.

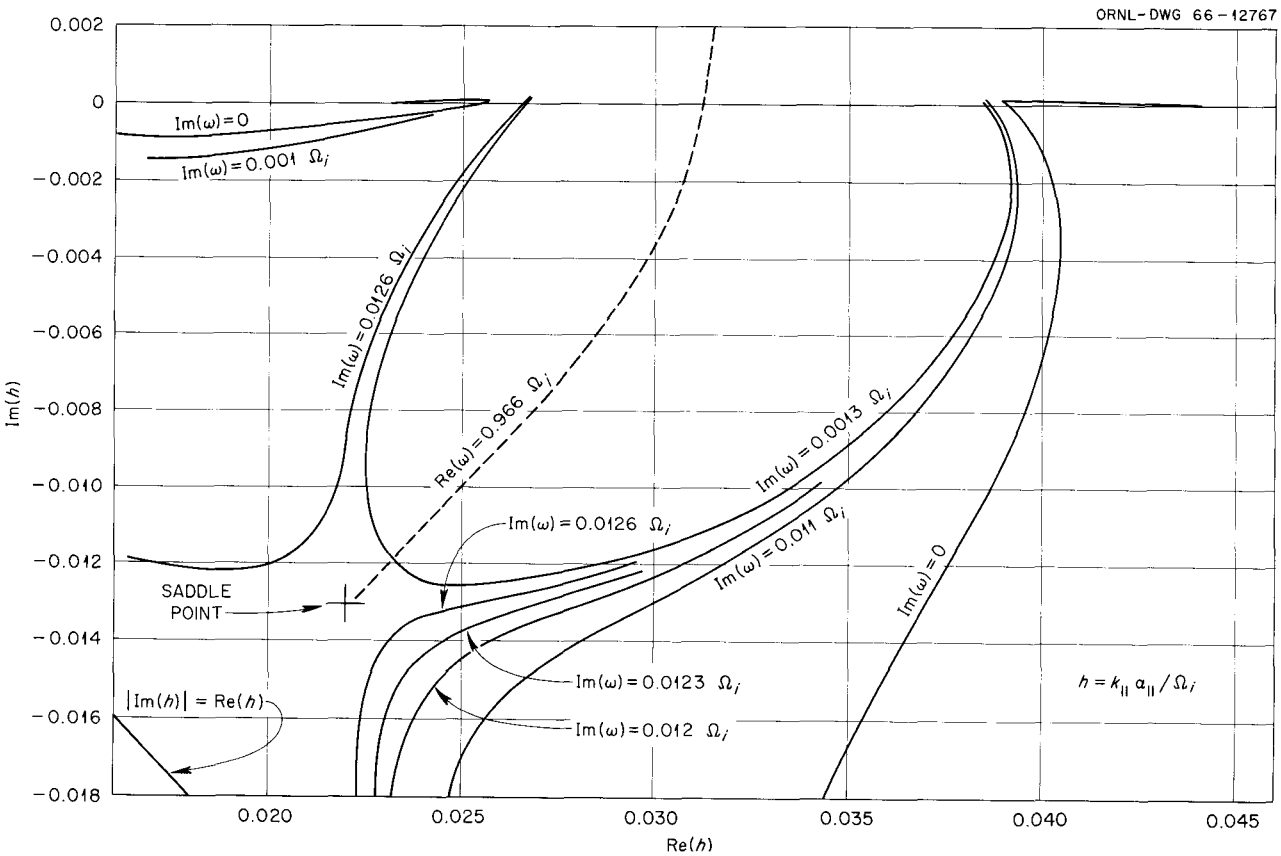

Fig. 8.3. Contours in the Complex h Plane of Constant Im(ω) and Constant Re(ω) for Case 4.

negative except in the interval 0.026 to 0.039. The contour $\mathrm{Im}(\omega) = 0$ does not extend continuously from one end of this interval to the other, but in the $\mathrm{Im}(h) < 0$ half plane it appears to be asymptotic to the line $\mathrm{Im}(h) = -\mathrm{Re}(h)$. In the $\mathrm{Im}(h) > 0$ half plane, the $\mathrm{Im}(\omega)$ contour suffers two very sharp turns and again does not bridge the gap from $h = 0.026 + i\cdot 0$ to $0.039 + i\cdot 0$. This would normally satisfy the conditions for absolute instability; but one would like to look more carefully at the sharp corners in the $\mathrm{Im}(\omega) = 0$ contours to eliminate the possibility of error, and it is this careful look that has been impeded by apparent numerical difficulties.

8.4 FLUTELIKE ELECTROSTATIC MODES IN TWO-COMPONENT ION PLASMAS

The dispersion relation for electrostatic waves propagating perpendicular ("flutelike") to a uniform external magnetic field **B** in a uniform plasma was given by Harris[32] and was considered by Dory, Guest, and Harris[33] and many others. In these papers attention was concentrated on instabilities caused by the energy reservoir inherent in a "loss-cone" distribution of a single species of particles. Two other papers[34,35] have discussed unstable modes which occur when the system consists of two groups of particles, otherwise identical, which have different temperatures for their distributions of $v_\perp$ (velocity perpendicular to **B**) or which have non-Maxwellian distribution of $v_\perp$. The article by Hall, Heckrotte, and Kammash[34] presents data for instabilities, near cyclotron harmonics in a plasma with one component having no $v_\perp$ and another with a monoenergetic distribution of $v_\perp$. Perlstein, Rosenbluth, and Chang[35] analyze the behavior of a two-component system at high plasma density for very short wavelengths ($k_\perp \rho_i \gg 1$, where ρ_i is the mean gyroradius for the hotter species).

For purposes of comparison with experiment and for assessing the instability properties of experiments not intended to reach the high-density "reactor regime," it would be useful to have detailed information which includes the effect of spreading of the velocities of the components and the behavior when $k_\perp \rho_i \lesssim 1$.

The dispersion relation for plane electrostatic waves with $k\cdot \mathbf{B} = 0$ is[36]

$$1 = 2 \sum_{\text{species}} \left(\frac{\omega_p}{k\alpha_\perp}\right)^2 \sum_{m=-\infty}^{\infty} \frac{m\Omega}{\omega - m\Omega} \times D_m(k\alpha_\perp/\Omega) , \quad (1)$$

where

$$D_m(b) = -\frac{1}{2}\alpha_\perp^2 \int d^3v\, J_m^2 \left(b\frac{v_\perp}{\alpha_\perp}\right)\frac{1}{v_\perp}\frac{\partial F_0}{\partial v_\perp} , \quad (2)$$

in which ω_p, Ω, and ω = plasma, cyclotron, and wave frequency, $k = k_\perp$ = wave number, F_0 = velocity distribution function with $\int d^3v F_0 = 1$, and $\alpha_\perp$ is a velocity scaling parameter. We consider distribution functions which have arbitrary dependence on $v_{\parallel} = v\cdot \mathbf{B}/|\mathbf{B}|$ and which are proportional to $(v_\perp/\alpha_\perp)^{2j} \exp(-v_\perp^2/\alpha_\perp^2)$. If $j = 0$, the distribution is Maxwellian (in $v_\perp$), and if $j = 1, 2, 3, \ldots$, the distribution simulates the loss-cone plasma in a mirror trap.

The functions D_m obtained for this set of distributions are described in ref. 36, where parameter $\lambda = \frac{1}{2}B^2$ is used. Using a superscript to indicate j, we have

$$\begin{aligned} D_m^{(0)} &= I_m(\lambda)\, e^{-\lambda} , \\ D_m^{(j+1)} &= (j+1)^{-1}\,[j D_m^{(j)} + \lambda(d/d\lambda)\, D_m^{(j)}] , \end{aligned} \quad (3)$$

from which

$$\begin{aligned} D_m^{(1)} &= e^{-\lambda}\{[\lambda]\, I_m'(\lambda) - [\lambda]\, I_m(\lambda)\} , \\ D_m^{(2)} &= e^{-\lambda}\{[-\lambda^2 + \tfrac{1}{2}\lambda]\, I_m'(\lambda) - [-\lambda^2 + \lambda - \tfrac{1}{2}m^2] \\ &\qquad \times I_m(\lambda)\} , \quad (4) \\ D_m^{(3)} &= e^{-\lambda}\{[\tfrac{2}{3}\lambda^3 - \tfrac{3}{2}\lambda^2 + \tfrac{1}{3}\lambda + \tfrac{1}{6}m^2\lambda]\, I_m'(\lambda) \\ &\quad - [\tfrac{2}{3}\lambda^3 - 1\tfrac{1}{6}\lambda^2 + \lambda + \tfrac{1}{2}m^2\lambda - \tfrac{1}{2}m^2]\, I_m(\lambda)\} \ldots , \end{aligned}$$

where the $I_m(\lambda)$ are modified Bessel functions of the first kind. From Eqs. (3), one can easily find

[32] E. G. Harris, *Phys. Rev. Letters* **2**, 34 (1959); *J. Nucl. Energy* **C2**, 138 (1961).

[33] R. A. Dory, G. E. Guest, and E. G. Harris, *Phys. Rev. Letters* **14**, 131 (1965).

[34] L. S. Hall, W. Heckrotte, and T. Kammash, *Phys. Rev.* **139**, 117A (1965).

[35] L. O. Perlstein, M. N. Rosenbluth, and D. B. Chang, *Phys Fluids* **9**, 953 (1966).

[36] G. E. Guest and R. A. Dory, *Phys. Fluids* **8**, 1853 (1965).

the recurrence formula for the coefficients of the polynomials in brackets in the $D_m^{(j)}$ of Eqs. (4). The functions $D_m^{(j)}$ as functions of λ are then easily computed, and tables are available for j up to 20. For large j and for $\lambda \lesssim j^{1/2}$, the $D_m^{(j)}$ are qualitatively similar to their limit at $j = \infty$: $D_m^{(\infty)} = \lambda(d/d\lambda) J_m^2(\sqrt{2\lambda})$, where J_m is the usual Bessel function. Figure 8.4 shows the distribution functions for $j = 1, 2, \ldots$, and Figs. 8.5 to 8.11 show the $D_m^{(j)}$ as functions of λ. From the defining relation one easily establishes the following useful sum rules: For populations with $j > 0$, $\sum_{m=-\infty}^{\infty} D_m^{(j)} = 0$, while $\sum_{m=-\infty}^{\infty} D_m^{(0)} = 1$.

Consider a plasma consisting of "hot" ions, "warm" ions, and electrons. At frequencies $\omega \ll \Omega_e$, the electron contribution to Eq. (1) is constant and small compared to ion terms, and

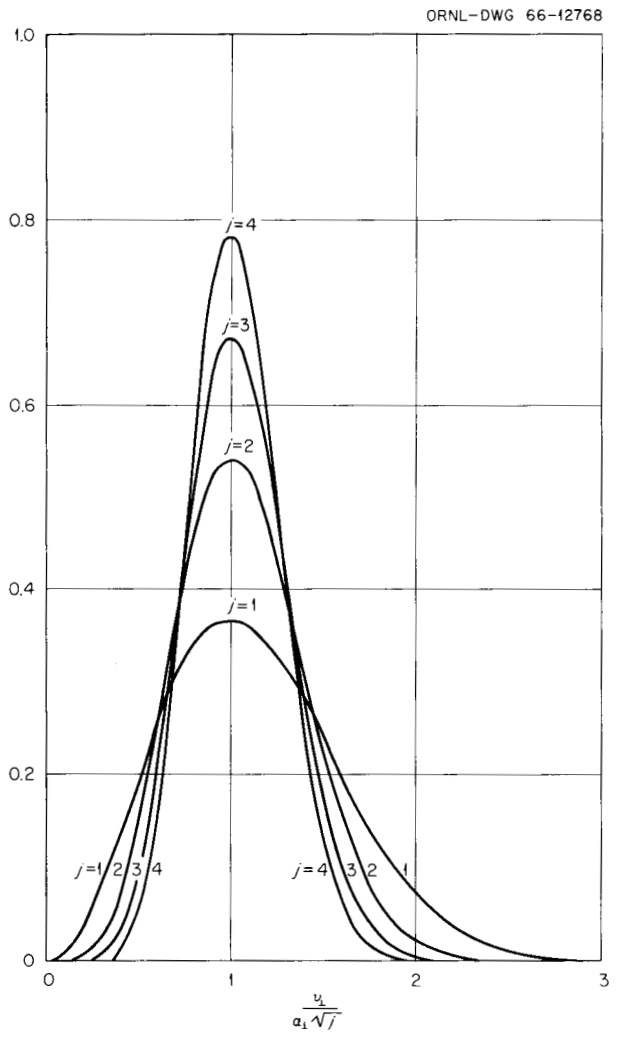

Fig. 8.4. Distribution of $v_\perp$ for $j = 1, 2, 3, 4$.

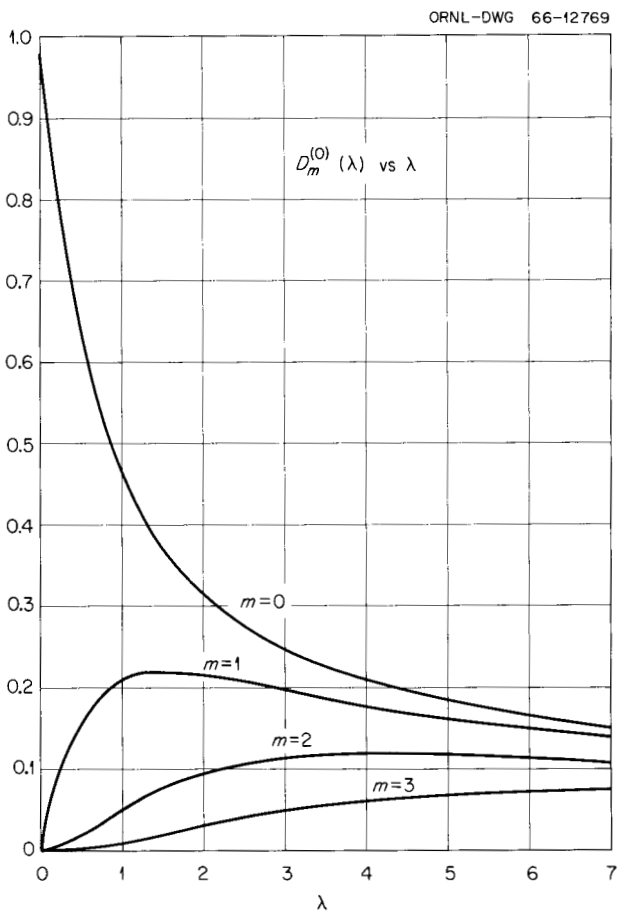

Fig. 8.5. $D_m^{(0)}$ as a Function of λ.

we drop it. We assume the two ion populations differ only in $v_\perp$ dependence, a situation representative of many experiments. The dispersion relation is then

$$1 = 2\left(\frac{\omega_p}{b\Omega}\right)^2 \sum_{m=-\infty}^{\infty} \frac{m\Omega D_m^{(T)}(b)}{\omega - m\Omega}$$

$$\equiv U\left(\frac{\omega}{\Omega}, b\right) \cdot \left(\frac{\omega_p}{\Omega}\right)^2 , \quad (5)$$

where ω_p is the total ion plasma frequency $[4\pi(n_1 + n_2)e^2/m]^{1/2}$; n_1, n_2, α_1, and α_2 are the density and $\alpha_\perp$ for the hot and warm ions; $b = k\alpha_1/\Omega$; $n_T = n_1 + n_2$, and

$$D_m^{(T)}(b) = \frac{n_1}{n_T} D_m^{(\text{hot})}(b) + \frac{n_2}{n_T}\frac{\alpha_1^2}{\alpha_2^2} D_m^{(\text{warm})}\left(\frac{\alpha^2}{\alpha_1} b\right) . \quad (6)$$

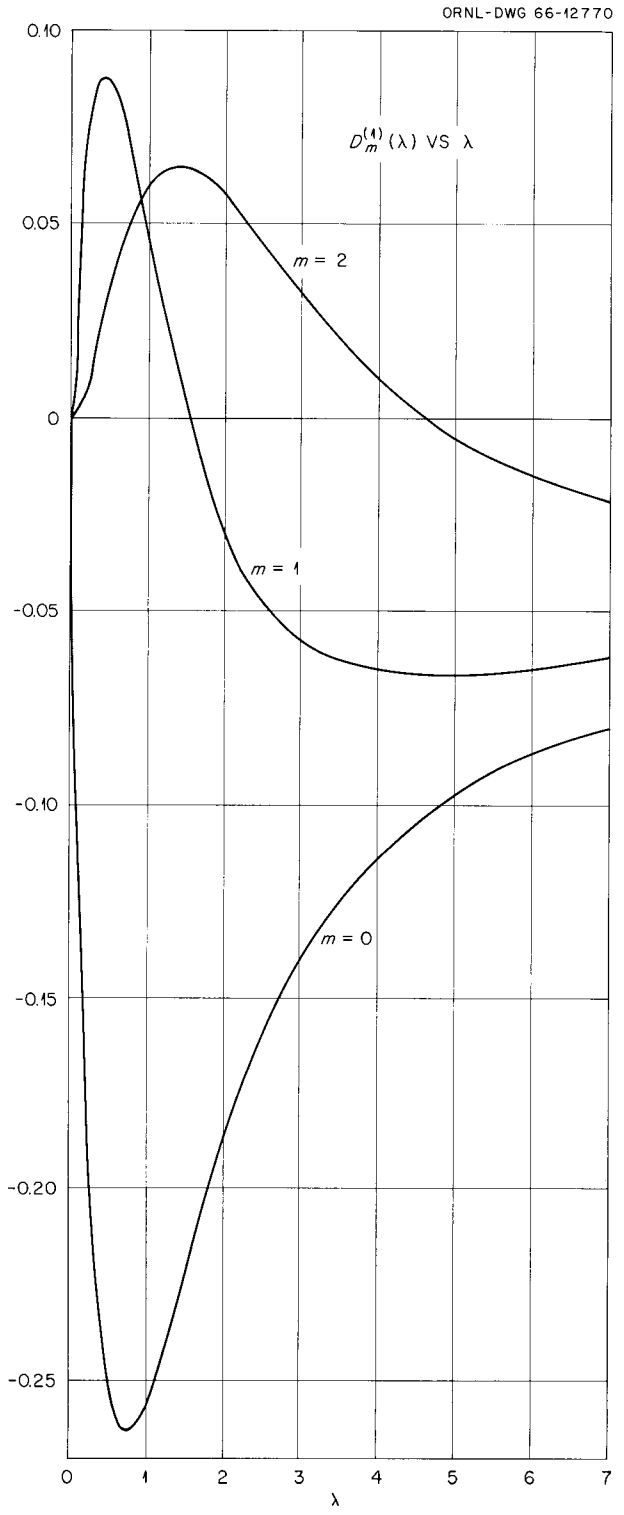

Fig. 8.6. $D_m^{(1)}$ as a Function of λ.

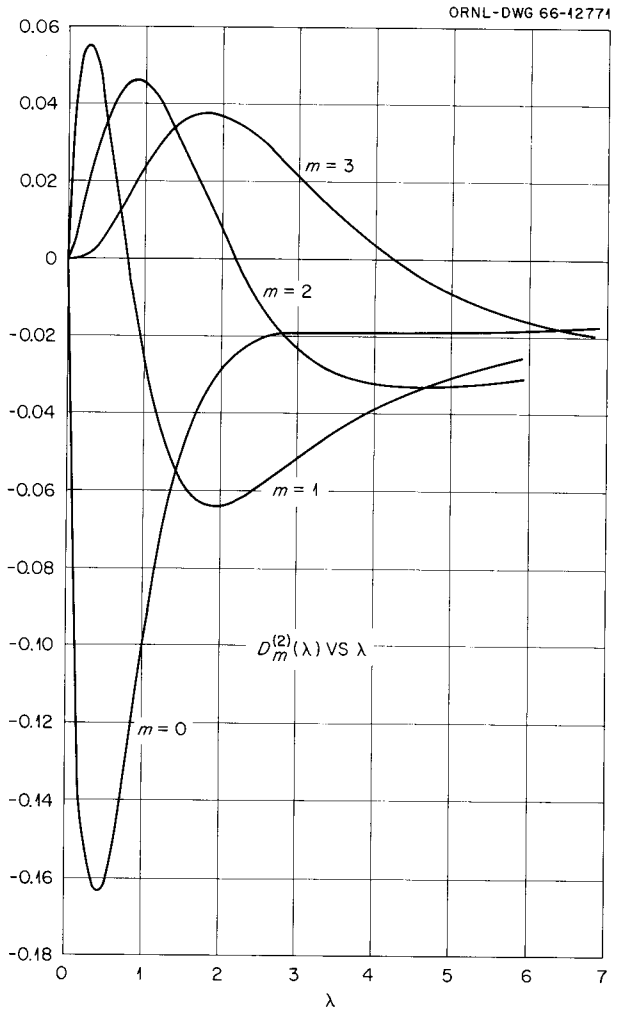

Fig. 8.7. $D_m^{(2)}$ as a Function of λ.

Conditions for instability at frequencies above gyrofrequency are those listed in ref. 33. Since the D_n have been defined differently here [by factor $-(1/2)\alpha_\perp^2$], the criteria take a slightly different form: If for some λ, $D_n^{(T)} > 0$ and $D_{n+1}^{(T)} < 0$, then one should carefully investigate the range $n < \omega/\Omega < n + 1$. In this range $U(\omega/\Omega, b)$ as a function of ω/Ω will have at least one minimum, say at $\omega/\Omega = x_0$. If $U(x_0, b) > 0$, then instability exists provided $(\omega_p/\Omega)^2 > 1/U(x_0, b)$. A maximum of U may also exist in conjunction with a second minimum. In that case there is a small range of $(\omega_p/\Omega)^2$ in which instability occurs. The latter situation is most likely very near ω/Ω = an integer and is usually characterized by a very narrow unstable density zone at high density,

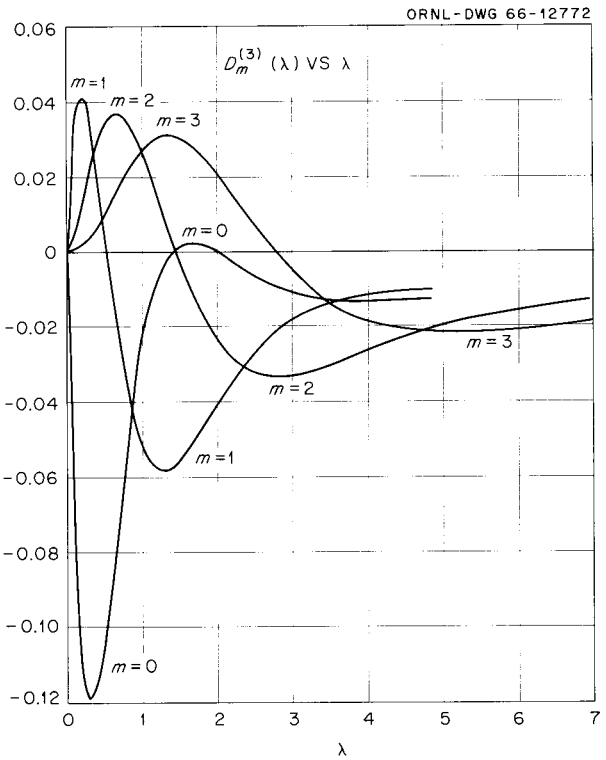

Fig. 8.8. $D_m^{(3)}$ as a Function of λ.

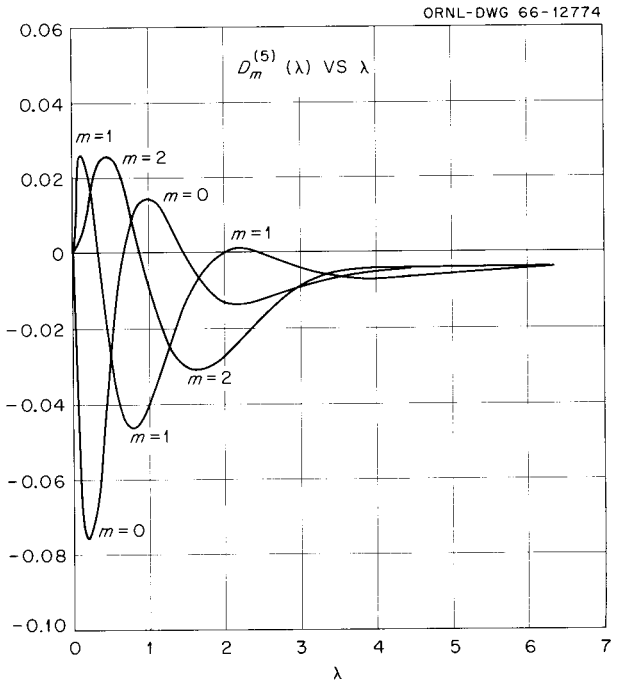

Fig. 8.10. $D_m^{(5)}$ as a Function of λ.

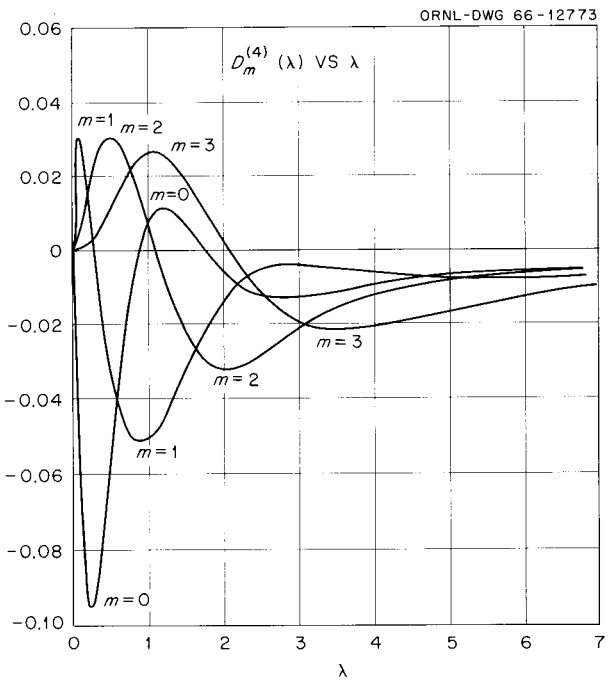

Fig. 8.9. $D_m^{(4)}$ as a Function of λ.

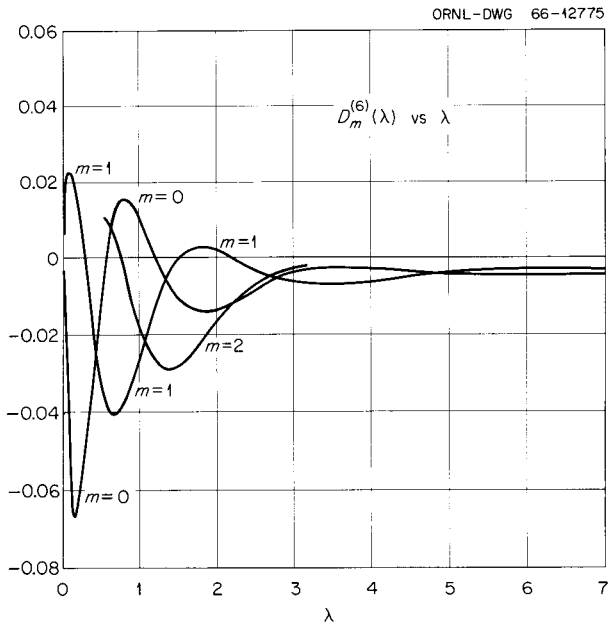

Fig. 8.11. $D_m^{(6)}$ as a Function of λ.

small growth rates ($\ll\Omega$), and distribution functions having very sharp peaks.

Instability can also exist below gyrofrequency. The first of two such types of unstable modes can exist very near $\omega = \pm\Omega$ if $D_1^{(T)}$ is much smaller than the other $D_m^{(T)}$ and can be observed by detailed analysis of $U(\omega/\Omega,\ b)$. It is also characterized by high densities, small unstable regions in both k and ω_p/Ω, small growth rates, and sharp distribution functions. The second type occurs with $\mathrm{Re}(\omega)$ identically zero. The criterion for its existence is that $U(0,b) > 0$ for some λ and that $(\omega_p/\Omega)^2 \gtrless 1/U\ (0,b)$ if $D_1^{(T)} \lessgtr 0$. The threshold density is especially easy to evaluate, since

$$U(0,b) = -\frac{2}{b^2}\left[\sum_{m=-\infty}^{\infty} D_m^{(T)} - D_0^{(T)}\right].$$

Detailed parametric studies have not yet been made, but from inspection of the graphs of the $D_m^{(j)}$ and using the almost-sufficient instability criteria $D_n^{(T)} > 0$ and $D_{n+1}^{(T)} < 0$, one concludes that instabilities arise even when the hot distribution has a fairly large relative half spread (for $j = 1$, $\delta v_\perp/v_\perp \cong 30\%$), in contradistinction to the single species modes of ref. 33. The $\mathrm{Re}(\omega) \equiv 0$ modes are special in that they occur only when one population is strongly peaked at nonzero $v_\perp$.

The growth rates for large $\delta v_\perp/v_\perp$ are expected to be very small ($\ll\Omega$) and the unstable ranges of density and wavelength very narrow, so that here, as in the cases considered in ref. 34, one is left quite dissatisfied by the answer to the question, "Where are modes damped and where antidamped?" It is hoped that by understanding the quantitative growth rates in unstable zones, one may be able to provide a realistic evaluation of threshold conditions.

8.5 NONLINEAR PLASMA PHENOMENA FROM A QUANTUM-MECHANICAL VIEWPOINT

E. G. Harris[37]

8.5.1 Introduction

We have taken the unconventional approach of describing nonlinear phenomena by quantum mechanics and ultimately taking the classical limit. This has the conceptual advantage of describing the phenomena in terms of the emission, absorption, and scattering of particles (electrons and ions) and quasi-particles (i.e., the quanta of the elementary excitations of the plasma such as plasmons, phonons, photons, etc.). Once the interaction Hamiltonian is known, the rate for any process is found by using the standard formulas of time-dependent perturbation theory – the so-called Fermi Golden Rules.

We shall give a qualitative discussion of calculations which have been made using this approach. The details of the calculations have been or will be published elsewhere. It is convenient to describe the work by means of diagrams. We shall adopt the convention of representing electrons and ions by solid lines ($\xrightarrow{e}$) and the symbol e, plasmons (plasma oscillations) by wavy lines ($\lambda\rightsquigarrow$) and the symbol λ, phonons (ion sound waves) by broken lines ($\xleftarrow{\nu}$ $- - \longrightarrow$) and the symbol ν, and photons by dashed lines ($\text{----}\gamma\text{----}>$) and the symbol γ. When we discuss particles in a magnetic field we will draw the particle lines as (e ⌇⌇⌇⌇) to represent the particle spiraling about a magnetic field line.

8.5.2 Plasma with No Magnetic Field

If $\mathbf{B} = 0$, the elementary excitations of a plasma are plasmons (plasma oscillations), phonons (ion sound waves), and photons (transverse electromagnetic waves).

As a first step we shall ignore the ions, phonons, and photons and discuss the processes in which electrons emit and absorb plasmons. The interaction Hamiltonian for these processes has been given by Pines and Schrieffer.[38] We can write coupled equations for $N_\lambda(\mathbf{q})$, the number of plasmons of wave vector $\mathbf{q}$, and $N_e(\mathbf{k})$, the number of electrons of momentum $\hbar\mathbf{k}$. Schematically they are

$$\frac{\partial N_\lambda(\mathbf{q})}{\partial t} \sum_{\mathbf{k}}$$

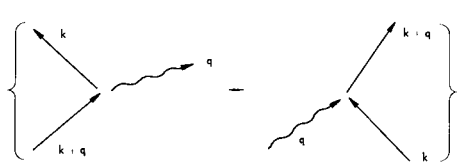

(1)

[37]Consultant, the University of Tennessee, Knoxville.

[38]D. Pines and J. R. Schrieffer, *Phys. Rev.* **125**, 804 (1962).

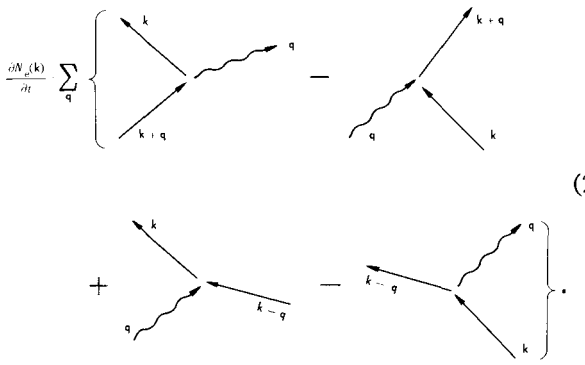

(2)

In Eq. (1) we have added all processes in which a plasmon of wave number **q** is produced and subtracted those in which a plasmon of wave number **q** is destroyed. Equation (2) was obtained in a similar way. The diagrams in Eqs. (1) and (2) are replaced by the transition probabilities per unit time, given by

$$\frac{2\pi}{\hbar}|\text{matrix element}|^2\,\delta(E_{\text{initial}} - E_{\text{final}})\,. \qquad (3)$$

When this is done and the classical limit is taken, one finds

$$\frac{\partial P(\mathbf{q})}{\partial t} = 2\gamma_{\mathbf{q}} P(\mathbf{q}) + S(\mathbf{q})\,, \qquad (4)$$

$$\frac{\partial f(\mathbf{v})}{\partial t} = \frac{\partial}{\partial \mathbf{v}}\cdot\left[\mathbf{D}(\mathbf{v})\cdot\frac{\partial f}{\partial \mathbf{v}}\right] + \frac{\partial}{\partial \mathbf{v}}\cdot\left[\mathbf{A}(\mathbf{v})f\right]\,, \qquad (5)$$

where

$$\gamma_{\mathbf{q}} = \frac{2\pi^2 e^2 \Omega_q}{mq^2}\int d^3v\,\mathbf{q}\cdot\frac{\partial f}{\partial \mathbf{v}}\,\delta(\mathbf{q}\cdot\mathbf{v} - \Omega_q) \qquad (6)$$

is the usual growth rate for plasma oscillations of frequency Ω_q, and

$$S(\mathbf{q}) = \frac{4\pi^2 e^2 \Omega_q^2}{q^2}\int d^3\mathbf{v}\; f(\mathbf{v})\,\delta(\mathbf{q}\cdot\mathbf{v} - \Omega_q\,, \qquad (7)$$

$$\mathbf{D}(\mathbf{v}) = \frac{4\pi^2 e^2}{m^2}\int \frac{d^3q}{(2\pi)^3}\,P(\mathbf{q})\,\frac{\mathbf{q}\mathbf{q}}{\mathbf{q}^2}\,\delta(\mathbf{q}\cdot\mathbf{v} - \Omega_q), \qquad (8)$$

$$A(\mathbf{v}) = \frac{4\pi^2 e^2}{m}\int \frac{d^3q}{(2\pi)^3}\,\Omega_q\,\frac{\mathbf{q}}{\mathbf{q}^2}\,\delta(\mathbf{q}\cdot\mathbf{v} - \Omega_q)\,. \qquad (9)$$

In the above $P(\mathbf{q})\,d^3q/(2\pi)^3$ is the energy density of plasma oscillation with wave vector **q** in d^3q.

Equations (4) and (5) differ from the usual quasi-linear equations by the last term in each equation.[39] These terms come from the spontaneous emission of plasmons, which is neglected in the usual theory. The new terms cause $P(\mathbf{q})$ and $f(\mathbf{v})$ to approach the thermal equilibrium

$$P(\mathbf{q}) = kT\ (\text{Rayleigh} - \text{Jeans})\,, \qquad (10)$$

$$f(\mathbf{v}) = Ce^{-mv^2/kT}\ (\text{Maxwell} - \text{Boltzmann}). \qquad (11)$$

The approach to thermal equilibrium is absent from the usual quasi-linear theory. Computer studies of the rate of approach to thermal equilibrium for an initially unstable distribution are now in progress.

Next, we consider diagrams like

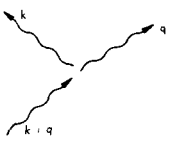

in which a plasmon decays into two plasmons. The interaction Hamiltonian for this process has been calculated.[40] Such a process would not contribute to Eq. (1) because energy and momentum could not be conserved. However, diagrams like

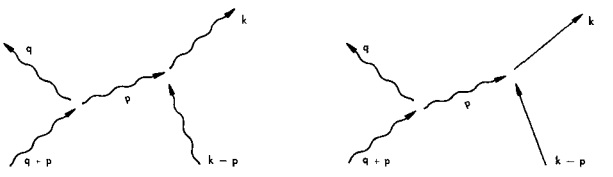

do contribute. They correspond to plasmon-plasmon and plasmon-electron scattering. The second process contributes to both Eqs. (1) and (2). The electron distribution function is also changed by electron-electron collisions for which the diagram is

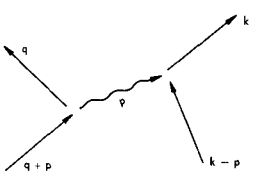

[39] E. G. Harris (to be published in the *Physics of Fluids*).

[40] E. G. Harris (to be published).

When properly calculated these terms lead in the classical limit to the Lenard-Balescu collision integral.[41] Terms describing plasmon-plasmon, plasmon-electron, and electron-electron scattering may be added without difficulty to Eqs. (1) and (2) or their classical limits, Eqs. (4) and (5).[40]

We now discuss processes in which phonons play a role. Pines and Schrieffer[38] have found the interaction Hamiltonian for the process

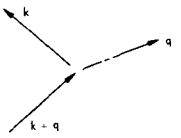

in which an electron or ion emits a phonon. There is also a process

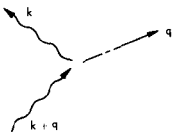

in which a plasmon emits a phonon.[42] It is straightforward to write equations for the rate of change of the distribution functions for electrons, ions, plasmons, and phonons. There are two interesting features which deserve comment. It is possible to get an exponential growth of phonons at the expense of the plasmons. One finds

$$\frac{\partial N_2(\mathbf{q})}{\partial t} = 2\gamma_{\nu\lambda} N_2(\mathbf{q}) + \text{Spontaneous Emission}, \tag{12}$$

with

$$\gamma_{2\lambda} = \frac{\pi\hbar\omega_{pe}^2 q}{8NMc_s} \int \frac{d^3k}{(2\pi)^3}\, \mathbf{q}\cdot\frac{\partial N_\lambda(\mathbf{k})}{\partial \mathbf{k}}\, \delta(\mathbf{q}\cdot\mathbf{v}_k - qc_s)\,, \tag{13}$$

where v_k is the group velocity of plasma oscillations, and c_s is the ion sound velocity. The similarity of Eq. (13) to Eq. (6) is clear. We have called such an exponential growth a "wave vector space instability" in analogy to the velocity space instability which yields Eq. (6).[42] The other interesting feature involves the process

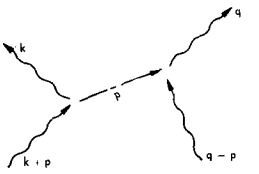

in which plasmons interact by exchanging a phonon. This can be an attractive interaction, leading to an instability in which the plasmons collect in bunches.[42]

We shall conclude this section by discussing some phenomena in which photons play a role.[43] The processes

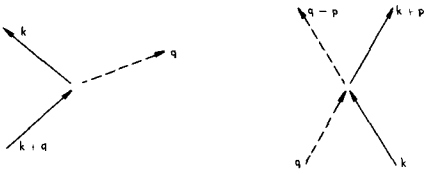

are well known from quantum electrodynamics. The first of these comes from the term in the Hamiltonian for a nonrelativistic particle which is linear in $\mathbf{A}(\mathbf{x})$, the vector potential. The second of these comes from the $A^2(\mathbf{x})$ term. It is possible to derive a photon-plasmon interaction Hamiltonian to describe processes like

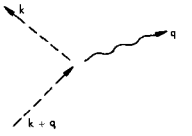

This process is an inelastic scattering of photons by a plasma. It has a resonance when the energy transfer is approximately ω_{pe}.

An interesting process is the excitation of plasma oscillations by transverse waves. We have treated the problem of two monochromatic light waves with a frequency difference approximately equal to the plasma frequency and obtained a result in essential agreement with that of Montgomery.[44] Plasma oscillations can also be excited by a broad spectrum if the width exceeds the plasma frequency.

---

[41] H. W. Wyld, Jr., and D. Pines, *Phys. Rev.* **127** 1851 (1962).

[42] E. G. Harris, *The Electron-Phonon, Electron-Plasmon, Plasmon-Phonon, and Plasmon-Plasmon Interactions and Some Instabilities That They Lead To*, ORNL-3871 (November 1965) (unpublished).

[43] E. G. Harris, R. Budwine, and R. Sugihara (to be published).

[44] D. Montgomery, *Physica* **31**, 693 (1965).

We have calculated the cross section for the scattering of light by light in a plasma. The diagram is

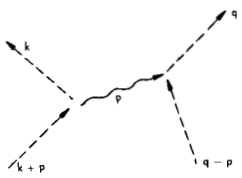

Our results are in agreement with previous calculations.[45]

Plasma oscillations may interact nonlinearly to produce transverse waves. This may be described by third-order processes like

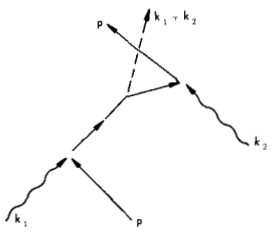

The particle leaves with the same momentum with which it entered. The net result is that two plasmons disappear and a photon is created. Our calculation of the energy radiated by plasma oscillations is essentially the same as that found by Aamodt and Drummond by a classical calculation.[46]

8.5.3 Plasma in a Strong Magnetic Field[47]

In a strong magnetic field the frequency of plasma oscillations of wave vector **k** is

$$\Omega_{\mathbf{k}} = \omega_{pe} \frac{k_3}{k} . \tag{14}$$

The growth or damping of waves may be thought of as being due to the emission and absorption of plasmons with energy $\hbar\Omega_{\mathbf{k}}$. Because of the relation between frequency and wave vector, it is possible to conserve energy and momentum in three-wave processes like

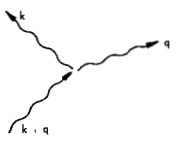

An equation analogous to Eq. (1) can be written as

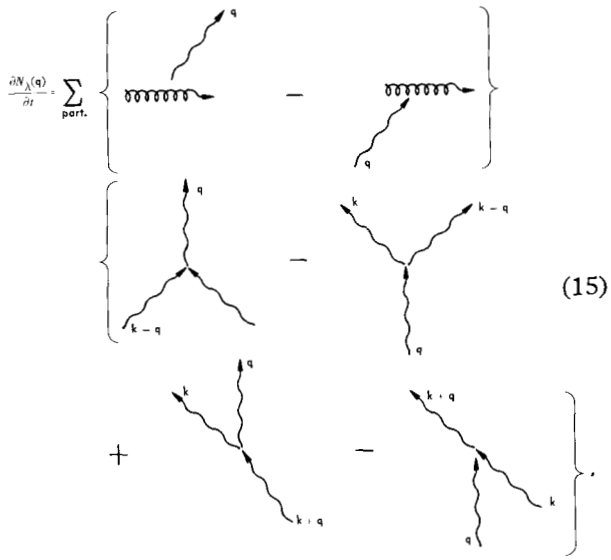

(15)

The first summation gives the emission and absorption of plasmons by energetic particles. In the classical limit it gives $2\gamma_q P(q)$ plus a spontaneous emission term. The γ_q is the same growth rate as is calculated from the Vlasov equation. From this point of view all the instabilities near the ion cyclotron frequency and its harmonics are seen to be essentially the same. Because of their helical motion, particles emit and absorb near ω_{ci} and its harmonics. Instabilities occur when emission exceeds absorption. This may occur because of anisotropic velocity distributions, loss-cone distributions, and streaming or spatial gradients.

The second summation in Eq. (15) includes the contribution of wave-wave coupling to the rate of change of $N_\lambda(\mathbf{q})$. Estimates of the importance of these terms for experiments such as DCX-2 have shown that they are indeed important. An equation for $\partial f(\mathbf{v})/\partial t$ can be derived. It is similar to Eq. (5) but **D** and **A** are more complicated.

We have had some success in applying these equations to the interpretation of the rf spectrum observed in DCX-2.[48]

---

[45] N. Krall, A. Ron, and N. Rostoker, *Phys. Rev. Letters* **13**, 83 (1964); P. M. Platzman and N. Tzoar, *Phys. Rev.* **136**, A11 (1964).

[46] R. E. Aamodt and W. E. Drummond, *J. Nucl. Energy: Pt. C.* **6**, 147 (1964).

[47] G. M. Walters and E. G. Harris (to be published).

[48] *Thermonuclear Div. Semiann. Progr. Rept. Apr. 30, 1966*, ORNL-3989.

9. Magnetics and Superconductivity

9.1 STUDY OF RIBBON COILS FOR USE IN B_{MIN} MAGNET SYSTEMS

J. N. Luton, Jr.

The previous two progress reports[1,2] contained a description of a type of ribbon coil being developed for applications requiring high current densities and the results of some tests on prototype coils. This section presents the possible use of ribbon coils in producing a B_{min} field, extends the test data on prototype coils, and describes new winding and cooling arrangements.

For plasma stability studies it is often desirable to have a containing magnetic field for which the magnitude $|\overline{B}|$ of the flux density $\overline{B}$ reaches a nonzero minimum inside the plasma volume, as described in Sect. 4 of this report. Figure 9.1 shows a coil system in which the mirrors would produce a field of 20 kG at the center of the system and 40 kG under a mirror. The currents in the "Ioffe" or "corrector" coils of Fig. 9.1 are 160% of those required to give a total field of 20 kG at a point in the midplane ½ in. from the axis in the direction of minimum field increase.

The prototype coils previously reported[1,2] appeared to be appropriate for the mirror of Fig. 9.1, because the length of the mirror coil is small enough to be the width of a single conductor ribbon and there is space available at each end of the coil to accommodate the annular headers which are necessary for supplying coolant to the grooves across the face of the ribbon. Six prototype coils have been wound and five of these have been operated; only the first failed to achieve the overall current density i_o of 1.3×10^5 A/in.^{2} required for the system of Fig. 9.1. The first coil failed because of insufficient water flow. The second coil was operated for more than 50 h at $i_o \approx 69{,}000$ A/in.^{2} and then moved to another unfiltered water system, where it developed turn-to-turn shorts at $i_o \approx 195{,}000$ A/in.^{2}. Subsequent coils were mounted for operation in an external field with a water filter immediately upstream. The third coil was run 15 h at varying loads, including 50 rapid cycles from $i_o \approx 140{,}000$ A/in.^{2} to zero. The external field was also varied, reaching 48 kG, for a total of 90 kG at the coil center. The coil was then unwound for inspection of its ribbons, which were then rewound, without cleaning or other improvement, to form another coil. This rewound coil operated about 5 h at $i_o = 147{,}000$ A/in.^{2} in an external field of 50 kG (total field 95 kG) and failed catastrophically by shorting through a structural member. The coil presently under test (Fig. 9.2) has been run 25 h at current densities up to 143,000 A/in.^{2} while in the external field, and has been exposed to stagnant and running water for two months.

The insulations of the latter four test coils were exposed to a compressive stress larger than that calculated for the system of Fig. 9.1. However, the upper limit for the tensile stress in the copper of the test coils is smaller than that for the mirror coils of Fig. 9.1 because of the larger bore of the latter coils. If additional tensile strength were required, the coil could be wound as in Fig. 9.2 with the thin flat ribbon composed of a material stronger than copper. Even if additional strength is not required, the design with two adjacent conductor ribbons has certain advantages. An insulator ribbon between smooth surfaces should be more durable; all sides of the coolant passages are metallic, and thus the heat transfer capability is increased; and finally there is an important economic advantage

[1] *Thermonuclear Div. Semiann. Progr. Rept. Oct. 31, 1965*, ORNL-3908, pp. 125–28.

[2] *Thermonuclear Div. Semiann. Progr. Rept. Apr. 30, 1966*, ORNL-3989, pp. 110–13.

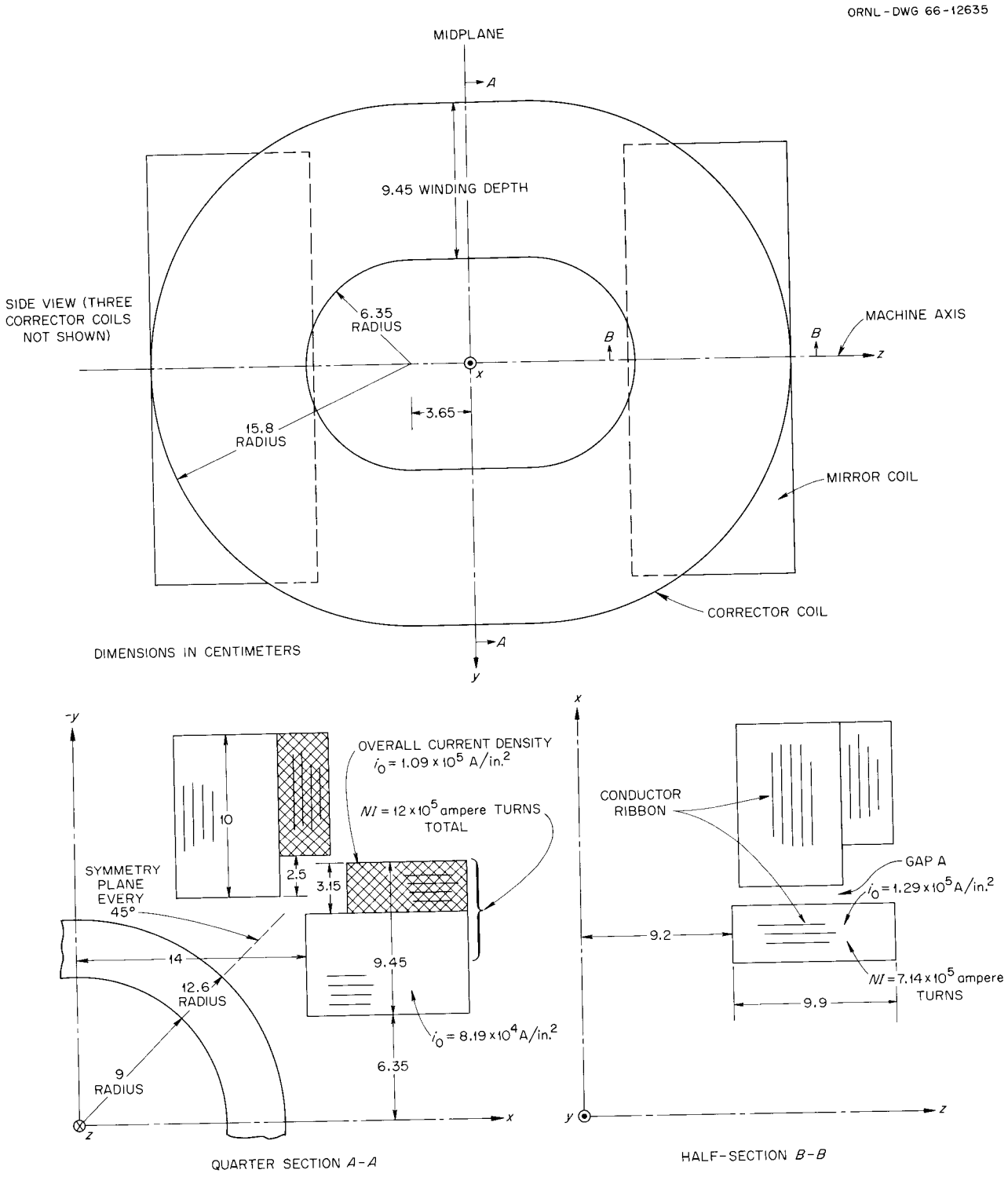

Fig. 9.1. Mirror-Quadrupole Coil System Having a 20-kG Central Field, 2 to 1 Axial Mirror Ratio, and a Compensation Ratio of 1.61.

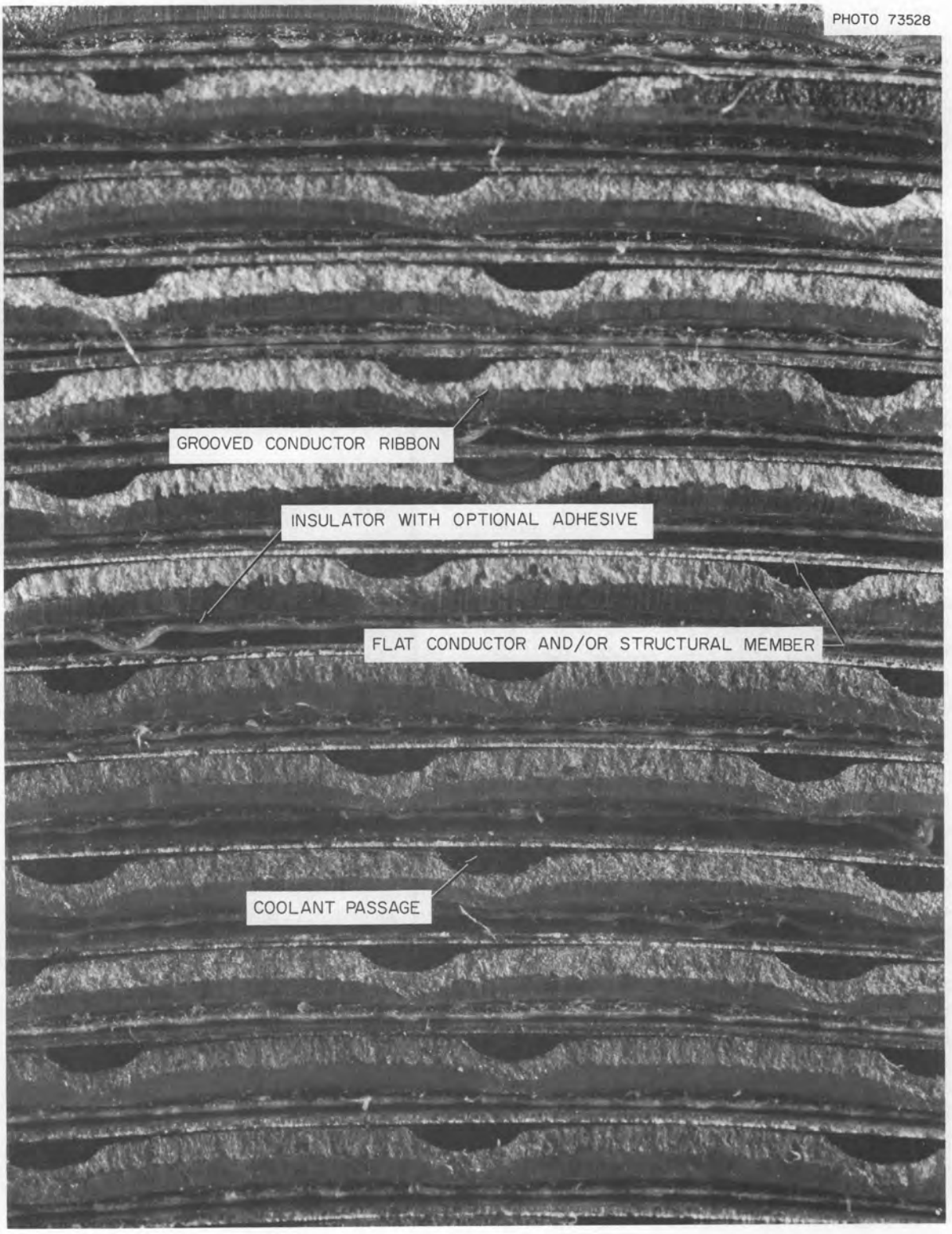

Fig. 9.2. Portion of the Winding of Transverse Ribbon Coil No. 4 Showing Two-Ribbon Conductor.

in that the conductor edges need not be specially treated: the burr that forms as the ribbon is commercially slit from the wider roll of strip protrudes from only one face of the ribbon, and if two ribbons are used in parallel the burrs need not be removed but can simply be oriented away from the insulator ribbon.

In all test coils the forces tending to unwind the ribbon spirals were resisted only by frictional forces between adjacent turns, although the extent of such unwinding was limited by an exterior retaining ring. The magnitude of these frictional forces has been varied from one coil to another by using different insulating ribbons. The coils operated satisfactorily with either Mylar or Teflon-impregnated glass, with a range of the coefficient of friction of perhaps 10 to 1. Although in the latter case some motion of the conductor was evident, the coil is still operating without difficulty. We infer from the series of tests described above that such ribbon coils are appropriate for the mirror coils of the B_{min} system of Fig. 9.1. However, the durations of the prototype tests have not been long enough either to indicate a limited life expectancy of the coils or to prove them sufficiently durable for "permanent" use. Life tests are under way, but for the present any design using ribbon coils for a plasma experiment should include provision for convenient replacement of the coils.

To gain the most effect from the ampere turns of the corrector bars of a mirror-quadrupole system, the bars should be as close to the axis as the plasma volume will allow. They should also be long enough to produce the proper field, but not too long, or the power consumption becomes excessive. From these obvious requirements it follows that the ends of the corrector coils should fall over the mirrors, and the gap A of Fig. 9.1 should be only large enough for a structural member. But the "transverse"[3] type of ribbon coil considered previously requires a water header covering each edge of the ribbon. Although this type of coil would be usable for such an application, one is led to search for a coil type that has the inner end free of any obstructions, because this measure will reduce the power requirement. In this case the coolant grooves must not terminate at the inner edges of the ribbon. This can be achieved by letting the grooves run lengthwise along the conductor, parallel to the electric current; this coil type is called a "longitudinal" coil. Unfortunately, the coolant grooves now run the full length of the conductor ribbon, and the application of reasonable water pressure at one end would give a completely inadequate flow of coolant. In fact, the dimensions and power densities for the coil of Fig. 9.3 are such that in order to achieve sufficient cooling, each groove must be subdivided into so many parallel hydraulic paths that one path can trace out only one-quarter of the outer turn. Even so, in contrast to the transverse case, the power density is limited by the bulk temperature rise of the water rather than by the temperature drop across the stagnant water film at the copper surface.

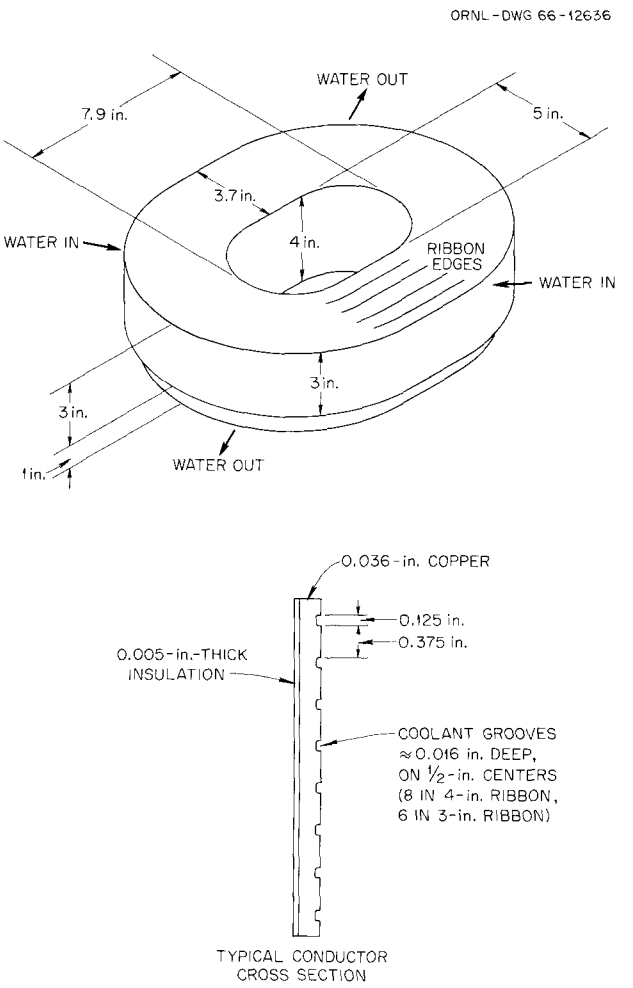

Fig. 9.3. One Corrector Coil with Longitudinally Cooled Conductor. Water grooves parallel ribbon edges.

[3]So called because the coolant grooves run perpendicular to the electric current.

One way to subdivide the grooves into suitable lengths would be to form the coil by winding the grooved conductor with its insulator ribbon, and then to drill radial holes through the winding at any even number of azimuths, each hole intersecting one groove in each turn of the winding. The flow path would be down one hole, through the grooves on both sides of the hole, and out the two holes azimuthally adjacent to the entrance hole. Thus only the outer surface of the coil need be hydraulically accessible. The coil of Fig. 9.3 has eight grooves along the conductor, with a maximum length of coolant path equal to one-quarter of the length of the longest turn. It could be made in the following way: After winding the coil, eight radial holes would be drilled to but not through the innermost turn at each 90° point around the coil periphery, with each hole intersecting a different set of grooves. The four groups of holes would be covered in sequence by inlet and outlet headers.

Since it proved to be quite difficult to form the holes mentioned above without shorting turns or obstructing the grooves, the holes were explosively punched through the ribbon before it was wound, thus making inspection and repair feasible. Figure 9.4 shows a segment of a sample ribbon with four grooves ready for winding. The holes are elongated both to increase their cross section and to reduce the flow restrictions caused by inadvertent misalignment of the holes in succeeding turns. The holes are offset so that at the locations of highest current density the conductor cross section is cut down by only two holes rather than four.

A single coil was wound of the conductor of Fig. 9.4, and turn-to-turn ac voltage measurements indicated that the coil was free of shorts. Unfortunately, it was seriously damaged during installation and has not yet been repaired. A second coil with longitudinal water flow (Fig. 9.5) was wound to test the feasibility of using the alternate conductor of Fig. 9.6. The water access for a coil using this conductor would be at the end plane where the slots intersect the edge of the ribbon and the other three surfaces of the coil would be free. The azimuthal locations of inlet and outlet headers are as with the punched hole coil. Aside from utilizing different surfaces of the coil, there are practical differences between the slotted and punched designs: The slots are much easier and more economical to

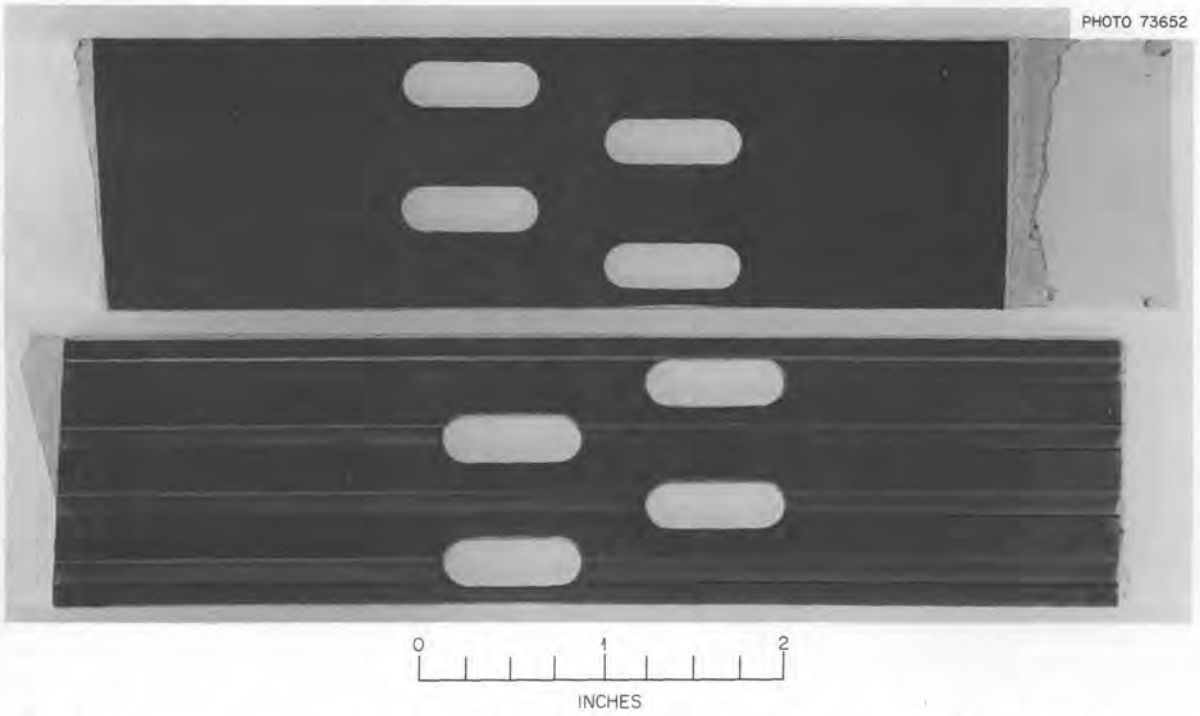

Fig. 9.4. Segment of Longitudinally Cooled Ribbon with Holes Explosively Punched Through the Copper and the Adherent Polyimide Insulation.

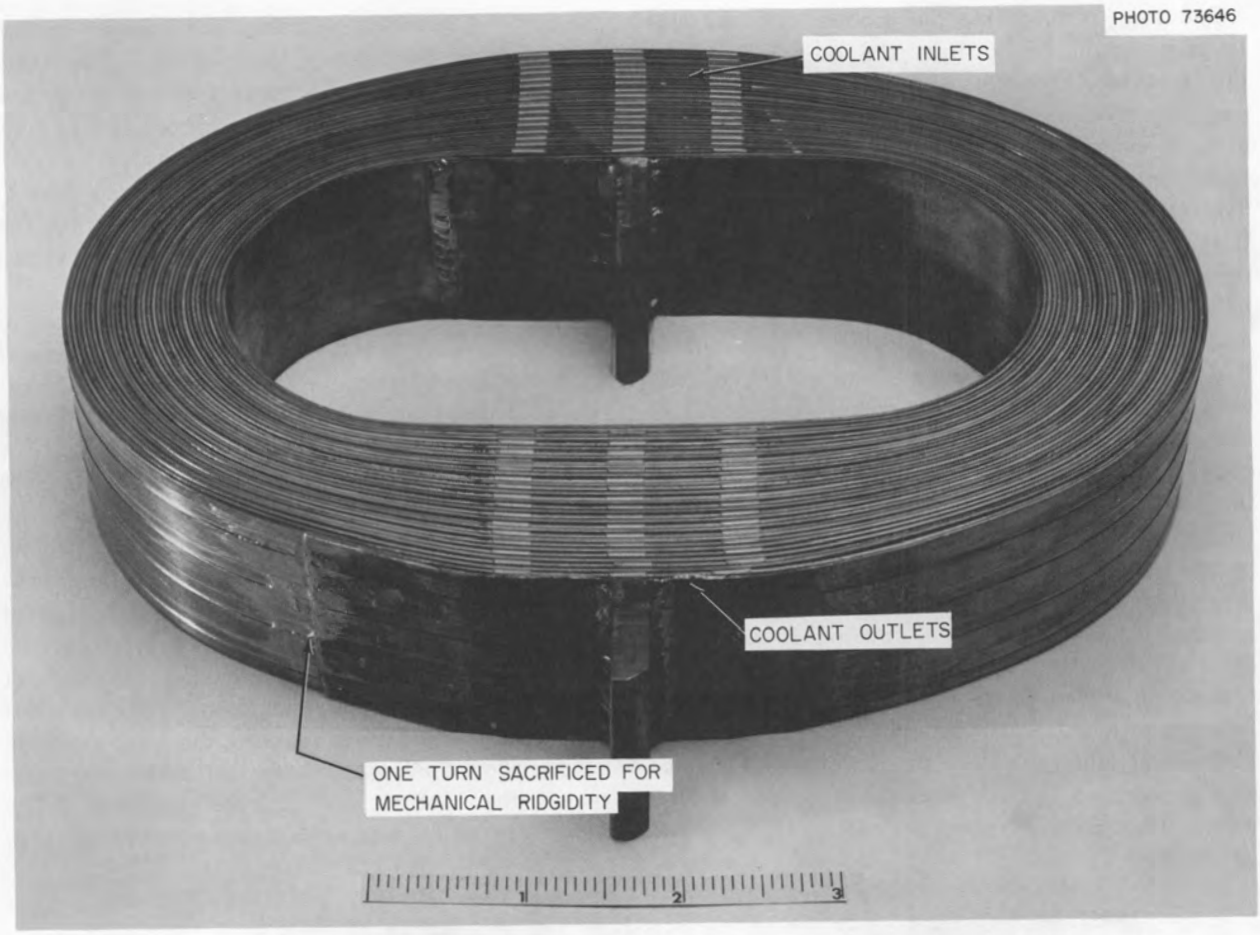

Fig. 9.5. Longitudinal Ribbon Coil No. 2 Before Insertion in Its Case.

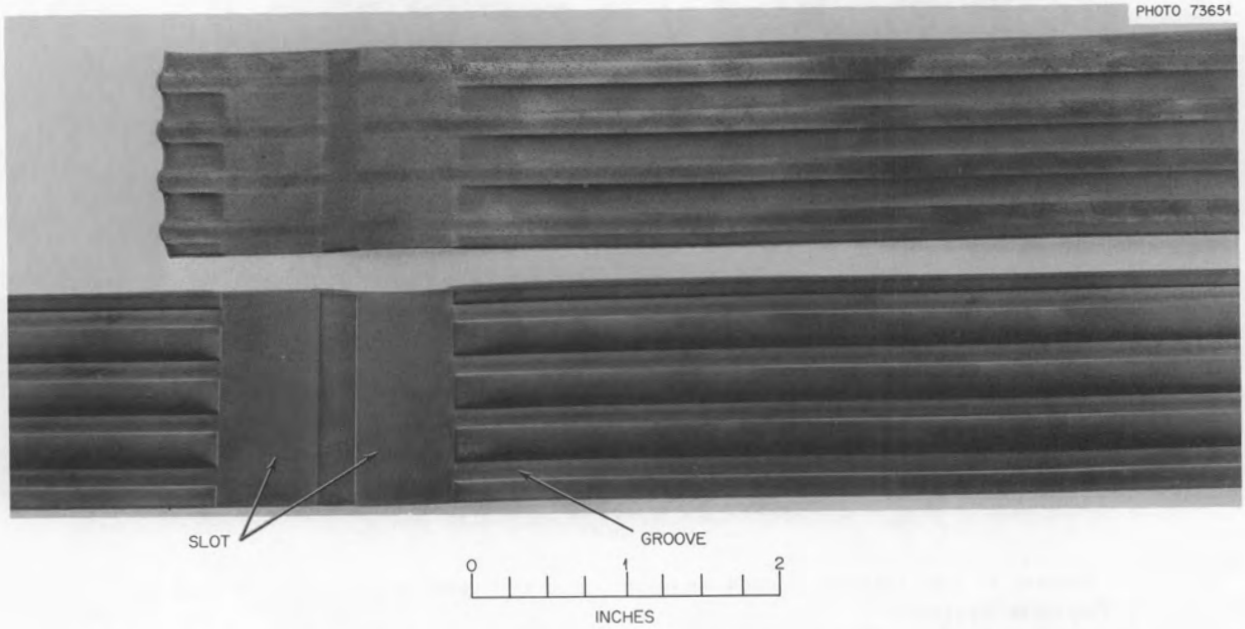

Fig. 9.6. Segment of Longitudinally Cooled Ribbon with Slots and Grooves Rolled Simultaneously.

form, the rolling process cannot form burrs, and the alignment of the slots is less critical; however, the punched conductor gives a structurally more solid coil, and the adherence of the insulation is less important for the punched coil. The punched coils will be pursued further if the slotted coils prove unsatisfactory.

The entire conductor is naturally exposed to outward magnetic forces, and the rib between the slots of Fig. 9.6 was left to reduce the length of unsupported span across the slots, thereby reducing the deflection of the thin strip of conductor stretching across the slot. Flow calculations and tests[4] indicate that if a still shorter span were required, more ribs could be left without severely affecting the relative flow through the various grooves fed by the slots, if the grooves continue through all ribs except the center one. The coil of Fig. 9.5 uses a grooved but unslotted conductor; the slots are simulated by inserting insulating spacers. The resulting increase of winding depth at the two feed locations can be observed in the figure. The coil has been partially tested and has achieved a current density in the copper of 152,000 A/in.^{2}, which exceeds that required for the corrector coils of Figs. 9.1 and 9.3. The temperature rise of the bulk water was 40°C. It was anticipated that aging of the longitudinal coils would be substantially the same as for the transverse coils discussed above; therefore, life tests on the longitudinal coils were not begun. The longitudinal coil is now mounted inside a larger coil so that it may be tested in an external field. The axes of the coils are perpendicular in order to make the test more severe and to produce twisting forces such as would occur in a B_{min} system.

9.2 VOLTAGE-CURRENT CHARACTERISTICS OF COMPOUND CONDUCTORS

W. F. Gauster K. R. Efferson
J. B. Hendricks H. A. Ullmaier[5]
W. R. Wilkes[6]

We consider a piece of a "compound conductor" (Fig. 9.7) in which

$$\frac{dI_{Cu}}{dx} = -k(V_{Cu} - V_s)\,, \tag{1}$$

$$\frac{dV_{Cu}}{dx} = -rI_{Cu}\,, \tag{2}$$

where $r = \rho_{Cu}/A_{Cu}$ stands for the resistance per unit length of the stabilizer, and $k = 1/\rho_{tr}$ for the conductance per unit length of the interlayer.

If the superconductor is in the nonresistive state ($I_s < I_{cB}$, where I_{cB} is the critical current of the superconductor at the given magnetic field and at the bath temperature $T = T_b$), then $V_s = 0$, and from Eqs. (1) and (2) we obtain with $\alpha = \sqrt{kr}$:

$$V_{Cu} = V_{Cu\,1}\cosh \alpha x - \frac{V_{Cu\,1}\cosh \alpha s - V_{Cu\,2}}{\sinh \alpha s}\sinh \alpha x\,, \tag{3}$$

$$I_{Cu} = \sqrt{\frac{k}{r}}\left(\frac{V_{Cu\,1}\cosh \alpha s - V_{Cu\,2}}{\sinh \alpha s}\cosh \alpha x - V_{Cu\,1}\sinh \alpha x\right). \tag{4}$$

Therefore

$$I_{Cu\,1} = \sqrt{\frac{k}{r}}\,\frac{V_{Cu\,1}\cosh \alpha s - V_{Cu\,2}}{\sinh \alpha s}\,, \tag{5}$$

$$I_{Cu\,2} = \sqrt{\frac{k}{r}}\,\frac{V_{Cu\,1} - V_{Cu\,2}\cosh \alpha s}{\sinh \alpha s}\,. \tag{6}$$

Using Eqs. (3) to (6) it can be easily shown that

ORNL-DWG 66-8686RA

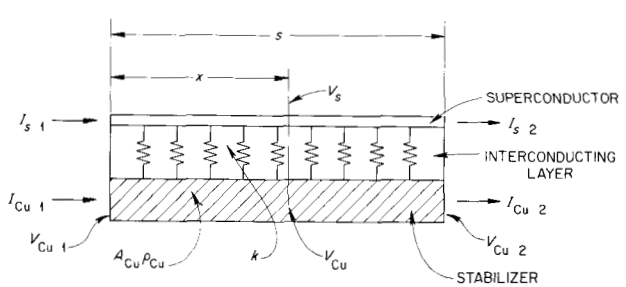

Fig. 9.7. Compound Conductor.

[4]Both carried out by G. W. Kidd of the Reactor Division.

[5]Present address: Institute for Applied Physics, Kernforschungslaboratorium, Jülich, Germany.

[6]Summer research participant from Wake Forest College, Winston-Salem, N.C.

ORNL-DWG 66-12638

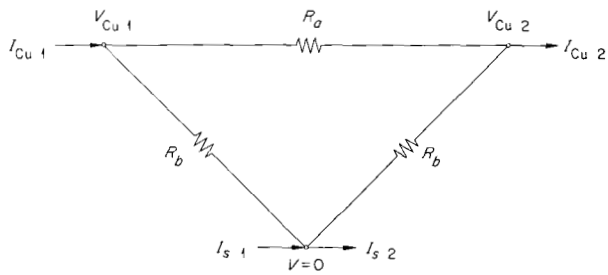

Fig. 9.8. Equivalent Network of a Compound Conductor.

ORNL-DWG 66-8692A

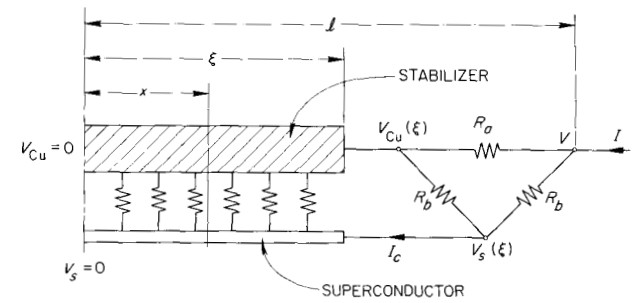

Fig. 9.9. Model of Compound Conductor in Flux Flow State.

for $I_s < I_{cB}$ the compound conductor can be replaced by the simple equivalent triangular network represented in Fig. 9.8 if

$$R_a = \sqrt{\frac{r}{k}} \sinh \alpha s \,, \tag{7}$$

$$R_b = \sqrt{\frac{r}{k}} \frac{\sinh \alpha s}{\cosh \alpha s - 1} \,. \tag{8}$$

If $I_s > I_c(H, T)$ the superconductor is in the flux flow state and displays a flux flow (differential) resistivity $\rho_f = dE/dJ$, where E is the electric field strength, and $J = I/A$ is the current density. Kim *et al.*[7] from their experiments derived the following simple empirical relation between ρ_f and the resistivity ρ_n of the superconductor in the normal state:

$$\rho_f = \rho_n \frac{H}{H_{c2}(0)} \,. \tag{9}$$

For an element of a compound conductor (Fig. 9.7) in flux flow state, we obtain

$$\frac{dV_s}{dx} = -\frac{\rho_f}{A_s}(I_s - I_c) \,. \tag{10}$$

In such a compound conductor, the total current I enters and leaves through the stabilizer, and the current through the superconductor increases from zero at the ends to a maximum in the middle of the compound conductor. Therefore, we can assume that with increasing magnitude of the total current I, the flux flow zone starts at the middle and reaches the length 2ξ for a certain value of I (Fig. 9.9). The two end pieces of the compound conductor with the lengths $(l - \xi)$ can be replaced by the equivalent triangular networks. This model yields the boundary condition for solutions of Eqs. (1), (2), and (10).

These solutions are discussed in detail in another report.[8] There it is shown that Stekly's concept of the "overflow current"[9] $[I_{Cu} = I_{total} - I_s \doteq I_{total} - I_c(H, T)$, where I_c is the critical current of the superconductor at the field H and temperature $T]$ is a good approximation to the performance of a compound conductor in flux flow state as long as joint regions are ignored, that is, $\xi < l$. Therefore in the following we will use this simple phenomenological relation.

The heat produced per unit length of the compound conductor in flux flow state is

$$w = \frac{\rho_{Cu} I_{Cu}}{A_{Cu}} I = \frac{\rho_{Cu}}{A_{Cu}} (I - I_c) I \,. \tag{11}$$

It is dissipated to the helium bath in such a way that the heat dissipation per cm^2 is $q = w/S$, where S stands for the wetted perimeter of the compound conductor, and A is its cross-sectional area.

[7] Y. B. Kim, C. F. Hempstead, and A. R. Strnad, *Phys. Rev.* **139**, A1163 (1965); Y. B. Kim, C. F. Hempstead, and A. R. Strnad, *Phys. Rev.* **131**, 2486 (1963); Y. B. Kim, C. F. Hempstead, and A. R. Strnad, *Rev. Mod. Phys.* **36**, 43 (1964); C. F. Hempstead and Y. B. Kim, *Phys. Rev. Letters* **12**, 145 (1964); A. R. Strnad, C. F. Hempstead, and Y. B. Kim, *Phys. Rev. Letters* **13**, 794 (1964).

[8] W. F. Gauster *et al.*, ORNL-TM-1598, pp. 13–17 (August 1966).

[9] Z. J. J. Stekly and J. L. Zar, *IEEE Trans. Nucl. Sci.* **NS-12**, 367 (1965).

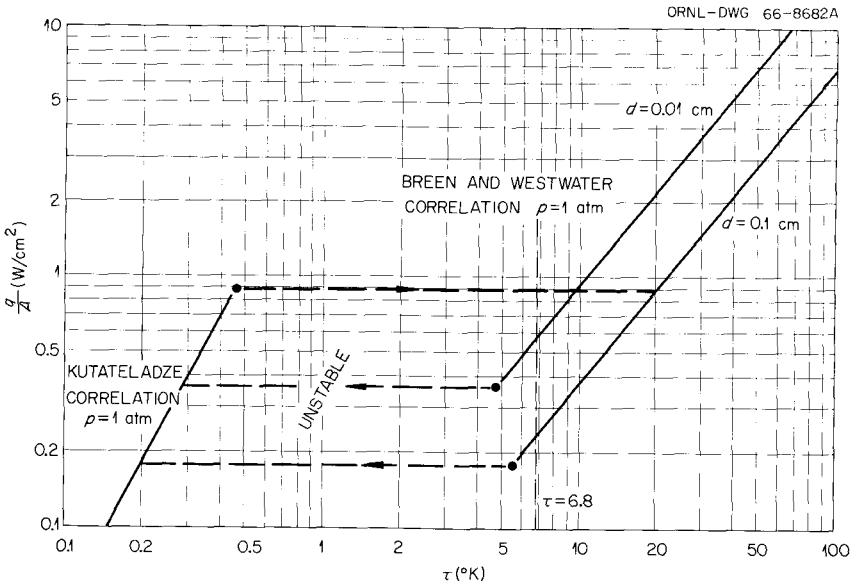

Fig. 9.10. Heat Transfer Characteristic of a Wire in Boiling Helium.

Using Eq. (11), Stekly derives his stability criterion by assuming q proportional to the difference τ between the temperature T of the compound conductor and the bath temperature T_b:

$$q = h(T - T_b) = h\tau. \tag{12}$$

We think, however, that Eq. (12) should be replaced by the more realistic heat transfer characteristic of a heated wire in boiling helium as represented in Fig. 9.10. The numerical values shown hold only for thin wires (d = diameter of wire surrounded by liquid helium), and an appropriate heat transfer diagram must be used for any special type of compound conductor. This is not only due to different cross-section dimensions; in addition, any kind of electrical insulation also influences the heat transfer characteristic. Likewise, any obstruction of the flow of helium about the wire will influence the heat transfer.

At any rate, we must distinguish between the zones of heat convection and nucleate boiling and the unstable transition between nucleate boiling and film boiling. Using Eq. (11) we obtain

$$\frac{\rho_{Cu}}{A_{Cu}}[I(\tau) - I_c(\tau)]I(\tau) = Sq(\tau)\,. \tag{13}$$

The quantities I, I_c, and q are functions of the temperature difference $\tau = T - T_b$. The solution for I is

$$I = \frac{I_c}{2} + \sqrt{\left(\frac{I_c}{2}\right)^2 + p^2}\,, \tag{14}$$

where

$$p^2 = \frac{SA_{Cu}}{\rho_{Cu}} q(\tau)\,.$$

Here we did not make any specific assumption concerning the temperature dependence of the critical current I_c, whereas in Stekly's theory a linear temperature dependence of the critical current is assumed.

Equation (14) can be used for a simple graphical solution which is shown in Fig. 9.11. Instead of a $q - \tau$ diagram (Fig. 9.10), a $p - \tau$ diagram (Eq. 14) is used. We assume any special value τ' of τ, take $p(\tau')$ in the compass, and plot this distance on the τ axis. The hypotenuse of the right triangle with the sides $p(\tau')$ and $\frac{1}{2} I_c(\tau')$ is

$$\sqrt{\left(\frac{I_c}{2}\right)^2 + p^2}\,.$$

This distance added to $\frac{1}{2} I_c(\tau')$ yields I. The current I_{Cu} appears in Fig. 9.11 as the difference

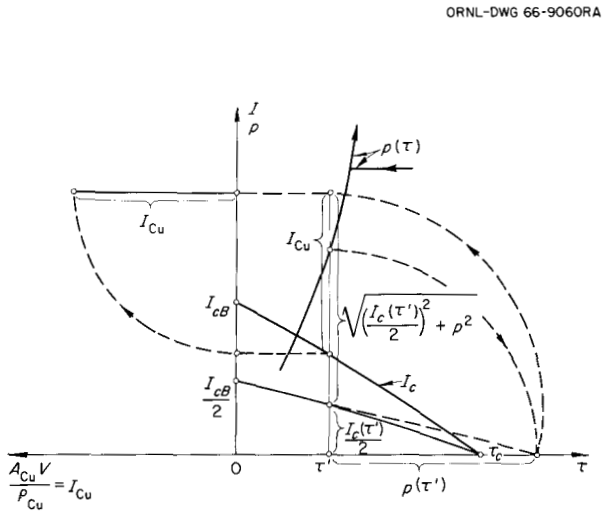

Fig. 9.11. Graphical Method for Determining the *I-V* Characteristic of a Compound Conductor.

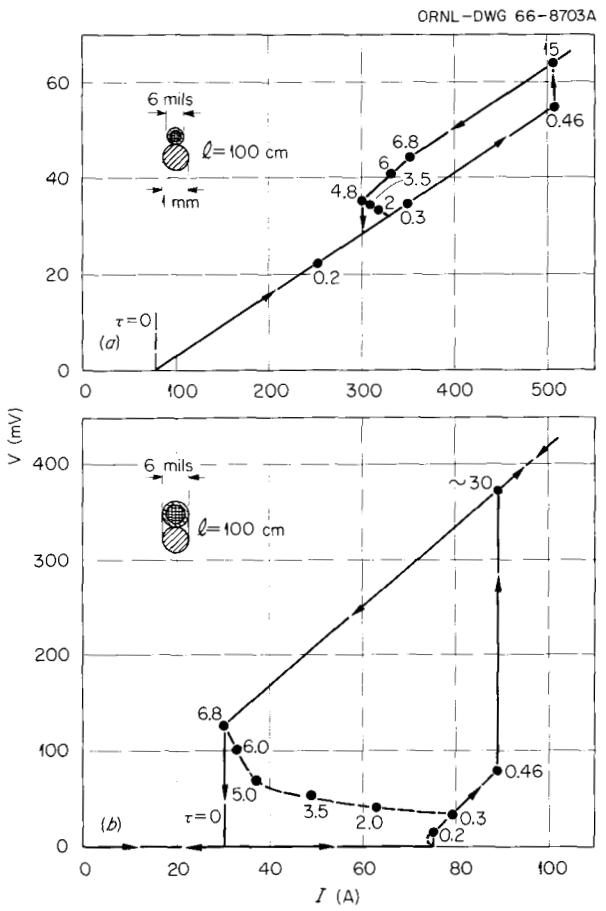

Fig. 9.12. Current-Voltage Characteristics of Compound Conductors in Flux Flow State.

between I and I_c. Since the voltage V is proportional to I_{Cu}, we can easily obtain a voltage-current diagram (as shown in the second quadrant of Fig. 9.11) by plotting $I_{Cu} = A_{Cu}V/\rho_{Cu}$ in the (negative) horizontal direction. In this way the *V-I* diagrams, Figs. 9.12*a* and *b*, have been obtained for the special cases indicated.

Our experiments described with short samples of compound conductors with the superconductor in zero-resistance state ("ideal compound conductor")[10] showed good quantitative agreement with our calculations. However, our experiments with compound conductors in flux flow state[11] cannot be fully understood by means of our simple nonlinearized approach. Additional investigations are in progress.

Finally, it should be mentioned that bare superconducting wires or wires with only slight copper coating show stable performance when the power source is operated in voltage mode ("postquenching performance"). Compared with the previously considered cases of compound conductors, this performance is entirely different. Under appropriate conditions, a normal zone whose length is almost proportional to the voltage across the sample develops on the superconductor. When raising the voltage, the current remains approximately constant until the entire superconducting wire becomes normal. Then the current increases with voltage corresponding to the resistance characteristic of the superconductor in normal state. More details concerning the postquenching performances are presented in the previously mentioned report.[12]

9.3 MAGNETORESISTANCE OF COMPOUND CONDUCTORS

J. B. Hendricks D. M. Kroeger

In Sect. 9.2 it was shown that an "ideal compound conductor" can be represented by an equivalent triangular network as represented in Fig. 9.8. The values of the elements are

[10] *Thermonuclear Div. Semiann. Progr. Rept. Apr. 30, 1966*, ORNL-3989, pp. 7–8.

[11] *Thermonuclear Div. Semiann. Progr. Rept. Apr. 30, 1966*, ORNL-3989, pp. 17–20.

[12] *Thermonuclear Div. Semiann. Progr. Rept. Apr. 30, 1966*, ORNL-3989, pp. 1–5.

$$R_a = \sqrt{\frac{r}{k}} \sinh \alpha s \,, \tag{1}$$

$$R_b = \sqrt{\frac{r}{k}} \frac{\sinh \alpha s}{\cosh \alpha s - 1} \,, \tag{2}$$

where

r = resistance per unit length of the normal conductor,

k = conductance per unit length of the connecting layer ("transverse conductance"),

s = length of the conductor section,

$\alpha = \sqrt{rk}$.

It was also mentioned that the equations can be inverted to obtain

$$k = \frac{1}{s} \frac{\sqrt{1 + 2R_b/R_a}}{R_b} \cosh^{-1} (1 + R_a/R_b) \,, \tag{3}$$

$$r = \frac{1}{s} \frac{R_b}{\sqrt{1 + 2R_b/R_a}} \cosh^{-1} (1 + R_a/R_b) \,. \tag{4}$$

By making two independent measurements, the parameters k and r can be determined for a section of a compound conductor. Two possible measurements are shown in Figs. 9.13*a* and *b*. In the first measurement (Fig. 9.13*a*) the current flows into the stabilizer and out of the stabilizer. The voltage measured, V_1, will be

$$V_1 = IR_{e1} = I \frac{R_a(2R_b)}{R_a + 2R_b} \,. \tag{5}$$

For the second measurement (Fig. 9.13*b*) the current flows into the superconductor and out of the stabilizer. In this case the measured voltage, V_2, will be

$$V_2 = IR_{e2} = I \frac{R_b(R_a + R_b)}{R_a + 2R_b} \,. \tag{6}$$

As αs becomes large, R_a becomes large, and R_b tends toward the value $\sqrt{r/k}$. In this case V_1 approaches a limiting value $2V_2$. The two measurements will not be independent and will only give the ratio r/k. Therefore the length of the conductor section must be short enough so that $\sinh \alpha s$ is not too large (say, <10).

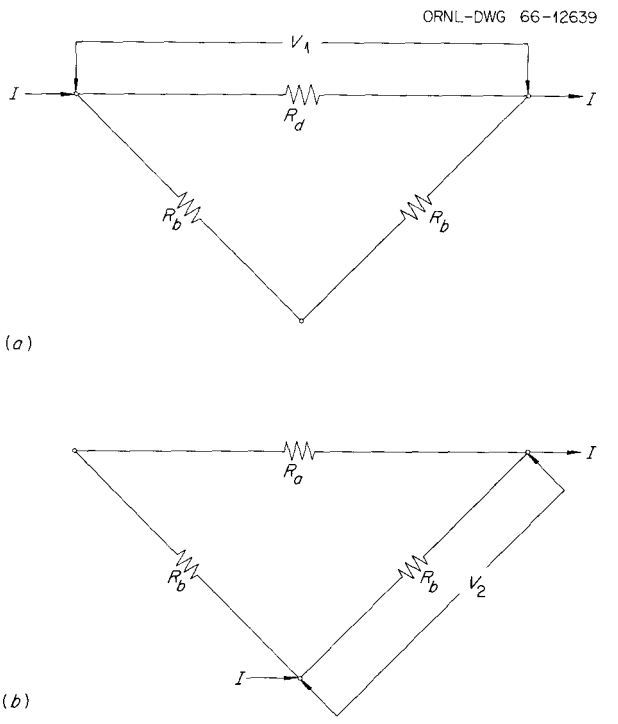

Fig. 9.13. Resistance Measurements on a Compound Conductor.

We have made measurements on a compound conductor made up of a 5-mil Nb–25% Zr wire coated with 0.5 mil radial thickness of electrolytic copper on a No. 30 B&S copper wire twisted together and coated with indium. The length of the section was 3.9 cm. The values of r and k are shown in Fig. 9.14 as a function of the applied transverse magnetic field. The resistance per unit length of a bare No. 30 B&S copper wire in liquid helium is shown for comparison, and we see that the agreement is very good.

The magnetic-field dependence of the transverse conductance k is surprising. The magnetoresistance of the indium used for soldering should saturate above a few kilogauss,[13] and therefore its resistance should not vary at higher fields. This is confirmed by the measurements by Efferson and Simpkins and is presented in Fig. 9.15. Furthermore, the copper layer on the superconductor

[13] G. T. Meaden, *Electrical Resistance of Metals*, p. 133, Plenum, New York, 1965.

is very impure, and its resistance should also be almost independent of field. Hence the source of the measured magnetoresistance of the connecting layer is still an open question, and further work is being done to clarify this point.

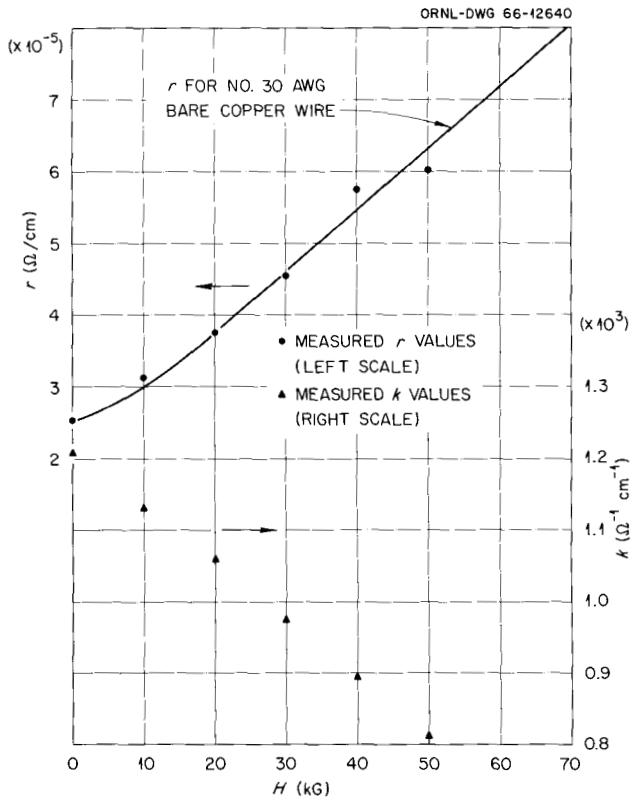

Fig. 9.14. Resistance and Transverse Conductance of a Compound Conductor vs Magnetic Field.

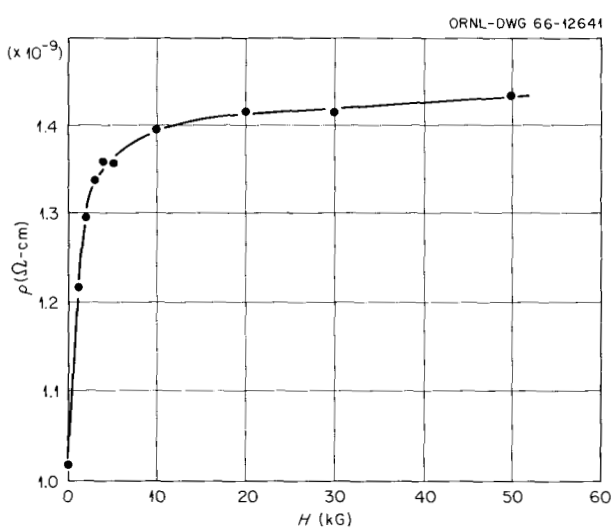

Fig. 9.15. Resistivity of Pure Indium Wire vs Magnetic Field.

9.4 CURRENT-CARRYING CAPACITY OF A HARD SUPERCONDUCTING WIRE IN ZERO EXTERNAL FIELD (THEORY)

H. Koppe[14]

A type III superconducting wire in zero external field can carry a certain current I_M before superconductivity breaks down. One could assume that this maximum current is determined either by the fact that the magnetic field on the surface of the wire is equal to H_{c2} (which would correspond to a modified Silsbee hypothesis), or that the wire carries everywhere exactly the critical current J_c. We shall show that this is only true for very thick wires; in reality the maximum current is determined by a condition inside the wire.

The behavior of a type III superconductor can be described by the equation

$$\text{curl}\,\vec{H} = J_c\,, \tag{1}$$

where the critical current J_c is a function of H.

We shall apply this equation to a cylinder of radius R in its own magnetic field. If we introduce polar coordinates Z, r, α, it is obvious that H has only an α component, which depends on r only. Then we obtain from Eq. (1)

$$\frac{1}{r}\frac{d}{dr}rH = \frac{dH}{dr} + \frac{H}{r} = J_c\,. \tag{2}$$

We shall first consider the (unrealistic) case for which J_c is constant. Then the integral of Eq. (2) is

$$H = \frac{1}{2}J_c \cdot r + A/2\pi r\,. \tag{3}$$

The constant of integration A can be determined from the total current I:

$$I = 2\pi R \cdot H(R) = \pi R^2 J_c + A\,. \tag{4}$$

A is therefore the difference between the total current and the current one would obtain with a constant current density J_c throughout the wire.

In order to obtain I_m, one has to take into account that Eqs. (1) to (4) hold only for those regions of the wire where flux lines are present,

[14]On temporary assignment. Present address: Institute for Theoretical Physics, University of Kiel, Germany.

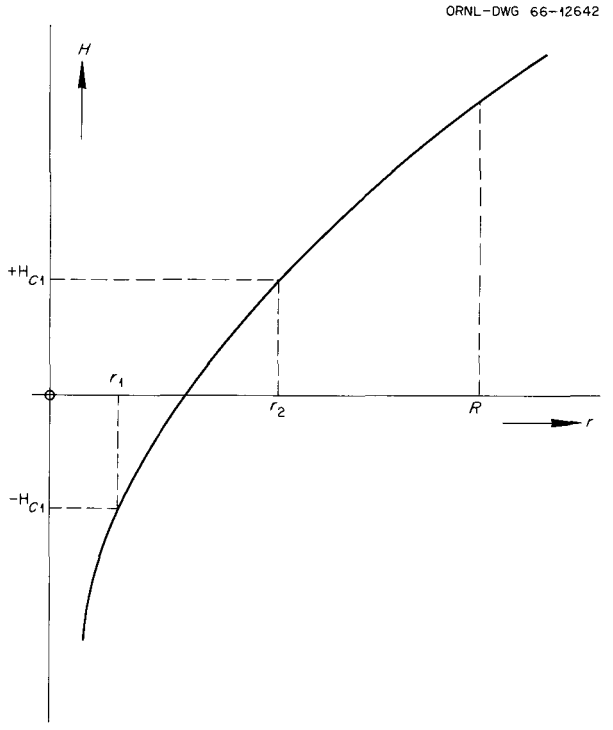

Fig. 9.16. Magnetic Field as a Function of r for Negative A.

that is, where $|H| > H_{c1}$. Let us first assume that A is negative (Fig. 9.16). The condition $|H| > H_{c1}$ is fulfilled for the two regions $0 < r < r_1$ and $r_2 < r < R$, which are separated by a gap which contains no flux lines. However, since the flux lines can only enter from the outside, they cannot penetrate this barrier, and therefore the whole region inside r_2 is free of flux lines and behaves as a type I superconductor.

If we now consider positive values of A, the situation is essentially the same as long as

$$A \leqq 4\pi H_{c1}^2/J_c \,, \tag{5}$$

since in this case the equation

$$H_{c1} = \frac{1}{2} J_c r + A/2\pi r \tag{6}$$

has two real positive roots r_1 and r_2, and Eq. (1) again holds only for $r > r_2$. If, however, Eq. (5) is not fulfilled, then $H > H_{c1}$ everywhere, and Eq. (3) would hold for all r; and H would, after passing though a minimum, go to infinity at $r = 0$. This is clearly an unphysical situation, and therefore Eq. (5) gives the condition for the maximum current. If A has the largest possible value, then Eq. (6) has a double root $r_1 = r_2 = \rho$, with

$$\rho = \frac{H_{c1}}{J_c(H_{c1})} \,. \tag{7}$$

In order to understand the meaning of this critical radius, we go back to Eq. (2). The left side is proportional to the force on a flux line, and consists of two parts: (a) the term dH/dr which comes from the pressure exerted from the adjoining flux lines, and (b) the term H/r. This is due to the fact that the flux lines have a certain free energy per unit length, and therefore circular flux lines tend to shrink like expanded rubber rings.

Equation (7) then expresses the condition that this contracting force is just balanced by the pinning force. As soon as one compresses a circular flux line to a radius smaller than ρ, it starts to contract by itself, and the situation becomes unstationary.

Equation (7) is independent of the special (and unrealistic) assumptions about J_c we have made so far, provided one uses the value of J_c for H_{c1}, as indicated. We have therefore under all circumstances a core of radius ρ into which no flux has penetrated. If the radius of the wire is less than ρ, we cannot get any partial penetration of flux, and the wire behaves like a type I superconductor with a "critical field" H_{c1}. For larger R the maximum current can be formed by integrating Eq. (2) with the initial condition $H = H_{c1}$ for $r = \rho$. Then $I_m = 2\pi RH(R)$. This integration has to be done numerically. As a qualitative illustration, we give the analytical result for the Ansatz

$$J_c = G(H_{c2} - H) \,,$$

which at least satisfies the two conditions that J_c decreases monotonically with H and vanishes at $H = H_{c2}$. We obtain

$$I_m = 2\pi R{\cdot}H(R) = 2\pi RH_{c2}\left(1 - \frac{1}{GR} + A\,\frac{e^{-GR}}{GR}\right),$$

with

$$A = \frac{H_{c2} - H_{c1}}{H_{c2}} \exp\left(\frac{H_{c1}}{H_{c2} - H_{c1}}\right).$$

This formula exhibits two features which are true in the general case: (1) Unless R is very small, the last term in the bracket which comes from the region $r < \rho$ can be neglected. This means, paradoxically, that the condition which determines the maximum current has in most cases very little influence on its actual value. (2) For rather large radii, $I_m \sim 2\pi R H_{c2}$, which means that in the limit of thick wires the maximum current obeys "Silsbee's rule with H_{c2}."

9.5 CURRENT-CARRYING CAPACITY OF A HARD SUPERCONDUCTING WIRE IN ZERO EXTERNAL FIELD (EXPERIMENTAL)

H. A. Ullmaier[15] R. H. Kernohan[16]

The full text of this paper is published in *Phys. Status Solidi* **17**, K233 (1966). The abstract follows:

Using a theory of Koppe, the value of the maximum transport current of a hard superconductor is calculated from the magnetization measured in a longitudinal field. Numerical values obtained in this way for two wire samples of Nb–25% Zr are in good agreement with the experimentally determined critical currents (zero external field).

9.6 AC MEASUREMENTS ON HARD SUPERCONDUCTORS

H. A. Ullmaier[15]

The full text of this paper is published in *Phys. Status Solidi* **17**, 631 (1966). The abstract follows:

Cylindrical samples of Pb-In, Nb-Zr, and Nb-Ta were exposed to a longitudinal, static magnetic field with a colinear alternating field, and the voltages produced in pickup coils wound around the samples were observed on an oscilloscope. The shape of the voltage-time curves can be adequately explained by considering a surface sheath which is able to carry a certain critical surface current and a bulk region where the pinning forces dominate the magnetic behavior. It is shown that an analysis of the voltage-time curves obtained yields values for the critical surface current and the bulk critical current density which are in good agreement with static measurements. While the bulk critical current density goes to zero when the external field reaches the upper critical field H_{c2}, the surface currents can be seen up to a field $H_{c3} > H_{c2}$. Values of the bulk critical current density obtained were then used to determine the pinning force per unit volume and the pinning force on a single vortex line, as a function of the vortex line density.

9.7 IRON-CORE MINIMUM "B" MAGNET

I. Alexeff W. Halchin

Since the last semiannual report the iron-core magnet[17] was modified by the addition of more iron laminations to the pole pieces. The pole pieces, after modification, were in the form of pyramids with base dimensions 23 by 48 in. This change increased the base area of each pole piece by a factor of more than 4. The weight of the assembled magnet (Fig. 9.17) was 5500 lb.

For a center magnetic field of 3 kG, the axial field ratio was 1.6 to 1, and the radial field ratio was 2 to 1. At full power of the facility, there was a field of 9 kG in the center and an axial ratio of 1.2 to 1 and a radial ratio of 1.1 to 1.

Fig. 9.17. Assembled Iron-Core Magnet.

[15]Present address: Institute for Applied Physics, Kernforschungslaboratorium, Jülich, Germany.

[16]Solid State Division.

[17]*Thermonuclear Div. Semiann. Progr. Rept. Apr. 30, 1966*, ORNL-3989, pp. 116–17.

The ratio in the region midway between pole pieces was comparatively low, so a $\frac{1}{2}$-in.-diam steel rod was formed and placed there as shown in Fig. 9.18. For a central field of 7 kG, this arrangement improved the minimum mirror ratio from 1.1 to about 1.3 to 1. From these results it appears that an even larger diameter rod should be placed in this region in order to obtain a higher mirror ratio.

Another iron-core magnet has been assembled with an oblong cavity 16 in. along the axis by 10 in. in diameter. This oblong configuration was chosen to obtain a minimum *B* field with higher mirror ratios.

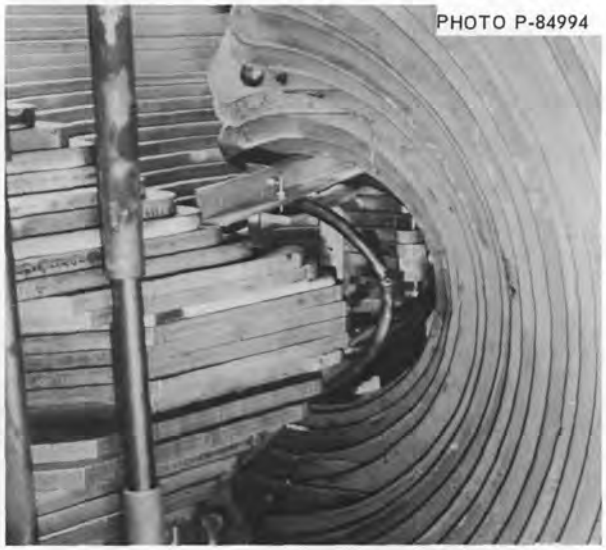

Fig. 9.18. Iron-Core Magnet with $\frac{1}{2}$-in.-diam Rod Between Pole Pieces.

10. Vacuum Studies

R. A. Strehlow[1] D. M. Richardson[1]

10.1 INTERPRETATION OF DCX-2 MASS SPECTRA

Twenty DCX-2 mass spectra obtained during a single day were subjected to detailed examination. Four types of impurity gases (not hydrogen) were distinguished by peak height comparisons. These four types were:

1. those species generated or evolved near the spectrometer,
2. the so-called "base" pressure gases,
3. impurity gases introduced with intentionally admitted gas,
4. impurity gases generated during beam injection.

As noted earlier,[2] the spectrometer species decayed rapidly for 30 to 50 min after the spectrometer filament was turned on. Those species, primarily organic, apparently have no significant relation to gases impinging on the DCX-2 plasma. However, quantitative interpretation of the mass spectra is complicated by their presence.

Of far more significance is the behavior of the base pressure species other than hydrogen. Air leaks have been only occasionally responsible for a significant part of the background gases. Water vapor, carbon dioxide, and methane were the principal identifiable species in the background gas on the day of the study (August 11, 1966); water vapor constituted about three-quarters of the impurity background gases. Although the water partial pressure increased during admission of hydrogen, it was possible to notice the variation of this component of the background during the day. The variation is shown in Fig. 10.1. This dominant change, except during a period of probe adjustment at noon, indicates that the water off-gassing rate increased during the morning and presumably was a thermal effect. Because of the dominance of water vapor and its slow removal from unbaked vacuum systems, a study of some of the parameters affecting water behavior in unbaked stainless steel systems was made separately.[3] The partial pressure of carbon dioxide has been generally observed to follow that of water vapor. The average carbon dioxide partial pressure appeared to be about 15% of the water vapor pressure during the day. Methane (present during the titanium evaporation) was about 5% of the water partial

[1]Reactor Chemistry Division.

[2]*Thermonuclear Div. Semiann. Progr. Rept. Apr. 30, 1966*, ORNL-3989, pp. 128–32.

[3]See sect. 10.3, this report.

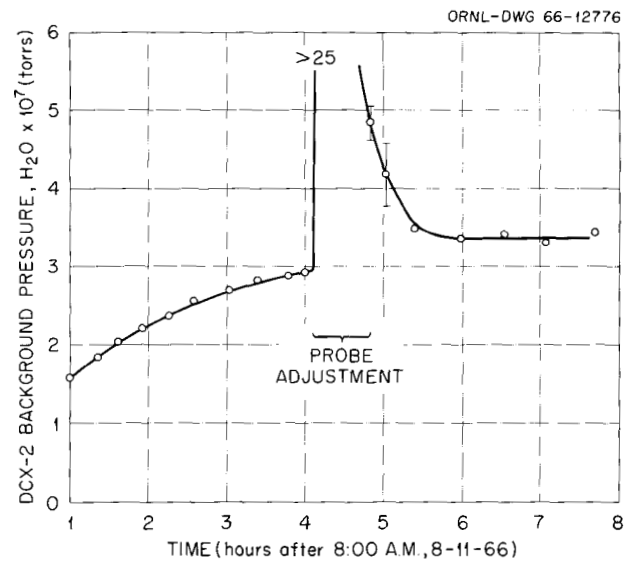

Fig. 10.1. Partial Pressure (H_2O) in DCX-2 (8-11-66) as Function of Time (Background Impurity).

pressure. Other organic species and carbon monoxide comprised the balance of the base pressure gases, but were not studied.

Among the gases introduced along with intentionally admitted gas, water vapor and air have been observed. Air from leaks in the gas manifold is present in amounts which depend upon the length of time subsequent to manifold evacuation as well as the leak rate. Water vapor is usually the dominant manifold impurity, and was for this study. The water partial pressure variation with ion gage reading for a hydrogen leak is shown in Fig. 10.2. The linearity of the data points and the times involved in the exposure indicated that this increase was not an artifact of the spectrometer, but was a net increase of water partial pressure admitted with or due to admission of the hydrogen. The water pressure was observed to vary only slightly during beam injection. It was therefore concluded not to be a gas of the fourth type (gases produced during beam injection).

Figure 10.3 shows the variation of indentifiable species with ion gage reading during beam injection. The fractional contribution of these species is shown in parentheses. Water, though not produced by the injection process, is shown for comparison. The variation of mass 28 (primarily from ethane, ethylene, carbon dioxide, carbon monoxide, and nitrogen) after adjusting for CO_2 and ethane appeared to be primarily carbon monoxide and ethylene, in about equal amounts. The variation of mass 28 so adjusted contributed slightly less to the total pressure than did methane. A fractional abundance of 0.003 to 0.004 for each of these gases relative to hydrogen was indicated. This behavior appeared to be typical for the mode of DCX-2 operation at the time this work was done.

The principal organic species identified as being produced during beam injection were methane, ethylene, acetylene, and ethane. The partial pressure of these gases was found for one day to be about 2.5% of the indicated pressure.

For many plasma experiments in DCX-2 it has not been as necessary to maintain a high-purity environment as to have some knowledge of the purity level. A purity index can be defined as $p_{H_2}/(p_{total} - p_{H_2})$. This index (P.I.) is approximately given by

$$\frac{2.2(p_{ind} - p_{B'})(1 - x)}{x\, p_{ind} + p_{B'}},$$

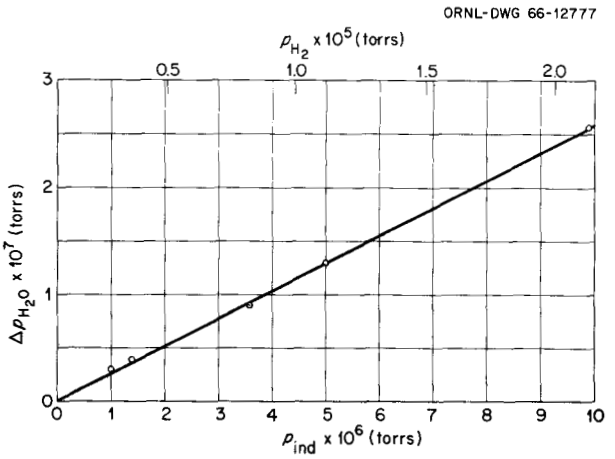

Fig. 10.2. Increase of Pressure of H_2O vs p Indicated (H_2 Admitted from Manifold).

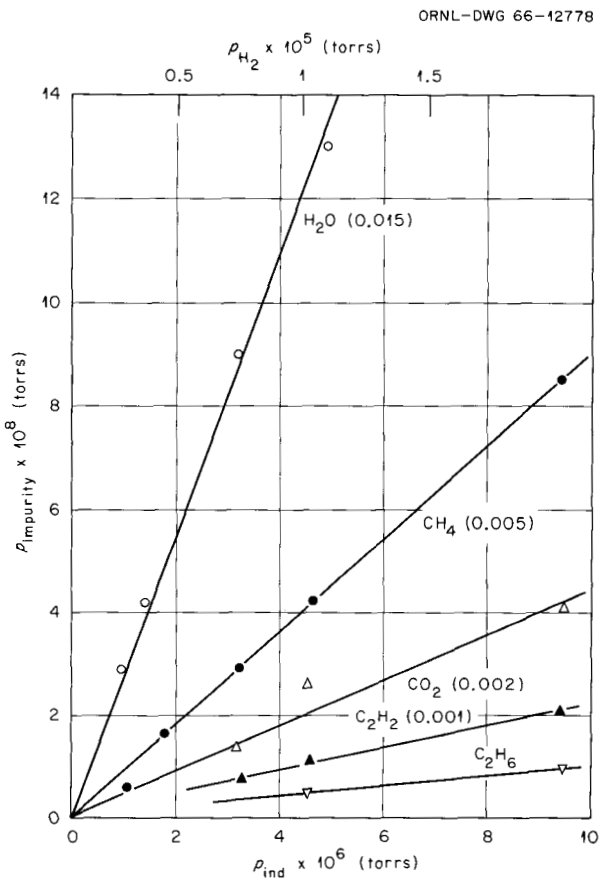

Fig. 10.3. Partial Pressures of CH_4, CO_2, C_2H_2, and C_2H_6 (Produced Impurities) in DCX-2 (8-11-66) During Injection vs H_2 Partial Pressures (p_{H_2O}, see Fig. 10.2, Is Shown for Comparison).

where

2.2 is the ion gage factor for H_2,

p_{ind} is the indicated ion gage pressure,

$p_{B'}$ is the partial pressure of "base" pressure contaminants other than H_2,

x is the fraction of the ion gage reading (p_{ind}) due to contaminants produced by the injection, introduced with bleed gas, or generated by these species (a gage factor of unity is assumed).

For the data described here, using the values

$p_{ind} = 2 \times 10^{-6}$ and 9×10^{-6} torr,

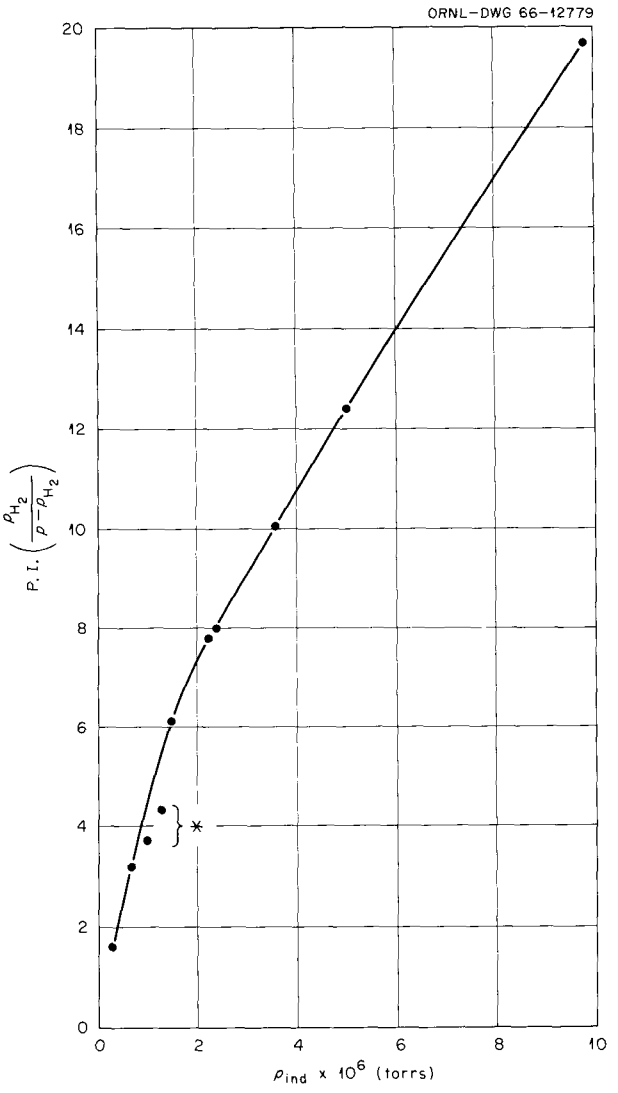

Fig. 10.4. Purity Index Variation (DCX-2, 8-11-66) vs Uncorrected Ion Gage Reading.

$p_{B'} = 3.5 \times 10^{-7}$ torr,

$x = 0.057$ (based on the mass spectral analysis),

one obtains, for the two indicated pressures, purity indexes of 7.0 and 20.8 respectively. The data obtained on August 11 yielded the purity index variations as shown in Fig. 10.4. These data were obtained over a period of several hours in the morning when the water partial pressure was increasing as discussed above. The points at indicated pressures of 1.0 and 1.3×10^{-6} torr, which were obtained later, were accordingly somewhat lower than the values interpolated from the earlier determinations. The agreement of the calculated values of P.I. with those shown in Fig. 10.4 indicates that unidentified species are not present in significant amounts.

Residual gas analysis strongly depends on the useful mass range of the spectrometer, the existence of identifiable parent mass peaks, and a knowledge of fragmentation patterns. We have little knowledge of species with molecular weights higher than 44 for the DCX-2 spectrometer, or higher than about 92 for the instrument used in the calibration and chemistry studies. A spectrometer design study has been started with the goal of improving the analytical capability.

10.2 MASS SPECTROMETER CALIBRATION STUDIES

Dispersion of mass spectrometer ion beams affects both the cracking patterns and the relative partial pressure sensitivities for different gases. Calibration studies carried out with the type of mass spectrometer used on DCX-2 (Veeco model RGA-3) showed that the instrument has a significant degree of mass dispersion. This dispersion is attributable to space-charge effects and to thermal velocities in the direction parallel to the magnetic field, during the ion's life.

Space-charge effects at higher pressures were observed as a diminution of ion intensities upon increasing the hydrogen pressure. As expected, this effect is most pronounced for gases of higher molecular weight, for example, Ar and Kr. Hydrogen pressures of as much as 2 to 3×10^{-5} torr were needed before a significant decrease of the 28 and 18 mass peaks occurred.

Table 10.1. Relative Transmissions for the RGA-3 Spectrometer

M/e	Species	Estimated Fraction Transmitted Analyzer Region Only	Experimental Fraction Transmitted Entire Flight Path
12	CO	1.0	1.0
18	H_2O	0.9	0.8
28	CO	0.7	$\approx$0.4 – 0.5
44	CO_2	0.5	0.2
78	C_6H_6	0.2	
2	Low mass range, H_2 [a]	0.98	
18	Low mass range, H_2O	0.1	$\approx$0.1

[a]Low masses are obtained by shunting the magnet, which reduces the field by a factor of about 0.55.

At lower pressures the mass discrimination can be attributed principally to thermal drift in the direction of the magnetic field during the flight time of ions to the collector. Estimation of this effect for the analyzer region only, using as parameters the flight path (23 cm), the ion velocity derived from the ion energy meter, the average thermal velocity (at 100°C), and relative spectrometer slit lengths, leads to the estimated transmissions listed in Table 10.1 along with the transmission as determined from experimental data described below. The observed transmission fractions were uniformly lower than those estimated. This is presumably due to mass discrimination in the source. For this 60° spectrometer (supplied with almost equal source and collector slit lengths), it should be possible to decrease the mass discrimination of the analyzer region by perhaps 60%, but probably with little overall improvement of this parameter because of the source contribution.

The method used to experimentally determine the extent of mass discrimination was simply to measure the peak height ratios for A (+1, +2, and +3) and compare these with the literature values.[4] (The electron energy for the RGA-3 is 145 ± 4 V.) The same technique applied to the spectrometer on DCX-2 yielded similar results. The data shown in Table 10.1 were estimated using a smooth curve drawn through the points at M/e = 13.3, 20, and 40. Relative calibration of the spectrometer to an ion gage for nitrogen and water vapor yielded additional points within 15 and 5%, respectively, of the derived argon transmission curve. The ion gage sensitivity factor for water vapor was incidentally determined from measured flow rates, assuming the pumping speed for water vapor to be $\sqrt{28/18}$ that of nitrogen (with water cooling of the trap). This value of the gage sensitivity of water vapor was found to be 0.9 ± 3% that of nitrogen.

These data were used in the measurement of contaminant levels in the DCX-2 work described above. The results should not be indiscriminately applied to other similar analyzers, because the extent of mass discrimination is strongly affected by operating parameters such as repeller potential. In order to avoid overly harsh evaluation, two things should be noted. The first is that residual gas analyzers are designed primarily for qualitative assessment of vacuum conditions and that their application to quantitative work is usually restricted to individual mass peaks or simple ratios. The second is that the analytical capability is restricted generally to masses less than 44. The spectrometer model used in our studies performs these tasks well. The need for more quantitative data, however, does markedly strain the instrument's capability.

[4]H. S. W. Massey and E. H. S. Burhop, *Electronic and Ionic Impact Phenomena*, p. 38, Oxford Clarendon Press, Oxford, England, 1956.

10.3 WATER VAPOR CHEMISORPTION ON STAINLESS STEEL

The dominance of water vapor impurity in DCX-2 and the lack of information about its sorption kinetics prompted a study of water sorption at low partial pressures. The results of the study showed distinctly that chemisorption occurred in the experimental vacuum system. The experiments were conducted in a manner to give assurance that the observed chemisorption occurred primarily on stainless steel surfaces. Thus, since a large body of information on chemisorption exists,[5] the description of water vapor behavior in vacuum systems can be greatly simplified. Specifically, a selection from empirical relations between the extent of sorption and time, exposure, pressure, and temperature, which are observed for other chemisorption reactions, may be applied to studies of water vapor.

Chemisorption may be distinguished from physical adsorption using several criteria, including the following:

1. Chemisorption requires an appreciable (>0.1 eV) heat of activation.
2. Chemisorption usually involves sorption heat values greater than about 0.5 to 1.0 eV, whereas physical adsorption is usually associated with smaller values.
3. Chemisorption or chemi-desorption is (as a consequence of item 1) a slow process.
4. The quantity of substance chemisorbed often is related to time by the empirical relation

$$dq/dt = ae^{-\alpha q} , \qquad (1)$$

where q is the amount sorbed at time t, and a and α are constant during any *single* experiment or at the very least have discontinuous derivatives with respect to time during a single experiment.

Water chemisorption studies have been made for ThO_2,[6,7] Al_2O_3,[6,8] TiO_2,[9,10] and SiO_2 (ref. 11) sorbents, principally calorimetically. (Infrared, gravimetric, and pressure-change techniques have also been used.) No report has been found in the literature on water sorption kinetics at low pressures ($<10^{-4}$ torr) or on metals.

The technique used in this study was to observe the pressure fall after water vapor exposures at different pressures and durations in a dynamically pumped vacuum system, Fig. 10.5. The apparatus was designed to have two regions, *A* and *B*, which could be separately heated. To minimize temperature nonuniformity, region *A*, a steel tube with 1.1×10^4 cm^2 area, was baked by resistance heaters strapped to the outside of an aluminum pipe which fitted concentrically around the steel tube with a uniform ½-in. gap. Insulation material and aluminum foil were applied around the aluminum pipe. A copper tubing cooling circuit was strapped to the steel tube in order to achieve a rapid cooling capability. Region *B* down to below the conductance limiting baffle was heated with strapped-on and serpentine heaters, and an air heater assembly to heat the trap. The mass spectrometer (Veeco RGA-3) was heated with tape heaters. Glass ion gages

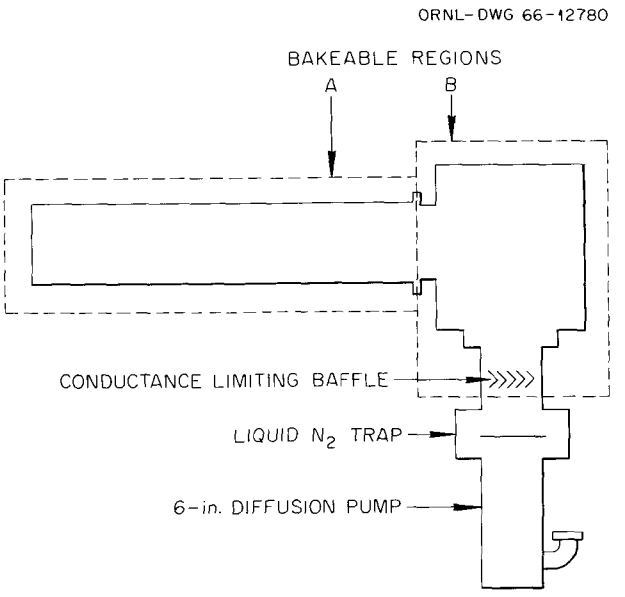

Fig. 10.5. Vacuum System Used for the Studies of Water Vapor Chemisorption.

[5]The review article by M. J. D. Low with 342 references is especially recommended; *Chem. Rev.* **60**, 267–312 (1960).

[6]M. E. Winfield, *Australian J. Chem.* **6**, 221 (1953).

[7]H. F. Holmes, L. L. Fuller, and C. H. Secoy, *J. Phys. Chem.* **70**, 436 (1966).

[8]R. L. Venable, W. H. Wade, and N. Hackerman, *J. Phys. Chem.* **69**, 317 (1965).

[9]C. M. Hollabaugh and J. J. Chessick, *J. Phys. Chem.* **65**, 109 (1961).

[10]W. D. Haskins and G. Jura, *J. Am. Chem. Soc.* **66**, 919 (1944).

[11]J. W. Whalen, *J. Phys. Chem.* **65**, 1876 (1961).

(used only for early experiments) were heated by lamps. Only metal seals were used.

The water was admitted through a valve from a regulated pressure of 1 or 2 torrs. The gas line was periodically baked and was operated with cold water cooling to minimize organic contamination. Water vapor with less than 0.03% total organic contamination could be admitted to the system. Two temperature conditions were studied. The elevated temperature condition was 180 ± 20° (as monitored by several thermocouples) for all regions of the apparatus. The lower temperature condition was reached following a rapid cooling of region *A* to 28°C. The temperature of region *B* was not changed. At the elevated temperature, typical partial pressures in torrs were 3×10^{-8} H_2, $4\text{–}8 \times 10^{-10}$ H_2O, and $1\text{–}2 \times 10^{-9}$ CO (produced almost entirely by gage and spectrometer filaments). No effort was made to reduce the hydrogen pressure by higher temperature baking, since the gas under study was water.

Water was admitted for periods of time ranging from about 0.5 sec to as long as 30 min, after which the valve was closed and the exhaust curve was obtained. The partial pressure of water was followed by monitoring mass 18 with the spectrometer. As was expected, agreement with glass ion gages was good only when the gages were heated. For most of the determinations, however, to minimize the possibility that the glass might be affecting the results, they were replaced by nude gages.

For the hot-system short-exposure cases, the slope of log p_{H_2O} vs t (the usual exhaust relation) initially corresponded to a value of 540 liters/sec ± 10% except when the initial pressure exceeded 1×10^{-5} significantly; for these cases the mass 18 spectrometer peak was not exactly proportional to pressure.

Four typical log p_{H_2O} vs log t plots are shown in Fig. 10.6 for the cases of hot and cold region *A* and for 0.5-sec and 10-min exposures. The exposure pressures, p_{exp}, were all within 20% except for case II, where p_{exp} was about a factor of 5 lower. Exponential exhaust, indicated for water by curve V, was observed for N_2 over almost four orders of magnitude of pressure.

We observed that the log p_{H_2O} vs log t plot of our data closely approximated straight lines of reproducible slopes which, of course, varied with exposure conditions.[12] Integrating each curve from the extrapolated limit of 0.1 to 1000 sec and multiplying the result by our measured H_2O pumping speed (590 liters/sec ± 3%) yielded the quantity desorbed isothermally following the exposure. The value of q (quantity absorbed) is believed to be within 20% of the measured quantity desorbed.

The Elovich plots (Eq. 1) from our data for two temperatures and normalized to the same exposure pressure (assuming variation of q with the first power of p_{exp}) are shown in Fig. 10.7. The exposure pressures were from 0.7 to 4.0×10^{-5} torr. Determination of q for exposure pressures as low as 4×10^{-7} torr led to the following relation of q and p_{exp}:

$$q = p_{exp}^{\,1.05 \pm 0.1} f(t_{exp}) .$$

The only study found in the literature of the pressure dependence of q is that of Winfield,[6] who reported an exponent of 1.2 with thoria at, of course, higher water vapor pressures. The value of 1.2 introduces an error band of somewhat less than 15% to our data. The quantities observed correspond to about 0.1 monolayer at room temperature following a 10-min exposure and about 0.15 monolayer after 30 min. Dust or other impurities could be responsible for some or even all of the observed sorption. We believe, however, that the method is reliable and that sufficient care was exercised to be able to attribute the observed chemisorption to the steel surface.

Some effect on water chemisorption kinetics by ion or electron bombardment is to be anticipated by analogy to other chemisorption phenomena. Neither the magnitude nor the direction of change seems to be presently predictable. Water sorption by unbaked and baked stainless steel during a pressure excursion to an atmosphere of different humidities has been observed and is reported in the literature, but with inadequate reported data to permit scaling the parameters studied here over the required five to six orders of magnitude. Samples with different specific surface areas may be expected to show different sorption capabilities.

The conclusion that water chemisorption phenomena exist leads to possible practical application in operating nonbakeable vacuum systems. First,

[12]See: J. Howard and H. S. Taylor, *J. Am. Chem. Soc.* **56**, 2259 (1934), and other references in Low, *op. cit.*, ref. 5.

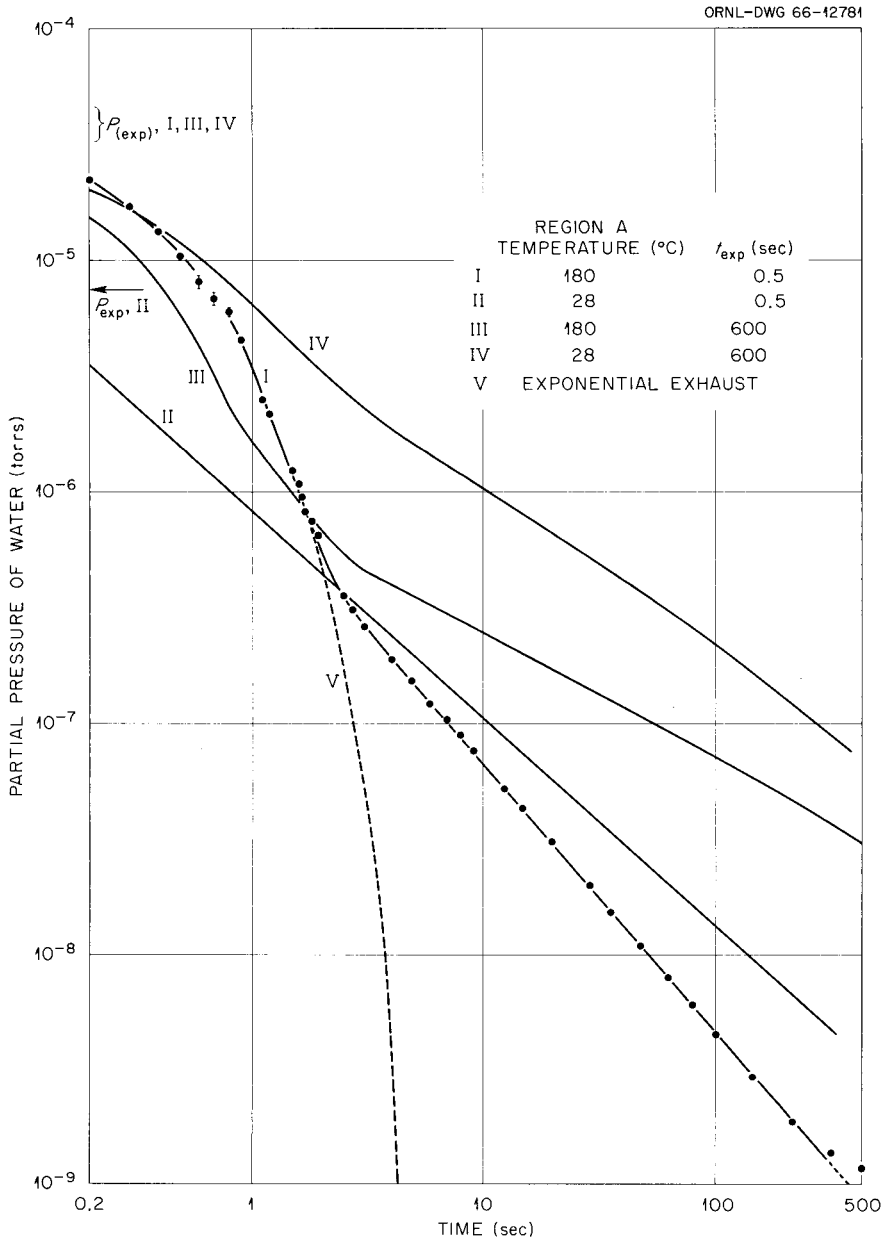

Fig. 10.6. Typical Log p_{H_2O} vs Log t (sec) Plots for Four Exposure Conditions.

since chemisorption occurs at even very low pressures and is a strong function of exposure time, maintenance of very low partial pressures of water by liquid-nitrogen cooling of appreciable areas in the system followed by intermittent warming of the cooled areas, desorption, and rapid exhaust should result in a lower water impurity level than the same period of pumping would produce. Another consequence of the observations reported here is that even small water impurity levels introduced from gas manifolds are expected to result in significant impairment of the base pressure of water vapor.

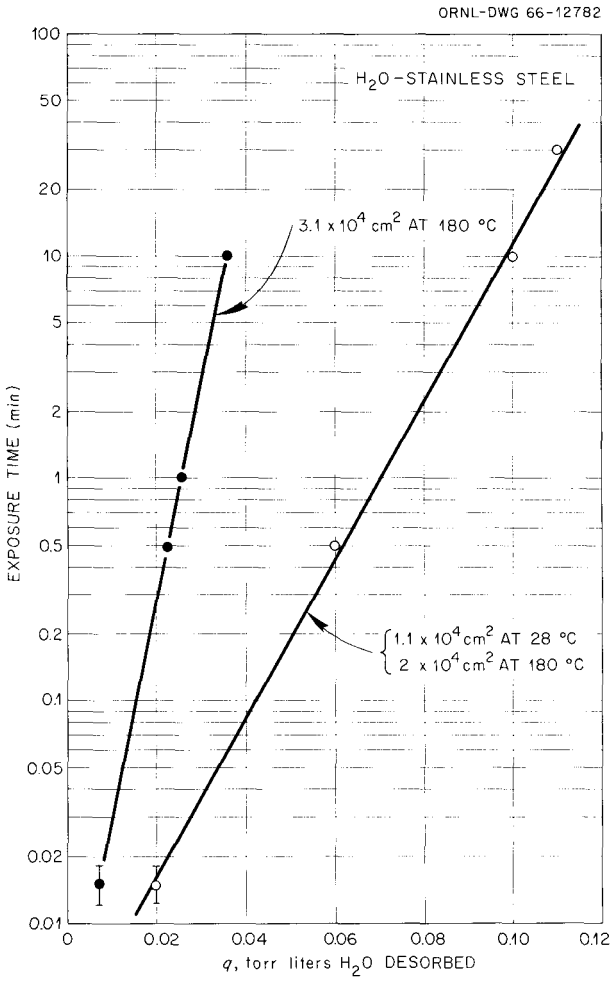

Fig. 10.7. Elovich Plots for Water Chemisorption on Stainless Steel.

10.4 DECOMPOSITION OF DC-705 DIFFUSION PUMP FLUID

A white solid was found condensed on the cold caps and wall of one 10-in. diffusion pump on the DCX-2 vacuum system. It melted sharply at 47°C. The infrared spectrum[13] was not distinguishable from that of the diffusion pump fluid, a pentaphenyl trimethyl trisiloxane, structure I, below:

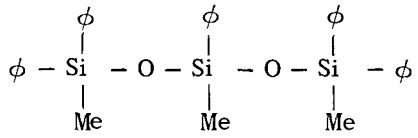

(I)

($\phi = C_6H_5$, $Me = CH_3$.)

The manufacturer indicated that decomposition to the dimer might occur if the operating temperature were too high, in a radiation field, or if the fluid were heated in the presence of alkali impurities in the pump. Proton nuclear magnetic resonance (60 Mc) spectra were obtained[14] for the solid and for a sample of the pump fluid. The results are summarized in Table 10.2.

The dimer structure II (below) may therefore be assigned to the solid material:

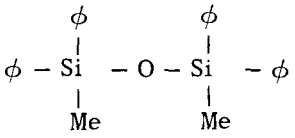

(II)

It would appear that for the pump in question some period of excessive temperature operation probably occasioned the decomposition. The observed lowered pumping speed of this pump was presumably caused by the deposit.

[13]G. Goldberg and H. L. Holsopple, Jr., Analytical Chemistry Division.

[14]J. R. Lund, Analytical Chemistry Division.

Table 10.2. Proton NMR Spectra of DC-705 Diffusion Pump Oil and a Decomposition Product

Signal Position	Height of Integral (mm)	Height × 0.1344	Protons per Signal	Assignment
		Structure I, 34 protons		
0				Me_4Si, reference
19	22	2.96	3	Me
32	46	6.18	6	2 equivalent Me groups
435	185	24.86	25	5 equivalent ϕ groups
	253 mm			
	0.1344 protons/mm			

Signal Position	Height of Integral (mm)	Assumed Group	Height / Protons per Group	Assignment
		Unknown Solid		
0				Me_4Si, reference
34	57	Me	19	2 equivalent Me groups per
436	196	ϕ	39.6	4 equivalent ϕ groups

11. Design and Engineering: Service Report

Design and engineering services are generally reported incidentally with those of the research groups of the Division. This work includes executing or coordinating engineering design, shop fabrication, building operations, and maintenance for the Division.

Design activities for this reporting period are summarized as follows:

Jobs on hand 5-1-66 on which work had not started	5
New jobs received	130
Total jobs	135
Jobs completed	123
Jobs in progress	6
Backlog of jobs 10-31-66	6
Total drawings completed for period (does not include drawings for slides, reports, etc.)	187

Shop fabrication for this reporting period is summarized as follows:

Machine shops	
Completed jobs requiring 16 man-hours or less	90
Completed jobs requiring 17 to 1200 man-hours	154
Completed jobs of miscellaneous character (in plating, carpenter, electrical, glass, lead, etc., shops)	62
Average manpower per week (Machine Shop)	12.2
Average manpower per week (miscellaneous)	2
Number of jobs in progress	24
Electromagnet fabrication	
Completed jobs	7
Number of jobs in progress	2
Completed jobs by outside contractors (Paducah)	1
Average manpower per week	2

Two additional motor-generator sets have been installed. Each set includes two tandem 2.5-MW generators driven by a common motor. These units bring the total available dc power to 35 MW, continuous operation.

Publications, ORNL Reports, and Papers

OPEN LITERATURE

Author(s)	Title of Article	Journal (or Book)
I. Alexeff, W. D. Jones, and John Lohr[1]	A Plasma Decay Technique to Measure Density in Discharge Tubes	*Phys. Fluids* **9**, 1403 (1966)
I. Alexeff, W. D. Jones, R. V. Neidigh, W. F. Peed, and W. L. Stirling	Plasma Heating and Burnout in Beam-Plasma Interaction	Pp. 781–98 in *Proc. Conf. Plasma Physics and Controlled Nuclear Fusion Research, Culham, England, 6–10 Sept. 1965*, IAEA, Vienna, 1966, STI/PUB/111, vol. II
I. Alexeff and W. D. Jones	Observations on the Velocity of Moving Striations	*Phys. Fluids* **9**, 1871 (1966)
W. B. Ard, R. A. Dandl, and R. F. Stetson[2]	Observations of Instabilities in Electron-Cyclotron Plasmas	*Phys. Fluids* **9**, 1498 (1966)
P. R. Bell	Demonstration of Vacuum Welding of Olivine	*Science* **153**, 410 (1966)
P. R. Bell and G. G. Kelley	Pressure Fluctuations in Vacuum Systems	*Vacuum* **16**, 241 (1966)
P. R. Bell, R. A. Dory, G. E. Guest, G. G. Kelley, N. H. Lazar, J. F. Lyon, and R. F. Stratton	Apparent High-Frequency Stability of a Highly Anisotropic Plasma	*Phys. Rev. Letters* **16**, 1152 (1966)
P. R. Bell, R. A. Gibbons,[3] G. G. Kelley, N. H. Lazar, J. F. Lyon, and R. F. Stratton	The Oak Ridge Multiple-Pass Injection Experiment, DCX-2	Pp. 77–91 in *Proc. Conf. Plasma Physics and Controlled Nuclear Fusion Research, Culham, England, 6–10 Sept. 1965*, IAEA, Vienna, 1966, STI/PUB/111, vol. II

[1] 1965 summer participant from the University of Texas.

[2] 1965 research participant from Florida Atlantic University.

[3] Deceased.

Author(s)	Title of Article	Journal (or Book)
R. A. Dandl, W. B. Ard, A. C. England, G. M. Haas, and N. H. Lazar	Energetic Neutral Injection into an Electron-Cyclotron Plasma	Pp. 153–60 in *Proc. Conf. Plasma Physics and Controlled Nuclear Fusion Research, Culham, England, 6–10 Sept. 1965*, IAEA, Vienna, 1966, STI/PUB/111, vol. II
J. L. Dunlap, H. Postma, G. R. Haste, and L. H. Reber[3]	Severe Microinstability-Driven Losses in an Energetic Plasma	Pp. 67–75 in *Proc. Conf. Plasma Physics and Controlled Nuclear Fusion Research, Culham, England, 6–10 Sept. 1965*, IAEA, Vienna, 1966, STI/PUB/111, vol. II
D. Gorman[4]	Plasma Waves at Singular Turning Points	*Phys. Fluids* **9**, 1262 (1966)
G. E. Guest and T. K. Fowler	Anomalous Plasma Diffusion in Magnetic Wells	Pp. 383–92 in *Proc. Conf. Plasma Physics and Controlled Nuclear Fusion Research, Culham, England, 6–10 Sept. 1965*, IAEA, Vienna, 1966, STI/PUB/111, vol. I
G. E. Guest and C. O. Beasley, Jr.	Cold Plasma Effects in Finite Length Plasmas	*Phys. Fluids* **9**, 1798 (1966)
David Montgomery[5] and I. Alexeff	Parametric Excitation of Transverse Waves in a Plasma	*Phys. Fluids* **9**, 1403 (1966)
David Montgomery[5] and I. Alexeff	Alternative Method for Exciting Electron Plasma Oscillations with Transverse Electromagnetic Waves	*Phys. Fluids* **9**, 2075 (1966)
H. A. Ullmaier	Über den Einfluss von Oberflächenströmen auf die Wechselstromverluste harter Supraleiter	*Phys. Letters* **21**, 507 (1966)

ORNL REPORTS

Author(s)	Title	Number	Date
J. R. McNally, Jr.	Preliminary Report on Ball Lightning	ORNL-3938	May 1966
A. H. Snell *et al.*	Thermonuclear Division Semiannual Progress Report for Period Ending April 30, 1966	ORNL-3989	August 1966
I. Alexeff, W. Halchin, W. D. Jones, and J. F. Potts	Plasma-Density Measurement in a Hollow-Cathode Arc by Arc Reversal	ORNL-4010	September 1966

[4] 1965 summer participant from Washington University, St. Louis, Mo.

[5] Consultant from State University of Iowa, Iowa City.

Author(s)	Title	Number	Date
P. R. Bell, G. G. Kelley, N. H. Lazar, and J. F. Lyon	Present Status and Objectives of the DCX-2 Experiment	ORNL-4011	September 1966
J. G. Hirschberg[6] and W. I. Fried[7]	A Fabry-Perot Duochromator for the Measurement of Small Wavelength Displacements of Spectral Lines	ORNL-4019	November 1966
W. F. Gauster, K. R. Efferson, J. B. Hendricks, R. H. Kernohan,[8] H. W. Koppe,[9] H. A. Ullmaier,[10] and W. R. Wilkes[11]	Experimental Simulation of Large, High Field, Superconducting Magnet Operation	ORNL-TM-1598	August 1966

[6]Summer faculty, ORNL, 1966; Head, Department of Physics, University of Miami, Coral Gables, Florida.

[7]1966 summer participant from the University of Miami.

[8]Solid State Division.

[9]Now at Institute for Theoretical Physics, University of Kiel, Germany.

[10]Now at Institute for Physics, Jülich, Germany.

[11]1966 research participant from Wake Forest College, Winston-Salem, N.C.

PAPERS PRESENTED AT SCIENTIFIC AND TECHNICAL MEETINGS

Seminar on Research Safety, U.S. Academy of Sciences, Washington, D.C., May 18–19, 1966

H. C. Hoy, "Research Safety."

Annual Meeting, Society of Nuclear Medicine, Philadelphia, Pa., June 23–25, 1966

D. A. Ross, "The Measurement of Radiation from a Patient."

American Physical Society, Division of Plasma Physics, Minneapolis, Minn., June 20–22, 1966

I. Alexeff, W. Halchin, W. D. Jones, and J. F. Potts, "Plasma Density Measurement in a Hollow-Cathode Arc by Arc Reversal."

R. A. Dory, "Relativistic Instability in Hot Ion Plasmas."

J. R. McNally, Jr., and M. R. Skidmore, "Further Studies on Excitation-Heating of Ions."

W. L. Stirling, I. Alexeff, W. D. Jones, R. V. Neidigh, and V. J. Meece, "Production of a Hot-Electron Plasma Blanket."

Institute of Austrian Electrical Engineers, Vienna, Austria, Sept. 21, 1966

W. F. Gauster, "Über Supraleitfähigkeit und einige ihrer technischen Anwendunger" (On Superconductivity and Some of Its Technical Applications).

Colloque International Sur Les Champs Magnetiques Intenses: Leur Production, Leurs Applications, Grenoble, France, Sept. 12–14, 1966

W. F. Gauster, "The Large Volume, High Uniformity Magnets at the Oak Ridge National Laboratory."

Symposium on Engineering Problems of Controlled Thermonuclear Research, Gatlinburg, Tenn., Oct. 3–5, 1966

J. S. Culver, "A Cryogenically Cooled, Scanning Energy Spectrometer."

R. C. Davis, R. R. Hall, G. G. Kelley, O. B. Morgan, and R. F. Stratton, "Engineering Problems in the Production and Use of Intense d.c. Ion Beams."

H. O. Eason, Jr., "CW Microwave Systems for Electron-Cyclotron Resonance Heating."

R. S. Edwards and H. Postma, "A Method for Introducing Energy Spread in Injection Machines."

W. F. Gauster, "On the Stability of Superconducting Magnets."

W. Halchin, "Iron-Core Minimum (B) Magnet."

W. J. Leonard,[1] "Investigations of Material Failures in the DCX-1 Liner."

J. N. Luton, Jr., "Ribbon Coils for High Current Densities."

O. D. Matlock, "Mechanical Design and Methods for Constructing Plasma Probes."

J. A. Ray and C. F. Barnett, "Detection of Energetic Neutral Particles."

---

[1]Metals and Ceramics Division.

ORNL-4063
UC-20 – Controlled Thermonuclear Processes

INTERNAL DISTRIBUTION

1. I. Alexeff
2. W. B. Ard
3. C. F. Barnett
4. C. O. Beasley
5. M. C. Becker
6-11. P. R. Bell
12. D. S. Billington
13. C. W. Blue
14. C. J. Borkowski
15. G. E. Boyd
16. R. L. Brown
17. R. E. Budwine
18. J. F. Clarke
19. D. L. Coffey
20. R. J. Colchin
21. F. L. Culler
22. J. S. Culver
23. R. A. Dandl
24. R. C. Davis
25. S. M. DeCamp
26. R. A. Dory
27. J. L. Dunlap
28. H. O. Eason, Jr.
29. R. S. Edwards
30. K. R. Efferson
31. A. C. England
32. J. C. Ezell
33. W. M. Farr
34. J. L. Fowler
35. J. E. Francis, Jr.
36. J. H Frye, Jr.
37. W. F. Gauster
38. D. A. Griffin
39. W. R. Grimes
40. G. E. Guest
41. E. Guth
42. W. Halchin
43. C. C. Harris
44. G. R. Haste
45. J. B. Hendricks
46. K. C. Hines
47. J. L. Horton
48. H. C. Hoy
49. R. P. Jernigan, Jr.
50. W. D. Jones
51. M. A. Kastenbaum
52. G. G. Kelley
53. M. T. Kelley
54. M. O. Krause
55. D. M. Kroeger
56. C. E. Larson
57. R. A. Langley
58. N. H. Lazar
59. G. F. Leichsenring
60. W. J. Leonard
61. J. Lewin
62. R. S. Livingston
63. J. N. Luton, Jr.
64. J. F. Lyon
65. H. G. MacPherson
66. F. C. Maienschein
67. J. R. McNally, Jr.
68. O. D. Matlock
69. D. B. Nelson
70. R. V. Neidigh
71. J. Neufeld
72. C. E. Parker
73-74. R. B. Parker
75. H. Postma
76. F. M. Rankin
77. J. A. Ray
78. R. G. Reinhardt
79. D. M. Richardson
80. M. Roberts
81. D. A. Ross
82. P. W. Rueff
83. H. E. Seagren
84. D. J. Sigmar
85. E. D. Shipley
86. J. E. Simpkins
87. M. J. Skinner
88-107. A. H. Snell
108. W. L. Stirling
109. R. F. Stratton, Jr.
110. R. A. Strehlow
111. E. H. Taylor
112. H. L. Watts
113. A. M. Weinberg

114. E. R. Wells
115. G. C. Williams
116. W. L. Wright
117. O. C. Yonts
118. Gale Young
119. A. Bers (consultant)
120. P. B. Burt (consultant)
121. Owen Eldridge (consultant)
122. J. W. Flowers (consultant)
123. D. C. Freeman, Jr. (consultant)
124. M. W. Garrett (consultant)
125. H. Grad (consultant)
126. G. M. Haas (consultant)
127. E. G. Harris (consultant)
128. G. W. Hoffman (consultant)
129. J. W. Hooper (consultant)
130. V. W. Hughes (consultant)
131. W. E. Hunt (consultant)
132. D. W. Martin (consultant)
133. E. W. McDaniel (consultant)
134. D. R. Montgomery (consultant)
135. S. H. Neff (consultant)
136. C. E. Nielsen (consultant)
137. J. M. Reynolds (consultant)
138. H. S. Robertson (consultant)
139. H. E. Rorschach (consultant)
140. D. J. Rose (consultant)
141. P. M. Stier (consultant)
142. T. H. Stix (consultant)
143. R. Sugihara (consultant)
144. E. W. Thomas (consultant)
145. J. H. Wise (consultant)
146-165. Thermonuclear Div. Library
166. Biology Division Library
167-169. Central Research Library
170. Laboratory Shift Supervisor
171-246. Laboratory Records Department
247. Laboratory Records, ORNL R.C.
248-249. ORNL – Y-12 Technical Library Document Reference Section

EXTERNAL DISTRIBUTION

250. P. L. Auer, College of Engineering, Cornell University, Ithaca, N.Y.
251. L. M. Branscomb, Joint Institute, Laboratory of Astrophysics, Boulder, Colorado
252. S. C. Brown, Massachusetts Institute of Technology, Cambridge, Mass. 02139
253. S. J. Buchsbaum, Bell Telephone Laboratories, Murray Hill, N.J. 67971
254. O. Buneman, Stanford Electronics Laboratories, Stanford, Calif. 94305
255. Director, Technical Library, Defense Atomic Support Agency, Sandia Base, Albuquerque, New Mexico
256. W. A. Fowler, Calif. Inst. Technology, 1201 E. Calif. Blvd., Pasadena, Calif. 91109
257. F. W. Crawford, Stanford Electronics Laboratories, Stanford, Calif. 94305
258. M. B. Gottlieb, Princeton University, Princeton, New Jersey 08540
259. W. W. Grigorieff, Asst. to the Executive Director, Oak Ridge Associated Universities
260. J. G. Hirschberg, Dept. of Physics, Univ. of Miami, Coral Gables, Fla. 33124
261. D. W. Kerst, Univ. of Wisconsin, Madison, Wisconsin 53706
262. A. C. Kolb, Naval Research Laboratory
263. Morton A. Levine, Air Force Cambridge Research Laboratories
264. H. W. Lewis, Physics Dept., Univ. of California, Santa Barbara, Calif. 93106
265. J. S. Luce, Aerojet-General Nucleonics, P.O. Box 77, San Ramon, Calif.
266. J. A. Phillips, Los Alamos Scientific Laboratory
267. J. F. Potts, Union Carbide Corp., Parma Technical Center, P.O. Box 6116, Cleveland, Ohio 44101
268. R. F. Post, University of California, Lawrence Radiation Laboratory
269. John R. Roth, NASA Lewis Research Center (Mail Stop 301-1), 21000 Brookpark Road, Cleveland, Ohio 44135
270. A. E. Ruark, Division of Research, AEC, Washington

271. Russell Shelton, Chief, Nuclear and Plasma Physics Branch, Marshall Space Flight Center, Huntsville, Alabama 35812
272. Albert Simon, Dept. of Mechanical and Aerospace Sciences, University of Rochester, Rochester, N.Y.
273. L. D. Smullin, Massachusetts Institute of Technology
274. J. A. Swartout, 270 Park Avenue, New York, New York
275. R. F. Taschek, Los Alamos Scientific Laboratory
276. C. M. Van Atta, University of California, Lawrence Radiation Laboratory

277-278. Research and Development Division, AEC, ORO (1 copy each to H. M. Roth and R. B. Martin)

279-282. Controlled Thermonuclear Research Branch, AEC, Washington (A. S. Bishop)

283-292. USAEC, Division of Research, Controlled Thermonuclear Research Program (Stephen O. Dean)

293-554. Given distribution as shown in TID-4500 under Controlled Thermonuclear Processes category (25 copies – CFSTI)